

# Evolution of nuclear structure in exotic nuclei and nuclear forces

Takaharu Otsuka

*Department of Physics and Center for Nuclear Study,  
University of Tokyo,  
Hongo, Bunkyo-ku,  
Tokyo 113-0033,  
Japan*

*RIKEN Nishina Center,  
2-1 Hirosawa, Wako,  
Saitama 351-0198,  
Japan*

*Instituut voor Kern- en Stralingsphysica,  
Katholieke Universiteit Leuven, B-3001 Leuven,  
Belgium*

*National Superconducting Cyclotron Laboratory,  
Michigan State University,  
East Lansing, Michigan 48824,  
USA*

*Department of Physics and Astronomy,  
Michigan State University,  
East Lansing, Michigan 48824,  
USA*

Alexandra Gade

*National Superconducting Cyclotron Laboratory,  
Michigan State University,  
East Lansing, Michigan 48824,  
USA*

*Department of Physics and Astronomy,  
Michigan State University,  
East Lansing, Michigan 48824,  
USA*

Olivier Sorlin

*Grand Accélérateur National d'Ions Lourds (GANIL),  
CEA/DSM-CNRS/IN2P3,  
BP 55027, F-14076 Caen Cedex 5,  
France*

Toshio Suzuki

*Department of Physics and Graduate School of Integrated Basic Sciences,  
College of Humanities and Sciences,  
Nihon University,  
Sakurajosui, Setagaya-ku,  
Tokyo 156-8550,  
Japan*  
*National Astronomical Observatory of Japan,  
Mitaka, Tokyo 181-8588,  
Japan*

Yutaka Utsuno

*Advanced Science Research Center,  
Japan Atomic Energy Agency,  
Tokai, Ibaraki 319-1195,  
Japan*  
*Center for Nuclear Study,  
University of Tokyo,  
Hongo, Bunkyo-ku,  
Tokyo 113-0033,  
Japan*

(Dated: December 3, 2024)

We review how distinct features of exotic nuclei arise from characteristics of nuclear forces, with a focus on shell structure. Many of those features are not found in stable nuclei, and are related to an unbalanced proton/neutron ratio combined with unique characteristics of various components of nucleon-nucleon interactions, such as central, tensor, two-body spin-orbit and three-nucleon forces. The basics of the monopole interaction are reinvestigated starting from the definition for open-shell nuclei. We discuss how the evolution of shell structure, or shell evolution, occurs due to the monopole interactions of those forces. We survey, utilizing actual examples, the signatures of shell evolution in many experimental observables of low-energy nuclear physics. Those signatures suggest a massive shift of the “magic paradigm”, which includes the appearance of new magic numbers, such as 16, 32, 34, *etc.*, the disappearance of traditional magic numbers, such as 8, 20, 28 *etc.*, and other substantial changes of the shell structure, in certain regions of the Segrè chart. This article reviews further how combined efforts by theoretical and experimental studies provide a comprehensive picture of exotic nuclei from the shell evolution up to their many-body consequences such as shape change/coexistence, mixing/merging of the shells, intruder bands, weak binding effects, *etc.* We shall thus see the richness of the shell evolution in exotic nuclei and the resulting diversity of the physics of nuclei with wide unexplored frontiers.

PACS numbers: 21.60.-n,21.10.-k,21.30.Fe

## CONTENTS

I. Introduction	3	IV. Two-body LS and Three-body Forces	35
II. Monopole interaction and empirical analysis based on it	6	A. 2-body LS	35
A. Monopole interaction	6	B. Three-body forces	36
B. Multipole interaction	9		
C. Monopole matrix element in the $j-j$ coupling scheme	9	V. Actual cases	38
D. Effective single particle energy	9	A. Measuring the key indicators of shell evolution in unstable nuclei	38
E. Relations to earlier formulations	11	1. Sketch of the Island of Inversion	39
F. Sample analyses in terms of the effective single particle energy	12	2. Masses and separation energies	40
1. $N=9$ isotones	12	3. Radii and quadrupole moments from precision measurements	41
2. Evolution of the $g_{7/2}$ orbit in the Zr-Mo region	13	4. Excitation energy	42
3. Systematic trend of shell evolution caused by proton-neutron interaction	14	5. Transition strength	43
4. Emerging the $N = 28$ shell gap: like-particle interaction	14	6. Identifying shapes at the boundary of the island of inversion	44
III. Shell evolution, Monopole Interaction and Nuclear Forces	15	7. Spectroscopy of the nuclear wave function through direct reactions	45
A. Contributions from the central forces	15	8. Tracking single-particle strengths to learn about the spin-orbit force	46
B. Shell Evolution due to Tensor force	19	9. At the southern border: continuum and shell evolution	48
1. Tensor force	19	B. Neutron-rich $N = 28$ region	50
2. Tensor force and two-nucleon system	19	1. Overview	50
3. Tensor-force effect and orbital motion: intuitive picture	19	2. Shell evolution and its effect on nuclear structure	52
4. Tensor-force effect and orbital motion: analytic relations	20	C. Other cases in heavy nuclei	57
C. Combination of the central and tensor forces	24	VI. Shell Evolution and Nuclear Shape	57
D. Examples of tensor-force driven shell evolution	25	VII. Summary and remarks	58
1. Inversion of proton $1f_{5/2}$ and $2p_{3/2}$ in Cu isotopes	25	VIII. Acknowledgments	58
2. Shell Evolution from $^{90}\text{Zr}$ to $^{100}\text{Sn}$	27	A. Proton-neutron monopole interaction	59
3. Appearance of $N=16$ magic number and disappearance of $N=20$	28	B. Alternative definition of the monopole interaction	61
4. Appearance of $N=34$ magic number in the isotonic chain	28	C. Closed-shell properties	61
5. Repulsion between proton $1h_{11/2}$ and $1g_{7/2}$ orbits in the Sb isotopes	30	D. 2-body LS force	62
6. Other remarks	30	References	66
E. Renormalization persistency of the tensor force	31		
F. Related theoretical studies on tensor-force driven shell evolution	31		

## I. INTRODUCTION

The atomic nucleus is composed of protons and neutrons (called *nucleons* collectively) bound into one entity by nuclear forces. Its properties have been studied extensively for over a century since its discovery by E. Rutherford in 1911 (Rutherford, 1911), providing a rather comprehensive picture of certain nuclei, *i.e.*, the stable ones. Here, stable nuclei are atomic nuclei with infinite or almost infinite life times, and these are actually characterized by balanced ratio between the number of protons ( $Z$ ) and that of neutrons ( $N$ ), *i.e.*,  $N/Z \sim 1 - 1.5$ . Matter on the earth is essentially made up of stable nuclei, including long-lived isotopes like  $^{235}\text{U}$ . Almost all visible matter of the entire universe is comprised of atomic nuclei.

While the overall picture had thus been conceived for stable nuclei, the landscape of atomic nuclei has been and is still being changed and expanded significantly in recent years. Such changes are associated with the major shift of the frontiers of nuclear physics from stable nuclei to exotic (or unstable) ones. Here, exotic nuclei imply atomic nuclei with unbalanced  $N/Z$  ratio compared to stable ones, and hence they lose binding energy due to reduced symmetry energies (or enlarged asymmetry energies) (Bethe and Bacher, 1936; von Weizsäcker, 1935). Relatively smaller binding energies mean that  $\beta$ -decay channels open up towards more  $N/Z$  balanced systems, resulting in finite (often short) life times.

Unbalanced  $N/Z$  ratios change not only life times of exotic nuclei but also their quantum many-body structure relative to that of stable nuclei. This is the main subject of this review article, with a particular emphasis on the variations of the shell structure and its link to nuclear forces.

Figure 1 is a nuclear chart (or Segré chart), where an individual nucleus is specified by two coordinates,  $Z$  and  $N$ . In Fig. 1, stable nuclei (blue squares) stretch along a “line”, called the  $\beta$ -stability line. Exotic nuclei are widely distributed as indicated by light brown or light green squares. Their existence limit on the neutron-rich (proton-rich) side is called the neutron (proton) dripline. Figure 1 marks the  $^{11}\text{Li}$  nucleus right on the neutron dripline for  $Z=3$ . Although a certain number of exotic nuclei have been familiar to nuclear physics since its very initial stage, systematic studies of them have begun in the 1980’s. For instance, the measurement of the matter radius of  $^{11}\text{Li}$  was carried out (Tanihata *et al.*, 1985), marking a milestone in the development of experiments with radioactive ion (or rare isotope) beams (RI-beams). Many experiments have been conducted in the last decades, re-drawing the landscape of nuclear physics.

The nucleus  $^{11}\text{Li}$  is known for its extraordinarily large matter radius due to the formation of a neutron halo, inherent to a tunneling effect of the loosely-bound last two neutrons, as pointed out in (Hansen and Jonson,

1987). The neutron halo is a characteristic phenomenon at and near the dripline, and seems to have led us to a paradigm shift away from assumptions that the nucleon density is almost constant inside the nucleus and the nuclear radius is proportional to  $A^{1/3}$  where  $A = Z + N$ , called the mass number. While  $^{11}\text{Li}$  is only  $\Delta N=4$  off the  $\beta$ -stability line, the distance between the  $\beta$ -stability line and the neutron dripline increases with  $Z$  (Figure 1). The nuclei shown in Fig. 1 are all bound, and most of them are even well bound. In fact, the inset of Fig. 1 counts the number of bound neutron-rich exotic nuclei. It starts with just a few for  $Z \sim 1$ , but grows rapidly up to more than fifty for  $Z=82$ . Weakly bound nuclei near the dripline are shown in dark blue, where neutron halo or phenomena connected to the continuum can be expected even for the ground state. One sees, on the other hand, that the majority is well bound. Partly because such well-bound exotic nuclei are so plentiful, but also because the combination of  $Z$  and  $N$  varies so much, we can ask ourselves whether the structure of thousands of those nuclei is just like that of the stable ones or not. If not, an intriguing question arises: what changes can we find there and why?

We also note that the r-process, where heavy elements are created in explosive scenarios such as neutron star mergers or supernovae, actually passes through extremely neutron-rich exotic nuclei (as shown schematically in Fig. 1) to create elements beyond iron. Thus, from this point of view also, it is crucial to clarify the structure of these exotic nuclei.

Extensive precision electron scattering experiments carried out on stable targets starting in the 60’s combined with other experiments showed that the nucleon density  $\rho(r)$  is essentially constant well inside the nucleus with smooth but rapid damping at the surface as shown in Fig. 2 (a): the paradigm of density saturation as discussed above. The mean potential for a nucleon inside the nucleus represents mean effects of the nucleon-nucleon ( $NN$ ) interaction, or nuclear force, from the other nucleons. The  $NN$  interaction is strongly repulsive at short distances (below 0.7 fm), becomes strongly attractive at medium range ( $\approx 1.0$  fm) and vanishes at large distances (beyond 2 fm). In the nuclear interior, the nuclear density,  $\rho$ , is  $\sim 0.17$  nucleons/fm $^3$  common to most nuclei, and nucleons interact mainly with their immediate neighbors. This leads to a saturation of the binding energy. Combining those properties of the density and the nuclear force, a nucleon well inside the nucleus feels the same mean effect independent of its location. In other words, the mean potential has a flat bottom inside the nucleus. The potential becomes shallower gradually towards the surface similar to the density, as shown in Fig. 2 (b). Such a mean potential can be further modeled by a Harmonic Oscillator (HO) potential also shown in Fig. 2 (b). The nucleons there move on the orbits which are the eigenstates of this HO poten-

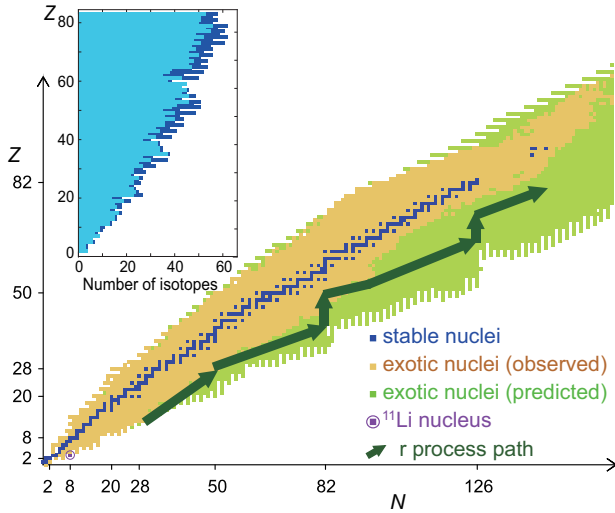


Figure 1 The nuclear chart as a function of neutron and proton number,  $N$  and  $Z$ . Each nucleus is expressed by a box specified by  $Z$  and  $N$ . Blue squares represent stable nuclei. Exotic nuclei observed experimentally as of the year 2012 are shown by light-brown squares (NNDC, 2016), while light-green squares denote those predicted by a theoretical model (Koura, 2005). The  $^{11}\text{Li}$  nucleus is highlighted in purple. A possible path of the r-process is given schematically by the green arrows. Inset: Number of bound neutron-rich exotic nuclei as a function of  $Z$  based on Ref. (Koura, 2005). The light and dark blue parts count nuclei with two-neutron separation energy  $S_{2n} >$  and  $< 2$  MeV, respectively. Adapted from Otsuka (2013); Otsuka and Schwenk (2012).

tial, and the energies are given in terms of the oscillator quanta  $N$  as shown in the column “H.O.”. The minor difference between the H.O. and the original mean potentials is remedied to a certain extent by the so-called  $\ell^2$  term, which lowers perturbatively orbits with larger orbital angular momenta,  $\vec{\ell}$ , as shown in the middle column. In order to resolve systematic discrepancies with experiment, Mayer and Jensen included, to this approach, the spin-orbit (SO) coupling ( $\vec{\ell} \cdot \vec{s}$ ) where  $\vec{s}$  denotes the spin ( $s=1/2$ ) and  $(\cdot)$  implies a scalar product (Haxel *et al.*, 1949; Mayer, 1949). This  $(\vec{\ell} \cdot \vec{s})$  term with the proper strength produces the spin-orbit splitting, where the orbit with the total angular momentum  $j_> = \ell + 1/2$  becomes lower than the one with  $j_< = \ell - 1/2$ . The resultant single-particle levels are shown in the right column above  $\vec{\ell} \cdot \vec{s}$  in Fig. 2 (c).

Without the SO coupling, the single-particle states are classified by  $N$  and  $\ell$  as shown in the center column of Fig. 2 (c). The single-particle states are grouped according to  $N$ , forming *shells*. Shells are separated by *shell gaps*. The number of protons or neutrons below a certain gap is a *magic number*. The magic number is related to the stability of the nucleus: for instance, up to 20 protons can be put into the shells formed by  $2s$ ,  $1d$ ,  $1p$  and  $1s$  orbits, whereas the 21st proton must occupy either

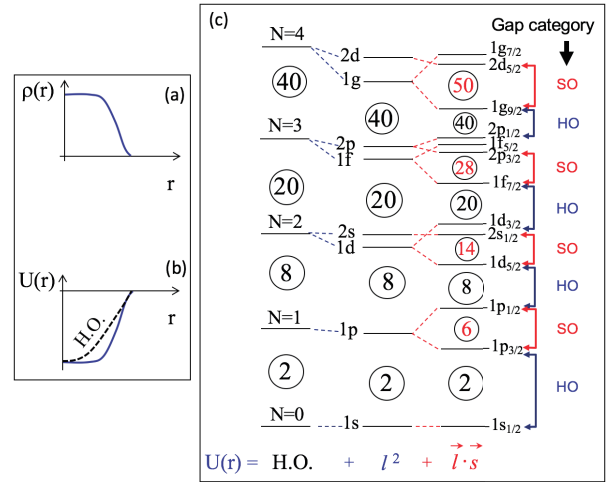


Figure 2 Schematic pictures. (a) Nucleon density distribution  $\rho(r)$  and (b) mean potential  $U(r)$  are shown as a function of the distance from the center of the nucleus,  $r$ . (c) Single-particle energies for a Harmonic Oscillator (HO) potential well, with an added  $\ell^2$  term and a spin-orbit interaction (SO)  $\vec{\ell} \cdot \vec{s}$ . Shell-gap categories are shown by HO and SO. The  $N$  label refers here to the oscillator shell  $N = 2(n - 1) + \ell$ , with  $(n - 1)$  being the number of nodes of the radial wave function and  $\ell$  the orbital angular momentum.

the  $1f$  or  $2p$  orbit at higher energy (*i.e.*, smaller binding energy). The magic numbers up to 20 work well, but the SO coupling splits the  $1f$  orbit into  $1f_{7/2}$  and  $1f_{5/2}$  strong enough, creating a magic number 28, as shown in Fig. 2 (c). The  $1f_{7/2}$  state is sandwiched by two magic numbers 20 and 28: the former has HO origin, whereas the latter has SO origin. Other shells and magic numbers are shown in the same figure. The major magic numbers, which correspond to larger shell gaps, are 2, 8, 20, 28, 50, ... These shell structure and magic numbers turned out to be so successful in the description of the nuclei over half of a century.

We note that the above argument is based only on a few properties: density saturation, short-range nuclear force, and spin-orbit splitting. As these properties look robust, the shell/magic structure seemed to be global over all nuclei.

However, such expectation has been shown in recent years to be inapplicable particularly to exotic nuclei. In fact, the above properties do not exhaust all relevant features. We shall see how the shell/magic structure change or evolve, reflecting the many-body physics and the basic nature of  $NN$  interaction in nuclei, over the Segré chart and also over states of varying characters within a nucleus.

At this point, we show Fig. 3 as a typical example illustrating the physics of this article. In this figure, single-particle levels of neutrons are shown for Ca and Ni isotopes schematically, *i.e.*, in an ideal single-particle model. The left half is a part of the single-particle levels

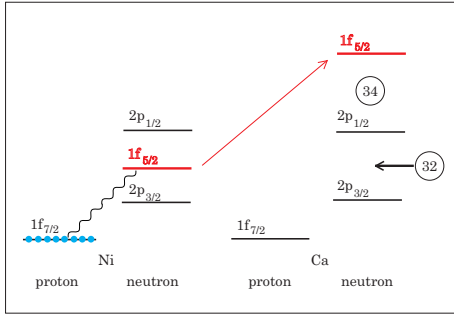


Figure 3 Schematic illustration of shell evolution from Ni back to Ca for neutron orbits. Light blue circles exhibit protons. The wavy line is the interaction between the proton  $1f_{7/2}$  orbit and the neutron  $1f_{5/2}$  orbit. The numbers in circles indicate (semi-) magic numbers. From Otsuka and Tsunoda (2016).

of Ni isotopes, which is consistent with Fig. 2 (c). The right side exhibits the single-particle levels of Ca isotopes where additional magic numbers, 32 and 34, are shown and the ordering is different from Fig. 2 (c). We shall discuss throughout this article why and how such changes occur, referring to these changes as *shell evolution*.

Thus, the magic numbers and shell structure are not a fixed scheme but a variable framework. As we look back several decades ago, the concept of immutable magic numbers was jeopardized already in the 1970's by the observation of combined anomalies in experimental masses, nuclear radii and spectroscopy of nuclei far from stability, around  $N = 20$  since (Thibault *et al.*, 1975) with (Détraz *et al.*, 1979; Guillemaud-Mueller *et al.*, 1984; Huber *et al.*, 1978). A much weakened effect of the  $N = 20$  gap, combined with the emergence of apparently deformed intruder states, was seen in various observables as a sign of certain underlying phenomena unexpected in the conventional shell structure. The complete picture is still being investigated. We note that another even earlier observation of the deviation from the conventional understanding was the discovery of the abnormal ground state of  $^{11}\text{Be}$  by (Wilkinson and Alburger, 1959) followed by a theoretical analysis including  $^{12}\text{N}$  and  $^{13}\text{C}$  (Talmi and Unna, 1960). These will be touched upon in subsequent sections.

The advent of radioactive ion beam facilities worldwide, together with constantly improved experimental techniques, has since enabled a more thorough study of the structure changes in exotic nuclei, including those of magic numbers away from the valley of stability, ultimately reaching the nuclear driplines. Such developments in experiments and theory have been pushed forward.

Over the years, the local disappearance of many of the previously well-established shell structures has been pointed out far from stability, leading to a complete

paradigm change in our vision of the magic number and shell structure in general. One of the major purposes of the present article is to summarize the presently available understanding, to extract basic underlying principles on the shell evolution and its mechanism, and to overview various nuclear phenomena related to them. Such outcomes will enable us to foresee new physics cases in hitherto unexplored regions of the Segrè chart.

While there has been enormous progress in the physics on exotic nuclei, we rather concentrate on the shell evolution including appearance and disappearance of magic numbers in this article, partly because this subject alone is exhaustive.

The article is organized in the following manner. In Sec. II, we start with the definition of the monopole component of the  $NN$  interaction in nuclei. Although the monopole interaction has been discussed since (Bansal and French, 1964), there are still questions as to whether it can be defined only at the closed shells. We shall formulate here the monopole interaction in general (open-shell) cases referring to the rotational isotropy. Although the derivation principle is straightforward, the proton-neutron monopole interaction is complicated due to its isospin dependence. The here obtained monopole interaction compares well to several existing formulations. The effective single-particle energy (ESPE) is then derived from this monopole interaction, and can be viewed again in close relations to existing earlier works. The variation of the ESPE is nothing but the quantitative expression of the shell evolution, and Sec. II depicts actual examples in a pedagogical way. We emphasize here that the importance of the monopole interaction lies particularly in the linearity of its effect as a function of the particle number. This feature holds only for the monopole interaction, and has much practical significance in many cases.

In Sec. III, we discuss the major sources of the monopole interaction. The central force is taken first, and the orbital dependence of the monopole matrix elements is illustrated with concrete examples. The tensor force is then considered, and the unique feature of its monopole interaction is reviewed including somewhat schematic, intuitive pictures. Actual examples are indicated. We note here that the terminology "shell evolution" has appeared for the first time in (Otsuka *et al.*, 2005) to explain the monopole effects from the tensor force. In fact, the title of this paper is "Evolution of Nuclear Shells due to the Tensor Force", and we cannot find a reference depicting this phrase earlier. The robustness of the tensor-force monopole interaction is shown also with modern chiral Effective Field Theory (EFT) interactions. Sec. III also presents examples including predictions verified by recent experiments, such as single-proton states in exotic Cu isotopes, new  $N=32, 34$  magic numbers in Ca isotopes, *etc.* The treatment of the tensor force in other theories is summarized.

The monopole effects of the two-body spin-orbit (2b-*LS*) force and three-nucleon force are explained in Sec. IV. In particular, the present intuitive and general discussions on the shell-evolution mechanism due to the 2b-*LS* force have not been reported elsewhere.

Actual cases are discussed with relevant experiments in Sec. V, covering the island of inversion, the  $N=28$  region, *etc.* as well as relations to neutron halo and continuum physics taking examples of  $^{22}\text{C}$  and O isotopes, respectively.

Relations to shape deformation and/or collective motion are briefly mentioned in Sec. VI.

Before closing this section, we comment on the comparisons of the shell structure of atomic nuclei to the shell structure of other many-body systems. First, as the nuclear potential is generated by its constituents, any movement on the nuclear chart can change the shell structure, leading to shell evolution. We mention here that the shell/magic structure appears in the metallic micro clusters as described, for instance, in (Sugano, 1991), where the correspondence to the classical motion and geometrical symmetries is important. This aspect may be less relevant to nuclei, as the energy of the single-particle orbit is determined by the constituents, their occupation pattern and their interactions, *i.e.*, nuclear forces.

It has been argued that the damping of the nucleon density in the radial direction may be more gradual in neutron-rich exotic nuclei than in stable nuclei, causing reduced spin-orbit splittings and single-particle levels distributed more evenly (Dobaczewski *et al.*, 1994). This phenomenon was called the “quenching of the shell” or the “shell quenching”. Despite significant experimental efforts to find evidence for this shell quenching, only cases denying this possibility have been reported, for instance, (Watanabe *et al.*, 2013). Although this hypothetical phenomenon may be found in nuclei right on or very near the dripline in the future, it is rather unlikely to see this in a majority of exotic nuclei. The present article is independent of the issue of the shell quenching, and addresses the shell evolution driven by the combination of characteristic features of nuclear forces and exotic proton/neutron composition of the nucleus, as we shall see throughout this article. *May the force be with you.*

## II. MONPOLE INTERACTION AND EMPIRICAL ANALYSIS BASED ON IT

The shell structure can be specified by a set of single-particle energies of valence (or active) orbits on top of a closed shell (or inert core). As more neutrons or protons are added to the nucleus, the single-particle energies of those valence orbits may change due to the interaction between valence nucleons. This implies some changes of shell structure, called *shell evolution* as introduced in Sec. I. The shell evolution is generated by

the monopole part of the nucleon-nucleon (*NN*) interaction, which will be abbreviated hereafter as the *monopole interaction*. In this section, we first introduce the definition of the monopole interaction, and discuss how it acts. The monopole interaction has been discussed in the past, for instance, by Bansal and French (Bansal and French, 1964) and by Poves and Zuker (Poves and Zuker, 1981). The latter is a generalization of the former, where the discussion seems to be based on closed-shell properties. We introduce the monopole interaction in a different way, as an average of correlation energies of two nucleons in an open-shell nucleus, without necessarily referring to closed-shell energies. The final outcome of this formulation turns out to be basically consistent with the earlier works mentioned above. The effective single-particle energy will then be discussed for open-shell nuclei in a close connection to the monopole interaction there, in a possibly more transparent and straightforward way than the simple interpolation between the beginning and end of a given shell.

We therefore define and discuss the monopole interaction in detail in the next subsection. We will then move forward to discuss its effect on the closed-shell properties and the evolution of the shell structure. The relation to other approaches will be mentioned. We also present applications of the monopole interaction to some examples taken from actual nuclei. At this point, we stress that the monopole interaction is a part of the *NN* interaction, and that the rest of the interaction produces various dynamical correlations and must be taken into account for a more precise description of the nuclear structure. Nevertheless, as the monopole interaction generates unique and crucial effects, it deserves special efforts and attention.

### A. Monopole interaction

We start with single-particle orbits. For each orbit, the total angular momentum is specified by  $\vec{j} = \vec{\ell} + \vec{s}$  with its orbital angular momentum  $\vec{\ell}$  and spin  $\vec{s}$ . The single-particle orbits are labelled by the magnitudes of their  $\vec{j}$ 's, referred to as  $j, j', \dots$  hereafter. They are combined with the corresponding magnetic quantum numbers,  $m, m', \dots$  as  $(j, m), (j', m'), \dots$ . The symbol  $j, j', \dots$  are put in a fixed order, and may carry implicitly such a sequential ordering as well as other quantum numbers like the node of the radial wave function  $n$ . Having these single-particle orbits on top of the inert core (*i.e.*, closed shell), we denote the single-particle energies (SPEs) of those orbits as  $\epsilon_j^0, \epsilon_{j'}^0, \dots$ . As usual, this SPE  $\epsilon_j^0$  stands for the sum of the kinetic energy of a nucleon on this orbit  $j$  and the total effects of nuclear forces on this nucleon from all nucleons in the inert core.

We shall begin with the simpler case by assuming that there is only one kind of nucleons, *e.g.*, neutrons. The

Hamiltonian is expressed then as

$$\hat{H}_n = \sum_j \epsilon_j^0 \hat{n}_j + \hat{v}_{nn}, \quad (1)$$

where  $\hat{n}_j$  denotes the number operator for the orbit  $j$  and  $\hat{v}_{nn}$  stands for the neutron-neutron effective interaction.

The product state with the first and second neutron in the states  $j, m$  and  $j', m'$ , respectively, is written as

$$|j, m \otimes j', m'\rangle. \quad (2)$$

Their antisymmetrized state is indicated by

$$|j, m; j', m'\rangle = \left\{ |j, m \otimes j', m'\rangle - |j', m' \otimes j, m'\rangle \right\} / \sqrt{2}. \quad (3)$$

A two-body interaction between two neutrons can be written as

$$\hat{v}_{nn} = \sum_{(j_1, m_1; j'_1, m'_1), (j_2, m_2; j'_2, m'_2)} \langle j_1, m_1; j'_1, m'_1 | \hat{v}_{nn} | j_2, m_2; j'_2, m'_2 \rangle a_{j_1, m_1}^\dagger a_{j'_1, m'_1}^\dagger a_{j_2, m_2} a_{j'_2, m'_2}, \quad (4)$$

where  $(j, m; j', m')$  in the summation is an ordered pair of two states  $j, m$  and  $j', m'$ ,  $\langle \dots | \hat{v} | \dots \rangle$  denotes an anti-symmetrized two-body matrix element, and  $a_{j, m}^\dagger$  ( $a_{j, m}$ ) implies the creation (annihilation) operator of the state  $j, m$ . Regarding the ordered pair  $(j_1, m_1; j'_1, m'_1)$ , we can assume without generality that  $m_1 < m'_1$  if  $j_1 = j'_1$  or  $j_1 < j'_1$  in their prefixed ordering as mentioned above.

The monopole interaction is defined as a component extracted from a given interaction,  $\hat{v}_{nn}$ , so that it represents the effect averaged over all possible orientations of two neutrons in the orbits  $j$  and  $j'$ . Here, orientations refer to various combinations of  $m$  and  $m'$  within the orbits  $j$  and  $j'$ . Figure 4 provides a general visualization of the monopole matrix element, exhibiting different orientations by differently tilted orbiting planes. In order to formulate this, the monopole matrix element for the orbits  $j$  and  $j'$  is defined as

$$V_{nn}^m(j, j') = \frac{\sum_{(m, m')} \langle j, m; j', m' | \hat{v}_{nn} | j, m; j', m' \rangle}{\sum_{(m, m')} 1}, \quad (5)$$

where the summation over  $m, m'$  is taken for all ordered pairs allowed by the Pauli principle.

As the denominator counts the number of allowed states, this is exactly the average mentioned above. The monopole interaction as an operator is then expressed as

$$\hat{v}_{nn, mono} = \sum_{j \leq j'} \hat{v}_{nn}^m(j, j') \quad (6)$$

with

$$\hat{v}_{nn}^m(j, j') = V_{nn}^m(j, j') \sum_{m, m'} a_{j, m}^\dagger a_{j', m'}^\dagger a_{j', m'} a_{j, m}. \quad (7)$$

After simple algebra, this turns out to be

$$\hat{v}_{nn}^m(j, j') = \begin{cases} V_{nn}^m(j, j) \frac{1}{2} \hat{n}_j (\hat{n}_j - 1) & \text{for } j = j' \\ V_{nn}^m(j, j') \hat{n}_j \hat{n}_{j'} & \text{for } j \neq j' \end{cases} \quad (8)$$

where  $\hat{n}_j$  stands for the number operator for the orbit  $j$ . The form in eq. (8) appears to be in accordance with what can be expected intuitively, from the concept of average, for identical fermions. The two neutrons in the orbits  $j$  and  $j'$  can be coupled to the total angular momentum,  $J$ , where  $\vec{J} = \vec{j} + \vec{j}'$ , and the wave function with a good  $J$  value is given by a particular superposition of the states in eq. (6) over all possible values of  $m$  and  $m'$ . It is obvious that the effects of the monopole interaction in eq. (8) is independent of the total angular momentum,  $J$ . We emphasize again that the monopole interaction is simply an average of a given general interaction over all possible orientations, and its effect can be expressed by the orbital number operator as in eq. (8) for the neutron-neutron interaction.

We next discuss systems composed of protons and neutrons. The total Hamiltonian is then written as

$$\hat{H} = \hat{H}_n + \hat{H}_p + \hat{v}_{pn}, \quad (9)$$

where  $\hat{H}_p$  stands for the proton Hamiltonian defined similarly to eq. (1) and  $\hat{v}_{pn}$  means the proton-neutron effective interaction.

The proton and neutron number operators in the orbit  $j$  are denoted, respectively, as  $\hat{n}_j^p$  and  $\hat{n}_j^n$ . We introduce the isospin operators in the orbit  $j$ :  $\hat{\tau}_j^+$ ,  $\hat{\tau}_j^-$  and  $\hat{\tau}_j^z$ . We adopt the convention that protons are in the state of isospin z-component  $\tau_z = +1/2$ , whereas neutrons are in  $\tau_z = -1/2$ . Here,  $\hat{\tau}_j^+$  ( $\hat{\tau}_j^-$ ) denotes the operator changing a neutron (proton) to a proton (neutron) in the same  $(j, m)$  state, and  $\hat{\tau}_j^z$  equals  $(\hat{n}_j^p - \hat{n}_j^n)/2$ . In other words,  $\hat{\tau}_j^+$  and  $\hat{\tau}_j^-$  are nothing but the isospin raising and lowering operators restricted to the orbit  $j$ , while  $\hat{\tau}_j^0$  is its z component.

The magnitude of the usual isospin, *i.e.*, not specific to an orbit, is denoted by  $T$ , including that of two nucleons interacting through the  $NN$  interaction.

We now discuss the proton-neutron monopole interaction. Although the basic idea remains the same as the previous case for two neutrons, certain differences arise. To be precise, a proton and a neutron are coupled in a symmetric way for the  $T=0$  case, whereas in an anti-symmetric way for the  $T=1$  case. Details of the discussions are presented in Appendix A, and we show here only major points, referring to the corresponding parts in Appendix A.

The monopole interaction due to the  $T=0$  part of  $\hat{v}_{pn}$  is expressed as (see discussions in Appendix A up to

Monopole matrix element between orbits  $j$  and  $j'$

$$\begin{aligned}
 & \left\langle \begin{smallmatrix} \text{pink} \\ \text{blue} \end{smallmatrix} \middle| v \middle| \begin{smallmatrix} \text{pink} \\ \text{blue} \end{smallmatrix} \right\rangle + \left\langle \begin{smallmatrix} \text{pink} \\ \text{blue} \end{smallmatrix} \middle| v \middle| \begin{smallmatrix} \text{pink} \\ \text{blue} \end{smallmatrix} \right\rangle + \left\langle \begin{smallmatrix} \text{pink} \\ \text{blue} \end{smallmatrix} \middle| v \middle| \begin{smallmatrix} \text{pink} \\ \text{blue} \end{smallmatrix} \right\rangle + \dots \\
 = & \frac{\left\langle \begin{smallmatrix} \text{pink} \\ \text{blue} \end{smallmatrix} \middle| v \middle| \begin{smallmatrix} \text{pink} \\ \text{blue} \end{smallmatrix} \right\rangle + \dots + \left\langle \begin{smallmatrix} \text{pink} \\ \text{blue} \end{smallmatrix} \middle| v \middle| \begin{smallmatrix} \text{pink} \\ \text{blue} \end{smallmatrix} \right\rangle + \dots + \dots + \left\langle \begin{smallmatrix} \text{pink} \\ \text{blue} \end{smallmatrix} \middle| v \middle| \begin{smallmatrix} \text{pink} \\ \text{blue} \end{smallmatrix} \right\rangle}{\text{number of matrix elements in the summation}}
 \end{aligned}$$

$\begin{smallmatrix} \text{pink} \\ \text{blue} \end{smallmatrix} \dots \begin{smallmatrix} \text{pink} \\ \text{blue} \end{smallmatrix}$  : magnetic substates of orbit  $j$

$\begin{smallmatrix} \text{blue} \\ \text{pink} \end{smallmatrix} \dots \begin{smallmatrix} \text{blue} \\ \text{pink} \end{smallmatrix}$  : magnetic substates of orbit  $j'$

Figure 4 A schematic visualization of monopole matrix elements for the two-body interaction  $v$ .

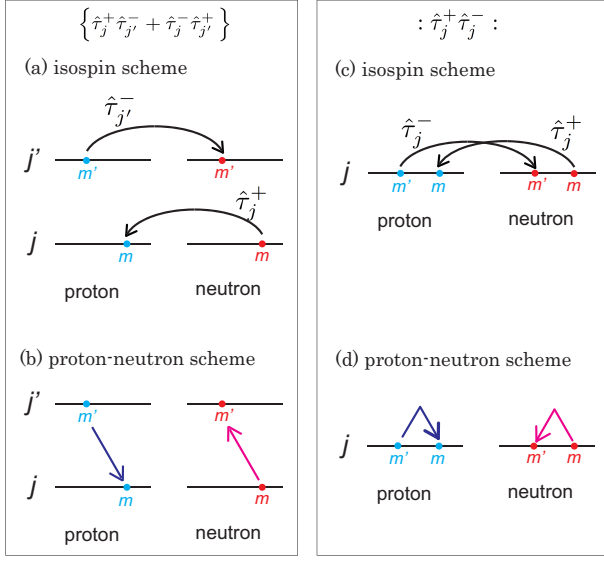


Figure 5 Implication of  $\hat{\tau}_j^+ \hat{\tau}_{j'}^-$  terms. Panels (a) and (c) are for the  $\{\hat{\tau}_j^+ \hat{\tau}_{j'}^- + \hat{\tau}_j^- \hat{\tau}_{j'}^+\}$  and  $:\hat{\tau}_j^+ \hat{\tau}_j^-:$  cases in the isospin scheme, respectively. Panels (b) and (d) are similar to (a) and (c), respectively, in the proton-neutron scheme. The magnetic substates are indicated by  $m$  and  $m'$ .

eq. (A16)),

$$\begin{aligned}
 \hat{v}_{pn,mono,T=0} = & \sum_{j,j'} V_{T=0}^m(j, j') \frac{1}{2} \hat{n}_j^p \hat{n}_{j'}^n \\
 & - \sum_{j < j'} V_{T=0}^m(j, j') \frac{1}{2} \{ \hat{\tau}_j^+ \hat{\tau}_{j'}^- + \hat{\tau}_j^- \hat{\tau}_{j'}^+ \} \\
 & - \sum_j V_{T=0}^m(j, j) \frac{1}{2} : \hat{\tau}_j^+ \hat{\tau}_j^- :,
 \end{aligned} \quad (10)$$

where the symbol  $: \dots :$  denotes a normal product and the  $T=0$  monopole matrix element is defined as an average over states with all possible orientations with the symmetric coupling of proton and neutron, as indicated by  $\mathcal{S}$  (see discussions in Appendix A linked to eqs. (A5, A15)):

$$V_{T=0}^m(j, j') = \frac{\sum_{(m,m')} (m; m' : \mathcal{S} | \hat{v}_{pn} | m; m' : \mathcal{S})}{\sum_{m,m'} 1}. \quad (11)$$

If the interaction  $\hat{v}$  is isospin invariant as usual, the monopole matrix element in eq. (5) is nothing but the  $T = 1$  monopole matrix element,

$$V_{T=1}^m(j, j') = V_{nn}^m(j, j'). \quad (12)$$

Coming back to antisymmetric couplings of a proton and a neutron, we apply the procedures similar to those for  $T = 0$  states, and obtain (see discussions in Appendix A linked to eq. (A22))

$$\begin{aligned}
 \hat{v}_{pn,mono,T=1} = & \sum_{j,j'} V_{T=1}^m(j, j') \frac{1}{2} \hat{n}_j^p \hat{n}_{j'}^n \\
 & + \sum_{j < j'} V_{T=1}^m(j, j') \frac{1}{2} \{ \hat{\tau}_j^+ \hat{\tau}_{j'}^- + \hat{\tau}_j^- \hat{\tau}_{j'}^+ \} \\
 & + \sum_j V_{T=1}^m(j, j) \frac{1}{2} : \hat{\tau}_j^+ \hat{\tau}_j^- :.
 \end{aligned} \quad (13)$$

By combining eqs. (10) and (13), the whole expression of the proton-neutron monopole interaction becomes

$$\begin{aligned}
 \hat{v}_{pn,mono} = & \sum_{j,j'} \frac{1}{2} \{ V_{T=0}^m(j, j') + V_{T=1}^m(j, j') \} \hat{n}_j^p \hat{n}_{j'}^n \\
 & - \sum_{j < j'} \frac{1}{2} \{ V_{T=0}^m(j, j') - V_{T=1}^m(j, j') \} \\
 & \quad \{ \hat{\tau}_j^+ \hat{\tau}_{j'}^- + \hat{\tau}_j^- \hat{\tau}_{j'}^+ \} \\
 & - \sum_j \frac{1}{2} \{ V_{T=0}^m(j, j) - V_{T=1}^m(j, j) \} : \hat{\tau}_j^+ \hat{\tau}_j^- :.
 \end{aligned} \quad (14)$$

Although the meaning of the first term on the right-hand side of eq. (14) is straightforward, it needs some explanations to understand the other two terms in depth. Figure 5 may help, by showing how they work. In the case of  $j \neq j'$ , panels (a) and (b) indicate the same process in the isospin and proton-neutron schemes, respectively. Panel (a) indicates that the  $\{\hat{\tau}_j^+ \hat{\tau}_{j'}^- + \hat{\tau}_j^- \hat{\tau}_{j'}^+\}$  term produces a monopole interaction with a charge exchange process, whereas the same process may look differently in panel (b). Panels (c) and (d) are for the case of one orbit  $j$  with

similar implications. One thus see, from Fig. 5, how the charge exchange processes can be incorporated into the monopole interaction. We will come back to this figure. We note that the  $T = 0$  and  $T = 1$  monopole matrix elements contribute with opposite sign relations as compared to the first term.

The neutron-neutron and proton-proton monopole interactions can be re-written in similar ways, as

$$\begin{aligned}\hat{v}_{nn,mono} &= \sum_j V_{T=1}^n(j, j) \frac{1}{2} \hat{n}_j^n (\hat{n}_j^n - 1) \\ &+ \sum_{j < j'} V_{T=1}^n(j, j') \hat{n}_j^n \hat{n}_{j'}^n,\end{aligned}\quad (15)$$

and

$$\begin{aligned}\hat{v}_{pp,mono} &= \sum_j V_{T=1}^p(j, j) \frac{1}{2} \hat{n}_j^p (\hat{n}_j^p - 1) \\ &+ \sum_{j < j'} V_{T=1}^p(j, j') \hat{n}_j^p \hat{n}_{j'}^p.\end{aligned}\quad (16)$$

We thus gain the complete expression for the total monopole interaction,

$$\hat{v}_{mono} = \hat{v}_{pp,mono} + \hat{v}_{nn,mono} + \hat{v}_{pn,mono}. \quad (17)$$

## B. Multipole interaction

We have discussed the monopole interaction which is a part of the  $NN$  interaction. The remaining part of the  $NN$  interaction is called the *multipole interaction*. The multipole interaction is often expressed as  $\hat{v}_M$ , and it includes, in particular the quadrupole interaction. In this article, we denote the multipole interaction as  $\hat{v}_{multi}$ , being defined by

$$\hat{v}_{multi} = \hat{v} - \hat{v}_{mono}, \quad (18)$$

where  $\hat{v}$  stands for the full interaction, and  $\hat{v}_{mono}$  is defined in eq. (17). The multipole interaction may have subscript  $pp$ ,  $nn$ , or  $pn$ , if necessary.

## C. Monopole matrix element in the $j - j$ coupling scheme

The monopole matrix element is defined, in some cases, by an alternative but equivalent expression.

$$\begin{aligned}V_T^m(j, j') &= \frac{\sum_J (2J+1) \langle j, j'; J, T | \hat{v} | j, j'; J, T \rangle}{\sum_J (2J+1)} \\ \text{for } T &= 0 \text{ and } 1,\end{aligned}\quad (19)$$

where  $J$  takes only even (odd) integers for  $j = j'$  with  $T = 1$  ( $T = 0$ ). Appendix B shows that this expression is indeed equivalent to the one presented here.

The closed-shell properties are derived from the expressions shown so far. The actual derivations and results are given in Appendix C.

## D. Effective single particle energy

We discuss, in this subsection, effective single particle energy and its derivation from the monopole interaction.

As one moves on the Segre chart, the proton number,  $Z$ , and the neutron number,  $N$ , change, and the single-particle energy  $\epsilon_j^0$  mentioned in Sec. II.A will change also. This change has the following two aspects. One is due to the kinetic energy: as  $A$  increases, the radius of the nucleus becomes larger, and consequently the radial wave function of each orbit becomes wider. This lowers the kinetic energy. The other aspect is the variation in the effects from nucleons in the inert core. As  $A$  increases, the radial wave functions of the orbits in the inert core also become stretched out radially. This can reduce the magnitude of their effects. While these two changes can be of relevance, for instance, over a long chain of isotopes, they are considered to be rather minor within each region of current interest on the Segre chart (Bohr and Mottelson, 1969), and we do not take them into account in this article.

The single-particle energy has another origin: the contribution from other nucleons outside the inert core, *i.e.*, valence nucleons. This valence contribution to the orbit  $j$  is referred to as  $\hat{\epsilon}_j$  hereafter. The total single-particle energy, called *effective single particle energy (ESPE)* usually, is denoted as,

$$\epsilon_j = \epsilon_j^0 + \hat{\epsilon}_j. \quad (20)$$

We shall discuss, in this subsection, the valence contribution,  $\hat{\epsilon}_j$ , in some detail. Note that  $\epsilon_j^0$  is a constant for a given nucleus, whereas  $\hat{\epsilon}_j$  is an operator by nature because of its dependence on the states of other valence nucleons.

The magnetic substates of the orbits  $j$  and  $j'$  are denoted, respectively, by  $m$  ( $m = j, j-1, \dots, -j+1, -j$ ) and  $m'$  ( $m' = j', j'-1, \dots, -j'+1, -j'$ ). The matrix element  $\langle m, m' | \hat{v} | m, m' \rangle$  varies for different combinations of  $m$  and  $m'$ . On the other hand, as  $\hat{\epsilon}_j$  is a part of the single-particle energy of the orbit  $j$ , it should be independent of  $m$ . We therefore extract the  $m$ -independent component from these matrix elements, in order to evaluate their contribution to  $\hat{\epsilon}_j$ . Because of the  $m$  and  $m'$  dependences, this can be done by taking the average over all possible combinations of  $m$  and  $m'$ , which is nothing but the monopole interaction discussed in Sec. II.A.

In the case of two neutrons in the same orbit  $j$ , the monopole interaction is included in eq. (15). The difference due to the addition of one neutron,  $\hat{n}_j^n \rightarrow \hat{n}_j^n + 1$ , gives the contribution to  $\hat{\epsilon}_j$  as

$$\begin{aligned}\Delta^{(j,nn)} \epsilon_j &= V_{T=1}^n(j, j) \frac{1}{2} \{ (\hat{n}_j^n + 1) \hat{n}_j^n - \hat{n}_j^n (\hat{n}_j^n - 1) \} \\ &= V_{T=1}^n(j, j) \hat{n}_j^n.\end{aligned}\quad (21)$$

The difference due to the increase,  $\hat{n}_j^n \rightarrow \hat{n}_j^n + 1$ , for  $j \neq j'$

is written as

$$\begin{aligned}\Delta^{(j',nn)}\epsilon_j &= V_{T=1}^m(j, j')\{\hat{n}_{j'}^n(\hat{n}_j^n + 1) - \hat{n}_{j'}^n \hat{n}_j^n\} \\ &= V_{T=1}^m(j, j') \hat{n}_{j'}^n.\end{aligned}\quad (22)$$

Thus, the contribution from neutron-neutron interaction results in

$$\hat{\epsilon}_j^{n \rightarrow n} = \sum_{j'} V_{T=1}^m(j, j') \hat{n}_{j'}^n. \quad (23)$$

The contribution from the proton-proton interaction can be shown similarly,

$$\hat{\epsilon}_j^{p \rightarrow p} = \sum_{j'} V_{T=1}^m(j, j') \hat{n}_{j'}^p. \quad (24)$$

In the case of the proton-neutron interaction, the monopole interaction is shown in eq. (14). We first discuss the effect from the first term on the right-hand-side. The difference due to the increase,  $\hat{n}_j^n \rightarrow \hat{n}_j^n + 1$ , gives the contribution to  $\hat{\epsilon}_j$  (of neutrons) as

$$\begin{aligned}\hat{\epsilon}_j^{p \rightarrow n;0} &= \sum_{j'} \frac{1}{2} \left\{ V_{T=0}^m(j', j) + V_{T=1}^m(j', j) \right\} \\ &\quad \times \left\{ \hat{n}_{j'}^p(\hat{n}_j^n + 1) - \hat{n}_{j'}^p \hat{n}_j^n \right\} \\ &= \sum_{j'} \frac{1}{2} \left\{ V_{T=0}^m(j', j) + V_{T=1}^m(j', j) \right\} \hat{n}_{j'}^p.\end{aligned}\quad (25)$$

Likewise, the difference due to the increase,  $\hat{n}_j^p \rightarrow \hat{n}_j^p + 1$ , gives the contribution to  $\hat{\epsilon}_j$  (of protons) as

$$\hat{\epsilon}_j^{n \rightarrow p;0} = \sum_{j'} \frac{1}{2} \left\{ V_{T=0}^m(j, j') + V_{T=1}^m(j, j') \right\} \hat{n}_{j'}^n. \quad (26)$$

We next discuss the effect from the second and third terms on the right-hand-side of eq. (14). Because the operator  $\hat{\tau}_j^+ \hat{\tau}_{j'}^- + \hat{\tau}_j^- \hat{\tau}_{j'}^+$  working between  $j \neq j'$  shifts a proton  $j' \rightarrow j$  and a neutron  $j \rightarrow j'$  and vice versa (see Fig. 5 (a,b)), the second term does not contribute to the ESPE. Note that effects of this term are fully included when the Hamiltonian is diagonalized.

The situation is different for the last term on the right-hand-side of eq. (14),  $-\hat{\tau}_j^+ \hat{\tau}_j^-$ . Note that the protons and neutrons occupy the same orbit  $j$  now. Since the term,  $-\hat{\tau}_j^+ \hat{\tau}_j^-$ , exchanges a proton and a neutron, a subset of its effect is relevant now, if this term annihilates a proton and a neutron both in the *same* magnetic substate  $m$ , and creates them in exactly the same substate. Formally speaking, this process cannot be written like the first term on the right-hand side of eq. (14). We, however, can introduce a practical approximation. If there are  $n_j^n$  neutrons in the orbit  $j$ , they can be assumed, in first approximation, to be equally distributed over all possible  $m$ -states. In this equal distribution approximation, a proton in the magnetic substate  $m$  can feel an interaction with a neutron in the substate  $m$  with a probability

$\hat{n}_j^n/(2j + 1)$ . This approximation can be expressed as

$$-\hat{\tau}_j^+ \hat{\tau}_j^- : \sim \frac{\hat{n}_j^p \hat{n}_j^n}{2j + 1}. \quad (27)$$

This approximation can be understood also by considering the case of  $m = m'$  in Fig. 5 (d). By combining eq. (27) with the first term on the right-hand side of eq. (14), we define the *effective* proton-neutron monopole interaction as

$$\begin{aligned}\hat{v}_{pn,mono-eff} &= \sum_{j \neq j'} \frac{1}{2} \left\{ V_{T=0}^m(j, j') + V_{T=1}^m(j, j') \right\} \hat{n}_j^p \hat{n}_{j'}^n \\ &\quad - \sum_j \frac{1}{2} \left\{ V_{T=0}^m(j, j) \frac{2j + 2}{2j + 1} + V_{T=1}^m(j, j) \frac{2j}{2j + 1} \right\} \hat{n}_j^p \hat{n}_j^n.\end{aligned}\quad (28)$$

The ESPE is evaluated with this effective monopole interaction hereafter.

The proton-neutron interaction thus contributes to the ESPE of the neutron orbit  $j$  as

$$\hat{\epsilon}_j^{p \rightarrow n} = \sum_{j'} \frac{1}{2} \left\{ \tilde{V}_{T=0}^m(j', j) + \tilde{V}_{T=1}^m(j', j) \right\} \hat{n}_{j'}^p, \quad (29)$$

while to the ESPE of the proton orbit  $j$  as

$$\hat{\epsilon}_j^{n \rightarrow p} = \sum_{j'} \frac{1}{2} \left\{ \tilde{V}_{T=0}^m(j, j') + \tilde{V}_{T=1}^m(j, j') \right\} \hat{n}_{j'}^n, \quad (30)$$

where  $\tilde{V}$ 's are modified monopole matrix elements defined by

$$\tilde{V}_{T=0,1}^m(j, j') = V_{T=0,1}^m(j, j') \quad \text{for } j \neq j', \quad (31)$$

$$\tilde{V}_{T=0}^m(j, j) = V_{T=0}^m(j, j) \frac{2j + 2}{2j + 1}, \quad (32)$$

and

$$\tilde{V}_{T=1}^m(j, j) = V_{T=1}^m(j, j) \frac{2j}{2j + 1}. \quad (33)$$

We note that this substitution of  $V_{T=1}^m(j, j)$  by  $\tilde{V}_{T=1}^m(j, j)$  is only for the proton-neutron interaction, keeping eqs. (23,24) unchanged. It is worth mentioning that the effective monopole interaction in eq. (28) produces the energy exactly for a closed shell,  $\langle \hat{n}_j^p \rangle = 2j + 1$  or  $\langle \hat{n}_j^n \rangle = 2j + 1$ , because the equal distribution approximation turns out to be exact.

We summarize the valence contribution to the ESPE from eqs. (23,24,26,29), by introducing

$$\tilde{V}_{pn}^m(j, j') = \frac{1}{2} \left\{ \tilde{V}_{T=0}^m(j, j') + \tilde{V}_{T=1}^m(j, j') \right\}. \quad (34)$$

It is then for the proton orbit  $j$ ,

$$\hat{\epsilon}_j^p = \sum_{j'} V_{T=1}^m(j, j') \hat{n}_{j'}^p + \sum_{j'} \tilde{V}_{pn}^m(j, j') \hat{n}_{j'}^n, \quad (35)$$

and for the neutron orbit  $j$ ,

$$\hat{\epsilon}_j^n = \sum_{j'} V_{T=1}^m(j, j') \hat{n}_{j'}^n + \sum_{j'} \tilde{V}_{pn}^m(j', j) \hat{n}_{j'}^p . \quad (36)$$

Note that one can use  $V_x^m(j, j') = V_x^m(j', j)$  for any subscript  $x$ , if more convenient.

In many practical cases, the occupation number operators  $\hat{n}_j^p$  and  $\hat{n}_j^n$  can be treated as c-numbers. For instance, we may take the filling scheme, where nucleons are put into the possible lowest orbit one by one. In this scheme, these operators are c-numbers for a given nucleus, and the ESPEs become c-numbers as well. We omit the symbol  $\hat{\cdot}$  accordingly.

The difference of ESPE is more relevant than the ESPE itself, in some applications. The difference can be taken between different nuclei, between different states or between some others. It is written for the proton orbit  $j$  as,

$$\Delta\hat{\epsilon}_j^p = \sum_{j'} V_{T=1}^m(j, j') \Delta\hat{n}_{j'}^p + \sum_{j'} \tilde{V}_{pn}^m(j, j') \Delta\hat{n}_{j'}^n , \quad (37)$$

and for the neutron orbit  $j$  as,

$$\Delta\hat{\epsilon}_j^n = \sum_{j'} V_{T=1}^m(j, j') \Delta\hat{n}_{j'}^n + \sum_{j'} \tilde{V}_{pn}^m(j', j) \Delta\hat{n}_{j'}^p . \quad (38)$$

Here  $\Delta\hat{n}_{j'}^p$  or  $\Delta\hat{n}_{j'}^n$  can be zero, or can be c-numbers. Thus, the difference of ESPE may be a c-number to be related to observed properties. Such change of the ESPE of a specific orbit as a function of occupation number(s) is nothing but a part of the shell evolution.

We point out that for the closed-shell-plus-one-nucleon systems, the results shown in eqs. (35,36) produce the exact energy for a single proton state  $j$ ,

$$\begin{aligned} \epsilon_j^p = & \sum_{occ. j'_p} V_{T=1}^m(j, j'_p) (2j'_p + 1) \\ & + \sum_{occ. j'_n} \tilde{V}_{pn}^m(j, j'_n) (2j'_n + 1) , \end{aligned} \quad (39)$$

and for a single neutron state  $j$ ,

$$\begin{aligned} \epsilon_j^n = & \sum_{occ. j'_n} V_{T=1}^m(j, j'_n) (2j'_n + 1) \\ & + \sum_{occ. j'_p} \tilde{V}_{pn}^m(j'_p, j) (2j'_p + 1) , \end{aligned} \quad (40)$$

where the summation of  $j'_p$  or  $j'_n$  is taken for all fully occupied orbits in the valence space and the ESPEs are treated as c-numbers. This is partly because the approximation in eq. (27) becomes an equality relation due to the apparent equal distribution in the closed shell. Single-hole states can be treated similarly, if needed.

We also note once again that the ESPEs are formally operators, but can be treated as c-numbers if the wave function of the other nucleons is fixed. This happens very often in actual cases.

## E. Relations to earlier formulations

We discuss, in this subsection, relations of the present approach to earlier ones. [Bansal and French \(1964\)](#) introduced “the average two-body interaction energy (taken with a  $(2J+1)(2T+1)$  weighting)” and also “Another average, taken without the  $(2T+1)$  weighting”. Thus, Bansal and French regarded these approaches as two different schemes. The former is basically suitable for a closed shell where both proton and neutron shells are completely occupied. The averaging of all two-body matrix elements is carried out for all neutron-neutron, proton-proton and proton-neutron pairs, and the weighting factor  $(2J+1)(2T+1)$  arises. As the  $T=0$  and 1 two-body matrix elements are very different in size, another parameter was introduced to account for it. The formulation of the present work is based on an averaging also. But this is the averaging over all possible orientations of a given two-nucleon configuration  $j \otimes j'$ , and the idea is visualized in Fig. 4 with the definition in eq. (5) and in other related equations. The derived monopole interaction is shown in Sec. II.A with eqs. (14,15,16,17). These equations include the terms proportional to  $\hat{n}_j^p \hat{n}_{j'}^n$ , which may be related to Bansal-French’s second scheme mentioned above. This second scheme is described further in [\(Bansal and French, 1964\)](#) as “This is the average which one encounters in an n-p formalism (one in which neutrons and protons are separately numbered) in those cases where the neutron is necessarily in one orbit, the proton in the other”. Equations (14,15,16,17) include terms dependent on isospin operators as illustrated in Fig. 5, which enables us to remove such a restriction of the orbits and allow protons and neutrons to be in the same orbit.

[Poves and Zuker \(1981\)](#) developed the first scheme of Bansal and French, stating “ $H_m$  and  $H_{mT}$  can be thought of as generalization of the French-Bansal formulae”. The weighting factors  $(2J+1)(2T+1)$  are included in  $H_{mT}$ , while the isospin is not considered in  $H_m$ . The monopole interaction  $H_{mT}$  presented in [\(Poves and Zuker, 1981\)](#) produces the same energy for closed-shell states as the present approach. So, the result of [\(Poves and Zuker, 1981\)](#) and the relevant result of the present approach are obtained, most likely, by different procedures with consistent outcome. Although the derivation is not documented much in [\(Poves and Zuker, 1981\)](#), this consistency may be supported by the fact that the monopole interaction can be composed of the number and isospin operators of individual orbits, and closed shells can give sufficient constraints on the values of their parameters. The monopole Hamiltonian of [\(Poves and Zuker, 1981\)](#) was not used for further derivation of the effective single-particle operators (contrary to the present approach), but was used to calculate single-particle levels for some systems composed of a closed shell  $\pm$  one particle. Systematic studies were then carried out [\(Caurier \*et al.\*, 2005\)](#)

using such single-particle energies. Related studies were presented in (Utsuno *et al.*, 1999), and these works will be discussed later.

The present approach thus shows that the two approaches mentioned by Bansal and French are basically two facets of one common monopole interaction. It has been derived from the orientation averaging in the present scheme, fully keeping isospin properties. In this way, we can settle a long question, frustrating to some, on the definition and uniqueness of the monopole interaction, finding that basically all those arguments are along the same line leading to the correct result. The primary addition of the present theoretical formulation to the general aspect of the monopole interaction is, as mentioned, that all results can be derived without referring to closed-shell properties, which appear as consequences. The additional  $\tau\tau$  term of eq. (14) is of interest.

Another interest can be in the variational approach with monopole interaction in open-shell nuclei as discussed in (Yazaki, 1977).

#### F. Sample analyses in terms of the effective single particle energy

We present, in this subsection, some cases where the ESPE can be discussed.

##### 1. N=9 isotones

The  $N = 9$  isotones of C-N-O nuclei show a clear example of the change of ESPE's, as shown in Fig. 6. This figure is taken from Fig. 2 of Ref. (Talmi and Unna, 1960), as one of the earliest related papers. We discuss here how the changes shown in Fig. 6 can be described within the framework presented in the previous subsection. The discussions are somewhat detailed because this is the first actual example.

We assume the  $^{14}\text{C}$  core with  $Z = 6$  and  $N = 8$ . Figure 7 illustrates the shell structure on top of this  $^{14}\text{C}$  core. The levels shown in Fig. 7 are taken from experimental data (NNDC, 2016), assuming that the observed lowest levels are of single-particle nature, and are almost the same as the corresponding ones in Fig. 6. Figure 7 (a) indicates somewhat schematically neutron  $2s_{1/2}$  and  $1d_{5/2}$  orbits on top of the  $^{14}\text{C}$  core. Note that in Fig. 7 (a), the  $2s_{1/2}$  orbit is 0.74 MeV below  $1d_{5/2}$ .

We then add protons into the  $1p_{1/2}$  orbit, as shown in Fig. 7 (b). The proton  $1p_{1/2}$  orbit is fully occupied, or closed now. The ESPE's of neutron  $2s_{1/2}$  and  $1d_{5/2}$  orbits are both lowered, but more interestingly, their order is reversed due to protons in the  $1p_{1/2}$  orbit, following eq. (36) with  $j' = 1p_{1/2}$ , and  $j = 2s_{1/2}$  or  $1d_{5/2}$ . The ESPEs are treated here as c-numbers because the wave function of the other nucleons is fixed, as mentioned in

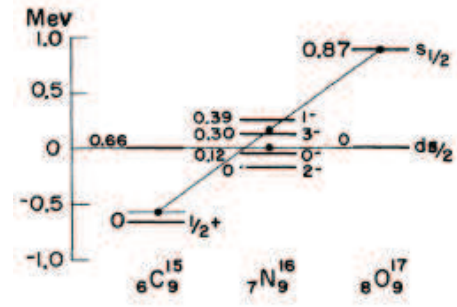


Figure 6 Experimental energy levels of  $N=9$  isotones, some of which are regarded as neutron  $2s_{1/2}$  and  $1d_{5/2}$  single-particle energies. See the text. Reprinted with permission from Talmi and Unna (1960).

Sec. II.D. The difference of ESPEs can be written as

$$\begin{aligned} & \epsilon_{2s_{1/2}}^n(^{17}\text{O}) - \epsilon_{1d_{5/2}}^n(^{17}\text{O}) \\ &= \epsilon_{2s_{1/2}}^n(^{15}\text{C}) - \epsilon_{1d_{5/2}}^n(^{15}\text{C}) \\ &+ \{V_{pn}^m(1p_{1/2}, 2s_{1/2}) - V_{pn}^m(1p_{1/2}, 1d_{5/2})\} \times 2 . \end{aligned} \quad (41)$$

The proton sector of the Hamiltonian produces the common effect between the  $J^\pi=1/2^+$  and  $5/2^+$  states. Thus, the above difference of ESPEs corresponds to the difference of experimental levels in the assumption that these states are of single-particle nature (which will be re-examined later), and the monopole matrix elements satisfying

$$\begin{aligned} & V_{pn}^m(1p_{1/2}, 2s_{1/2}) - V_{pn}^m(1p_{1/2}, 1d_{5/2}) \\ &= (0.87 + 0.74)/2 = 0.805 \text{ (MeV)} \end{aligned} \quad (42)$$

explain the change in Fig. 7. This result indicates that  $V_{pn}^m(1p_{1/2}, 1d_{5/2})$  is more attractive by  $\sim 0.8$  MeV than  $V_{pn}^m(1p_{1/2}, 2s_{1/2})$ . Thus, what actually occurs is more rapid lowering of the neutron  $1d_{5/2}$  orbit than that of the neutron  $2s_{1/2}$  orbit, as protons fill the  $1p_{1/2}$  orbit. This can be explained as a consequence of very important and general features of the monopole interactions as discussed later extensively.

If the energy is measured relative to the neutron  $1d_{5/2}$  orbit, the monopole-matrix-element difference in eq. (42) pushes up the neutron  $2s_{1/2}$  orbit from  $^{15}\text{C}$  to  $^{17}\text{O}$ . We shall describe the approach by Talmi and Unna (1960) with this convention such that the energy is measured from the neutron  $1d_{5/2}$  ESPE with the filling scheme. The energy levels in Fig. 7 can be viewed in this convention, including  $^{16}\text{N}$  ( $Z=7$  and  $N=9$ ) with one proton in the  $1p_{1/2}$  orbit. This proton is coupled with a neutron either in  $2s_{1/2}$  or  $1d_{5/2}$ . The former coupling yields  $J^\pi=0^-$  and  $1^-$  states, while the latter  $J^\pi=2^-$  and  $3^-$  states. In this simple configuration, the proton-neutron

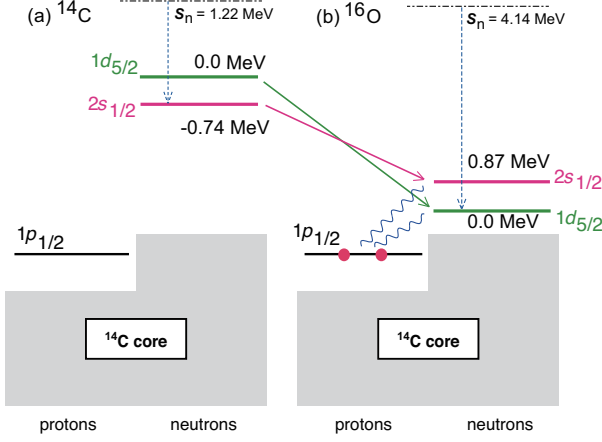


Figure 7 (a) Schematic picture of shell structure (a) on top of the <sup>14</sup>C core. (b) Two more protons (red solid circles) are added into the  $1p_{1/2}$  orbit. Experimental levels are identified as single-particle states: green level for  $1d_{5/2}$ , and pink level for  $2s_{1/2}$ . Numbers near the levels are energies relative to  $1d_{5/2}$ . The wavy lines imply proton-neutron interactions. Solid arrows indicate the changes of SPE's. The dashed-dotted line denotes neutron threshold, and downward dashed arrows mean one neutron separation energy ( $S_n$ ).

interaction,  $\hat{v}_{pn}$ , shifts the energies of these states by

$$\frac{1}{2} \left\{ \langle j, j'; J, T = 0 | \hat{v}_{pn} | j, j'; J, T = 0 \rangle + \langle j, j'; J, T = 1 | \hat{v}_{pn} | j, j'; J, T = 1 \rangle \right\}. \quad (43)$$

The  $(2J+1)$ -weighted average of the quantities in eq. (43) is nothing but the corresponding monopole matrix element, because of eqs. (19, 31, A2). Thus, those averages can be discussed as the ESPEs driven by the monopole interaction, and the aforementioned convention can be adopted. As the change from <sup>15</sup>C to <sup>17</sup>O is then twice the monopole-matrix-element difference due to two additional protons, the middle point of the line connecting the states of the same spin/parity of <sup>15</sup>C and <sup>17</sup>O represents the corresponding monopole quantity. Thus, if the present scheme works ideally, the  $1/2^+$  levels and the relevant average quantity of <sup>16</sup>N should be on a straight line. Talmi and Unna did, in Ref. (Talmi and Unna, 1960), this analysis in a slightly different way: they took the observed energy levels of <sup>17</sup>O and the weighted averages for the observed levels of <sup>16</sup>N, and extrapolated to <sup>15</sup>C. The extrapolated value appeared rather close to the observed one, implying the validity of this picture, which will be re-visited later.

We note that Talmi and Unna discussed another case with <sup>11</sup>Be - <sup>12</sup>B - <sup>13</sup>C ( $N=7$  isotones with  $Z=4, 5$  and  $6$ ) (Talmi and Unna, 1960). Although the  $1/2^+$  levels change almost linearly as a function of  $N$ , the mechanism is different from the  $N=9$  isotope case discussed above. Since protons occupy the  $1p_{3/2}$  orbit now, one

has to take into account the coupling of two protons. It was taken to be  $J = 0$  (see eq. (1) in (Talmi and Unna, 1960)), which enables us to connect the change of the structure to the monopole interaction, because multipole interactions are completely suppressed. Note that the terminology of monopole interaction was not used then, but the same quantity was used. This restriction to the  $J = 0$  coupling, however, may not be appropriate, because the deformation of the shape is crucial and simultaneously configuration mixings occur even between the  $1p_{3/2}$  and  $1p_{1/2}$  proton orbits. The single-particle nature is broken also on the neutron side due to configuration mixing between the  $2s_{1/2}$  and  $1d_{5/2}$  orbits. Thus, the  $N=7$  isotones may not be a good example of the change of single-particle energies. In fact, the magnitude of the change is twice larger than the  $N=9$  isotope case, which may be indicative of dominant additional effects.

## 2. Evolution of the $g_{7/2}$ orbit in the Zr-Mo region

The evolution of shells driven by the proton-neutron interaction is also observed in heavier mass regions. Here we pick up the case of the evolution of the neutron  $1g_{7/2}$  orbit when filling the proton  $1g_{9/2}$  orbit, along the line of Federman and Pittel (1977).

Experimental evidences for the strong proton-neutron interaction between  $1g_{9/2}$  and  $1g_{7/2}$  are suggested by Federman and Pittel (1977) in terms of what we call ESPE now. Having a neutron on top of the  $N = 50$  core, energy levels in  $N = 51$  isotones provide useful information on the evolution of neutron ESPE with increasing  $Z$ . It has been pointed out by Federman and Pittel (1977) that the lowest  $7/2^+$  levels rapidly decrease from 2.67 MeV in <sup>89</sup>Sr to 1.37 MeV in <sup>93</sup>Mo. Although these levels are not pure  $1g_{7/2}$  states, the main source of this decrease should be the lowering of the ESPE of neutron  $1g_{7/2}$  relative to neutron  $2d_{5/2}$  when protons occupy the  $1g_{9/2}$  orbit. The ESPE difference between the neutron  $1g_{7/2}$  and  $2d_{5/2}$  orbits is changed by  $V_{pn}^m(1g_{9/2}, 1g_{7/2}) - V_{pn}^m(1g_{9/2}, 2d_{5/2})$ , as more protons occupy the  $1g_{9/2}$  orbit. In fact, a large negative value of  $V_{pn}^m(1g_{9/2}, 1g_{7/2})$  accounts for the lowering. This trend should continue until the proton  $1g_{9/2}$  orbit is fully occupied. It is indeed observed as shown in Fig. 8.

It has been argued by Federman and Pittel (1977) that the proton-neutron central force in the  $^3S_1$  channel, where  $S$  stands for the  $s$  wave ( $L=0$ ) with the spin triplet and the relative orbital (total) angular momentum  $L=0$  ( $J=1$ ), gives rise to a strong attraction between two orbitals ( $n_P, l_P, j_P$ ) and ( $n_N, l_N, j_N$ ) when  $n_P = n_N$  and  $l_P \approx l_N$  is satisfied because of a large spatial overlap (de Shalit and Goldhaber, 1953). Relevant further studies were reported in (Umeya and Muto, 2004, 2006). Although the present combination of the single-particle orbits matches this condition, the central force is not the

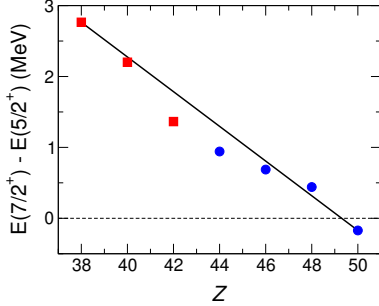


Figure 8 Energies of the lowest  $7/2^+$  level with large  $1g_{7/2}$  single-neutron strength measured from the  $5/2_1^+$  states for  $N = 51$  isotones (Federman and Pittel, 1977). The squares are experimental data based on the  $(d,p)$  reaction, and the circles stand for the lowest observed  $7/2^+$  level without information on single-particle strength. The present assignment for  $^{101}\text{Sn}$  is by Darby *et al.* (2010). The straight line connects the points at  $Z=38$  and  $50$ , depicting the monopole effect, while deviations from it are due to correlations beyond it.

whole story as we shall see.

### 3. Systematic trend of shell evolution caused by proton-neutron interaction

Recent experimental advances in radioactive isotope beams enable revealing shell evolution along long isotope or isotope chains. The levels of single-particle-like states on top of the  $N(Z) = 28$  and  $50$  closure were discussed by (Grawe, 2004), with sharp decreases of (a) neutron  $1f_{5/2}$  with proton  $1f_{7/2}$  filled, (b) proton  $1f_{5/2}$  with neutron  $1g_{9/2}$  filled, (c) proton  $1g_{7/2}$  with neutron  $1h_{11/2}$  filled, and (d) neutron  $1g_{7/2}$  with proton  $1g_{9/2}$  filled. For instance, the proton  $1f_{5/2}$  orbital is located nearly at the same position up to  $N = 40$ , while a sudden and sharp decrease occurs after that. These features certainly cannot be described by simple one-body potential models, which cause gradual evolution, and are clear signatures that the shell structure strongly depends on which orbital is filled because of the variation of the monopole matrix elements. The features shown by (Grawe, 2004) seem to be consistent with the Federman-Pittel mechanism (see Sec. II.F.2). The  $1h_{11/2}$ - $1h_{11/2}$  proton-neutron interaction, however, should not be as strong as the  $1h_{11/2}$ - $1g_{7/2}$  one in spite of  $n_P = n_N$  and  $l_P = l_N$ , because the position of proton  $1h_{11/2}$  orbit is almost unchanged with the neutron  $1h_{11/2}$  filled. Thus the above rule regarding the quantum numbers  $n$  and  $l$  are not enough to characterize the strengths of monopole matrix elements. Actually, as shown in Sec. III, the spin-isospin degrees of freedom plays a crucial role.

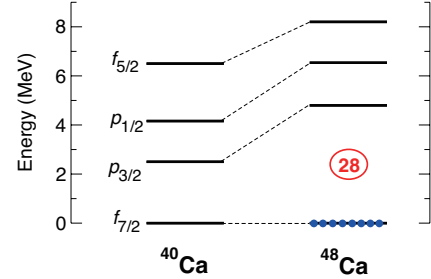


Figure 9 Evolution of neutron  $pf$  orbitals in going from  $^{40}\text{Ca}$  to  $^{48}\text{Ca}$  based on experimental data (Uozumi *et al.*, 1994a,b).

### 4. Emerging the $N = 28$ shell gap: like-particle interaction

We now move on to the shell evolution due to like-particle ( $T=1$ ) interactions, by pursuing neutron shell structure with varying neutron number [see also Sorlin and Porquet (2008, 2013)].

The magic number 28 is known as the first one that arises from the  $j$ - $j$  coupling scheme. This magic number is rather stable at least for  $N = 28$  isotones with  $Z \geq 20$ . Actually, the strength of the  $N = 28$  shell gap, i.e., single-particle-energy difference between  $1f_{7/2}$  and  $2p_{3/2}$ , is estimated to be 4.8 MeV on top of the  $^{48}\text{Ca}$  core from one-neutron separation energies of  $^{48,49}\text{Ca}$ . The  $\sim 5$  MeV shell gap at  $N = 28$  is also supported by comparing the first excited levels in  $^{47,48}\text{Ca}$ , which are dominated by neutron  $(2p_{3/2})^1(1f_{7/2})^{-2}$  and neutron  $(2p_{3/2})^1(1f_{7/2})^{-1}$  configurations, respectively, between experiment and shell-model calculations. Note that the  $7/2_1^+$  level at 3.13 MeV in  $^{49}\text{Ca}$ , whose spin and parity has recently given by Broda (2006); Montanari *et al.* (2011), is also consistent with shell-model results with the  $\sim 5$  MeV shell gap.

The  $N = 28$  shell gap is, on the other hand, much smaller on top of the  $^{40}\text{Ca}$  core. Experimentally, this quantity is deduced to be 2.5 MeV from the distribution of the spectroscopic strengths for the  $^{40}\text{Ca}(\bar{d},p)$  reaction (Uozumi *et al.*, 1994a).

Thus, as illustrated in Fig. 9,  $N = 28$  becomes one of the classical magic numbers by 2-3 MeV enlarging the neutron  $1f_{7/2}$ - $2p_{3/2}$  shell gap when the neutron  $1f_{7/2}$  orbit is filled. Assuming the inert  $^{40}\text{Ca}$  core, the present shell evolution can be attributed to like-particle interaction. By using Eqs. (21) and (22), the change of the  $N = 28$  shell gap is written as

$$\begin{aligned} & \Delta^{(f_{7/2}, nn)} \epsilon_{p_{3/2}} - \Delta^{(f_{7/2}, nn)} \epsilon_{f_{7/2}} \\ &= 8 \times \{ V_{T=1}^m(p_{3/2}, f_{7/2}) - V_{T=1}^m(f_{7/2}, f_{7/2}) \}. \end{aligned} \quad (44)$$

The impact of the monopole interaction on the evolution of the  $N = 28$  shell gap was first pointed out by McGroarty *et al.* (1970), where the Kuo-Brown interaction is shown to be incapable of reproducing low-lying

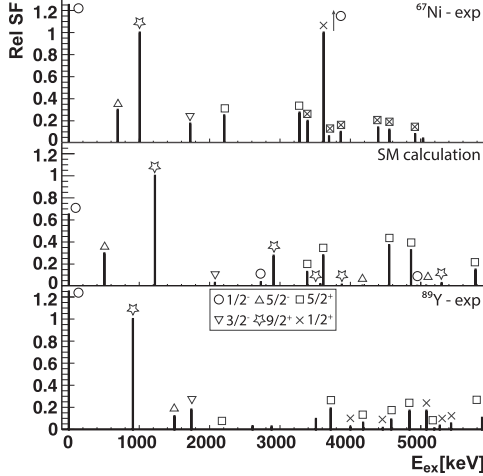


Figure 10 Distribution of spectroscopic factors associated with one-neutron addition in  $^{67}\text{Ni}$  (top and middle). This distribution is compared to one-proton strength distribution in  $^{89}\text{Y}$  (bottom), where the  $Z = 50$  magic number is well established. Reprinted with permission from [Diriken \*et al.\* \(2014\)](#).

energy levels in Ca isotopes in the vicinity of  $N = 28$ . This defect was then shown to be remedied by shifting  $V_{T=1}^m(p_{3/2}, f_{7/2})$  by +0.3 MeV, which leads to the additional 2.4 MeV enlargement of the  $N = 28$  shell gap. A similar monopole correction was also implemented by [Poves and Zuker \(1981\)](#) in their KB3 interaction, making the KB3 interaction frequently used for the  $pf$ -shell nuclei.

The formation of the  $N = 28$  magic number can be regarded as the stabilization of the intruder orbit,  $1f_{7/2}$ , when this orbit is filled. Whether this is a universal property over the Segrè chart is worth investigating, and experimental data have recently been accumulated pointing in this direction. For the  $sd$  shell, a high  $2_1^+$  energy in  $^{22}\text{O}$  measured by [Thirolf \*et al.\* \(2000\)](#) clearly indicates the enlargement of the shell gap between the neutron  $1d_{5/2}$  and  $2s_{1/2}$  orbits with the former filled. On the basis of a shell-model analysis using the USD interaction, this shell gap changes from 0.8 MeV to 4.3 MeV in going from  $^{16}\text{O}$  to  $^{22}\text{O}$ . For the  $1g$ - $2d$ - $3s$  shell, the analogous case is the evolution of the neutron  $1g_{9/2}$ - $2d_{5/2}$  shell gap with the neutron  $1g_{9/2}$  orbit filled. While the  $N=50$  gap has been discussed in the past (see [Sorlin and Porquet \(2013\)](#), for instance), a recent  $(d, p)$  measurement in inverse kinematics ([Diriken \*et al.\*, 2014, 2015](#)) shows that this shell gap is possibly reduced as the neutron  $1g_{9/2}$  occupation decreases. As shown in Fig. 10, significant strengths of the neutron  $2d_{5/2}$  orbit are observed at 1-2 MeV above the neutron  $1g_{9/2}$  state in  $^{67}\text{Ni}$ , suggesting a considerable reduction of the  $N = 50$  shell gap in comparison to the vicinity of  $^{78}\text{Ni}$  [estimated to be  $> 4$  MeV in [Orlandi \*et al.\* \(2015\)](#)], where the neutron  $1g_{9/2}$  orbit

is filled. It is noted that the change of the  $N = 50$  shell gap is estimated to be approximately 3 MeV by [Sorlin and Porquet \(2013\)](#).

### III. SHELL EVOLUTION, MONPOLE INTERACTION AND NUCLEAR FORCES

The effective single-particle energy (ESPE) is shown to be varied according to the relations in eqs. (37, 38). Since it depends linearly on the proton or neutron number operators of particular orbit  $j$ , denoted respectively as  $\hat{n}_j^p$  and  $\hat{n}_j^n$ , the ESPE can be changed to a large extent if the occupation number of a given orbit becomes large. This further can result in a substantial change of the shell structure, called *shell evolution*. Thus, the shell evolution can occur, for instance, as a function of  $N$  along an isotopic chain. We shall discuss, in this section, some basic points of the shell evolution in close relations to nuclear forces.

The nuclear shell model originates in the shell structure and its magic numbers proposed by Mayer and Jensen ([Haxel \*et al.\*, 1949](#); [Mayer, 1949](#)). The magic numbers (corresponding to major closed shells) proposed with the independent particle shell model ([Haxel \*et al.\*, 1949](#); [Mayer, 1949](#)) have been considered, more or less, to remain for all the nuclei, taking the values 2, 8, 20, 28, 50, 82, 126, ... . This paradigm of the magic-number constancy has been working very well for stable nuclei and their neighborhood on the Segrè chart, but is being challenged for exotic nuclei where large variations of occupation numbers can occur and change the shell structure. We shall discuss characteristic features of contributions from various components of the nuclear force.

We note here that the multipole interaction defined in Sec. II.A produces a variety of correlations, for instance, quadrupole deformation, and that the final structure is determined jointly by the monopole and multipole interactions, as is done automatically when the Hamiltonian is diagonalized. Although there is no *a priori* separation of effects of the monopole interaction from those of the multipole interaction, the monopole effects, particularly the shell evolution, can be made visible in many cases. We shall focus, in this section, on such effects of the monopole interactions due to various constituents of the  $NN$  interaction, such as central, tensor and two-body spin-orbit.

#### A. Contributions from the central forces

The central-force component of the nuclear force is the main driving force of the formation of the nuclear structure.

Let us start with an extreme case, if the effective nucleon-nucleon ( $NN$ ) interaction,  $\hat{v}$ , is a central force

with infinite range and no dependence on spin, the values of monopole matrix elements  $V_{T=1}^m(j, j')$  and  $V_{pn}^m(j, j')$  become independent of  $j$  and  $j'$ , being constants. If this  $\hat{v}$  is attractive,  $V_{T=1}^m(j, j')$  and  $V_{pn}^m(j, j')$  take separate constant negative values. This implies, for instance, that if more neutrons occupy the orbit  $j'$ , all proton orbits  $j$  become more bound to the same extent. In other words, the proton shell structure is conserved but becomes more deeply bound.

On the other hand, if  $\hat{v}$  is given by a  $\delta$ -function with a certain strength parameter, the values of  $V_{T=1}^m(j, j')$  and  $V_{pn}^m(j, j')$  become sensitive to the overlap between the wave functions of the orbit  $j$  and that of the orbit  $j'$ . This implies, for instance, that if more neutrons occupy the orbit  $j'$ , proton ESPE for the orbit  $j$  in eq. (37) become more bound, but the amount of the change is not uniform. In other words, the pattern of the proton single-particle orbits may change while they all become more bound as a whole.

The actual situation is certainly somewhere in between. We here show how monopole matrix elements look like for a central Gaussian interaction given by

$$v_c = \sum_{S,T} f_{S,T} P_{S,T} \exp(-(r/\mu)^2), \quad (45)$$

where  $S(T)$  means spin (isospin),  $P$  denotes the projection operator onto the channels  $(S, T)$  with strength  $f$ , and  $r$  and  $\mu$  are the internucleon distance and Gaussian parameter, respectively. We fix here all  $f$  parameters to a common value of +166 MeV just in order to see the effects of the four terms on the right-hand side. The  $\mu = 1$  fm is used as we shall discuss later, too. Note that we shall use this  $v_c$  later extensively with realistic values of parameters such as  $f_{1,0} = f_{0,0} = -166$  MeV (*i.e.*, the same magnitude with the opposite sign from the above value), and  $f_{0,1} = 0.6f_{1,0}$  and  $f_{1,1} = -0.8f_{1,0}$ . Such  $v_c$  gives basic features of effective  $NN$  interaction of the shell-model calculation, as called  $V_{MU}$  (Otsuka *et al.*, 2010b).

Figure 11 shows monopole matrix elements thus obtained. The harmonic oscillator wave functions are used as single-particle wave functions hereafter. We take  $A = 100$  in Fig. 11.

Figure 11 indicates that the  $(S = 1, T = 0)$  channel produces major contributions, apart from the actual  $f_{S,T}$  values. Furthermore, as mentioned just above, the actual value of  $f_{S=1,T=0}$  appears to be the largest among the four  $(S, T)$  channels (*e.g.*, in the  $V_{MU}$  (Otsuka *et al.*, 2010b)), this dominance becomes enhanced after considering the actual  $f_{S,T}$  values.

Within the  $(S = 1, T = 0)$  channel, Fig. 11 demonstrates that the coupling between orbits with  $n = 1$  (*i.e.*, no node in the radial wave function) like  $1g_{9/2}-1g_{9/2,7/2}$  or  $1g_{9/2}-1h_{11/2}$  are stronger than the others. This can be understood in terms of the larger overlap between their

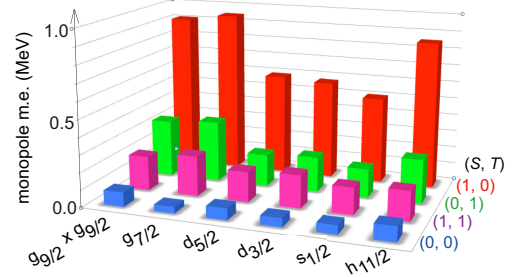


Figure 11 Monopole matrix elements of central Gaussian interactions of eq. 45 for all  $(S, T)$  channels with an equal strength parameter (*i.e.*, +166 MeV, see the text). One of the orbits is  $1g_{9/2}$ , and the other is shown.

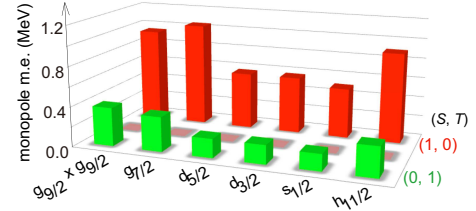


Figure 12 Monopole matrix elements of delta interactions for  $(S, T)$  channels. See the caption of Fig. 11.

radial wave functions than those in the other categories in Fig. 11. We shall come to this point later.

We show similar histograms for the  $\delta$ -function interaction in Fig 12. One finds rather good overall similarity to Fig. 11. On the other hand, the monopole matrix elements vanish for  $(S = 1, T = 1)$  or  $(S = 0, T = 0)$  channel, as not shown in Fig 12. This is a consequence of the Pauli principle which forbids two nucleons at the same place for  $S = 0, T = 0$  or  $S = 1, T = 1$ .

It is now of interest to survey the overall dependence of the monopole matrix element on the nodal structure of the radial wave function. Figure 13 shows monopole matrix elements in the  $(S = 1, T = 0)$  channel for the Gaussian and  $\delta$ -function interactions. In Fig. 13, various pairs of orbits are taken for the valence shells around (a)  $A = 100$  and also (b)  $A = 70$ , with their labels abbreviated like  $g7$  for  $1g_{7/2}$ . The strength of the  $\delta$ -function interaction is adjusted so that the monopole matrix element becomes equal to that given by the Gaussian interaction for (a) the  $g9-g7$  pair and (b) the  $f7-f5$  pair.

The orbital pairs are classified into categories according to the difference of the number of the nodes in their radial wave functions, as denoted by  $\Delta n$  in Fig. 13. It is noticed that the monopole matrix elements are generally large when the radial wave functions have the same number of the nodes (*i.e.*,  $\Delta n = 0$ ). The monopole matrix elements become smaller as  $\Delta n$  increases, while the difference between the two categories  $\Delta n = 1$  and  $\Delta n = 2$  is

much smaller. On the other hand, the monopole matrix element varies within the  $\Delta n = 0$  category. The large value of the  $s_1$ - $s_1$  in Fig. 13 (a) is exceptional. Among the others with  $\Delta n = 0$  in Fig. 13 (a), stronger coupling can be found between the following orbits:

$$j_> = \ell + 1/2 \text{ and } j_< = \ell - 1/2, \quad (46)$$

where  $\ell$  stands for the orbital angular momentum and  $1/2$  represents the spin. In other words,  $j_>$  and  $j_<$  are spin-orbit partners having the same radial wave functions in the Harmonic Oscillator scheme, and therefore the central force, both the Gaussian and the  $\delta$ -function interactions, produces stronger monopole interactions between them. This feature is seen in the cases of (i)  $g_9$  and  $g_7$ , (ii)  $d_5$  and  $d_3$ , (iii)  $f_7$  and  $f_5$ , and (iv)  $p_3$  and  $p_1$  in Fig. 13. We note that this type of enhanced coupling becomes weaker with the Gaussian interaction than with the  $\delta$ -function interaction.

We emphasize that the monopole matrix elements of the central force, as modeled by the Gaussian interaction in eq. (45), vary considerably, and can produce sizable shell evolution depending on the occupation pattern over relevant single-particle orbits. We shall discuss concrete examples later.

Regarding the dependence on the mass number,  $A$ , the monopole matrix elements of  $A = 100$  in Fig. 13 (a) is, as a whole, about  $2/3$  of those of  $A = 70$  in Fig. 13 (b). This feature can be expressed by a  $1/A$  dependence in a rough approximation if wished. This approximate scaling law appears to be reasonable because the probability to find the partner of a pair of interacting nucleons inside the interaction range is inversely proportional to the nuclear volume, as far as the density saturation holds. Note that this overall trend is seen in experimentally extracted data, while other  $A$ -dependences can be found locally in certain groups (see Fig. 8 of (Sorlin and Porquet, 2008)).

Stronger couplings between particular orbits are a natural idea, and were, in fact, discussed in earlier works, for instance, by Federman, Pittel, *et al.* as mentioned in Sec. II.F.2. While the importance of the  $^3S_1$  channel of the central force in the relative motion of two nucleons was emphasized in (Federman and Pittel, 1977), it certainly contributes to the present ( $S = 1, T = 0$ ) channel. Figure 13 (a) suggests that the monopole matrix element  $V_{T=0}^m(1g_{7/2}, 1g_{9/2})$  is about 0.3 MeV more attractive than  $V_{T=0}^m(2d_{5/2}, 1g_{9/2})$  with the realistic sign of the parameter mentioned above. Neglecting the other contributions which are minor, for the sake of simplicity, Equation (38) combined with eq. (29) indicates that the present Gaussian central force lowers the ESPE of the neutron  $1g_{7/2}$  orbit is lowered relative to the  $2d_{5/2}$  orbit by  $\sim \frac{1}{2} \times 0.3 \times 10 = 1.5$  MeV, in going from  $Z = 40$  to  $Z = 50$ . Here we assumed that the  $Z = 40$  and  $N = 50$  closed shells are kept, the neutron  $1g_{7/2}$  and  $2d_{5/2}$  orbits are on top of this closed shell, and additional 10 protons occupy the  $1g_{9/2}$  orbit. This change is quite sizable, and will be shown to

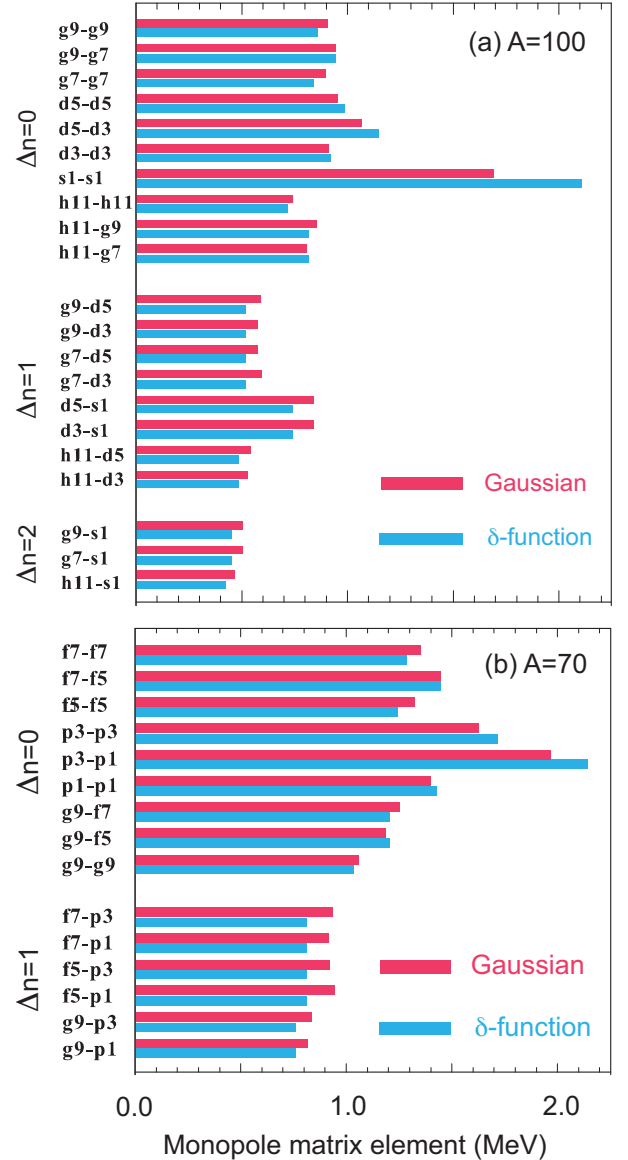


Figure 13 Monopole matrix elements of central Gaussian and  $\delta$  interactions for the ( $S = 1, T = 0$ ) channel. The orbit labeling is abbreviated like  $g_9$  for  $1g_{9/2}$ , etc. The orbits are from the valence shell for (a)  $A = 100$  and (b)  $A = 70$ .

be about a half of what has been known experimentally. This is clearly related to the observed levels depicted in Fig. 8, while the change will turn out to be larger due to corrections for fragmentation of single-particle strengths.

We here come back to the limit of long-range interaction, but include dependences on the spin and isospin (Otsuka *et al.*, 2001). If there is no spin dependence, an infinite-range interaction gives a constant shift as discussed above. Let us now take a spin-isospin interaction such as

$$v_{\tau\tau\sigma\sigma} = \vec{\tau} \cdot \vec{\tau} \vec{\sigma} \cdot \vec{\sigma} f(r), \quad (47)$$

where  $f(r)$  represents the dependence on the relative distance  $r$ , “.” implies a scalar product, and  $\vec{\sigma}$  ( $\vec{\tau}$ ) refers to spin (isospin) operators.

The matrix element of the term  $\vec{\tau} \cdot \vec{\tau}$  is trivial, being  $-\frac{3}{4}$  and  $\frac{1}{4}$  for  $T=0$  and 1, respectively. The monopole matrix elements of this interaction with  $f(r) \equiv 1$  show an interesting property, and we shall discuss it now. We consider antisymmetric states in eq. (3) or (A17) and symmetric states in eq. (A3) or eq. (A4). The monopole matrix element consists of direct and exchange contributions. The direct contribution from the  $\vec{\sigma} \cdot \vec{\sigma}$  term is

$$\sum_{m,m'} (j, m | \sigma_z | j, m) (j', m' | \sigma_z | j', m') = 0, \quad (48)$$

where  $\sigma_z$  stands for the  $z$ -component of  $\vec{\sigma}$  and  $\sum_m (j, m | \sigma_z | j, m) = 0$  is used. On the other hand, the exchange contribution is expressed as

$$\mp \sum_{m,m'} \left\{ \frac{1}{2} \{ (j, m | \sigma_+ | j', m') (j', m' | \sigma_- | j, m) \right. \\ \left. + (j, m | \sigma_- | j', m') (j', m' | \sigma_+ | j, m) \} \right. \\ \left. + (j, m | \sigma_z | j', m') (j', m' | \sigma_z | j, m) \right\}, \quad (49)$$

where  $\sigma_+$  and  $\sigma_-$  stand for the raising or lowering operator of  $\vec{\sigma}$ , and the overall sign  $\mp$  corresponds to the antisymmetric and symmetric states, respectively. Thus, direct terms do not contribute, and only exchange contributions remain. We point out that for interactions without the  $\vec{\sigma} \cdot \vec{\sigma}$  term, the situation is very different as the direct term is the major source of the monopole interaction. In order to have finite values in eq. (49),  $j$  and  $j'$  must have the same  $\ell$ , implying that  $j$  and  $j'$  are either  $j_>$  or  $j_<$  for the same  $\ell$ . After some algebra of angular momentum, the final results are tabulated in Table I. The  $j_> - j_<$  coupling appears to be about twice stronger than the  $j_> - j_>$  or the  $j_< - j_<$  couplings. This is precisely due to larger matrix elements of spin-flip transitions, like  $(j_> | \vec{\sigma} | j_<)$  or  $(j_< | \vec{\sigma} | j_>)$ , than spin-nonflip transitions like  $(j_> | \vec{\sigma} | j_>)$  or  $(j_< | \vec{\sigma} | j_<)$  (Otsuka *et al.*, 2001). The same mathematical feature applies to the isospin matrix elements, enhancing charge exchange processes like the one shown in Fig. 14 (d). The most important outcome of these features is the strong proton-neutron coupling between  $j_>$  or  $j_<$  with the same  $\ell$ , or between  $\ell + 1/2$  and  $\ell - 1/2$  (see Fig. 14 (c)).

A concrete example is shown in Fig. 14 (a,b). We assume here the simple filling configuration that the last six protons in  $^{30}\text{Si}$  are in the  $1d_{5/2}$  (shown as  $0d_{5/2}$ ) orbit in Fig. 14 (a). On the other hand,  $^{24}\text{O}$  has no proton in the  $1d_{5/2}$  orbit, and shows a large gap between neutron  $1d_{3/2}$  and  $2s_{1/2}$  orbits, consistent with experiment (Hoffman *et al.*, 2008).

The monopole matrix element of the  $\tau\tau\sigma\sigma$  interaction with  $f(r) \equiv 1$  vanishes for any pair involving an  $s_{1/2}$  orbit. Thus, these last six protons in  $^{30}\text{Si}$  lower the ESPE of the

Table I Monopole matrix elements of the  $\tau\tau\sigma\sigma$  interaction with  $f(r) \equiv 1$ . Based on Table 1 of (Otsuka, 2002).

$j_1$	$j_2$	$T=0$	$T=1$
$\ell + \frac{1}{2}$	$\ell + \frac{1}{2}$	$-3/16(2\ell+1)$	$-(2\ell+3)/16(2\ell+1)^2$
$\ell + \frac{1}{2}$	$\ell - \frac{1}{2}$	$-3/8(2\ell+1)$	$-1/8(2\ell+1)$
$\ell - \frac{1}{2}$	$\ell - \frac{1}{2}$	$-3(2\ell-1)/16(2\ell+1)^2$	$-1/16(2\ell+1)$

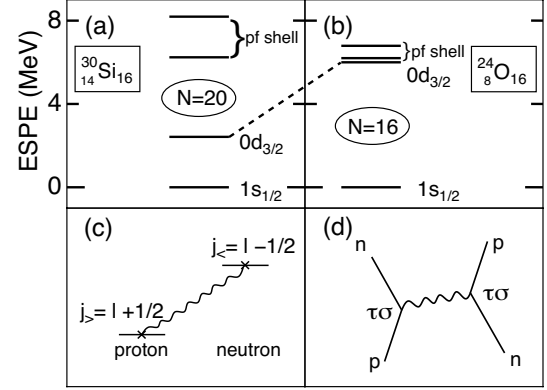


Figure 14 Neutron ESPEs for (a)  $^{30}\text{Si}$  and (b)  $^{24}\text{O}$ , relative to the  $2s_{1/2}$  (shown as  $1s_{1/2}$ ) orbit. The dotted line connecting (a) and (b) is drawn to indicate the change of the  $1d_{3/2}$  (shown as  $0d_{3/2}$ ) level. (c) The major interaction producing the basic change between (a) and (b). (d) The process relevant to the interaction in (c). From Otsuka *et al.* (2001).

neutron  $1d_{3/2}$  orbit relative to the  $2s_{1/2}$  orbit through the monopole matrix element,

$$V_{pn}^m(1d_{5/2}, 1d_{3/2}) = -\frac{1}{4(2 \times 2 + 1)}, \quad (50)$$

obtained from Table I, following eq. (38). Although not shown in Fig. 14, the ESPE of the neutron  $1d_{5/2}$  orbit is lowered by about half of the change of the neutron  $1d_{3/2}$  ESPE, as can be seen in Table I with  $\ell \gg 1$ . Thus, while the  $\tau\tau\sigma\sigma$  interaction can change the spin-orbit splitting, both spin-orbit partners are shifted in the same direction.

The above argument on a more attractive monopole matrix element between  $\ell + 1/2$  and  $\ell - 1/2$  orbits can be extended, with certain modifications, to finite-range and zero-range central interactions as we have seen numerically in Fig. 13. We note that in the case of the zero-range  $\delta$ -function central interaction, the total spin of two interacting nucleons is restricted to  $S=0$  for  $T=1$  and  $S=1$  for  $T=0$ , and this induces some spin-spin effects even for a simple  $\delta$ -function interaction without explicit spin dependence. We point out also that within the central forces, the coupling between orbits with  $\ell$  and  $\ell'$  with  $\ell \neq \ell'$  is not enhanced as can be understood from Fig. 14 (d) and as can be confirmed numerically from Fig. 13.

We will come back to these features after discussing the tensor-force effect.

## B. Shell Evolution due to Tensor force

### 1. Tensor force

We now study the shell evolution due to another major component of the nuclear force, the tensor force. Yukawa proposed the meson exchange process as the origin of the nuclear forces (Yukawa, 1935). Although this was on the exchange of a scalar meson and is not directly related to the tensor force, the meson exchange theory was developed further, and Bethe demonstrated that the tensor force is formulated with the coupling due to another kind of meson (i.e., referred to as pion presently), with explicit reference to the tensor force and its effect on the deuteron property (Bethe, 1940a,b). We can thus identify the tensor force with its unique features as one of the most important and visible manifestations of the meson exchange process initiated by Yukawa.

We start our discussion with the one-pion exchange potential between the i-th and j-th nucleons,

$$V_\pi = f(\vec{\tau}_i \cdot \vec{\tau}_j)(\vec{\sigma}_i \cdot \nabla)(\vec{\sigma}_j \cdot \nabla) \frac{e^{-m_\pi r}}{r}, \quad (51)$$

where  $\vec{\tau}_i$  and  $\vec{\sigma}_i$  indicate, respectively, the isospin and spin operators of the i-th nucleon,  $\vec{r}$  denotes the relative displacement between these two nucleons with  $r = |\vec{r}|$ , and  $\nabla$  stands for the derivative by  $\vec{r}$ . Here,  $f$  and  $m_\pi$  are the coupling constant and the pion mass, respectively. Equation (51) is rewritten as

$$V_\pi = \frac{f m_\pi^2}{3} (\vec{\tau}_i \cdot \vec{\tau}_j) \times \left\{ (\vec{\sigma}_i \cdot \vec{\sigma}_j) + S_{ij} \left\{ 1 + \frac{3}{m_\pi r} + \frac{3}{(m_\pi r)^2} \right\} \right\} \frac{e^{-m_\pi r}}{r}, \quad (52)$$

with

$$S_{ij} = 3(\vec{\sigma}_i \cdot \vec{r})(\vec{\sigma}_j \cdot \vec{r})/r^2 - (\vec{\sigma}_i \cdot \vec{\sigma}_j). \quad (53)$$

Here an additional  $\delta$  function term is omitted in eq. (52) as usual (because there are other processes at short distances). The first term within  $\{ \}$  on the right-hand side of eq. (52) produces a central force, and is not considered hereafter. The second term within this  $\{ \}$  generates the tensor force from the one-pion exchange process.

The tensor force has been known for a long time in connection to the one-pion exchange potential as stated here, and its effects were studied extensively from many angles. Early studies in connection to the nuclear structure include an extraction of the tensor-force component in the empirical  $NN$  interaction by Schiffer and True (Schiffer and True, 1976), a derivation of microscopic effective

$NN$  interaction (i.e., so-called “G-matrix interaction”) including second-order effects of the tensor force by Kuo and Brown (Kuo and Brown, 1966), a calculation of magnetic moments also including second-order tensor-force contributions by Arima and his collaborators (Shimizu *et al.*, 1974) and by Towner (Towner, 1987), etc.

Besides such effects, the tensor force produces another effect on the shell structure in its lowest order, or, by the one-pion exchange process. This effect must have been contained in numerical results, but its simple, robust and general features had not been mentioned or discussed until the work done in (Otsuka *et al.*, 2005), where the change of the shell structure, *i.e.*, the shell evolution, due to the tensor force was presented for the first time.

We now present the monopole interaction of the tensor force first, in order to clarify such tensor-force driven shell evolution. Because the  $S$  operator in eq. (53) between nucleons “1” and “2” can be rewritten as

$$S_{12} = \sqrt{24\pi} [(\vec{\sigma}_1 \times \vec{\sigma}_2)]^{(2)} \times Y^{(2)}(\theta, \phi)]^{(0)}, \quad (54)$$

where  $[\times]^{(K)}$  means the coupling of two operators in the brackets to an angular momentum (or rank)  $K$ , and  $Y$  denotes the spherical harmonics of the given rank for the Euler angles,  $\theta$  and  $\phi$ , of the relative coordinate. The tensor force can then be rewritten in general as

$$V^{ten} = (\vec{\tau}_1 \cdot \vec{\tau}_2) ([\vec{\sigma}_1 \times \vec{\sigma}_2]^{(2)} \cdot Y^{(2)}(\theta, \phi)) f^{ten}(r), \quad (55)$$

where  $f^{ten}(r)$  is an appropriate function of the relative distance,  $r$ . Note that the scalar product is taken instead of  $[\times]^{(K)}$ . Eq. (55) is equivalent to the usual expression containing the  $S_{12}$  function. Because the spins  $\vec{\sigma}_1$  and  $\vec{\sigma}_2$  are dipole operators and are coupled to rank 2, the total spin  $S$  (magnitude of  $\vec{S} = \vec{s}_1 + \vec{s}_2$ ) of two interacting nucleons must be  $S=1$ . This plays a crucial role in the shell evolution by the tensor force as pointed out later. If both of the bra and ket states of  $V^{ten}$  have  $L=0$ , with  $L$  being the relative orbital angular momentum, their matrix element vanishes because of the  $Y^{(2)}$  coupling. These properties are used later also.

Beside the pion ( $\pi$ ) exchange, the rho meson ( $\rho$ ) contributes to the tensor force. In the following, we use the  $\pi+\rho$  meson exchange potential with the coupling constants taken from (Osterfeld, 1992). The function  $f^{ten}(r)$  therefore corresponds to the sum of these exchange processes. The magnitude of the tensor-force effects to be discussed becomes about three quarters as compared to the results by the one-pion exchange only. The basic physics will not be changed. We will compare the  $\pi+\rho$  meson results with those by modern theories of nuclear forces.

### 2. Tensor force and two-nucleon system

Having these setups, we first recall the basic properties of the tensor force, by taking a two-nucleon system.

From the previous subsubsection, we know  $S = 1$  for two nucleons interacting through the tensor force. We therefore assign  $s_z = 1/2$  for each nucleon, taking the  $z$ -axis in the direction of the spin.

Figure 15 displays schematically this system in two different situations. The spins are shown by arrows pointing upwards, and are placed where two nucleons are placed at rest. In other words, two nucleons are displaced (a) in the direction of the spin or (b) in the perpendicular direction. This is certainly a modeling of the actual situation of which the wave function of the relative motion is shown schematically by yellowish shaded areas in Fig. 15.

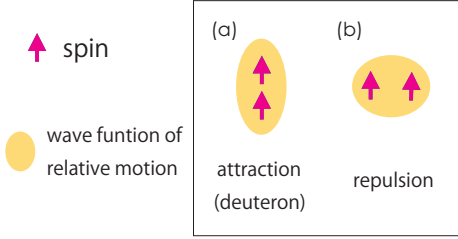


Figure 15 Intuitive picture of the tensor force acting on two nucleons.

We now consider the effect of the tensor force in these two cases, by denoting the value of the operator in eq. (53) by  $\mathcal{S}_{ij}$ . In the case of Fig. 15 (a), we obtain

$$(\vec{\sigma}_i \cdot \vec{r})/r \times (\vec{\sigma}_j \cdot \vec{r})/r = \frac{1}{2} \times \frac{1}{2}, \quad (56)$$

while this quantity vanishes for Fig. 15 (b) because of the orthogonality between  $\vec{\sigma}$  and  $\vec{r}$ . Because of  $S = 1$ ,

$$(\vec{\sigma}_i \cdot \vec{\sigma}_j) = \frac{1}{4} \quad (57)$$

holds. Combining these, we obtain

$$\mathcal{S}_{ij} = \begin{cases} \frac{3}{4} - \frac{1}{4} = \frac{1}{2} & \text{for (a)} \\ 0 - \frac{1}{4} = -\frac{1}{4} & \text{for (b)} \end{cases} \quad (58)$$

The tensor force works for the two cases in Fig. 15 (a) and (b) with opposite signs. The actual sign of  $f$  in eq. (52) is positive, while the  $(\vec{\sigma}_i \cdot \vec{\sigma}_j)$  term becomes  $-3/4$  for  $T = 0$  where  $T$  stands for the coupled isospin of the nucleons. The case in Fig. 15 (a) gains the binding energy from the tensor force, and indeed corresponds to the deuteron. The other case is actually unbound. In the case of  $T = 1$ , the attractive effect from the tensor force is three times weaker than in the  $T = 0$  case, in a naïve approximation.

### 3. Tensor-force effect and orbital motion: intuitive picture

We next consider tensor-force effects on the ESPEs in nuclei: the reduction of the spin-orbit splitting. As will

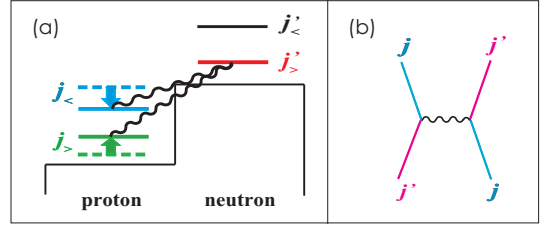


Figure 16 (a) Schematic picture of the monopole interaction produced by the tensor force between a proton in  $j_{>,<} = l \pm 1/2$  and a neutron in  $j'_{>,<} = l' \pm 1/2$ . (b) Exchange processes contributing to the monopole interaction of the tensor force. From Otsuka *et al.* (2005).

be shown in this and subsequent sections, the monopole interaction of the tensor force is always attractive between  $j_{>}$  and  $j'_{<}$  orbits, whereas it is always repulsive between  $j_{>}$  and  $j'_{>}$  as well as between  $j_{<}$  and  $j'_{<}$ . Figure 16 shows a typical case that the occupation of the neutron  $j'_{>}$  orbit changes the splitting between the proton  $j_{>}$  and  $j_{<}$  orbits, as expected by applying these monopole matrix elements to eq. (37). Such changes lead us to the significant variation of the shell structure, *i.e.*, shell evolution, in association with sizable occupations of a particular orbit. This basic feature has been presented in (Otsuka *et al.*, 2005) followed by further developments. We shall discuss here the mechanism and consequence of such tensor-force driven shell evolution in some detail including those developments.

Figure 17 shows, in an intuitive way, the phenomena we are looking into. Spins are shown by arrows, and they are set to be both up, because of  $S = 1$  for the tensor force. We compare two cases: (a) the tensor-force coupling between  $j_{>}$  and  $j'_{<}$  orbits, (b) the one between  $j_{>}$  and  $j'_{>}$  (and also  $j_{<}$  and  $j'_{<}$ ).

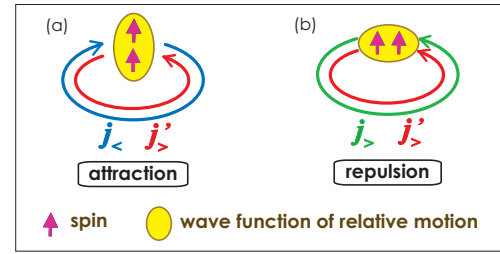


Figure 17 Intuitive picture of the tensor force acting on two nucleons on orbits  $j$  and  $j'$ . From Otsuka *et al.* (2005).

Before evaluating quantitatively these couplings, we present a simplified picture. This is based on the argument first shown briefly in (Otsuka *et al.*, 2005), followed by an elaborated description in (Otsuka, 2013) and by a further extended version with a figure in (Otsuka, 2014). As the last one is most extensive but in Japanese, we provide a slightly revised text and figure here.

We begin with the case shown in Fig. 17(a) where a nucleon in  $j_{<}$  is interacting with another in  $j'_{>}$  through the

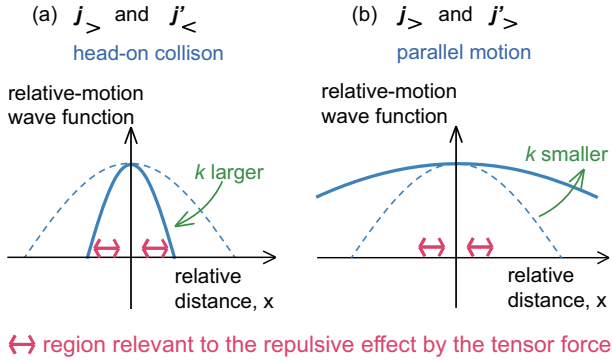


Figure 18 Intuitive picture of the tensor force acting between two nucleons in a one-dimensional model. The relative-motion wave function is shown for (a) head-on collision and (b) parallel motion cases. In (a), the change is shown as the relative momentum  $k$  becomes larger. See the text for explanation. Adapted from [Otsuka \(2014\)](#).

tensor force. Since the spin of each nucleon is fixed to be up, two nucleons must rotate on their orbits in opposite ways. We shall look into the relative motion of the two interacting nucleons, as the interaction between them is relevant only to their relative motion but not to their center-of-mass motion. We model the relative motion by a linear motion on the  $x$  axis. When two nucleons are close to each other within the interaction range, which is shorter than the scale of the orbital motion, the motion of two nucleons can be approximated by a linear motion, and the interaction works only within this region. It is also assumed that the two nucleons continue to move on the  $x$  axis, which is fulfilled in the present case. As the tensor-force potential becomes quite damped at the distance  $\gtrsim 2$  fm, this is a reasonable modeling for nuclei with larger radii.

In this linear motion model, the wave functions of the two nucleons are approximated by plane waves. The case (a), shown in Fig. 17 (a), correspond to the “head-on collision” in the linear motion model. The case (b), shown in Fig. 17, corresponds on the other hand to the parallel linear motion of the two nucleons. We assign indices 1 and 2 to the two nucleons. Their wave numbers on the  $x$  axis are denoted by  $k_1$  and  $k_2$ , while their coordinates are denoted by  $x_1$  and  $x_2$ . The wave function,  $\Psi$ , consists of products of two plane waves. We now take a system of a proton and a neutron in the total isospin  $T=0$ , which is antisymmetric with respect to the exchange of the nucleons 1 and 2. The spin part is  $S=1$ , which is symmetric. As the total wave function must be antisymmetric, the coordinate wave function has to be symmetric, taking the form such as,

$$\Psi \propto e^{ik_1 x_1} e^{ik_2 x_2} + e^{ik_2 x_1} e^{ik_1 x_2} = e^{iKX} \{ e^{ikx} + e^{-ikx} \} = 2 e^{iKX} \cos(kx), \quad (59)$$

where center-of mass and relative momenta are defined,

respectively, as,

$$K, = k_1 + k_2, \quad k = k_1 - k_2, \quad (60)$$

and center-of mass and relative coordinates are likewise as,

$$X, = (x_1 + x_2)/2, \quad x = (x_1 - x_2)/2. \quad (61)$$

With these definitions, we see that the relative motion is expressed by the wave function

$$\phi(x) \propto \cos(kx) \quad (62)$$

and the center-of-mass motion has a wave number  $K$  for  $e^{iKX}$ .

In the present case (*i.e.*, Fig. 17(a)),  $k_1 \sim -k_2$  can be assumed. The relative motion then has a large momentum,  $k \sim 2k_1$ . Its wave function  $\phi(x)$  is shown in Fig. 18 (a), with the trend with increasing  $k$ . We note  $K \sim 0$  with  $k_1 \sim -k_2$ , implying the center of mass being almost at rest, or a nearly uniform wave function of the center-of-mass motion.

Based on Fermi momentum in nuclei,  $k$  is considered to be of the order of magnitude  $1 \text{ fm}^{-1}$ , but not to exceed  $\sim 1.5 \text{ fm}^{-1}$ . From the range of the force, the area inside  $x \sim 1 \text{ fm}$  is relevant, as the tensor-force potential becomes very weak beyond 2 fm. Thus, the relevant range of  $kx$  in Eq. (62) is  $|kx| \lesssim \pi/2$ . Because of this, Fig. 18 (a) displays up to the first zeros in both directions. The wave function  $\phi(x)$  in Eq. (62) is damped more quickly for  $k$  larger within this range (see Fig. 18 (a)). Figure 15 shows that two nucleons attract each other if they are displaced in the direction of spin, but repel each other if they are displaced in the direction perpendicular to the spin, *i.e.*, the  $x$  axis now. We point out that if two nucleons are at a very short distance without high momenta, the tensor force does not work because its angular dependence comes from the spherical harmonics  $Y^{(2)}$  prohibiting a finite probability at zero distance. The two nucleons should have a certain distance in order to experience some effects, attractive or repulsive, from the tensor force. If the distance is too large, the effect is diminished also. Thus, although schematically, the region shown by bi-directional arrows in Fig. 18 is relevant to the tensor force, which is repulsive presently. With larger relative momentum  $k$ , Fig. 18 (a) suggests that the wave function is damped faster or the region of sizable probability amplitude is more compressed, along the  $x$  axis. This occurs in the region where the tensor force works repulsively. Thus the reduction of the repulsion takes place more strongly with  $k$  larger. This means that as  $k$  becomes larger, the repulsion becomes weaker, but the attraction remains basically unchanged. This is nothing but the net effect becoming more attractive.

We now come back from one-dimensional modeling to the three-dimensional orbital motion. The relative-motion wave function is discussed in a similar manner.

The yellow shaded area in Fig. 17(a) indicates, schematically, the region with a sizable probability amplitude of the relative-motion wave function, as discussed above. Its vertically stretched shape implies the attractive net effect, being consistent with the deuteron case.

We now move on to the case of Fig. 17(b). The corresponding case in the linear motion model is shown in Fig. 18 (b). The parallel motion of the two nucleons occurs, and  $k_1 \sim k_2$  can be assumed. The relative motion then has a small momentum,  $k \sim 0$ , implying a stretched wave function of the relative motion along the  $x$  axis, as shown in Fig. 18 (b). The probability amplitude then turns out to be large in the region of the repulsive effect of the tensor force, yielding the net repulsive effect, assuming that the net effect has vanished before this repulsive enhancement. This case corresponds to Fig. 17(b), where the two nucleons are apart from each other in the direction perpendicular to the total spin. The region of larger probability amplitude of the relative wave function (shown by the yellow area) is stretched horizontally, which is consistent with the case different from the bound deuteron shown in Fig. 15 (b).

In the above linear-motion model, the wave functions in the  $y$  and  $z$  directions are not discussed. The probability amplitude in the  $z$  direction contributes to the attraction, whereas those in the  $y$  direction to the repulsion. Those amplitudes are not constant, unlike the ideal plane-wave modeling. But they are not affected by the mechanism discussed so far. In short, by having  $k$  high enough for the case (a), the linear-motion wave function is pushed into the region with no sensitivity to the tensor force, and only the attractive effect remains. On the contrary,  $k$  becomes  $\sim 0$  for the case (b), and the full repulsion works out.

Thus, we obtain a robust picture that  $j_<$  and  $j'_>$  (or vice versa) orbits attract each other, whereas  $j_>$  and  $j'_<$  (or  $j_<$  and  $j'_>$ ) repel each other. As the monopole interaction represents average effects, it is natural that they follow the same trend. We will discuss below analytically and numerically how the monopole matrix elements behave. Note that the essence of the above one-dimensional explanation can also be considered as Heisenberg's uncertainty principle.

We make some remarks on the findings made so far. The coordinate wave function is symmetric in the above cases, corresponding the coupling between S and D waves of the relative motion. If the total isospin is  $T=1$ , the antisymmetric coordinate wave function is taken, corresponding to P waves. In this case, the wave function in Eq. (62) is replaced by  $\sin(kx)$ . This wave function produces horizontally stretched wave function, reversing the above argument for the case in Fig. 17(a). However, because of the isospin dependence (see  $(\vec{\tau}_1 \cdot \vec{\tau}_2)$  in eq. (55)), there is another sign change, producing an attractive effect in total. Thus,  $j_>-j'_<$  and  $j_<-j'_>$  couplings give us always attractive effect, whereas  $j_>-j'_>$  and  $j_<-j'_<$  cou-

plings repulsive.

The radial wave functions of the two orbits must be similar in order to have sizable monopole matrix elements. In addition, a narrow distribution in the radial direction is favored in order to have a “deuteron-like” shape for the relative-motion wave function. This is fulfilled if the two orbits are both near the Fermi energy, because their radial wave functions have rather sharp peaks around the surface. If the radial distributions of the two orbits differ, not only their overlap becomes smaller but also the relative spatial wave function is stretched in the radial direction, which weakens the deuteron-like shape, making the effect less pronounced. Note that for the same radial condition, larger  $\ell$  and  $\ell'$  enhance the tensor monopole effect in general, as their relative momentum increases (See Fig. 17).

#### 4. Tensor-force effect and orbital motion: analytic relations

We now move on to the analytic expression on the monopole matrix element. An identity on the monopole matrix element of the tensor force has been derived in (Otsuka *et al.*, 2005), showing the properties consistent with the discussions in the previous subsubsection. For the orbits  $j$  and  $j'$ , the following identity has been derived for the tensor force in (Otsuka *et al.*, 2005),

$$(2j_> + 1) V_T^{ten:m}(j_>, j') + (2j_< + 1) V_T^{ten:m}(j_<, j') = 0, \quad (63)$$

where  $j'$  is either  $j'_>$  or  $j'_<$ . The identity in eq. (63) can be proved, for instance, with angular momentum algebra by summing all spin and orbital magnetic substates for the given  $\ell$ , where  $j_{>,<} = \ell \pm 1/2$ . The quickest but somewhat more mathematical proof is described here: The left hand side of eq. (63) is equivalent to the total effect of the  $T = 0$  or 1 tensor force from the fully occupied  $j_>$  and  $j_<$  orbits coupled with a nucleon in the orbit  $j'$ . In the state comprised of fully occupied  $j_>$  and  $j_<$  orbits, all magnetic substates of  $\ell$  and those of spin  $1/2$  are fully occupied, respectively. This means that the total spin should be zero. The sole nucleon in the  $j'$  orbit has a spin  $1/2$ , which then constitutes the total spin  $0+1/2=1/2$ . The spin sector of the tensor force in eq. (55) is  $[\vec{\sigma}_1 \vec{\sigma}_2]^{(2)}$ , which has a rank 2 (angular momentum carried by the operator). If this operator is sandwiched by the states of spin  $1/2$ , the angular momentum can not be matched, and the outcome is zero. Thus, one can prove the identity. The proof can also be made through the re-coupling of angular momenta in the monopole matrix elements and the explicit form of the tensor force. In all these proofs, it is assumed that the radial wave function is the same for  $j_>$  and  $j_<$  orbits, which is exactly fulfilled in the harmonic oscillator and practically so in other models if the orbits are well bound.

We make some remarks on this identity.

- By moving the second term to the right-hand side of eq. (63), one sees that the  $j_>-j'$  and  $j_- - j'$  couplings have the opposite signs always, being perfectly consistent with the intuitive explanation in Sec. III.B.3. There is no exception. On the other hand, the identity in eq. (63) does not suggest which sign is positive and vice versa. The intuition explained in Sec. III.B.3 plays a crucial role for the general argument.
- Although this identity is not applicable to the cases with  $j_>$  or  $j_- = j'$  in eq. (63) with a good isospin ( $T=0$  or 1), quite similar behavior is found numerically. We note that despite this feature, this identity holds exactly for the proton-neutron interaction in the proton-neutron formalism. Thus, the opposite sign is a really universal feature of the monopole matrix elements of the tensor force, and can be used in all cases.
- One can prove that  $V_T^{ten;m}(j_>, j') = 0$  for  $j$  or  $j' = s_{1/2}$ . This is reasonable as one cannot define  $j_>$  or  $j_-$  for an  $s$  orbit.

- As already mentioned, eq. (63) suggests that if both  $j_>$  and  $j_-$  orbits are fully occupied, there is no monopole effect from the tensor force on any orbit. Consequently,  $LS$  closed shells produce no monopole effect from the tensor force.
- The above derivation indicates also that only exchange processes shown in Fig. 16(b) contribute to the monopole matrix elements of the tensor force, while the contribution of direct processes vanishes. The same property holds for a spin-isospin central interaction discussed in Sec. III.A. This can be understood from the point of view that the vertex  $(\vec{\sigma} \cdot \nabla)$  in eq.(51) does not allow a monopole direct process. If only exchange terms remain, the spin-coordinate contributions of  $T=0$  and 1 are just opposite. Combining this property with  $(\vec{\tau}_1 \cdot \vec{\tau}_2)$  in eq. (55), one obtains

$$V_{T=0}^{ten;m}(j, j') = 3 \times V_{T=1}^{ten;m}(j, j') \text{ for } j \neq j'. \quad (64)$$

Thus, the proton-neutron tensor monopole interaction is twice as strong as the  $T=1$  monopole interaction. This implies also that the monopole effect from the tensor force has the same sign between  $T=0$  and 1, provided that the  $(\vec{\tau}_1 \cdot \vec{\tau}_2)$  is included in the potential.

Figures 19 and 20 display some examples of the monopole matrix elements of the  $\pi$ -meson +  $\rho$ -meson exchange tensor force with the parameters of (Osterfeld, 1992). The same set of single-particle orbits are taken as in Fig. 13. The identity in eq. (63) is exactly fulfilled.

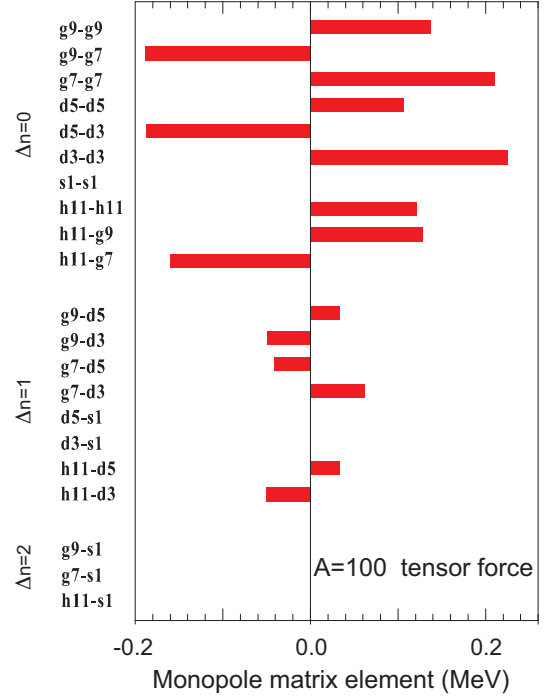


Figure 19 Monopole matrix elements of the tensor force in the  $T=0$  channel. The orbit labeling is abbreviated like  $g9$  for  $1g_{9/2}$ , etc. The orbits are from valence shell for  $A = 100$ .

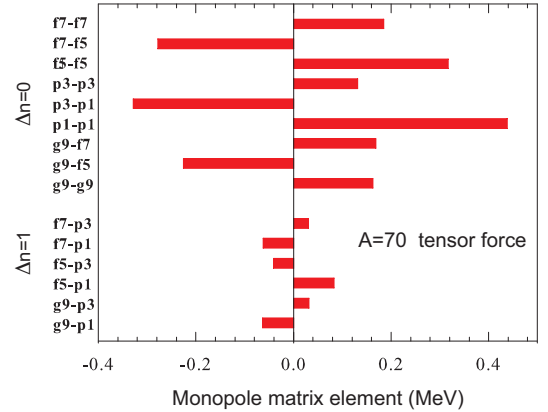


Figure 20 Monopole matrix elements of the tensor force in the  $T=0$  channel. The orbit labeling is abbreviated like  $f7$  for  $1f_{7/2}$ , etc. The orbits are from the valence shell for  $A = 70$ .

The magnitude of the monopole matrix elements is generally larger for the central force, while the variations, for instance within the spin-orbit partners, are of the same order of magnitude between the central and the tensor forces. Their competition produces intriguing phenomena in many cases.

Figure 21 (a) illustrates how the monopole interaction of the tensor force works, if two neutrons occupy this  $j'_>$  orbit. Due to the repulsive monopole interaction (red wavy line), the ESPE of the proton  $j_>$  orbit is raised. On the other hand, owing to the attractive monopole

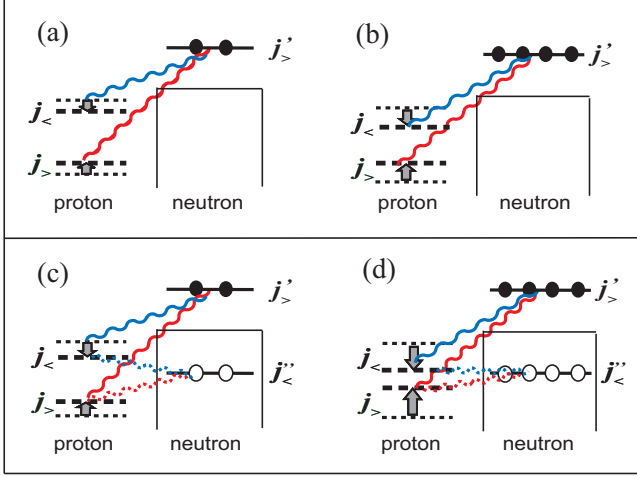


Figure 21 (Color online) Illustration of the Type I (a,b) and Type II (c,d) shell evolutions due to the tensor force. In the Type II case, both particle and hole contributions can act to further reduce the  $j>-j<$  energy splitting. Adapted from Otsuka and Tsunoda (2016).

interaction (blue wavy line), the ESPE of the proton  $j<$  orbit is lowered. These changes combined produce the reduction of spin-orbit splitting. (Note that the proton-neutron central force is always attractive, and makes the total monopole effect attractive apart from the variation of its magnitude, as we shall see.)

Since the monopole effect is linear, four neutrons in the  $j'>$  orbit as shown in Fig. 21 (b) double the effect exhibited in Fig. 21 (a). Thus, the proton spin-orbit splitting becomes smaller and smaller, as more neutrons occupy the  $j'>$  orbit.

These effects are due to the addition of neutrons into the orbit  $j'>$ . We can generalize this effect to similar effects due to particle-hole excitations, as shown in Fig. 21 (c,d). Here, neutrons on the  $j'>$  orbit are supplied by particle-hole excitations. In addition, holes created in the core can produce similar effects, reducing the proton spin-orbit splitting further more. This is called Type-II shell evolution, and will be discussed later in more detail.

### C. Combination of the central and tensor forces

The previous two subsections presented the monopole interactions from the central and tensor forces. We combine them in this subsection.

The central and tensor forces are major components in the effective  $NN$  interaction used for nuclear structure studies. As typical examples of such effective  $NN$  interactions, we take the interactions listed in Table II, where SDPF-M, GXPF1A and G-matrix interactions are described, respectively, in (Utsuno *et al.*, 1999), (Honma *et al.*, 2005), and (Hjorth-Jensen *et al.*, 1995). The for-

Table II Effective  $NN$  interactions to be studied.

shell	fitted	microscopic
sd shell	SDPF-M	G-matrix + in-medium
pf shell	GXPF1A	G-matrix + in-medium

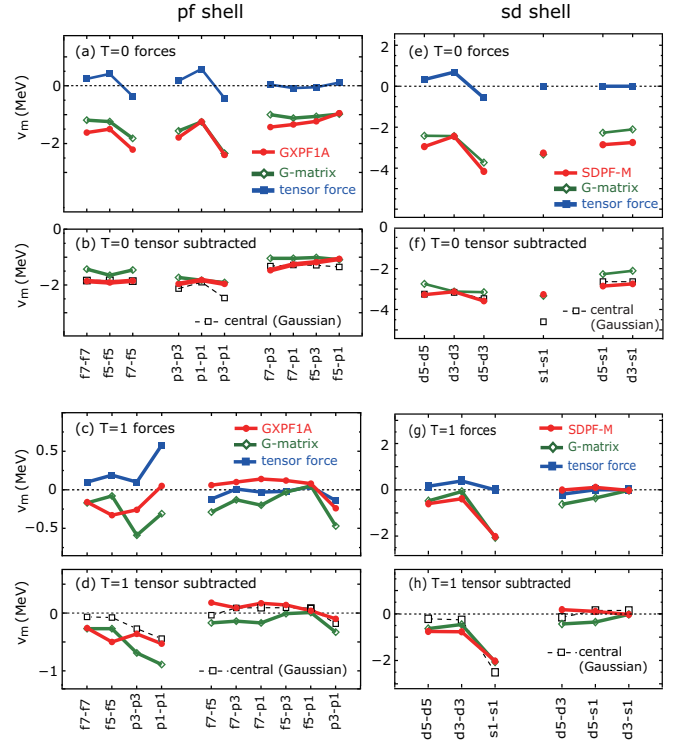


Figure 22 Monopole matrix elements of various forces for (a)-(d) pf and (e)-(h) sd shells. In (b),(d),(f),(h), the tensor force effect is subtracted from the others, and results from a Gaussian central force are shown. Adapted from Otsuka *et al.* (2010b).

mer two have been obtained by fitting some two-body matrix elements to experimental energy levels using microscopically derived interactions as initial input. In addition, the sd-shell part of SDPF-M was obtained by modifying the USD interaction (Brown and Wildenthal, 1988). The G-matrix interaction refers to G-matrix + in-medium corrections by the Q-box formalism, and will be called this way hereafter, for the sake of brevity.

The monopole matrix elements of these interactions are shown in Fig. 22, where the panels (a)-(d) are for the  $pf$  shell, while (e)-(h) for the  $sd$  shell. The  $T=0$  matrix elements are shown in the panels (a), (b), (e), and (f), while the  $T=1$  are in (c), (d) (g) and (h).

In the panel (a), the monopole matrix elements from GXPF1A and G-matrix interactions are shown as well as those obtained from the  $\pi$ -meson +  $\rho$ -meson exchange

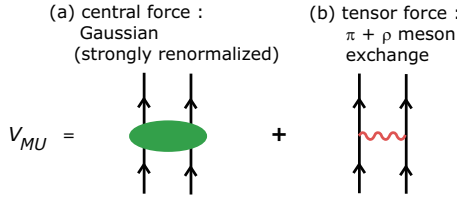


Figure 23 (Color online) Diagrams for the  $V_{MU}$  interaction. From [Otsuka \*et al.\* \(2010b\)](#).

tensor force with the parameters in [\(Osterfeld, 1992\)](#).

It was pointed out in [\(Otsuka \*et al.\*, 2010b\)](#) that the kink pattern is quite similar among the GXPF1A, the G-matrix, and the tensor-force monopole matrix elements. This similarity is indeed remarkable, and is indicative of the tensor-force origin of the kinks of the other two. We can subtract this tensor-force contribution from the GXPF1A or G-matrix results, as shown in the panel (b). It was also noted in [\(Otsuka \*et al.\*, 2010b\)](#) that the remaining monopole matrix elements are surprisingly flat. In order to reproduce such monopole matrix elements, a Gaussian central force was introduced in [\(Otsuka \*et al.\*, 2010b\)](#). This interaction is called the monopole based universal interaction, or  $V_{MU}$ , and it was already mentioned in eq. (45). The parameters selected in [\(Otsuka \*et al.\*, 2010b\)](#) are  $f_{1,0} = f_{0,0} = -166$  MeV,  $f_{0,1} = 0.6f_{1,0}$  and  $f_{1,1} = -0.8f_{1,0}$ , and  $\mu = 1$  fm. The  $V_{MU}$  interaction was described in [\(Otsuka \*et al.\*, 2010b\)](#) as “we can describe the monopole component by two simple terms: the tensor force generates “local” variations, while the Gaussian central force produces a flat “global” contribution.”, as illustrated graphically in Fig. 23. Here, “local” refers to the strong dependences on the single-particle orbits up to sign changes, whereas “global” to the weak dependences with large magnitudes.

The  $T=1$  monopole matrix elements are shown in panel (c). One notices that they are much weaker than the  $T=0$  monopole matrix elements, by a factor of about 1/10. This large difference is a general trend. Within such small monopole matrix elements, the pattern is not so simple. Panel (d) shows that the repulsive  $T=1$  monopole interaction in the central Gaussian potential is important.

Moving from the  $pf$ -shell to the  $sd$ -shell, quite similar properties can be found in panels (e)-(h). Note that the parameters of the  $V_{MU}$  potential are independent of the orbits or the shells. The good description is remarkable in this respect. The reason for this with respect to the tensor force will be discussed later.

The  $V_{MU}$  interaction has been used rather successfully, and some examples are presented in the next subsection.

#### D. Examples of tensor-force driven shell evolution

We present some examples of shell evolution driven by the tensor force. The tensor force is taken from the  $\pi$ -meson +  $\rho$ -meson exchange potential in all cases in order to clarify the underlying mechanism. Likewise, the central force is modeled by the  $V_{MU}$  interaction for all cases, exhibiting different roles of these interactions in a consistent manner.

##### 1. Inversion of proton $1f_{5/2}$ and $2p_{3/2}$ in Cu isotopes

One of the most visible examples of the shell evolution driven by the tensor force is the change of the proton  $1f_{7/2}$  -  $1f_{5/2}$  splitting due to neutron occupations of the  $1g_{9/2}$  orbit, from the theoretical viewpoint. We shall describe this case in some detail, as it is one of the early examples regarding the tensor force. The underlying mechanism can be understood by Fig. 21 in a straightforward way. Namely, in this case, the neutron  $j'_>$  orbit is  $1g_{9/2}$ , and it is occupied by more neutrons as we move on the Segrè chart from  $^{69}\text{Cu}$  to heavier Cu isotopes. The changes of the ESPEs of the proton  $j_> = 1f_{7/2}$  and  $j_< = 1f_{5/2}$  orbits are given, by following eq. (37), as

$$\Delta\epsilon_{f_{5/2}}^p = V_{pn}^m(f_{5/2}, g_{9/2}) \Delta n_{g_{9/2}}^n, \quad (65)$$

and

$$\Delta\epsilon_{f_{7/2}}^p = V_{pn}^m(f_{7/2}, g_{9/2}) \Delta n_{g_{9/2}}^n, \quad (66)$$

where the symbol  $\hat{}$  is omitted because the occupation number of the neutron  $1g_{9/2}$  orbit is treated as a c-number here. Note that such a simpler treatment was mentioned as a possible option in Sec. II.D. From the  $V_{MU}$  interaction, the monopole matrix elements have two sources: one from the central force and the other from the tensor force. Table III shows their corresponding values. One sees that between the two couplings  $1f_{5/2}$  -  $1g_{9/2}$  and  $1f_{7/2}$  -  $1g_{9/2}$ , the central force gives a somewhat stronger attraction to the latter, as can be expected from Fig. 13 (b). On the other hand, the tensor force pushes the  $1f_{5/2}$  orbit down with more neutrons in the  $1g_{9/2}$  orbit, whereas it pulls the  $1f_{7/2}$  orbit up at the same time.

The ESPEs provided by eqs. (65) and (66) are shown in the left panel of Fig. 24, where the number of neutrons in the  $1g_{9/2}$  orbit is given by  $N - 40$  as the filling scheme is taken. The ESPEs at  $N=40$  are obtained from empirical values [\(Grawe \*et al.\*, 2005; Otsuka \*et al.\*, 2010b\)](#). The full  $V_{MU}$  interaction is taken for the ESPEs displayed by the solid lines in the left panel of Fig. 24, while the dashed lines depict results only with the central force. One confirms the same trends as discussed above: the central force (with neutrons in the  $1g_{9/2}$  orbit) slightly

Table III Monopole matrix elements from the central and tensor forces. The unit is MeV. The mass number  $A=70$  is taken for the Harmonic Oscillator Wave Function of the single-particle orbit.

proton orbit	neutron orbit	central	tensor
$1f_{5/2}$	$1g_{9/2}$	-0.63	-0.15
$1f_{7/2}$	$1g_{9/2}$	-0.70	+0.11
difference between $1f_{5/2}$ and $1f_{7/2}$		+0.07	-0.26
$2p_{3/2}$	$1g_{9/2}$	-0.46	+0.02
difference between $1f_{5/2}$ and $2p_{3/2}$		-0.17	-0.17

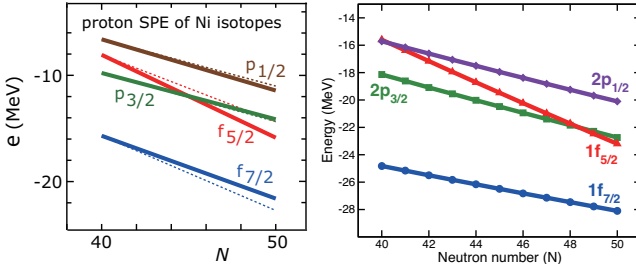


Figure 24 (left) Proton ESPEs of Cu isotopes as predicted by the  $V_{MU}$  interaction (solid lines). Dashed lines are obtained only with the central-force part. The neutron number in the  $1g_{9/2}$  orbit is equal to  $N-40$ , as the filling scheme is assumed. (right) Same quantities by the A3DA-m Hamiltonian used in (Sahin *et al.*, 2017). From Otsuka *et al.* (2010b) (left) and Sahin *et al.* (2017) (right).

repels the  $1f_{5/2}$  and  $1f_{7/2}$  orbits from each other, while the tensor force brings them distinctly closer. The  $1f_{5/2}$  -  $1f_{7/2}$  splitting is  $\sim 8$  MeV at  $N=40$ , but is decreased to  $\sim 6$  MeV at  $N=50$ . The  $Z=28$  gap is between the  $2p_{3/2}$  and  $1f_{7/2}$  orbits at  $N=40$  with a gap of  $\sim 6$  MeV, whereas it is between the  $1f_{5/2}$  and  $1f_{7/2}$  orbits at  $N=50$  with a gap of  $\sim 6$  MeV.

The lowering of the proton  $1f_{5/2}$  orbit produces another significant consequence. The left panel of Fig. 24 shows that the proton  $2p_{3/2}$  orbit comes down, as a function of  $N$  more slowly than the  $1f_{5/2}$  orbit, and their order is inverted around  $N=45$ . In fact, Table III suggests that the central-force contribution to the lowering of the proton  $2p_{3/2}$  orbit is  $\sim 2/3$  of the one for  $1f_{7/2}$  or  $1f_{5/2}$  and the tensor-force contribution almost negligible. These properties are quite natural due to differences in the radial wave functions. Table III shows also how the  $1f_{5/2}$ - $2p_{3/2}$  gap is changed by the central and tensor forces. Both contribute to the inversion equally, and the total effect is large enough.

The change of the ESPE of the proton  $1f_{5/2}$  orbit has been investigated experimentally. The earlier ones (Franchoo *et al.*, 1998, 2001) were made for  $^{69,71,73}\text{Cu}$  prior to the theoretical studies presented above. The experimental findings were compared to shell-model calculations (Ji and Wildenthal, 1989), (Sinatkas *et al.*, 1992). The

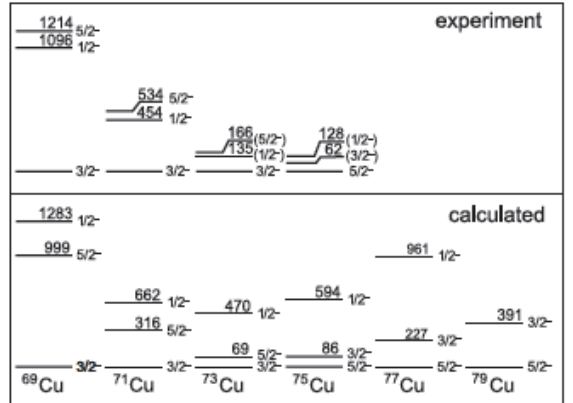


Figure 25 Energy of the lowest levels from experiment and shell-model calculations. Reprinted with permission from Flanagan *et al.* (2009).

main message may be found in the quoted statements as “unexpected and sharp lowering of the  $\pi f_{5/2}$  orbital” and “the energy shift originates from the residual proton-neutron interaction, while its magnitude is proportional to the overlap of the proton and neutron wave function” (Franchoo *et al.*, 2001). There was no mention of the tensor force, and the lowering of the proton  $1f_{5/2}$  orbit seems to have been attributed to the central force. We can see from Table III that the central force accounts for one half of the effect. Note that spectroscopic factors have been measured for  $^{69,71}\text{Cu}$  (Morfouace *et al.*, 2015).

The experimental studies were further extended in (Flanagan *et al.*, 2009) up to  $^{75}\text{Cu}$ , as shown in Fig. 25. The inversion between the lowest  $5/2^-$  and  $3/2^-$  levels was observed for the first time in the Cu isotopic chain. The role of the tensor force was known then, and the work was recognized as “a crucial step in the study of the shell evolution” (Flanagan *et al.*, 2009). The observed levels were compared to shell-model calculations by (Brown and Lisetskiy, 2009) with a reasonable agreement. It is very likely that a proper amount of the tensor force was included in the shell-model interaction as a result of the fit well-done (Lisetskiy *et al.*, 2004, 2005). The single-particle nature of the lowest  $5/2^-$  being the  $1f_{5/2}$  single-particle state in  $^{75}\text{Cu}$  was confirmed by the measured magnetic moment and by the shell-model calculation, as well as the lowest  $3/2^-$  being the  $2p_{3/2}$  single-particle state in  $^{69}\text{Cu}$ . On the other hand, the ground state (*i.e.*,  $3/2^-$  state) of  $^{71,73}\text{Cu}$  was shown to have mixed nature. Besides such intermediate situations, the inversion between the  $1f_{5/2}$  and the  $2p_{3/2}$  states has thus been suggested (Flanagan *et al.*, 2009), and the trend was extended to heavier Cu isotopes (Daugas *et al.*, 2010; Köster *et al.*, 2011). This series of experiments showing a clear signal of the lowering of the  $1f_{5/2}$  orbit can be considered as a major milestone in establishing the shell evolution.

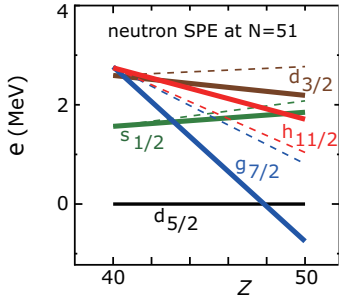


Figure 26 Shell evolution of neutrons from  $Z=40$  to  $50$ . Neutron ESPEs are shown relative to that of the  $2d_{5/2}$  orbit. Dashed and full lines have the same meaning as in Fig. 24. Adapted from [Otsuka \*et al.\* \(2010b\)](#).

Effects of various correlations including collective ones were investigated both theoretically and experimentally, but the main conclusion will remain apart from minor changes. For instance, the precise point of the inversion is sensitive theoretically to the adopted values of ESPEs at  $N=40$  which are not known so accurately constrained to date (see Fig. 24).

The structure of neutron-rich  $^{77}\text{Cu}$  isotope has recently been studied experimentally, and experimental data were compared well to the results of the shell-model calculation with the A3DA-m Hamiltonian ([Sahin \*et al.\*, 2017](#)). The obtained data show sensitivities to the  $Z=28$  gap. The right panel of Fig. 24 indicates the ESPEs obtained from this Hamiltonian, where one sees the  $1f_{5/2}$ - $2p_{3/2}$  crossing occurs at this nucleus. As the shell-model calculations contain correlations fully in the configuration space and the agreement with experiment is quite good, the  $Z=28$  gap behaves as in the right panel of Fig. 24, where the  $1f_{7/2}$ - $1f_{5/2}$  splitting becomes smaller by about 4 MeV quite similarly to the left panel. Thus, the reduction of this splitting due to the tensor force seems to be seen experimentally.

## 2. Shell Evolution from $^{90}\text{Zr}$ to $^{100}\text{Sn}$

Another typical case of the tensor-force-driven shell evolution is shown in Fig. 26 taken from ([Otsuka \*et al.\*, 2010b](#)). Here, from  $^{90}\text{Zr}$  to  $^{100}\text{Sn}$ , the number of protons in the  $1g_{9/2}$  orbit increases from 0 to 10, in the filling scheme adopted for the sake of simplicity. Figure 26 exhibits the ESPE of neutron orbits on top of the  $N=50$  core calculated with the  $V_{\text{MU}}$  interaction. The ESPEs at  $Z=40$  were adjusted to experimental data including the fragmentation of single-particle strengths ([NNDC, 2016](#)), and their evolution follows eq. (38). Figure 26 shows the ESPEs relative to the one for the  $2d_{5/2}$  orbit. The corresponding experimental data are shown in Fig. 8, while the values at  $Z=40$  differ slightly from those in Fig. 26. We ignore this minor difference.

One finds, in Fig. 26, two sets of calculated results: one (solid lines) is obtained with the full  $V_{\text{MU}}$  interaction, while the other (dashed lines) is only with the central-force part of  $V_{\text{MU}}$ . A sharp drop of the  $1g_{7/2}$  ESPE with the full  $V_{\text{MU}}$  interaction is remarkable, ending up with an ESPE below  $2d_{5/2}$ . A similar behavior is seen with experimental data shown in Fig. 8. This drop is largely due to a strong proton-neutron monopole interaction on a proton in the  $1g_{7/2}$  orbit generated by neutrons in the  $1g_{9/2}$  orbit. Although the scenario looks similar, at least qualitatively, to what [Federman and Pittel \(1977\)](#) presented (See Sec. II.F.2), there are interesting and notable differences as discussed below. This case is different also from the previous example for Cu isotopes in several aspects. We shall look into them now.

The first point is that the  $1g_{7/2}$  and  $1h_{11/2}$  orbits come down together (dashed lines in Fig. 26) if the central-force part only is taken. In contrast, these two ESPEs exhibit an increasing splitting towards  $Z=50$  if the tensor force is included. This is because a repulsive monopole interaction works on the  $h_{11/2}$  orbit due to the  $j> - j'_>$  coupling (see Fig. 17), whereas the tensor interaction is attractive on the  $1g_{7/2}$  due to the  $j< - j'_>$  coupling. This attraction produces an additional lowering of  $1g_{7/2}$ , letting it reach below  $2d_{5/2}$  at  $Z=50$ . In the view of Federman and Pittel, the strong attraction was ascribed to the  $^3S_1$  channel central force ([Federman and Pittel, 1977](#)), while this tensor force effect is missing. The energy levels of  $^{101}\text{Sn}$  have been investigated experimentally ([Darby \*et al.\*, 2010](#); [Seweryniak \*et al.\*, 2007](#)), which are consistent with the lowering of the  $1g_{7/2}$  orbit. We note that the relation between the strong pairing and the present tensor force was pointed out in the discussion in ([Darby \*et al.\*, 2010](#)).

As the second interesting point, we mention that the bunching of three orbits,  $1h_{11/2}$ ,  $2d_{3/2}$  and  $3s_{1/2}$ , seems to be consistent with the shell structure of the Sn isotopes. Figure 26 demonstrates that the tensor force plays a crucial role for obtaining it.

The tensor-force contribution is thus essential for the shell structure of  $^{100}\text{Sn}$ , which has further relevance to various issues of exotic nuclei.

Another feature of interest is the relation to the Skyrme Hartree-Fock calculation as shown in Fig. 27. With the SIII interaction, the  $1g_{7/2}$  -  $2d_{5/2}$  gap is decreased by about 1.2 MeV. This change is comparable to the corresponding shift by the central force of the  $V_{\text{MU}}$  interaction. Note that the ESPE of the  $1g_{7/2}$  ( $2d_{5/2}$ ) orbit is predicted to be lower (higher) than the empirical value, and thereby the change of their splitting is smaller than that shown in Fig. 26. Thus, the tensor force is needed to account for a larger relative change between the  $2d_{5/2}$  and  $1g_{7/2}$  orbits, eventually leading to their crossing in Sn. Furthermore, Fig. 27 (b) indicates that the gap between the  $1g_{7/2}$  and  $2d_{5/2}$  orbits is even increased with the SLy4 interaction.

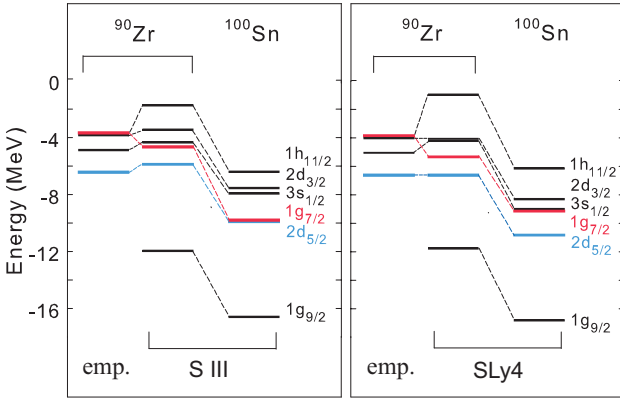


Figure 27 Single-particle energies of  $^{90}\text{Zr}$  and  $^{100}\text{Sn}$  calculated by (left) SIII and (right) SLy4 Skyrme interactions.

### 3. Appearance of $N=16$ magic number and disappearance of $N=20$

The change of the neutron  $1d_{3/2}$  ESPE was discussed in Sec. III.A. Figure 14 shows that the neutron  $1d_{3/2}$  ESPE is about 6 MeV above the  $2s_{1/2}$  ESPE in  $^{24}\text{O}$ , but comes down by about 4 MeV in  $^{30}\text{Si}$ .

This change was discussed, in Sec. III.A, as a consequence of the strong attractive monopole matrix element between  $\ell+1/2$  and  $\ell-1/2$  orbits. This strong coupling is included in shell-model effective interactions, *e.g.*, SDPF-M (Utsuno *et al.*, 1999) and in the G-matrix (Kuo and Brown, 1966), whereas it was weakened in some others, *e.g.*, USD (Brown and Wildenthal, 1988). It was indicated in Sec. III.A that the  $\tau\tau\sigma\sigma$  interaction in eq. (45) can lower, in principle, the neutron  $1d_{3/2}$  orbit as protons occupy the  $1d_{5/2}$  orbit. Although this coupling is strongest in Table I, if the  $\tau\tau\sigma\sigma$  interaction is taken, the neutron  $1d_{5/2}$  orbit is lowered by about half the amount, implying some difficulty. On the other hand, the strong attraction between the  $\ell+1/2$  and  $\ell-1/2$  orbit was suggested, leading us to a sizable spin-isospin coupling (Otsuka *et al.*, 2001).

Four years later (Otsuka *et al.*, 2005), another origin in nuclear forces was proposed for this spin-isospin coupling, the tensor force. In fact, the tensor force provides the relevant monopole matrix elements being  $V_{pn}^{ten;m}(1d_{5/2}, 1d_{3/2}) = -0.37$  MeV and  $V_{pn}^{ten;m}(1d_{5/2}, 2s_{1/2}) = 0$  MeV. By having six protons in the  $1d_{5/2}$  orbit, the  $1d_{3/2}$  orbit is then lowered by 2.2 MeV relative to the  $2s_{1/2}$  orbit. This implies that one half of the lowering of the  $1d_{3/2}$  orbit is due to the tensor force. We stress also that the neutron  $1d_{5/2}$  orbit is pushed up by the tensor force with six protons in  $1d_{5/2}$ , in contrast to the  $\tau\tau\sigma\sigma$  interaction.

The neutron  $1d_{3/2}$  orbit needs to be shifted down by another 2 MeV relative to the  $2s_{1/2}$  orbit by the central force, because the tensor-force effect is robust (not tunable much) as we shall discuss later. In fact, the central force should produce a weaker monopole matrix element for the  $1d_{5/2} - 2s_{1/2}$  coupling, and this is the case.

We mention here that some features of the  $\tau\tau\sigma\sigma$  interaction are shared by the tensor force, for instance, the spin-isospin operator  $\tau\sigma$  acts on the vertex in favor of spin-isospin-flip process, and only the exchange process contributes to the monopole matrix element (see Fig. 14 and Fig. 16). These properties produce stronger couplings between  $j_>$  and  $j_<$  orbits with a common  $\ell$  with both the central and tensor forces, but only the tensor force does it also for  $j_>$  and  $j'_<$ , *i.e.*,  $\ell \neq \ell'$ . In this sense, the special importance of the spin-isospin interaction in the shell evolution in exotic nuclei was pointed out as an initial study in (Otsuka *et al.*, 2001), being a precursor to more comprehensive studies including the tensor force.

The relative raising of the neutron  $1d_{3/2}$  orbit from Fig. 14 (a) to (b) occurs as  $Z$  is reduced from 14 to 8, while  $N$  is kept at 16. This isotonic change from a stable to an exotic nucleus creates an  $N=16$  gap, and diminishes the  $N=20$  conventional gap. Thus, the present shell evolution can change the magic numbers. We mention here that the large  $N=16$  gap was recognized in an earlier shell model study within the systematics of the oxygen isotopes (Brown, 1993). The gap was pointed out based on experimental data on the masses and radii (Ozawa *et al.*, 2000).

The  $N=20$  magic number will be discussed later again in relation to *ab initio* type shell model calculations.

### 4. Appearance of $N=34$ magic number in the isotonic chain

Another case of new magic numbers has been found in the Ca isotopes, with  $N=32$  and 34. A remarkable proton-neutron  $j_> - j_<$  coupling within a major shell is seen in the shell evolution between Ca and Ni. Figure 28 displays this shell evolution concretely in terms of the  $V_{\text{MU}}$  interaction. We take the filling scheme, where no proton occupies the  $1f_{7/2}$  orbit in  $^{48}\text{Ca}$ . In  $^{56}\text{Ni}$ , on the other side, eight protons occupy the  $1f_{7/2}$  orbit, changing the ESPEs of the neutron orbits  $1f_{5/2}$ ,  $2p_{3/2}$  and  $2p_{1/2}$ . Figure 28 then indicates how much each orbit is moved with the decomposition into the tensor- and central-force monopole contributions. It is found that in going from  $^{48}\text{Ca}$  to  $^{56}\text{Ni}$ , both forces contribute additively to the sharp rise of the  $1f_{5/2}$  orbit relative to the  $2p_{3/2}$  and  $2p_{1/2}$  orbits. The splitting between the  $2p_{3/2}$  and  $2p_{1/2}$  orbits is slightly increased, and becomes a (sub-) magic gap as the  $1f_{5/2}$  orbit is not in between any longer.

Figure 28 exhibits, the changes of the ESPEs with the decomposition into the tensor- and central-force monopole contributions. We point out that the monopole

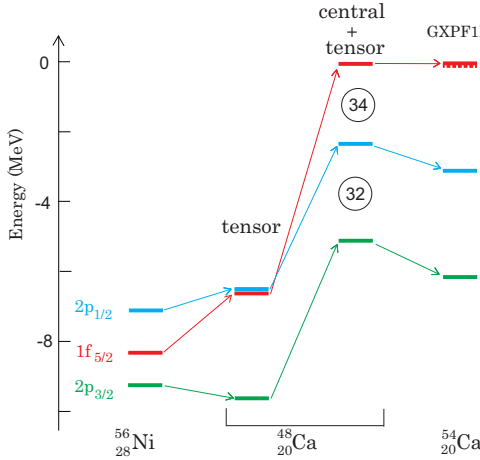


Figure 28 Change of ESPEs from  $^{56}\text{Ni}$  to  $^{48}\text{Ca}$ , and to  $^{54}\text{Ca}$ . The arrows indicate the change of the ESPE of each orbit. The arising magic numbers,  $N=32$  and  $34$ , are shown in black circles. The dashed line far right means the  $1f_{5/2}$  ESPE calculated with one neutron hole in the  $2p_{1/2}$  orbit.

components of the tensor and central forces contribute to the evolution of the  $1f_{5/2}$  ESPE, showing its sharp rise. The splitting between the  $2p_{3/2}$  and  $2p_{1/2}$  orbits remains almost unchanged, and becomes a (sub-)magic gap after the  $1f_{5/2}$  orbit is shifted above  $2p_{1/2}$ . It is noted that the tensor force enlarges the gap between the  $2p_{3/2}$  and  $2p_{1/2}$ . The magic numbers  $32$  and  $34$  thus appear in going from Ni to Ca as indicated also in Fig. 28, as the eight protons in  $^{56}\text{Ni}$  are taken away. We emphasize that the  $N=34$  gap basically vanishes when the tensor-force effect is taken away, and that is, since the present shell-evolution effect is linearly dependent on the number of proton holes in the  $1f_{7/2}$  orbit, as  $Z$  decreases, the  $N=34$  (sub-)magic structure fades away first and the  $N=32$  also disappears eventually.

The far-right part of Fig. 28 shows the shell evolution from  $^{48}\text{Ca}$  to  $^{54}\text{Ca}$  due to the neutron-neutron interaction, adding six more neutrons still in the filling scheme. The GXPF1Br shell-model interaction (Steppenbeck *et al.*, 2013) is used, as more fine details are relevant now. The neutron-neutron effective interaction produces the shell evolution with patterns very different from those of the proton-neutron interaction. Four and two neutrons occupy the  $2p_{3/2}$  and  $2p_{1/2}$  orbits, respectively, in  $^{54}\text{Ca}$ . The ESPE is shown for the  $1f_{5/2}$  orbit on top of the  $^{54}\text{Ca}$  core, with a very small change from  $^{48}\text{Ca}$ . As the  $2p_{3/2}$  and  $2p_{1/2}$  orbits are occupied in the  $^{54}\text{Ca}$  core, we show the ESPE for the last neutron to occupy these orbits. The  $2p_{3/2}$  ESPE is calculated for  $^{54}\text{Ca}$  by assuming a fully occupied  $2p_{1/2}$  orbit. In order to assess the energy needed for particle-hole excitation, in the far-right part of Fig. 28, the dashed line below the  $1f_{5/2}$  level shows the ESPE calculated with one neutron hole in the

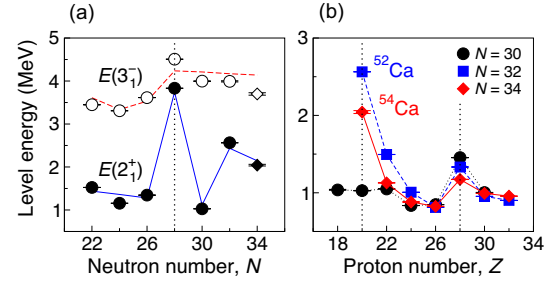


Figure 29 Observed first  $2^+$  levels as a function of (a)  $N$  and (b)  $Z$ . Observed first  $3^-$  levels are shown in panel (a). Adapted from (Steppenbeck *et al.*, 2013).

$2p_{1/2}$  orbit, which is very close to the solid line. Thus, the effects of the neutron-neutron monopole interaction is minor and can be repulsive. The  $2p_{3/2}$  and  $2p_{1/2}$  orbits are somewhat lowered due to the pairing component between the same orbit.

We can thus see the basic mechanism of the appearance of the  $N=32$  and  $34$  gaps. This was the prediction in Ref.(Otsuka *et al.*, 2001), being a consequence of the strong attractive coupling between the  $\ell + 1/2$  and  $\ell - 1/2$  orbit with  $\ell = 3$ , analogous to a similar coupling with  $\ell = 2$  leading to the  $N = 16$  new magic number. The corresponding text in (Otsuka *et al.*, 2001) is quoted as “we can predict other magic numbers, for instance,  $N=34$  associated with the  $0f_{7/2} - 0f_{5/2}$  interaction”, where  $0f_{7/2,5/2}$  means  $1f_{7/2,5/2}$  in the present notation. The experimental investigation of the  $N=34$  magic number in the Ca isotopes had not been feasible for more than a decade, casting doubt over this magic number (Janssens, 2005). In 2013, finally, the  $2^+$  excitation energy was measured at the RIBF (Steppenbeck *et al.*, 2013) to be significantly higher than in heavier isotones consistent with an  $N=34$  gap, as shown in Fig. 29. A sharp rise of the  $2^+$  excitation energy as a function of  $Z$  was thus confirmed experimentally for  $^{54}\text{Ca}$ , as shown in panel (b) of Fig. 29, in accordance with the rise of the  $1f_{5/2}$  orbit shown in Fig. 28. The intermediate situation between the Ca and Ni isotopes is discussed in (Steppenbeck *et al.*, 2013). The  $N=32$  gap in the Ca isotopes was investigated experimentally at ISOLDE in 1985 in terms of the  $2^+$  excitation energy (Huck *et al.*, 1985). The magic structures of Ca isotopes attracted much attention in recent years (Bürger *et al.*, 2005; Coraggio *et al.*, 2009; Crawford *et al.*, 2010; Dinca *et al.*, 2005; Gade *et al.*, 2006b; Hagen *et al.*, 2012; Holt *et al.*, 2012b; Honma *et al.*, 2008; Janssens *et al.*, 2002b; Kaneko *et al.*, 2011; Liddick *et al.*, 2004; Prisciandaro *et al.*, 2001; Rejmund *et al.*, 2007; Rodríguez and Egido, 2007; Steppenbeck *et al.*, 2015; Utsuno *et al.*, 2012b; Wienholtz *et al.*, 2013).

Figure 29 (b) exhibits that raising pattern towards  $Z=20$  of the  $2_1^+$  level differs between  $N=32$  and  $34$  iso-

tonic chains. Significant experimental efforts were made, particularly for Ti ( $Z=22$ ), for instance (Dinca *et al.*, 2005; Fornal *et al.*, 2004, 2005; Janssens *et al.*, 2002a; Liddick *et al.*, 2013), partly because Ti is only  $\Delta Z=2$  away from Ca. As three quarters of the shift from Ni to Ca occurs in Ti in Fig. 28, the  $1f_{5/2}$  level is located near the  $2p_{1/2}$  level, making the  $N=32$  gap rather visible but not the  $N=34$  gap, consistent with these experiments. Thus, studies on Ti isotopes rather support the appearance mechanism of  $N=32$  and 34 magic numbers in Ca isotopes.

## 5. Repulsion between proton $1h_{11/2}$ and $1g_{7/2}$ orbits in the Sb isotopes

Figure 30 shows the ESPEs of the proton  $1h_{11/2}$  and  $1g_{7/2}$  orbits in Sb isotopes as a function of  $N$ . There are 51 protons in the Sb isotopes: one proton on top of the  $Z=50$  magic core in the filling scheme. This last proton can be either in the  $1h_{11/2}$  orbit or the  $1g_{7/2}$  orbit. The experimental values are taken from (Schiffer *et al.*, 2004), which report that the centroid of fragmented single-particle strengths are evaluated as much as possible. Some questions on the validity of this analysis have been raised, for instance in (Sorlin and Porquet, 2008), in connection to the couplings to various collective modes including the octupole one. While this remains an open problem both experimentally and theoretically, we discuss it here from the viewpoint of the monopole effect, to explore what can be presented with such a simple argument. We expect more developments for further clarifications.

Around the middle ( $N \sim 66$ ) of the major shell between  $N=50$  and 82, the  $1h_{11/2}$  and  $1g_{7/2}$  orbits (or two corresponding experimental states) are close to each other with a gap of less than 1 MeV. The gap increases with  $N$ , as seen in Fig. 30. It was quite difficult to reproduce this enlargement of the gap within mean field models when the experimental values were published (Schiffer *et al.*, 2004). In those Sb isotopes, the neutron  $1h_{11/2}$  orbit is filled more and more as  $N$  increases. The monopole interaction from the tensor force is repulsive between the proton  $1h_{11/2}$  orbit and the neutron  $1h_{11/2}$  orbit (see Fig. 17). Its effect is, on the other hand, attractive between the proton  $1g_{7/2}$  orbit and the neutron  $1h_{11/2}$  orbit (see also Fig. 17). In fact, the theoretical ESPEs in Fig. 30 are calculated from the monopole matrix elements (see eq. (38)) of the  $V_{\text{MU}}$  interaction, which consists of the  $\pi+\rho$  meson-exchange tensor force and the Gaussian central force, as discussed in Sec. III.C.

The ESPEs in Fig. 30 are calculated with the monotonic increase of the uniform occupation probabilities of the neutron  $1h_{11/2}$ ,  $2d_{3/2}$  and  $3s_{1/2}$  orbits starting from  $N=64$ , for the sake of simplicity. Figure 30 shows the ESPEs calculated without the tensor force (dashed lines),

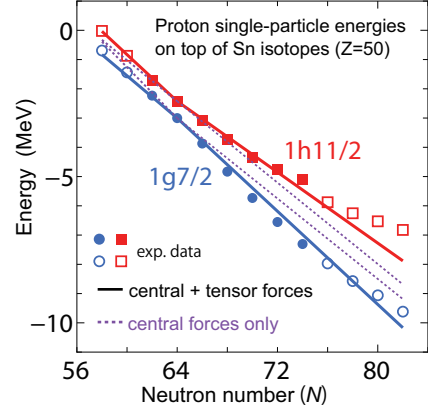


Figure 30 ESPEs of proton  $1h_{11/2}$  and  $1g_{7/2}$  orbits in Sb isotopes as functions of  $N$ . Assuming Sn-isotope core, the solid lines are calculated with the tensor-force effect, whereas the dotted lines are without it. Symbols are based on experimental values from (Schiffer *et al.*, 2004): fragmentation of single-particle strength is considered for filled circles, while bare energies are used for open symbols. See the text for relevant arguments on those values. From (Otsuka, 2013).

indicating that the two ESPEs come down together with the gap even slightly narrowing. Once the tensor force is included (solid lines in Fig. 30), however, it moves the two orbit more apart from each other as  $N$  increases. A similar but simpler figure was shown in Fig. 4 (d) of (Otsuka *et al.*, 2005), which was published immediately after (Schiffer *et al.*, 2004), demonstrating the explanation of the anomalous gap-widening in terms of the tensor force for the first time. It was remarkable that the gap increase can be explained almost perfectly once the tensor force is incorporated without adjustment of the tensor-force strength. This point has to be clarified with more precise calculations including other correlations. We also point out the upbending curvature towards  $N=82$  shown in Fig. 30 may suggest some effects beyond the monopole effect.

It is thus important and essential to examine to what extent other effects, for instance, couplings to collective excitations, affect the observed energy levels, while the tensor-force effects seem to remain as a major mechanism.

## 6. Other remarks

We mention, from a more general viewpoint, that the strong attraction between proton-neutron spin-orbit partners was noticed, as discussed in Sec. II.F.2, in relation to the onset of deformation in Zr isotopes (Federman *et al.*, 1979). The monopole interaction between proton  $2p_{3/2,1/2}$  orbit and neutron  $2d_{5/2}$  orbit was dis-

cussed for the description of Zr-Sr isotopes in (Federman *et al.*, 1984) by using the empirical interaction introduced in (Schiffer and True, 1976). Such monopole effects presented in earlier works without mentioning of the tensor force, *e.g.*, (Federman and Pittel, 1977; Federman *et al.*, 1979, 1984; Goodman, 1977; Pittel *et al.*, 1993; Zeldes *et al.*, 1983), can be understood now quite consistently as consequences of the shell evolution mainly due to the tensor force and particular orbital-dependent features of the central force.

### E. Renormalization persistency of the tensor force

The effects of the tensor force have been discussed in previous subsections in terms of the  $\pi+\rho$ -meson exchange potential. This potential is derived in the free space, and one has to investigate the changes due to various renormalization procedures for the short-range repulsion and the in-medium corrections. This study has been done in Refs. (Otsuka *et al.*, 2010b; Tsunoda *et al.*, 2011), which suggest that the changes are quite small for the tensor force, referred to as *renormalization persistency*.

An example is shown in Fig. 31 (Otsuka *et al.*, 2010b), where the AV8' interaction (Pudliner *et al.*, 1997) was used as the starting nuclear force in the free space. A low-momentum interaction  $V_{low\ k}$  (Bogner *et al.*, 2003) was derived in order to treat short-range correlations, and the third order Q-box calculation with folded diagram corrections (Hjorth-Jensen *et al.*, 1995) was performed in order to include medium effects like core polarization.

The spin-tensor decomposition has been carried out over decades (Brown *et al.*, 1988; Elliott *et al.*, 1968; Kirson, 1973; Klingenberg *et al.*, 1977; Osnes and Strottman, 1992; Yoro, 1980), in order to extract the tensor-force component. Here, the spin-tensor decomposition serves as a very useful classification technique of a given two-body interaction into several pieces such as the scalar-(central force), axial-vector- (two-body LS (spin-orbit) force), and tensor-coupled spin components.

We shall outline this now. A given two-body interaction can be rewritten in general as

$$V = \sum_{k=0,1,2} V_k = \sum_{k=0,1,2} U^k \cdot X^k, \quad (67)$$

where  $U^k$  and  $X^k$  are tensor operators of rank  $k$  in the coordinate and spin spaces, respectively. One can thus uniquely extract the LS-coupled matrix elements of each  $k$  component:

$$\begin{aligned} & \langle n_a \ell_a n_b \ell_b LS JT | V_k | n_c \ell_c n_d \ell_d L' S' JT \rangle \\ &= (-1)^J (2k+1) \left\{ \begin{array}{ccc} L & S & J \\ S' & L' & k \end{array} \right\} \\ & \times \sum_{J'} (-1)^{J'} (2J'+1) \left\{ \begin{array}{ccc} L & S & J' \\ S' & L' & k \end{array} \right\} \\ & \times \langle n_a \ell_a n_b \ell_b LS J' T | V | n_c \ell_c n_d \ell_d L' S' J' T \rangle. \end{aligned} \quad (68)$$

The  $k = 0, 1, 2$  matrix elements correspond, as mentioned above, to the central force, spin-orbit (plus antisymmetric spin-orbit) force(s), and tensor force, respectively.

These are all possible components for interactions with the dependence on relative coordinates. If dependence on the center-of-mass coordinate is allowed for some reason, other terms like antisymmetric LS appear. Since the shells being considered are full harmonic oscillator shells containing all spin-orbit partners, this spin-tensor decomposition is possible. We note that the tensor component here is obtained from a given interaction, and can differ from the one from the  $\pi+\rho$ -meson exchange potential. We will see that this turns out to be a minor difference in the present discussion with realistic interactions.

Figure 31 displays monopole matrix elements thus calculated for  $T = 0$  and 1 in the  $pf$  shell, starting with the AV8' interaction (Pudliner *et al.*, 1997) and varying the cutoff parameter in the  $V_{low\ k}$  process. For the usual value  $2.1 \text{ fm}^{-1}$ , the result is very close to those obtained directly from the bare AV8' tensor-force.

This feature that a nuclear-force component remains unchanged to a good extent by the renormalization processes has been referred to as *renormalization persistency* (Tsunoda *et al.*, 2011). The renormalization persistency was studied particularly well for the monopole interaction of the tensor force with a variety of the shell, the original interaction and the renormalization methods. Such studies, not only the earliest one (Tsunoda *et al.*, 2011) but also more recent ones with chiral EFT forces (Yoshida, 2017), indicate that the tensor force fulfills the renormalization persistency at least at the level of the monopole interaction. The renormalization persistency therefore provides us with a good rationale to discuss general features of the monopole effects of the tensor force in terms of the  $\pi+\rho$ -meson exchange potential, as was done so far.

As an example of the radial dependence of actual tensor potentials, Fig. 32 shows the triplet-even (TE) potential due to the tensor potentials in some approaches (see (Otsuka *et al.*, 2005) for details). Except for the  $\pi$ -meson exchange case (no  $\rho$  meson), the TE potentials exhibit rather similar behaviors outside  $\sim 0.6 \text{ fm}$ . While differences arise inside, the relative-motion wave functions of two interacting nucleons are suppressed there because of forbidden coupling between  $S$ -wave bra and ket states.

### F. Related theoretical studies on tensor-force driven shell evolution

The effects of the tensor-force has been included in various studies of nuclear models by now, including those referring to the spin-tensor decomposition (Smirnova *et al.*, 2010, 2012), as well as those based on the mean-field models (Bender *et al.*, 2009a; Brink and Stancu, 2007; Brown *et al.*, 2006; Colò *et al.*, 2007; Lalazissis *et al.*, 2009; Lesinski *et al.*, 2007; Long *et al.*, 2007a; Otsuka

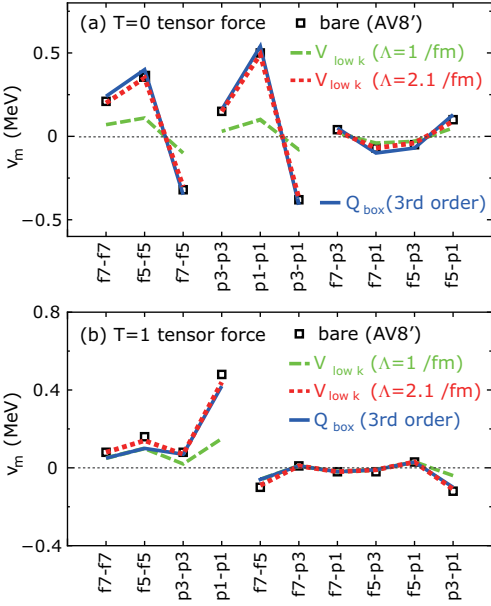


Figure 31 Monopole matrix elements from tensor forces in the AV8' interaction (Pudliner *et al.*, 1997), in low momentum interactions obtained from the AV8', and in the third order  $Q_{box}$  interaction for (a)  $T=0$  and (b)  $T=1$ . From Otsuka *et al.* (2010b).

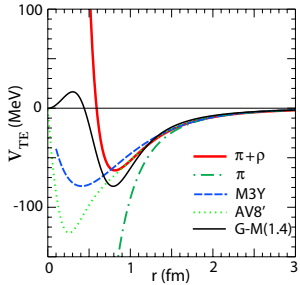


Figure 32 Triplet-even potential due to the tensor force for various interaction models. Adapted from (Otsuka *et al.*, 2005).

*et al.*, 2006). Regarding the inclusion of the tensor force into Skyrme-based mean field approaches, rather few studies have been done before these works, probably in considerations of some issues pointed out, for instance, in (Bender *et al.*, 2003).

Smirnova *et al.* (2010, 2012) applied the spin-tensor decomposition technique (Brown *et al.*, 1988; Elliott *et al.*, 1968; Kirson, 1973; Klingenbeck *et al.*, 1977; Osnes and Strottman, 1992; Yoro, 1980) to a realistic interaction for the  $sd$ - $pf$  shell (Nowacki and Poves, 2009) and examined  $k = 0, 1, 2$  contributions in eq. (67) to the ES-PEs. Figure 33 shows the evolution of the neutron effective single-particle energies with protons occupying  $d_{5/2}$  ( $Z = 8-14$ ),  $s_{1/2}$  ( $Z = 14-16$ ) and  $d_{3/2}$  ( $Z = 16-20$ ). It is demonstrated that the spin-orbit splittings, especially

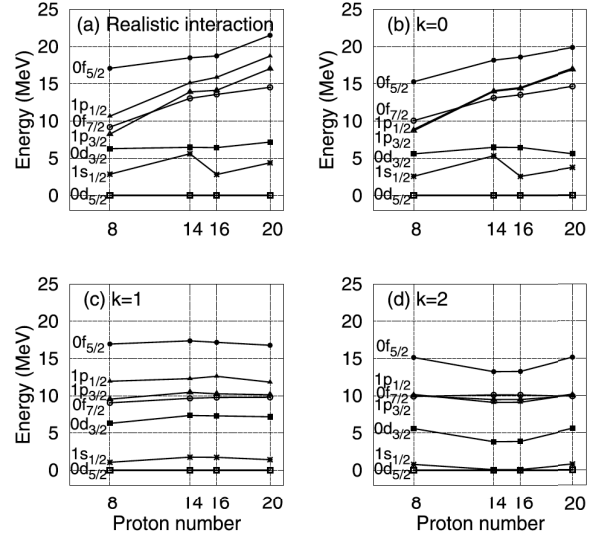


Figure 33 (a) Neutron effective single-particle energies of the SDPF-U interaction (Nowacki and Poves, 2009) and their (b)  $k = 0$ , (c)  $k = 1$ , and (d)  $k = 2$  contributions with increasing proton number. Reprinted with permission from Smirnova *et al.* (2010).

those of  $f_{7/2}$ - $f_{5/2}$  and  $d_{5/2}$ - $d_{3/2}$ , are changed notably by the tensor component and that their increase from  $Z = 16$  to 20 and decrease from  $Z = 8$  to 14 follow the way we have presented already, which can be regarded as a confirmation of the appropriateness of the empirically fitted shell-model interaction used in (Smirnova *et al.*, 2010, 2012). The tensor component also accounts for nearly half of the reduction of the  $N = 20$  shell gap (i.e.  $d_{3/2}$ - $f_{7/2}$  gap) when going from  $Z = 14$  to 8. These behaviors are in accordance with what the  $V_{MU}$  interaction gives (Otsuka *et al.*, 2010b), as discussed later.

The importance of the tensor force was anticipated by Skyrme, when the original form of the Skyrme interaction was proposed (Skyrme, 1958). The tensor force was, however, not much studied within the Skyrme-model calculations for a while, with probably only the exception of the work of Stancu, Brink and Flocard (Stancu *et al.*, 1977), who adopted the zero-range approximate form for the tensor force with terms mixing  $S$  and  $D$  waves of the relative motion as well as  $P$  waves (Skyrme, 1958; Vautherin and Brink, 1970). This form can be written as

$$\begin{aligned} v_T = & \frac{1}{2} T \{ [(\vec{\sigma}_1 \cdot \vec{k}')(\vec{\sigma}_2 \cdot \vec{k}') - \frac{1}{3}(\vec{\sigma}_1 \cdot \vec{\sigma}_2)k'^2] \delta(\vec{r}_1 - \vec{r}_2) \\ & + \delta(\vec{r}_1 - \vec{r}_2) [(\vec{\sigma}_1 \cdot \vec{k})(\vec{\sigma}_2 \cdot \vec{k}) - \frac{1}{3}(\vec{\sigma}_1 \cdot \vec{\sigma}_2)k^2] \} \\ & + U \{ (\vec{\sigma}_1 \cdot \vec{k}') \delta(\vec{r}_1 - \vec{r}_2) (\vec{\sigma}_1 \cdot \vec{k}') \\ & - \frac{1}{3}(\vec{\sigma}_1 \cdot \vec{\sigma}_2) [\vec{k}' \delta(\vec{r}_1 - \vec{r}_2) \vec{k}'] \} \end{aligned} \quad (69)$$

where  $\vec{k} = (\vec{\nabla}_1 - \vec{\nabla}_2)/2i$  acts on the right and  $\vec{k}' = -(\vec{\nabla}_1 -$

$\vec{\nabla}_2)/2i$  on the left.

The tensor term gives rise to additional spin-orbit strengths written as

$$\begin{aligned}\Delta W_n &= \alpha_T J_n + \beta_T J_p \\ \Delta W_p &= \alpha_T J_p + \beta_T J_n,\end{aligned}\quad (70)$$

where  $J_\rho$  ( $\rho = p, n$ ) are the spin densities given by

$$\begin{aligned}J_\rho(r) &= \frac{1}{4\pi r^3} \sum_a (2j_a + 1) \\ &\times [j_a(j_a + 1) - \ell_a(\ell_a + 1) - \frac{3}{4}] R_a^2(r)\end{aligned}\quad (71)$$

with occupied orbitals  $\{a\}$ . Since the spin-orbit potential for  $\rho = p, n$  is  $W_\rho \vec{\ell} \cdot \vec{\sigma}/r$ , a large negative  $W_\rho$  gives a strong spin-orbit splitting. From the sign of  $j_a(j_a + 1) - \ell_a(\ell_a + 1) - \frac{3}{4}$ , one can see that  $J_\rho$  increases and decreases with the occupation of  $\alpha = j_>$  and  $j_<$  orbitals, respectively, and that changing  $J_\rho$  causes the evolution of the spin-orbit coupling as discussed already. The  $\alpha_T$  and  $\beta_T$  correspond to like-particle and proton-neutron tensor forces. The equality  $\beta_T = 2\alpha_T$  holds if the tensor force has the same isospin structure,  $\tau_1\tau_2$ , as the  $\pi + \rho$  meson-exchange potential. Monopole terms of the tensor forces given by the two parameters are compared with those of the tensor forces by  $\pi + \rho$  meson exchanges to study the validity of the use of the approximate zero-range form.

Figure 34 depicts a comparison between monopole matrix elements of the zero-range tensor force of (Stancu *et al.*, 1977) to those of the  $\pi + \rho$  meson-exchange tensor force. For the former, the parameters obtained by a chi-square fitting to the monopole matrix elements of the  $\pi + \rho$  tensor forces for  $A \approx 40$  mass region are used with actual values  $(\alpha_T, \beta_T) = (64.38, 128.75)$  MeV·fm<sup>5</sup>. As shown in Fig. 34, the zero-range form for the tensor force can simulate the monopole interaction of the  $\pi + \rho$  tensor force to a certain extent, but there are rather large fluctuations and deviations, especially in case of light nuclei. We note that the present  $(\alpha_T, \beta_T)$  values are close to the G-matrix ones  $(\alpha_T, \beta_T) = (60, 110)$  MeV·fm<sup>5</sup> (Brown *et al.*, 2006). For lighter nuclei, larger parameters become necessary to reproduce the monopole matrix elements of the  $\pi + \rho$  tensor force, whereas the deviation is opposite in heavy nuclei. This variation of the parameters is not much in accordance of the Skyrme phenomenology where constant parameters for all nuclei are a major advantage.

Although the effect of the tensor force on the spin-orbit potential was thus recognized in the 1970s, the tensor term has been dropped in most of the Skyrme parametrizations until recently. One of the probable reasons for this is that the inclusion of the tensor term does not lead to significant improvement in the single-particle spectra for doubly magic nuclei (Stancu *et al.*, 1977). In addition, as pointed out by Sagawa and Colò (2014), not much attention was paid to the *evolution* of shells with successive mass numbers, likely due to the missing expectation of the shell evolution. We point out also that the

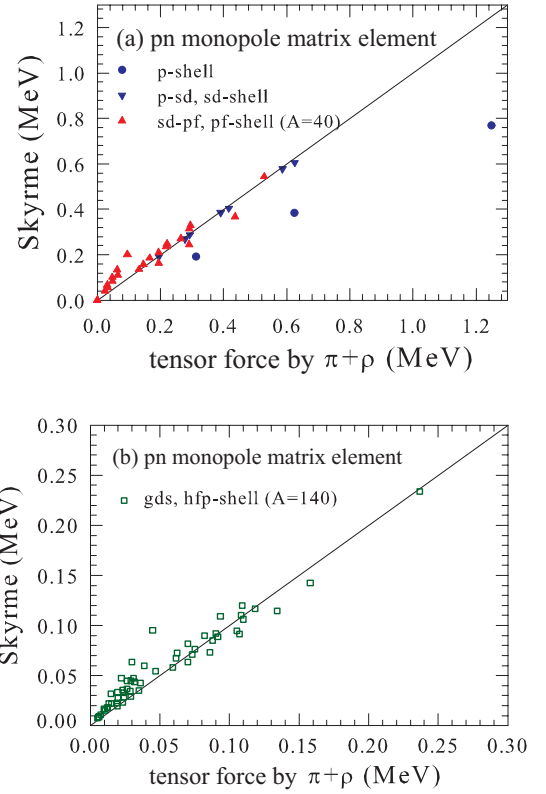


Figure 34 Comparison of monopole matrix elements of the zero-range tensor force of (Stancu *et al.*, 1977) to those of the  $\pi + \rho$  meson-exchange tensor force. The  $p$ ,  $sd$  and  $pf$  shells are covered in the upper panel, while the valence shell relevant to  $A \sim 140$  is considered in the lower panel. The parameter  $\beta_T = 128.75$  MeV·fm<sup>5</sup> is used.

meaning of the zero-range approximation of the tensor force remains to be investigated.

Following the work of (Otsuka *et al.*, 2005), the tensor term in the Skyrme forces has been revisited in terms of the shell evolution. For instance, Brown *et al.* (2006) reported the first investigation of the effects of the inclusion of tensor forces into the shell evolution based on the Skyrme density functionals, employing empirical values  $(\alpha_T, \beta_T) = (-118, 110)$  MeV·fm<sup>5</sup>. Brink and Stancu (Brink and Stancu, 2007) re-investigated, after their work in (Stancu *et al.*, 1977), the ESPE gaps between the proton  $1h_{11/2}$  and  $1g_{9/2}$  single-particle levels in Sb ( $Z=51$ ) isotopes as well as those between the neutron  $1i_{13/2}$  and  $1h_{9/2}$  single-particle levels in  $N=83$  isotones. Figures 35 and 36 depict results of various calculations on the proton  $1h_{11/2} - 1g_{9/2}$  gap in Sb isotopes. While this gap was discussed in case (5) in Sec. III.D with Fig. 30 from the viewpoint of the  $V_{\text{MU}}$  interaction, we shall survey other approaches, in some of which other correlation effects were investigated. Upper panel of Fig. 35 shows, as a reference, the monopole effect by the  $\pi + \rho$  meson-exchange tensor force on top of the usual mean potential

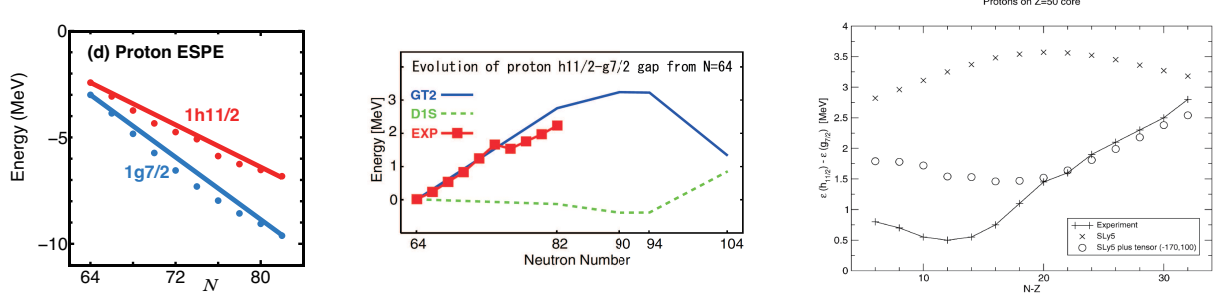


Figure 35 Evolution of the proton  $h_{11/2}$ - $g_{7/2}$  gap in the Sb isotopes with and without the tensor term. (left)  $\pi + \rho$  meson-exchange tensor force on top of the usual Woods-Saxon potential. (middle) A Gogny-type calculation with the tensor force (GT2) and without it (D1S). (right) A zero-range tensor force calculation added to the SLy5 force. From Otsuka *et al.* (2005) (left) and Otsuka *et al.* (2006) (middle), and reprinted with permission from Colò *et al.* (2007) (right).

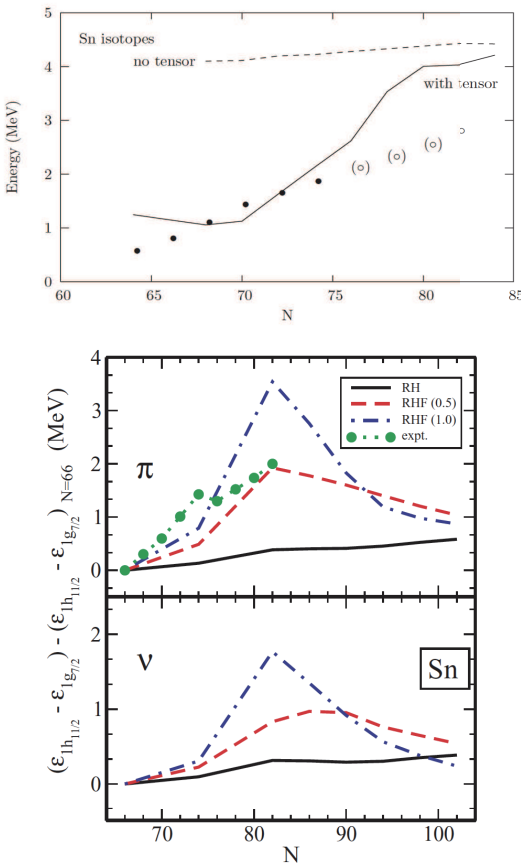


Figure 36 Same as Fig. 35. (upper) A zero-range tensor force calculation. (lower) A relativistic mean field calculation. Reprinted with permission from Brink and Stancu (2007) and from Lalazissis *et al.* (2009).

effect like a Woods-Saxon potential (Otsuka *et al.*, 2005). Colò *et al.* (2007) has examined this shell evolution as shown in the right panel of Fig. 35, confirming that the inclusion of the tensor term clearly improves the agree-

ment with experimental data with the adopted values  $(\alpha_T, \beta_T) = (-170, 100)$  MeV·fm<sup>5</sup>. Upper panel of Fig. 36 displays a similar calculation by (Brink and Stancu, 2007) with  $(\alpha_T, \beta_T) = (-118.75, 120)$  MeV·fm<sup>5</sup>. To the present shell evolution, the proton-neutron monopole interaction matters, which is controlled by the  $\beta_T$  parameter. We notice that three works (Brown *et al.*, 2006), (Colò *et al.*, 2007), and (Brink and Stancu, 2007) use, respectively, rather close values,  $\beta_T = 110, 100$ , and 120 MeV·fm<sup>5</sup>.

Besides the extension of Skyrme phenomenology, there was another early attempt based on the Gogny force plus Gaussian-type finite-range tensor force (Otsuka *et al.*, 2006) like the AV8' interaction (Pudliner *et al.*, 1997). The result for the shell evolution discussed above is shown in middle panel of Fig. 35, exhibiting a good reproduction of observed systematics. A relevant systematic study with the M3Y-type interactions was reported (Nakada, 2008). Combining these works with Skyrme-based calculations, the tensor-force driven shell evolution has been confirmed quite well.

We comment on  $\alpha_T$  values empirically determined. They causes the opposite direction of the evolution to the ones of the  $\pi + \rho$  meson exchange potential and the  $G$ -matrix results. The justification of using such negative  $\alpha_T$  values is not clear in connection to the nucleon-nucleon forces. Regarding open problems with Skyrme-based approaches, we quote a comment “The currently used central and spin-orbit parts of the Skyrme energy density functional are not flexible enough to allow for the presence of large tensor forces” from (Lesinski *et al.*, 2007), and another remark “Studies of tensor terms are extended to the case with deformations for future construction of improved density functionals” from (Bender *et al.*, 2009b).

In relativistic mean-field models, pion degrees of freedom were taken into account in relativistic Hartree-Fock (RHF) method by its exchange contributions (Bouyssy *et al.*, 1987; Lalazissis *et al.*, 2009; Long *et al.*, 2006). Lower panel of Fig. 36 depicts an example of such calcu-

lations for the proton  $1h_{11/2} - 1g_{9/2}$  gap in Sb isotopes, presenting the tensor-force effect within the relativistic framework and the more explicit treatment of  $\pi$  meson in contrast to Skyrme zero-range tensor force. Contributions from  $\rho$  meson were found to cure the pseudo-shell closures at  $N$  or  $Z=58$  and 92 leading to realistic subshell closure at 64 (Long *et al.*, 2007b). In recent RHF models, density dependent meson-nucleon couplings (Long *et al.*, 2007b, 2006) or softened parametrized couplings (Lalazissis *et al.*, 2009) are adopted, which result in smaller effects of tensor forces from  $\pi$  or  $\pi + \rho$  meson exchanges compared to non-relativistic models (Lalazissis *et al.*, 2009; Liang *et al.*, 2008). Inclusion of many-body correlations beyond RHF+RPA is still in progress (Litvinova, 2016; Litvinova and Ring, 2006) and left to future investigations.

#### IV. TWO-BODY LS AND THREE-BODY FORCES

In this section, we discuss effects of the two-body spin-orbit (2-body LS) force and those of three-body forces, mainly on the shell evolution.

##### A. 2-body LS

The 2-body LS (2b-*LS*) force is another substantial source of the monopole interaction. Its monopole component has, however, been studied rather little so far. We sketch its major features here with more detailed discussions presented in Appendix D.

The monopole matrix elements of the 2b-*LS* force contribute, in many cases, to the spin-orbit splitting in the usual sense. Schematic explanations on their basic properties are shown in Appendix D.

We list here characteristic features presented in Appendix D.

(1) The monopole interaction from the 2b-*LS* force turns out to be consistent with the usual one-body spin-orbit splitting (see, *e.g.*, (Bohr and Mottelson, 1969)) in many cases, as discussed below.

(2) A schematic semi-classical picture can be drawn for the intuitive understanding of the general and basic properties of the 2b-*LS* monopole interaction (see Fig. 65 in Appendix D). The usual one-body spin-orbit interaction (see (Bohr and Mottelson, 1969)) includes the radial derivative of the density,  $\partial\rho/\partial r$ , with  $\rho$  and  $r$  being, respectively, the nucleon density and the distance from the center of the nucleus. The present picture leads us to an explanation of this dependence in terms of the difference between the monopole contributions from nucleons inside  $r$  and those from nucleons outside  $r$ .

(3) Based on this feature, a standard value for each 2b-*LS* monopole matrix element can be introduced (see the text for eq. (D7)). The actual values of the 2b-*LS*

monopole matrix elements are not far from the corresponding standard values in many cases. This property may be related to the empirical systematics suggested in (Mairle, 1993).

(4) Sizable deviations are found in some cases, however. Among them, the coupling between an  $s$  and a  $p$  orbits can be quite strong with a large magnitude of monopole matrix element, (see Fig. 66 for examples). This anomaly can be explained in a simple quantum mechanical manner based on the range of the 2b-*LS* force and the relative motion of two interacting nucleons, being a robust effect.

Although this effect has been presented orally since 2004, the first publication of one of its outcome was as late as in (Suzuki and Otsuka, 2008), where a notable enlargement of the proton  $1p_{3/2}-1p_{1/2}$  splitting due to neutrons in the  $2s_{1/2}$  orbit was shown as a consequence of the 2b-*LS* force (see Fig. 1 of (Suzuki and Otsuka, 2008) and relevant texts). Another example was presented in (Burgunder *et al.*, 2014) for the effect of the proton  $2s_{1/2}$  occupation on the neutron  $2p_{3/2}-2p_{1/2}$  splitting in comparison to experiment as will be discussed in Secs. V.A.7, V.A.8. A trend consistent with the present robust effect can be extracted from Fig. 33 (c) obtained by the spin-tensor decomposition (Smirnova *et al.*, 2010).

(5) In some other cases, the sign of the monopole interaction can be opposite from the standard one mentioned above, due to the radial wave functions (see Fig. 68).

(6) If two nucleons are in the same orbit, the semi-classical picture is inapplicable, and another type of large deviation occurs, for instance, between two nucleons in the same  $2p_{1/2}$  orbit (see Fig. 69). This case is very interesting and important. In fact, the monopole matrix element represents the whole interaction for two neutrons in the  $2p_{1/2}$  orbit, and the tensor and 2b-*LS* forces produce strong repulsion (see Figs. 22 (c), 31 (b) and 69). This feature lowers the  $2^+$  level of  $^{54}\text{Ca}$  discussed in Sec. III.D.4, by reducing the pairing gap and thereby shifting the ground-state energy upward. Thus, the actual  $N=34$  shell gap is likely larger than what is expected from the actual  $2^+$  level. The present repulsive effect also gives a natural explanation to the unusually weak or even repulsive value of the  $2p_{1/2}^2$  pairing matrix element mentioned in (Brown, 2013). While the tensor-force effect was suggested earlier (Otsuka *et al.*, 2010b), another argument was given in (Brown, 2013).

We now look into the shell structure of  $^{15}\text{C}$  and  $^{17}\text{O}$ , as an example of notable contributions of the 2b-*LS* monopole interaction. Although this case has been discussed in II.F.1, we revisit it. Figure 6 depicts the inversion between neutron  $2s_{1/2}$  and  $1d_{5/2}$  orbits between  $^{15}\text{C}$  and  $^{17}\text{O}$ , and Fig. 37 (a) shows how the monopole matrix elements work for this inversion. We now illustrate the origins of those monopole matrix elements in

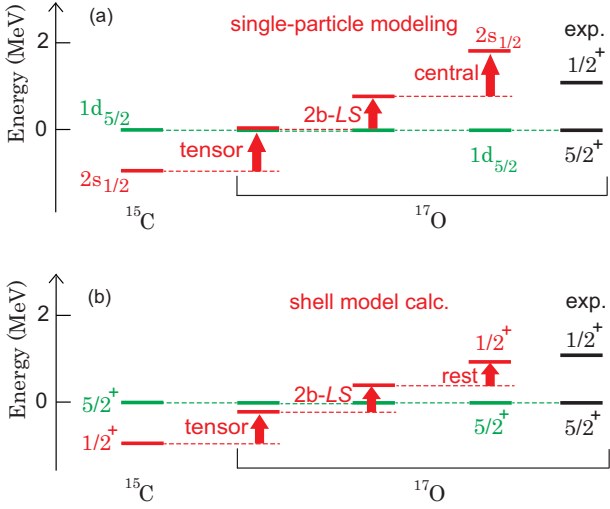


Figure 37 (a) Energy of the neutron  $2s_{1/2}$  orbit relative to the  $1d_{5/2}$  orbit in  $^{15}\text{C}$  and  $^{17}\text{O}$ , calculated within the single-particle scheme using the  $V_{\text{MU}}$  interaction plus the M3Y 2b-LS force (see the text). Contributions from the tensor, 2b-LS and central forces are decomposed. The changes are added to the experimental  $1/2_1^+$  level placed relative to the experimental  $5/2_1^+$  level. The experimentally observed level of  $^{17}\text{O}$  is shown far right. (b) Analysis similar to panel (a) in terms of the shell-model calculation with the YSOX (Yuan *et al.*, 2012) interaction. Some expectation values obtained by the YSOX calculation are shown correspondingly to (a) with respect to the shell-model eigenstates. See the caption of (a).

Fig. 37 in terms of the tensor, 2b-LS and central forces between protons and neutrons. Here it is assumed that from  $^{15}\text{C}$  to  $^{17}\text{O}$ , the proton  $1p_{1/2}$  orbit is fully occupied, and the last neutron is either in the  $2s_{1/2}$  or  $1d_{5/2}$  orbit. Figure 37 (a) displays how the neutron  $2s_{1/2}$  orbit is shifted relative to the  $1d_{5/2}$  orbit in going from  $^{15}\text{C}$  to  $^{17}\text{O}$  in this genuine single-particle limit.

Figure 37 (b) shows a related analysis. This is similar to Fig. 37 (a), but the contributions of the tensor, 2b-LS and the rest of Hamiltonian are shown with respect to the shell-model eigenstates obtained by the diagonalization of the Hamiltonian. These energy levels can be calculated by shell-model Hamiltonians recently developed, SFO-tls (Suzuki and Otsuka, 2008) and YSOX (Yuan *et al.*, 2012). The latter is taken in Fig. 37 (b), while the former gives a similar result. The contributions here mean the expectation values. The tensor and 2b-LS values are about 80% of the corresponding values in Fig. 37 (a), which appear to be very similar to the probability of the lowest configuration in the shell-model full wave functions of  $^{17}\text{O}$ . Thus, the discussions in terms of the monopole matrix elements and ESPEs are further proven to be sensible. On the other hand, the contributions from the central force in Fig. 37 (a) is reduced much in the rest part of Fig. 37 (b). Here the rest includes not only effects of the central force but also effects of the (bare)

single-particle energies due to excitations from lower to higher orbits. It is clear that various correlations due to the rest part decreases the raising of the  $1/2_1^+$  level. The general aspect of this feature is of certain interest. The importance of non-central forces is thus confirmed in the case shown in Figure 37, consistent with earlier remark (Millener and Kurath, 1975).

## B. Three-body forces

We now turn to another source of the shell evolution, three-nucleon force (3NF). While there are many subjects related to 3NF, we focus on the shell evolution due to 3NF in this paper. There is a recent review on the 3NF from various viewpoints in (Hammer *et al.*, 2013).

Three-nucleon forces were introduced in the pioneering work of Fujita and Miyazawa (1957) (FM), and one of its main sources is the fact that nucleons are composite particles. In fact, the FM 3N mechanism is due to one nucleon virtually exciting a second nucleon to the  $\Delta(1232 \text{ MeV})$  resonance, which is de-excited by scattering off a third nucleon, see Fig. 38(e). Three-nucleon interactions arise naturally also in the chiral effective field theory (EFT) (Epelbaum, 2006; Epelbaum *et al.*, 2009), where nucleons interact via pion exchanges and shorter-range contact interactions. The resulting nuclear forces are organized in a systematic expansion from leading to successively higher orders, and include the  $\Delta$  excitation as the dominant part of the leading 3NF (Epelbaum, 2006; Epelbaum *et al.*, 2009). The quantitative role of 3N interactions has been pointed out in ab-initio calculations made earlier with  $A \leq 12$  (Navratil *et al.*, 2007; Pieper, 2005; Pieper and Wiringa, 2001).

The monopole effect from the FM 3NF was first discussed in (Otsuka *et al.*, 2010a) with the actual example of the oxygen anomaly, while it was argued in (Zuker, 2003) that effective  $NN$  interaction is nearly perfect and any deviation suggested by experiment should be due to some three-body force. We sketch first the mechanism for the monopole effect presented in (Otsuka *et al.*, 2010a). Figure 38 (a) depicts the leading contribution to  $NN$  forces due to  $\Delta$ -resonance excitation, induced by the exchange of pions between nucleons. Because this is a second-order perturbation approach, its contribution to the monopole interaction is attractive. The same process changes the SPE of the state  $j, m$ , as illustrated in Fig. 38 (b), by the  $\Delta$ -nucleon-hole loop where the initial nucleon in the state  $j, m$  is virtually excited to another state  $j', m'$ . This lowers the energy of the state  $j, m$ . However, if another nucleon of the same kind occupies the state  $j', m'$  as shown in Fig. 38 (c), this process is forbidden by the Pauli exclusion principle. The corresponding contribution must be subtracted from the SPE change. This is taken into account by the inclusion of the exchange diagram shown in Fig. 38 (d), where the

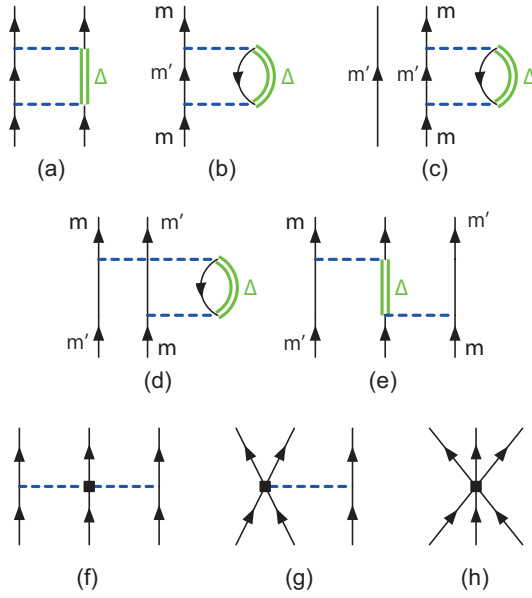


Figure 38 Processes involved in the discussion of 3N forces and their contributions to the monopole components of the effective interactions between two valence neutrons. The solid lines denote nucleons, the dashed lines denote pions, and the thick lines denote  $\Delta$  excitations. Nucleon-hole lines are indicated by downward arrows. The leading chiral 3N forces include the long-range two-pion-exchange parts, diagram (f), which take into account the excitation to a  $\Delta$  and other resonances, plus shorter-range one-pion exchange, diagram (g), and 3N contact interactions, diagram (h). From (Otsuka *et al.*, 2010a).

nucleons in the intermediate state are exchanged and this leads to the exchange of the final (or initial) labels  $j, m$  and  $j', m'$ . Because this process reflects a cancellation of the lowering of the SPE, the contribution from Fig. 38 (d) has to be repulsive. Finally, we can rewrite Fig. 38 (d) as the FM 3N force of Fig. 38 (e), where the middle nucleon is summed over all nucleons in the core. We thus obtain robustly repulsive monopole interactions between the valence nucleons originating in the FM 3NF. It is clear that only the monopole component is produced by this particular process, without touching on multipole components.

Figure 39 shows, as an example, neutron ESPEs of oxygen isotopes starting from the stable  $^{16}\text{O}$  to heavier ones with more neutrons. The ESPEs calculated (Otsuka *et al.*, 2010a) with  $NN$  interactions in the  $G$  matrix formalism (Hjorth-Jensen *et al.*, 1995), or in the approach based on low-momentum interactions  $V_{\text{low } k}$  (Bogner *et al.*, 2003, 2007) obtained from chiral  $NN$  interactions at next-to-next-to-next-to-leading order ( $N^3\text{LO}$ ) (Entem and Machleidt, 2003). The  $d_{3/2}$  orbital decreases rapidly as neutrons occupy the  $d_{5/2}$  orbit, and remains well-bound from  $N = 14$  on. This leads to bound oxygen isotopes out to  $N = 20$  and puts the neutron drip-line incorrectly beyond  $^{28}\text{O}$ . In Fig. 39 (b) the ESPE ob-

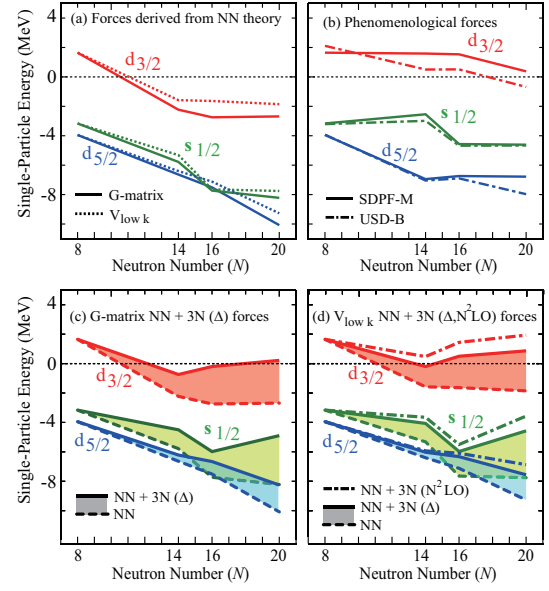


Figure 39 ESPE of neutron  $1d_{5/2}$ ,  $2s_{1/2}$  and  $1d_{3/2}$  orbitals measured from the energy of  $^{16}\text{O}$  as a function of  $N$ . Panel (a) presents the ESPE calculated from a  $G$  matrix and from low-momentum interactions  $V_{\text{low } k}$ . Panel (b) shows the ESPE obtained from the phenomenological forces SDPF-M (Utsuno *et al.*, 1999, 2004) and USD-B (Brown and Richter, 2006). The contributions from 3N forces due to  $\Delta$  excitations and all chiral EFT 3N interactions at  $N^2\text{LO}$  (Bogner *et al.*, 2009) are included in panels (c) and (d). The changes due to 3N forces based on  $\Delta$  excitations are highlighted by the shaded areas. From (Otsuka *et al.*, 2010a).

tained from the phenomenological forces SDPF-M (Utsuno *et al.*, 1999, 2004) and USD-B (Brown and Richter, 2006) are shown with a striking difference compared to Fig. 39 (a), which originate in differences in the monopole interaction.

In fact, Fig. 22(c,d) indicates that monopole components are modified to be more repulsive from  $G$ -matrix to GXPF1A in  $pf$  shell, except for the case with  $j=j'=f_{5/2}$ . Since GXPF1A reproduces the experimental data rather well, this general trend can be a hint as to what is missing in the microscopic  $NN$  interaction ( $G$ -matrix in this case) systematically. The situation is the same in the  $sd$  shell as shown in Fig. 22(g,h). It was thus concluded that there should be certain mechanism which makes effective  $NN$  interaction more repulsive in general.

The changes in the ESPE evolution due to the addition of FM 3NF are shown in Fig. 39 (c) for the  $G$  matrix formalism. The repulsive FM 3N contributions become significant with increasing  $N$  and the resulting ESPE pattern is similar to that of phenomenological forces, with higher  $1d_{3/2}$  orbit. Figure 39 (d) exhibits the ESPE calculated from chiral low-momentum interactions  $V_{\text{low } k}$  including the changes due to the leading ( $N^2\text{LO}$ ) 3N forces in chiral EFT (Epelbaum *et al.*, 2002;

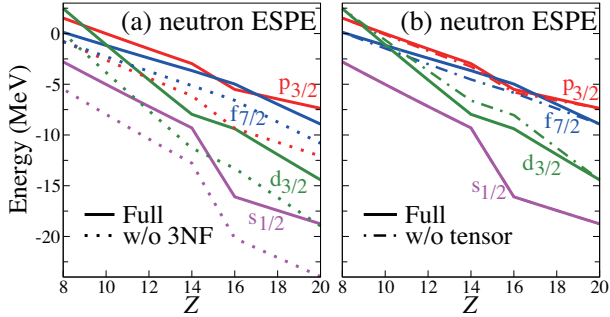


Figure 40 ESPEs of  $N=20$  isotones for neutrons obtained in the normal filling scheme. Solid (dotted) lines in (a) show the case with (without) three-nucleon forces, while the solid (dot-dashed) lines in (b) represent the case with (without) the tensor force. From (Tsunoda *et al.*, 2017).

van Kolck, 1994), (see Fig. 38 (f)–(h)), as well as due to  $\Delta$  excitations (Bogner *et al.*, 2009). The 3NF thus plays a key role for magic numbers, for the  $N = 14$  gap between the  $1d_{5/2}$  and  $2s_{1/2}$  orbitals (Staniou *et al.*, 2004), and they enlarge the  $N = 16$  gap between the  $2s_{1/2}$  and  $1d_{3/2}$  orbitals (Hoffman *et al.*, 2008; Kanungo *et al.*, 2009; Ozawa *et al.*, 2000).

Figures 38 (a,e) are relevant to neutron matter and neutron star through the competition between the attraction from Fig. 38 (a) and the repulsion from Fig. 38 (e) (Brown and Green, 1969; Fritsch *et al.*, 2005; Hebecker and Schwenk, 2009; Tolos *et al.*, 2008). This can be compared to the attraction in Fig. 38 (b) and the repulsion in Fig. 38 (c,d). Thus, neutron stars and exotic nuclei can be related also through the 3NF.

The 3NF effect on the ground-state energies of the oxygen isotopes are discussed, emphasizing its crucial effect at the dripline (Otsuka *et al.*, 2010a). A similar shell evolution is seen in exotic Ca isotopes, where the inclusion of 3NF effects improves binding energies, basically keeping shell structure (Holt *et al.*, 2012a; Otsuka and Suzuki, 2013). Coupled-cluster calculations in (Hagen *et al.*, 2012) show results consistent with those presented here. There are recent calculations on those nuclei (Lisetskiy *et al.*, 2008; Simonis *et al.*, 2016), where the shell evolution is not touched much. The treatment of the chiral EFT 3NF is being changed rapidly, and the resulting shell evolution should be discussed after the situation is settled.

Among such works, we present here the shell evolution across  $N=20$  based on the EKK method (Tsunoda *et al.*, 2014a) of the Many-Body Perturbation Theory (MBPT) calculation. The EKK method is suitable for this purpose, whereas some other MBPT calculations may have formal difficulty of divergence as pointed out in (Tsunoda *et al.*, 2017, 2014a). While we do not go into details here, we shall see major outcome related to the shell evolution.

Figure 40 shows SPE calculated from the chiral EFT

interaction at N3LO with the EKK treatment of in-medium effects and from the FM 3NF, for  $N=20$  isotones as a function of  $Z$ . Figure 40 (a) exhibits the SPEs obtained by the full calculation and those obtained after removing the FM 3NF. One finds that this 3NF shifts the SPEs upwards, with the trend that the shifts becomes larger as  $Z$  increases. Figure 40 (b) depicts the SPEs obtained by the full calculation and those obtained after removing the  $NN$  tensor force. Although the magnitude of the tensor-force effects is smaller than that of the 3NF as a whole, the tensor force effects are not monotonic and produce more rapid changes in the shell structure in contrast to the 3NF effects. In those calculations, although the SPEs are fitted at certain nuclei, their evolution as a function of  $Z$  (or  $N$ ) is given by the interaction, being free from the fit. In this sense, Figure 40 (a,b) present the first *ab initio* test of the shell evolution, appearing consistent with earlier results to be discussed in the next section.

In closing this subsection, as a general trend, the 3NF seems to shift SPEs upwards, while the spacing between neutron (proton) orbits may be more enlarged for larger  $N$  ( $Z$ ) in quite a few cases. This is a general robust consequence from the FM 3NF, but other 3NF contributions should be considered. As studies with chiral 3NF are still going on, we have to wait for the settled picture given by them. On the other hand, as the FM 3NF is expected to account for the major effect on the shell evolution from the 3NF, the 3NF effects on the shell evolution will remain in the way presented here.

## V. ACTUAL CASES

We discussed so far the underlying shell-evolution mechanisms due to nuclear forces and the resulting characteristic features in the nuclear structure. Actual cases, observed experimentally, reflect not only such mechanisms but also other many-body correlations. Although this aspect has been considered, we develop, in this section, more discussions as to how actual cases can be described and understood, by confronting experimental data mainly with shell-model calculations.

### A. Measuring the key indicators of shell evolution in unstable nuclei

Since short-lived “exotic” nuclei cannot be made into targets, measurements of their properties have to start from an ion beam which is subjected to an in-beam measurement in inverse kinematics, implanted into an active or passive stopper to observe its decay, or manipulated for ion trapping or laser spectroscopic approaches, for example.

The first challenge of any experiment with short-lived,

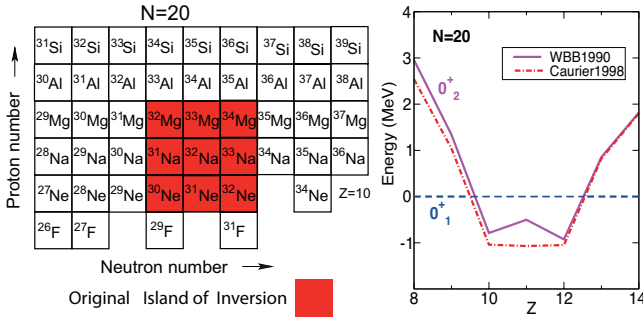


Figure 41 (Left) Part of the Segrè chart around the Island of Inversion. Red area indicates its original picture as of (Warburton *et al.*, 1990). By now, the Island of Inversion has extended much further (see the text). (Right) Relative energy of the lowest normal and lowest neutron 2p-2h intruder  $0^+$  states, resulting from diagonalizing in the separate subspace based on (Warburton *et al.*, 1990) and (Caurier *et al.*, 1998).

“exotic” nuclei is their production. Today, a broad range of rare isotopes is available for experiments in the form of ion beams. Two main production and separation mechanisms have emerged as the workhorse techniques in rare-isotope beam production and are employed in nuclear physics laboratories around the world:

- Beams of short-lived nuclei are produced and separated *in-flight* and are directly used for experiments (*in-flight* separation).
- Exotic nuclei are produced and thermalized in a thick target, extracted, ionized, transported or reaccelerated (isotope separation on-line – ISOL).

The production strategies for rare-isotope beams and the different types of rare-isotope facilities around the world were recently reviewed (Blumenfeld *et al.*, 2013).

In this subsection, we use the example of the “island of inversion” centered around  $^{32}\text{Na}$  (see Fig. 41), in order to describe how typical observables are measured and interpreted as indicators of structure changes.

### 1. Sketch of the Island of Inversion

We first sketch the island of inversion mainly from the viewpoint of the shell evolution. This discussion is rather brief, as the island of inversion was reviewed in (Caurier *et al.*, 2005). The island of inversion was named by (Warburton *et al.*, 1990), after earlier experimental studies had reported various anomalous features, for example, (Thibault *et al.*, 1975) followed by (Détraz *et al.*, 1979; Guillemaud-Mueller *et al.*, 1984; Huber *et al.*, 1978). It is characterized by deformation-related neutron particle-hole excitations from the *sd* shell into the *pf* shell across the  $N = 20$  shell gap. These neutron excitations are often referred to as intruder configurations, which can be energetically favored over the normal configurations and

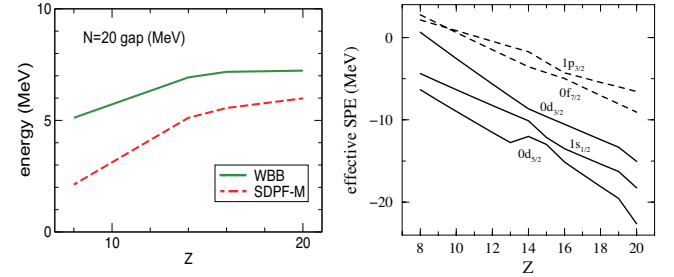


Figure 42 (Left) (Green solid line)  $N=20$  shell gap from (Warburton *et al.*, 1990) and (red dashed line) from the sdpm interaction (Utsuno *et al.*, 1999). (Right) ESPEs of  $N=20$  isotones for neutrons obtained in the normal filling scheme from SDPF-M interaction. From Utsuno *et al.* (1999).

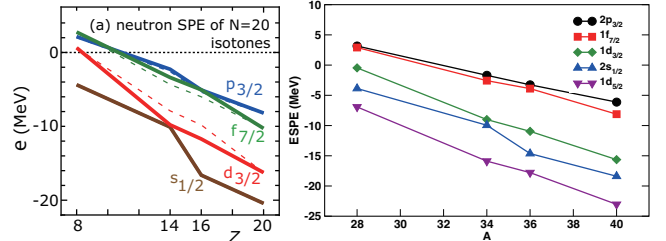


Figure 43 (Left) (a) neutron SPE of  $N=20$  isotones obtained in the normal filling scheme (left) from  $V_{\text{MU}}$  interaction and (right) from SDPF-NR interaction. From Otsuka *et al.* (2010b) (left) and reprinted with permission from Caurier *et al.* (2005) (right).

dominate the ground states of the nuclei in the island of inversion, as shown in the right panel of Fig. 41.

Early theoretical studies also indicated that the ground states can be deformed for nuclei in the island of inversion, such as a deformed Hartree-Fock solution for  $^{31}\text{Na}$  in (Campi *et al.*, 1975), and intruder shell-model ground-state configurations despite the rather constant  $N=20$  gap in (Poves and Retamosa, 1987). Regarding the shell evolution, so-called “modified single-particle energy” was introduced in (Storm *et al.*, 1983), corresponding to the present ESPE in the special case of a (sub)shell closure  $\pm$  one particle (see the texts around eqs. (39,40)). Although the monopole interaction was not mentioned, this may be the first appearance of the ESPE. The changes of the neutron shell structure was then discussed in (Storm *et al.*, 1983) with some differences from the current picture.

The left panel of Fig. 42 displays the  $N=20$  shell gap of  $N=20$  isotones obtained from (Warburton *et al.*, 1990), with values  $> 5$  MeV. The right panel of Fig. 42 presents ESPEs calculated from the SDPF-M interaction (Utsuno *et al.*, 1999), and the resulting  $N=20$  gap is included in the left panel of Fig. 42. The gaps now vary more, and become as low as 2 MeV for  $Z=8$ . A quite similar evolution of the ESPEs of the  $d_{3/2}$  and  $f_{7/2}$  orbitals were obtained

in (Fukunishi *et al.*, 1992), where large-scale shell-model calculations made successful predictions. The  $d_{3/2}$  ESPE changes more steeply with the SDPF-M interaction, however. This is because (Fukunishi *et al.*, 1992) uses the USD interaction where some change was made from G-matrix (Kuo, 1967). This change appeared to be rather inappropriate (Otsuka *et al.*, 2001), and was removed in the SDPF-M interaction, resulting in a better description. This is an example of the importance of nuclear forces to the shell evolution. This  $N=20$  gap reduction was schematically shown earlier in (Heyde and Wood, 1991) in terms of the proton-neutron monopole interaction of a  $\delta$ -function interaction, while the obtained pattern is too monotonic partly due to missing tensor force. The intruder states stay higher towards  $Z=8$  in (Caurier *et al.*, 1998), as exhibited in the right panel of Fig. 41. Thus, although the breakdown of the  $N=20$  magicity in the island of inversion was commonly accepted, in the 1990's, the vanishing of the  $N=20$  gap towards  $Z=8$  was suggested (in a quantitative way) rather uniquely in (Fukunishi *et al.*, 1992; Utsuno *et al.*, 1999). The situation is changed now, and other calculations also suggest a similar reduction, (see Fig. 43 as well as in Fig. 40), as a trend with more realistic interactions, particularly with the tensor force. Thus, anomalous features around  $N=20$  have been intensely studied, providing a strong motivation to clarify, both experimentally and theoretically, how the gap evolution occurs and what consequences arise. They are still very much contemporary subjects, as we shall see below.

## 2. Masses and separation energies

The mass of a nucleus is among the most basic properties directly accessible to measurements. Masses and derived quantities, *e.g.* one- and two-nucleon separation energies, frequently provide the first hints for the evolution of shell structure and signal the onset of deformation.

Experimental methods for the determination of atomic masses basically fall into two broad categories. Approaches that measure the  $Q$  values in decays or reactions make use of Einstein's mass-energy equivalence; mass measurements that are based on the deflection of ions in electromagnetic fields determine the mass-to-charge ratio. The most precise mass spectrometry is accomplished through frequency measurements (Myers, 2013). The cyclotron or revolution frequencies of ions in a magnetic field are measured to determine the mass-to-charge ratio in a Penning trap (Blaum, 2006) or in a storage ring (Franzke *et al.*, 2008).

A recent example for a precision mass measurement at the northern boundary of the  $N = 20$  island of inversion improved the precision of the masses of Al isotopes out to  $A = 34$  (Kwiatkowski *et al.*, 2015) from Penning-trap mass spectrometry at TRIUMF's Ion Trap

for Atomic and Nuclear science (TITAN) facility (Dilling *et al.*, 2006). In this experimental scheme, the mass of the ion of interest was deduced with a Penning trap by measuring the cyclotron frequency  $q/mB$ , where  $q/m$  is the charge-to-mass ratio of the ion and  $B$  is the magnetic field strength in the trapping volume. Inside the trap, the ions are excited by an azimuthal quadrupolar RF field with frequencies around the cyclotron frequency. The ions are released from the trap and their kinetic energy is determined from a time-of-flight measurement. In case of a resonant excitation, the radial kinetic energy of the released ion will be maximal and its time of flight minimal (TOF-ICR method, see (Bollen *et al.*, 1990)). A typical TOF resonance curve of  $^{34}\text{Al}^+$  is shown in Fig. 44. The magnetic field strength was calibrated relative to the well-known masses of  $\text{O}_2^+$  or  $^{39}\text{K}^+$  ions.

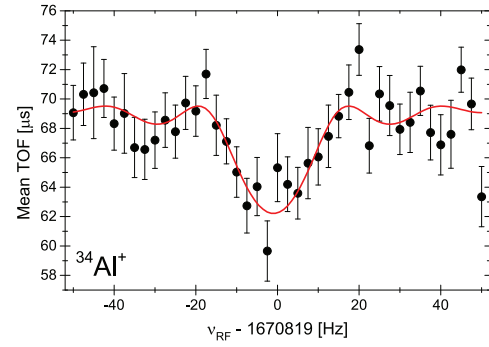


Figure 44 Resonance frequency of  $^{34}\text{Al}^+$  in the TITAN Penning trap determined from the time-of-flight minimum, signaling the maximum kinetic energy transferred at resonance. Reprinted with permission from Kwiatkowski *et al.* (2015).

The two-neutron separation energies ( $S_{2n}$  values) for the Al and Mg isotopic chains are shown in Fig. 45 with overlaid shell-model calculations in the  $sd$ - $pf$  model space using the SDPF-U effective Hamiltonian (Caurier *et al.*, 2014a). Typically, along an isotopic chain, the two-neutron separation energy,  $S_{2n}$ , decreases steadily towards the neutron dripline. The flattening in the trend for  $N = 19 - 21$  in the Mg chain indicates the increased correlation energy of these deformed nuclei relative to their neighbors with two neutrons less. In Al, a hint of this effect only appears beyond  $N = 21$ , putting  $^{31-34}\text{Al}$  outside and  $^{35-37}\text{Al}$  at the very boundary if not inside the island of inversion. Of interest is the unique crossing of  $S_{2n}$  in the Mg and Al isotopic chains at  $^{34}\text{Al}$ , which – in comparison to shell model – is attributed to Mg significantly gaining correlation energy upon entrance into the island of inversion between  $N = 20$  and 21, while the  $S_{2n}$  in the Al chain is still on its almost linear downward trend up to  $N = 22$ .

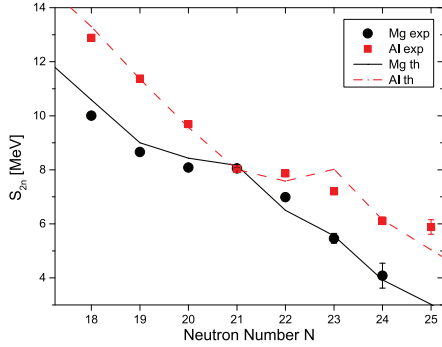


Figure 45 Symbols indicate two-neutron separation energies for the Mg and Al isotopic chains from the 2015 TITAN experiment and the mass compilation by Audi *et al.* (2012). Shell-model calculations in the *sd-pf* shell (Caurier *et al.*, 2014a) are shown also by lines. Reprinted with permission from Kwiatkowski *et al.* (2015).

### 3. Radii and quadrupole moments from precision measurements

The radii of the charge and neutron distributions of the nucleus are fundamental observables that are not only related to the basic properties of nuclear matter, e.g. the nuclear equation of state, but that are also revealing of changes in the nuclear structure and their driving forces. Matter radii have been accessed with a variety of experimental approaches, including measurements of interaction cross sections, reaction cross sections, charge-changing cross sections, and elastic scattering from which then the matter radius is extracted in a Glauber-model analysis (see Ozawa *et al.* (2001) for a review). Interaction cross section measurements famously led to the discovery of the extended size of neutron halo nuclei (Tanihata *et al.*, 1985). With electron scattering measurements not yet possible for rare isotopes, the charge radius of exotic nuclei is most often determined with the help of atomic physics techniques.

The charge distribution of the nucleus has a small but measurable effect on the atomic spectroscopy through the hyperfine structure of atomic transitions. Nuclear spins, isotope shifts (used to derive charge radii), magnetic dipole moments, and electric quadrupole moments can be determined with studies often based on laser spectroscopy (Blaum *et al.*, 2013). The radius of the neutron distribution can then be derived from the matter and charge radii by subtraction. In recent years, laser spectroscopy approaches have allowed the mapping of charge radii, or more precisely, of the changes in charge radii, for a number of isotopic chains (Angeli and Marinova, 2013), providing a unique view at the impact of shell structure on such a bulk property. The matter radius and thus neutron distributions are subject to significant model dependence and generally less well known.

The determination of changes in the charge radius from optical isotope shift measurements with laser

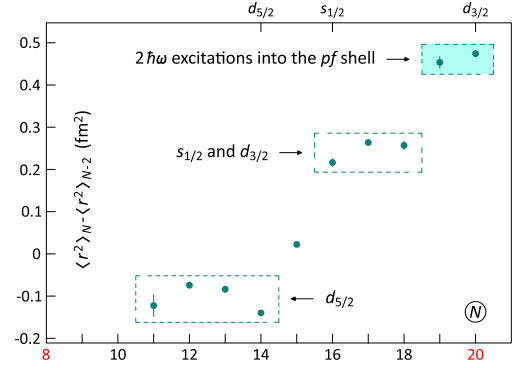


Figure 46 Differential mean square charge radii of Mg isotopes out to  $N = 20$  from laser spectroscopy measurements at ISOLDE/CERN.  $2\hbar\omega$  here refers to 2p-2h excitations across the  $N = 20$  shell gap. Reprinted with permission from Yordanov *et al.* (2012).

spectroscopy has advanced tremendously over the past decades and now routinely tackles measurements of rare isotopes (Blaum *et al.*, 2013). Isotope shifts in the island of inversion were extensively studied with pioneering laser spectroscopy at ISOLDE/CERN (Huber *et al.*, 1978; Marinova *et al.*, 2011; Yordanov *et al.*, 2012). The details of the various laser spectroscopy techniques were reviewed recently by Blaum *et al.* (2013). The determination of charge radii from isotope shifts is complex. The optical isotope shift, which is nothing but the difference in the resonance frequency of an electronic transition between two isotopes, has two contributions: The mass shift that originates from the center-of-mass motion of the nucleus and its obvious mass dependence, and the field shift that arises from the change in the electron energy due to the finite spatial extent of the nucleus. Evaluation of these contributions involves large-scale electronic many-body calculations or systematics and extrapolation as reviewed by Cheal and Flanagan (2010). For the Mg isotopes, for example, the changes in slope were associated with the occupation of the neutron  $d_{5/2}$ ,  $s_{1/2}$  and  $d_{3/2}$ , and the *pf* shell orbitals for  $^{23-26}\text{Mg}$ ,  $^{28-30}\text{Mg}$ , and  $^{31,32}\text{Mg}$ , respectively (Yordanov *et al.*, 2012), see Figure 46. The neutron 2p-2h excitations into the *pf* shell are a hallmark of the island of inversion and place  $^{31,32}\text{Mg}$  inside also with respect to the evolution of the charge radius as neutrons are added. The charge radius becomes larger with stronger deformation, and this can be the case in  $^{31,32}\text{Mg}$  where a stronger deformation is associated with a greater amount of p-h excitations.

The deviation from sphericity of nucleus that has non-zero spin can be quantified through its electric quadrupole moment, revealing itself in the electric hyperfine splitting of electronic states. The electric quadrupole moment was measured for the ground state of  $^{33}\text{Al}$  with the continuous-beam  $\beta$ -detected nuclear quadrupole resonance technique ( $\beta$ -NQR) at the LISE spectrometer at

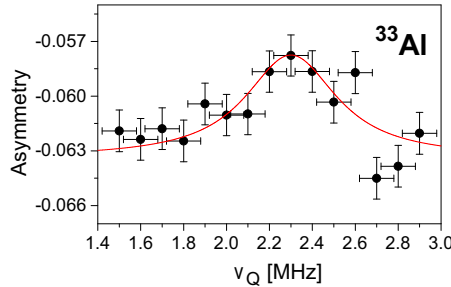


Figure 47 Measured asymmetry as function of the applied multi-frequency RF field that is characterized by the quadrupole coupling constant  $\nu_Q$  it probes. Reprinted with permission from Heylen *et al.* (2016).

GANIL (Heylen *et al.*, 2016) (see DeRydt *et al.* (2009) for the setup and the experimental approach). A polarized  $^{33}\text{Al}$  rare-isotope beam was produced by fragmentation of a  $^{36}\text{S}$  primary beam. The 94% pure beam was implanted into an  $\text{Al}_2\text{O}_3$  single crystal that was placed in a high static magnetic field along the spin polarization direction to maintain the polarization and induce Zeeman splitting. In addition to the Zeeman splitting from the external magnetic field, an axially symmetric electric field gradient inside the  $\text{Al}_2\text{O}_3$  crystal induced a shift due to the quadrupole interaction, leading to different transition frequencies of subsequent  $m$ -substates,  $\nu_m - \nu_{m+1}$ , of the  $^{33}\text{Al}$  ground state. When the Larmor frequency is known precisely, a simultaneous resonance measurement of all relevant transition frequencies through a multi-frequency RF field applied perpendicularly to the magnetic field direction allowed extracting the quadrupole coupling constant which is proportional to the absolute of the spectroscopic quadrupole moment and the crystal's internal electric field gradient (DeRydt *et al.*, 2009). As indicator, the  $\beta$  asymmetry inherent to the decay of polarized  $^{33}\text{Al}$  was monitored as function of the applied RF field. With this approach, the spectroscopic quadrupole moment  $|Q_s|$  was extracted for  $^{31,33}\text{Al}$  relative to  $^{27}\text{Al}$  (Heylen *et al.*, 2016). For  $^{33}\text{Al}$ , Fig. 47 shows the asymmetry as function of the applied multi-frequency RF field that is characterized by the quadrupole coupling constant  $\nu_Q$  it probes (Heylen *et al.*, 2016).

The implications for the structure of  $^{33}\text{Al}$  are shown in Fig. 48. The much improved uncertainty of  $|Q_s(^{33}\text{Al})|$  (Heylen *et al.*, 2016) led to argue the presence of neutron  $pf$ -shell intruder configurations in comparison to shell-model calculations that are restricted to the  $sd$  shell only (USD) and that allow for neutron particle-hole excitations across the  $N = 20$  shell gap (SDPF-M) (Utsuno *et al.*, 1999, 2004). One should be aware that these comparisons to shell model are sensitive to the effective charges used. It is noted that these conclusions contradict the ones from the mass measurements reviewed above, where  $^{33}\text{Al}$  was placed outside of the island of

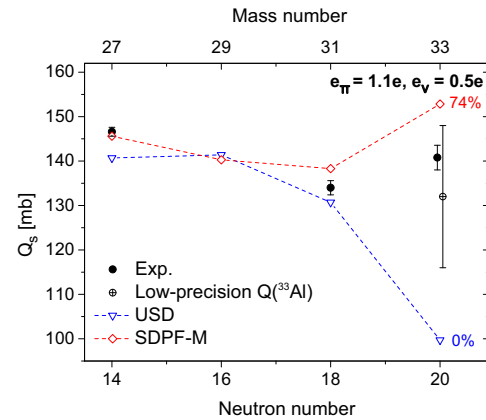


Figure 48 Measured spectroscopic quadrupole moments of Al isotopes compared to shell-model calculations limited to the neutron  $sd$  shell (USD) and allowing for particle-hole excitations across  $N = 20$  (SDPF-M). The given percentage signifies the amount of ground-state intruder configurations in the respective shell-model approach. Reprinted with permission from Heylen *et al.* (2016).

inversion and they are at odds with shell-model calculations using the SDPF-U-MIX effective interaction (Rotaru *et al.*, 2012) that also allows for neutrons in the  $pf$  shell. This may highlight the different levels of detail probed, with the moment measurement more sensitive to the very details of the configurations, or point to a puzzle in our understanding of  $^{33}\text{Al}$  at the northern border of the island of inversion.

#### 4. Excitation energy

Energies of excited nuclear states are often among the first quantities accessible in experiments (Gade, 2015). They can be measured directly and without any model dependence and are thus some of the key observables that can be tracked to unravel changes in the nuclear structure. For excited states below the nucleon separation energies, prompt or delayed  $\gamma$ -ray spectroscopy is frequently used to extract excitation energies of rare isotopes with great precision, measured from the spectroscopy of the  $\gamma$ -ray transitions that connect different states. Electric monopole transitions between  $0^+$  states (Wood *et al.*, 1999), of  $E0$  character, proceed to a large extent through conversion electron emission and electron spectroscopy or other charged-particle spectroscopy techniques, e.g. in transfer reactions, are required (Gade and Liddick, 2016). Excited states can be populated in nuclear reactions (Gade and Glasmacher, 2008) or  $\beta$  decay (Rubio and Gelletly, 2009), exploiting the selectivities inherent to the different population mechanisms. The energies of very long-lived isomeric states can be accessed, for example, with Penning-trap (Block *et al.*, 2008) or storage-ring (Reed *et al.*, 2010) mass spectrometry. For states

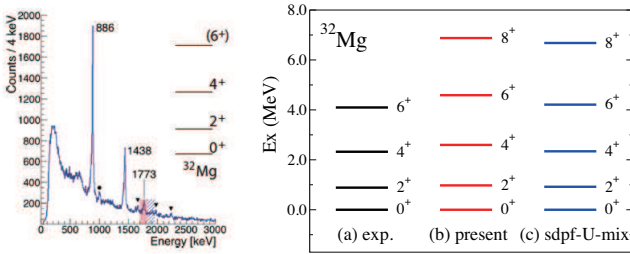


Figure 49 (Left) Prompt  $\gamma$ -ray spectrum detected with GRETINA in coincidence with the  $^{32}\text{Mg}$  projectile-like fragmentation residues identified in the S800 spectrograph. Reprinted with permission from Crawford *et al.* (2016). (Right) Comparison to theoretical calculations with EEdf1 and SDPF-U-MIX interactions. From (Tsunoda *et al.*, 2017).

that are unbound with respect to neutron or proton emission, excited-state energies can be deduced from invariant mass or missing mass spectroscopy. The spectroscopy of bound (Gade, 2015) and unbound (Baumann *et al.*, 2012) excited states was reviewed recently.

The most recent spectroscopy inside the  $N = 20$  island of inversion addressed one of the hallmark nuclei in this region of shell evolution,  $^{32}\text{Mg}$ , that has been subject to experimental study since its low-lying  $2_1^+$  energy contradicted the presence of the  $N = 20$  magic number in this isotopic chain (Détraz *et al.*, 1979). Using the advanced  $\gamma$ -ray tracking array GRETINA (Paschalis *et al.*, 2013) in tandem with the S800 spectrograph at NSCL (Gade and Sherrill, 2016), excited states in  $^{32}\text{Mg}$  (Crawford *et al.*, 2016) were populated in the secondary fragmentation of an  $^{46}\text{Ar}$  rare-isotope beam at 102 MeV/u delivered to a  $^9\text{Be}$  reaction target in the center of GRETINA. The  $\gamma$  rays emitted by  $^{32}\text{Mg}$  *in flight* were event-by-event Doppler corrected using the position sensitivity of GRETINA. The spectrum is displayed in Fig. 49. Aside from the previously known  $\gamma$ -ray transitions at 885 keV and 1438 keV that are attributed to the  $2_1^+ \rightarrow 0_1^+$  and  $4_1^+ \rightarrow 2_1^+$  transitions, respectively, a new transition at 1773 keV was observed that is proposed to connect the  $6_1^+$  and  $4_1^+$  states (Crawford *et al.*, 2016). With  $^{32}\text{Mg}$  suspected to be well-deformed, this would establish the lowest part of the yrast rotational band. Figure 49 shows good agreement with shell model calculation with the SDPF-U-MIX interaction (Crawford *et al.*, 2016) as well as that with the EEdf1 interaction which is of *ab initio* type (Tsunoda *et al.*, 2017). In a mean-field picture (cranked shell model), on the other hand, the observation may be attributed to a decrease in pairing correlations with increased angular momentum (Crawford *et al.*, 2016).

## 5. Transition strength

Nuclear structure can be probed experimentally in quantitative ways by a variety of nuclear reactions that are selective to specific degrees of freedom. Inelastic scattering, in particular Coulomb excitation, of nuclei has long been used to investigate collective degrees of freedom that involve the coherent motion of many nucleons.  $B(\sigma\lambda)$  reduced electromagnetic transition matrix elements are extracted from measured cross sections to quantify the degree of collectivity (Alder *et al.*, 1956; Cline, 1986; Glasmacher, 1998). Reduced electromagnetic transition strength can alternatively be deduced from excited-state lifetime measurement, extracted from Doppler energy shifts or lineshapes in  $\gamma$ -ray spectroscopy (Dewald *et al.*, 2012).

At collision energies below the Coulomb barrier, the excitation probabilities and interaction times are large enough to allow for multistep excitations and the determination of quadrupole moments and their signs, giving a glimpse at the degree and the character of deformation (Cline, 1986). In the regime of intermediate-energy or relativistic projectile energies, multistep processes are suppressed by several orders of magnitude. This greatly simplifies the analysis of the resulting excitation spectra, and the  $B(E2; 0_1^+ \rightarrow 2_1^+)$  value has been measured for  $^{32}\text{Mg}$  (Motobayashi *et al.*, 1995), establishing the strong deformation of this nucleus, for instance, a prediction by (Fukunishi *et al.*, 1992) shown in the left panel of Fig. 50. The higher-lying states of collective bands, on the other hand, remain out of reach with this technique in typical experiments lasting a few days with beam rates of a few per second (Gade and Glasmacher, 2008; Glasmacher, 1998). Excited-state lifetime measurements on the other hand do not require nuclear models to extract transition strengths but can suffer from observed and unobserved feeding from higher-lying states depending on the population mechanism of the excited states. The general experimental scheme exploits the Doppler shifts of  $\gamma$ -ray transitions from moving emitters to determine the point of  $\gamma$ -ray emission relative to the point in time the reaction occurred.

In a recent inelastic scattering experiment at RIBF in RIKEN (Nakamura *et al.*, 2017), the quadrupole collectivity or deformation of  $^{36}\text{Mg}$  and  $^{30}\text{Ne}$  was determined from measured  $0_1^+ \rightarrow 2_1^+$  excitation cross sections in comparison to coupled-channels calculations (Doornenbal *et al.*, 2016). The beams of  $^{30}\text{Ne}$  and  $^{36}\text{Mg}$  impinged upon Pb and C targets. The inelastic process was tagged through the detection of the  $2_1^+ \rightarrow 0_1^+$  de-excitation  $\gamma$  ray with the high-efficiency DALI2 NaI(Tl) array (Takeuchi *et al.*, 2014). Inelastic scattering off C and relativistic Coulomb excitation on a Pb target revealed a  $B(E2)$  value and deformation length, respectively, that indicates a quadrupole deformation parameter of  $\beta_2 \approx 0.5$  for both, showing that the quadrupole deformation in the Mg chain

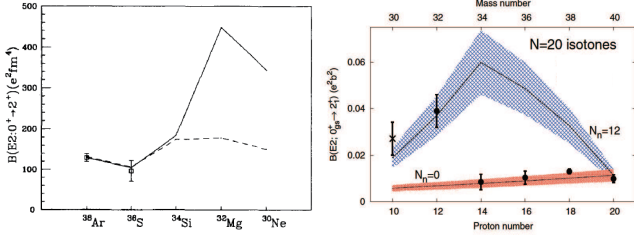


Figure 50  $B(E2)$  value of the  $N = 20$  isotones plotted as function of  $Z$ . (Left) Shell-model calculation by (Fukunishi *et al.*, 1992) where the solid line includes neutron excitations across the  $N = 20$  gap but the dashed line does not. (Right) The measured values are confronted with the  $N_p N_n$  scheme calculation (Casten and Zamfir, 1993) for  $N_n = 0$  ( $N = 20$  closed) and  $N_n = 12$  ( $sd$  and lower  $pf$  shells combined). See the text for details. From Fukunishi *et al.* (1992) (left) and adapted with permission from (Doornenbal *et al.*, 2016) (right).

persists towards the neutron dripline and that neutron excitations across  $N = 20$  are critical for reproducing the collectivity of  $N = 20$   $^{30}\text{Ne}$  (Doornenbal *et al.*, 2016). The telltale nature of the reduced  $B(E2; 0_1^+ \rightarrow 2_1^+)$  value as nuclear structure observable is illustrated in the right panel of Fig. 50, where the  $B(E2)$  strength of the  $N = 20$  isotones is plotted as function of  $Z$ . The measured values show good agreement with the much earlier shell-model prediction (Fukunishi *et al.*, 1992). Note that the order is inverted between the left and right panels. In addition, the measured values are confronted with the phenomenology of the  $N_p N_n$  scheme (Casten and Zamfir, 1993) for  $N_n = 0$  ( $N = 20$  shell closure intact and no valence neutrons) and  $N_n = 12$  ( $sd$  shell+ $f_{7/2}$ + $p_{3/2}$  combined as the neutron shell). The sharp onset of collectivity for  $Z \leq 12$  is consistent with the picture of dominant neutron particle-hole excitations across the  $N = 20$  shell gap for the Mg and Ne  $N = 20$  isotones, a hallmark of the island of inversion, at least for its northern boundary.

## 6. Identifying shapes at the boundary of the island of inversion

At the borders of the “island of inversion”, excited deformed intruder configurations can coexist with the still spherical ground states (Gade and Liddick, 2016). So far, shape-coexisting  $0^+$  states have been identified in  $^{34}\text{Si}$  (Rotaru *et al.*, 2012) and  $^{30}\text{Mg}$  (Schwerdtfeger *et al.*, 2009). Along the line of the  $N = 20$  isotones,  $^{34}\text{Si}$  is situated at the northern boundary of the island of inversion. In a pioneering measurement at GANIL, the  $\beta$  decay of the  $1^+$  isomer of  $^{34}\text{Al}$  was used to selectively feed  $0^+$  states in  $^{34}\text{Si}$ , including the previously unobserved excited  $0_2^+$  state at 2719(3) keV (Rotaru *et al.*, 2012). This state is located below the  $2_1^+$ , presenting an experimental challenge. Since  $\gamma$ -ray decays between  $0^+$  states are angular-momentum forbidden, this low-lying  $0^+$  state

can only de-excite via electron conversion or internal pair formation, where an electron-positron  $e^+e^-$  pair is released with a total energy of  $E_{e^-} + E_{e^+} = E(0_2^+) - 2 \times 511$  keV. In the GANIL experiment, Si-Si(Li) telescopes were used for the electron/positron spectroscopy. When correlating the total electron/positron energy detected in one telescope versus another, events were found for which the energy detected in the two telescopes sums to a peak at  $E_{e^+} + E_{e^-} = 1688(2)$  keV (Rotaru *et al.*, 2012). When accounting for an energy-loss correction of 9(1) keV, this establishes the first excited  $0^+$  state of  $^{34}\text{Si}$  to  $E(0_2^+) = 2719(3)$  keV (Rotaru *et al.*, 2012). From the difference timing between the  $\beta$ -decay events and the  $e^+e^-$  pair signals, a half-life of 19.4(7) ns was determined for the  $0_2^+$  state (Rotaru *et al.*, 2012). The resulting low  $E0$  transition strength indicates only weak mixing between the  $0_1^+$  ground state and the  $0_2^+$  excited state. Combining all spectroscopic information, including  $B(E2; 2_1^+ \rightarrow 0_2^+) = 61(40)e^2\text{fm}^4$ , as extracted from a small  $\gamma$ -ray branch and the  $2_1^+$  lifetime, results in a quadrupole deformation parameter for the  $0_2^+$  state of  $\beta = 0.29(4)$ , in agreement with SDPF-U-MIX shell-model calculations (Rotaru *et al.*, 2012).

Although there seem to be two distinct shapes at low excitation energy for  $^{34}\text{Si}$ , different types of structure features appear at the boundary of the island of inversion. We shall take, as an example,  $^{31}\text{Mg}$  located just outside of it. Figure 51 (b) shows its energy levels calculated with the EEdf1 interaction, in a good agreement with experiment in Fig. 51 (a) (Tsunoda *et al.*, 2017). The EEdf1 interaction is derived for the  $sd+pf$  shell microscopically by the EKK method in (Tsunoda *et al.*, 2017). The SDPF-U-MIX interaction shows the three lowest levels in Fig. 51 (d). This interaction is obtained partly by a fit, but the number of two-body-matrix-elements to be fitted is too large compared to the number of experimental data, if two major shells  $sd$  and  $pf$  are combined. The fitting procedure, which was successful for one-major-shell calculations, cannot be performed fully, and only a few levels are reported in (Caurier *et al.*, 2014b) as shown in Fig. 51 (d). Thus, the *ab initio* type interaction, where this difficulty is irrelevant, can play a more crucial role for the boundary of the island of inversion, producing much larger mixings in  $^{31}\text{Mg}$ . In fact, its ground state is composed of  $\sim 70\%$   $2p2h$  and  $\sim 30\%$   $4p4h$  configurations, whereas quite negligible fraction of the normal configuration (Tsunoda *et al.*, 2017), in contrast to the original picture of the island of inversion of (Warburton *et al.*, 1990). On the other hand, the shell evolution pattern resembles that of other approaches, as shown in Fig. 40. Some other nuclei are also discussed in (Tsunoda *et al.*, 2017). These features are really contemporary subjects, and should be clarified further.

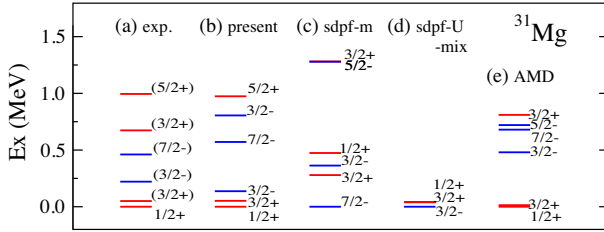


Figure 51 Energy levels of  $^{31}\text{Mg}$ . (a) experimental values, (b) present work, (c) SDPF-M (Utsuno *et al.*, 1999), (d) SDPF-U-MIX (Caurier *et al.*, 2014b) and (e) AMD+GCM calculation (Kimura, 2007), respectively. From Tsunoda *et al.* (2017).

## 7. Spectroscopy of the nuclear wave function through direct reactions

Direct nuclear reactions have proven to be a vital tool for the spectroscopy of the single-particle components in the nuclear wave function. In a glancing collision of a projectile and a target nucleus, one or a few nucleons are transferred directly without formation of an intermediate compound system.

The classic low-energy transfer reactions, that for stable target nuclei use a variety of light projectiles to probe occupied single-particle levels and valence states (Macfarlane and French, 1960), e.g., the  $(d, p)$  neutron-adding and the  $(d, {}^3\text{He})$  proton-removing transfers, are now employed at low-energy rare-isotope facilities in inverse kinematics when low-emittance, high-intensity rare-isotope beams are available (see (Burgunder *et al.*, 2014; Catford *et al.*, 2010; Fernández-Domínguez *et al.*, 2011; Gaudefroy *et al.*, 2006; Kanungo *et al.*, 2010; Wimmer *et al.*, 2010) for examples from different facilities). At intermediate beam energies ( $\sim 100$  MeV/u), thick-target  $\gamma$ -ray tagged one- and two-nucleon knockout reactions on  ${}^9\text{Be}$  or  ${}^{12}\text{C}$  targets have been developed into spectroscopic tools to study single-nucleon hole states and correlations of two like nucleons in exotic nuclei (Bazin *et al.*, 2003; Gade *et al.*, 2008; Hansen and Tostevin, 2003; Simpson and Tostevin, 2010; Simpson *et al.*, 2009; Tostevin *et al.*, 2004; Yoneda *et al.*, 2006).

By comparing cross sections with C and Pb targets, it is also possible to extract Coulomb reaction cross sections, which are used to look into neutron shell structure through the halo formation in  ${}^{31}\text{Ne}$  and  ${}^{37}\text{Mg}$  (Kobayashi *et al.*, 2014; Nakamura *et al.*, 2009, 2014).

At the high beam energies, typically exceeding 70 MeV/nucleon, a theoretical description (Tostevin, 1999) in the framework of eikonal trajectories and sudden approximation is applicable. Therefore, the model dependence is limited as compared to the classical low-energy transfer reactions, whose description involves the Distorted Wave Born Approximation (DWBA) or higher-order formalisms, that depend strongly on entrance- and

exit-channel optical model potentials (Kramer *et al.*, 1988), which have not been established yet for nuclei with extreme neutron-to-proton ratios. It was shown recently that low-energy transfer reactions and nucleon removal reactions can be analyzed to give consistent results (Mutschler *et al.*, 2016b). Both knockout and transfer reactions have been used to track the descent of intruder states along isotopic chains approaching the island of inversion. Two complementary examples are reviewed in the following.

The onset of  $pf$  shell intruder configurations was quantified along the Mg chain with  $\gamma$ -ray tagged one-neutron removal measurements,  ${}^9\text{Be}({}^{30}\text{Mg}, {}^{29}\text{Mg} + \gamma)\text{X}$  and  ${}^9\text{Be}({}^{32}\text{Mg}, {}^{31}\text{Mg} + \gamma)\text{X}$ , performed at NSCL (Terry *et al.*, 2008). From the shapes of the  ${}^{29,31}\text{Mg}$  parallel momentum distributions (reconstructed with the S800 spectrograph) gated on the individual  $\gamma$ -ray transitions in these knockout residues (measured with SeGA), the 1.095 and 1.431 MeV states in  ${}^{29}\text{Mg}$  and the 0.221 and 0.461 MeV levels in  ${}^{31}\text{Mg}$  were shown to be of  $\ell = 1$  and  $\ell = 3$  orbital angular momentum, respectively, identifying  $p_{3/2}$  and  $f_{7/2}$  single-neutron configurations in the ground states of both  ${}^{30}\text{Mg}$  and  ${}^{32}\text{Mg}$  (Terry *et al.*, 2008). From the partial cross sections for the population of the negative-parity states in the knockout residues,  $f_{7/2}$  and  $p_{3/2}$  spectroscopic factors were deduced. The resulting quantification of the onset of  $f$  and  $p$  intruder configurations in the ground states of  ${}^{30}\text{Mg}$  and  ${}^{32}\text{Mg}$  is seen in Fig. 52: The neutron  $pf$ -shell strengths increase significantly at  $N = 20$ , signaling a dramatic shift in the nuclear structure of  ${}^{32}\text{Mg}$  as compared to  ${}^{30}\text{Mg}$ . The spectroscopic factors calculated with EEdf1 interaction (Tsunoda, 2018; Tsunoda *et al.*, 2017) show a good agreement with experiment, when this calculation includes a reduction factor of 0.75 that is inherent to knockout reactions (Tostevin and Gade, 2014). The occupation numbers obtained with the SDPF-M interaction (Utsuno *et al.*, 1999) were used in the analysis of (Terry *et al.*, 2008) as shown in Fig. 52, depicting a similar trend. The EEdf1 interaction, in contrast to the SDPF-M interaction, is comprised of a two-body interaction derived fully microscopically from a  $\chi$ EFT interaction (Tsunoda *et al.*, 2014a) (see Sec. IV.B). It gives a better and nearly perfect description for the energy levels for  ${}^{32,31}\text{Mg}$  in Figs. 49 and 51, respectively, as well as for the spectroscopic factors in Fig. 52. The latter illustrates the amount of the excitations across the  $N=20$  magic gap. We stress that the shell evolution through this EEdf1 interaction (see Fig. 40) exhibits similarities to earlier results shown in Figs. 42 and 43.

In the Ne isotopic chain, a  $\gamma$ -ray tagged neutron-adding transfer reaction,  $d({}^{26}\text{Ne}, {}^{27}\text{Ne} + \gamma)p$ , performed at GANIL with TIARA for proton detection, VAMOS for projectile-like residue identification and EXOGAM for  $\gamma$ -ray spectroscopy identified for the first time the (neutron unbound)  $7/2_1^-$  state at 1.74(9) MeV in  ${}^{27}\text{Ne}$  (Brown

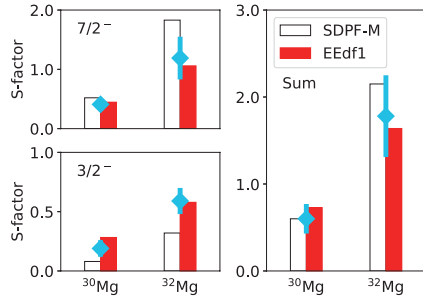


Figure 52 Spectroscopic factors from  $^9\text{Be}(^{32,30}\text{Mg}, ^{31,29}\text{Mg})\text{X}$  knockout reactions to two negative-parity states of  $^{32,30}\text{Mg}$ . Deduced spectroscopic factors are indicated by blue point with error bar (Terry *et al.*, 2008). Single-particle occupancies obtained from SDPF-M shell model (Utsuno *et al.*, 1999) are represented by blanc histograms. Spectroscopic factors calculated with the EEdf1 interaction are shown by red histograms (Tsunoda, 2018).

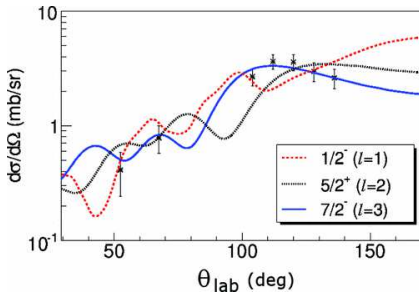


Figure 53 Proton angular distribution for the new neutron-unbound state discovered at 1.74 MeV in  $^{27}\text{Ne}$ . In comparison to reaction theory,  $\ell = 3$  orbital angular momentum was assigned (Brown *et al.*, 2012). Reprinted with permission from Brown *et al.* (2012).

(Terry *et al.*, 2012). A previous one-neutron knockout experiment failed to observe this state since the experimental approach was limited to levels that decay by  $\gamma$ -ray emission (Terry *et al.*, 2006). The  $\ell = 3$  orbital angular momentum of the state was concluded from the proton angular distribution in comparison to ADWA transfer reaction calculations (see Figure 53).

The  $3/2^-$  state could be identified at 0.765 MeV, confirming earlier work that could only restrict the orbital angular momentum of this state to  $\ell = 0, 1$  (Terry *et al.*, 2006). The fact that the  $7/2^-$  state is higher in energy than the  $3/2^-$  level presents a remarkable inversion from the ordering closer to stability and disagrees with the sequence predicted by the SDPF-M Hamiltonian (Brown *et al.*, 2012). This result will serve as an important benchmark for new effective shell-model Hamiltonians in the region in their quest to describe the shell evolution in and around the island of inversion.

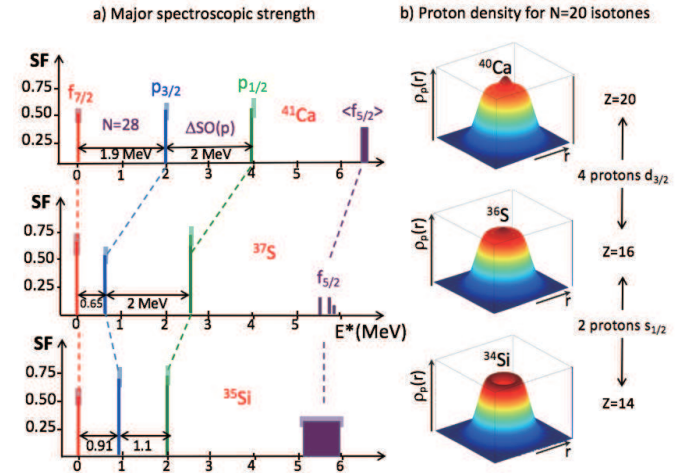


Figure 54 (a) Evidence for a reduction of the  $2p_{3/2}$ - $2p_{1/2}$  spin-orbit splitting in the  $N = 21$  isotonic chain at  $^{35}\text{Si}$ . For comparison, the spin-orbit splitting remains unchanged between  $^{41}\text{Ca}$  and  $^{37}\text{S}$ . Reprinted with permission from Burgunder *et al.* (2014). (b) Change of the proton density along the  $N = 20$  isotope line from density functional theory (relativistic mean-field with the DDME2 interaction). The vanishing proton occupation of the  $s_{1/2}$  orbital leads to a central depletion in the density that has been likened to a “bubble” (Figure by O. Sorlin, J. P. Ebran).

## 8. Tracking single-particle strengths to learn about the spin-orbit force

The spin-orbit splitting is a corner stone of the nuclear shell model. Recent work using inverse-kinematics transfer reactions (Burgunder *et al.*, 2014) and one-proton knockout reactions (Mutschler *et al.*, 2016a) on the key nucleus  $^{34}\text{Si}$ , located at the boundary of the island of inversion, explored the signatures and evolution of the spin-orbit splitting in neutron-rich nuclei.

At GANIL, in a first experiment, a stable beam of  $^{36}\text{S}$  and a radioactive  $^{34}\text{Si}$  beam impinging on a  $\text{CD}_2$  target at about 20 MeV/u were used in inverse-kinematics ( $d, p$ ) neutron-adding transfer reactions to determine the single-particle nature of states in  $^{37}\text{S}$  and  $^{35}\text{Si}$  and the associated spectroscopic strengths (Burgunder *et al.*, 2014). The projectile-like residues were tracked and identified with multi-wire proportional counters and the protons were measured in the MUST2 light charged-particle array (Pollacco *et al.*, 2005). In comparison to reaction theory, the proton angular distributions were measured (i) to assign  $\ell$  values for the transferred neutrons from their shape and (ii) to extract spectroscopic factors from their absolute scale. By tracking the location of the dominant  $2p_{1/2}$  and  $2p_{3/2}$  fragments, it was shown that the spin-orbit splitting between the  $2p_{3/2}$  and  $2p_{1/2}$  neutron orbits decreases by 25% in  $^{35}\text{Si}$  relative to the less exotic isotope  $^{37}\text{S}$ , while almost no change was observed for the neutron  $1f_{7/2} - 1f_{5/2}$  spin-orbit splitting (Figure 54

(a)) (Burgunder *et al.*, 2014). We can understand this feature as explained below. The major difference from  $^{35}\text{Si}$  to  $^{37}\text{S}$  is the occupancy of the proton  $2s_{1/2}$  orbit, which has a large effect on the  $2p_{3/2}$ - $2p_{1/2}$  splitting due to the 2b-*LS* force (see Sec. IV.A). On the other hand, the  $2s_{1/2}$  occupancy has a weak (vanishing) effect on the  $1f_{7/2}$ - $1f_{5/2}$  splitting due to the 2b-*LS* (tensor) force (see the third item of the remarks in Sec. III.B.4).

Further studies on the neutron  $2p_{3/2}$ - $2p_{1/2}$  splitting has been made recently (Kay *et al.*, 2017). Some relevant results obtained to date are summarized in Fig. 55 (a), where the centroid of the single-particle strengths presented in (Evaluated Nuclear Structure Data File (ENSDF), 2017) for  $^{37}\text{S}$  is used as the origin of the changes. The centroid for  $^{41}\text{Ca}$  has been obtained by the  $^{40}\text{Ca}(\vec{d}, p)$  reaction (Uozumi *et al.*, 1994a), where the error is estimated from the cross sections in the present work. The centroids were reported by (Kay *et al.*, 2017) for  $^{41}\text{Ca}$  and  $^{39}\text{Ar}$ , as well as an error bar for  $^{37}\text{S}$ . The error by (Kay *et al.*, 2017) for  $^{37}\text{S}$  is also shown. Figure 55 displays also the splitting taken from the energy difference between peaks of the highest strength. This is only quantity available for  $^{35}\text{Si}$ . One sees a monotonic decrease from  $^{41}\text{Ca}$  to  $^{35}\text{Si}$ , while the reduction from  $^{37}\text{S}$  overwhelms the rest. This general feature was explained above, and we now show quantitative comparisons. Figure 55 (a) includes the present splitting calculated with the filling configuration. The decrease from  $^{41}\text{Ca}$  to  $^{37}\text{S}$  is mainly due to the monopole interaction of the central and tensor forces, and their contributions are destructive with a weak net effect consistently with experiment. The subsequent change down to  $^{35}\text{Si}$  is much larger, and seems to explain the experimental trend obtained earlier (Burgunder *et al.*, 2014). The first  $1/2^-$  state of  $^{35}\text{Si}$  is weakly bound ( $\sim -0.43$  MeV) (Evaluated Nuclear Structure Data File (ENSDF), 2017), and we take this into account: Fig. 55 (b) shows the energy of the  $2p_{1/2}$  orbit calculated by a standard Woods-Saxon potential (Bohr and Mottelson, 1969), as a function of the depth parameter,  $V$ . As the depth of the potential is raised, this energy goes up almost linearly for deeply bound cases, as depicted in Fig. 55 (b). When the potential becomes shallower, a deviation from this linear dependence arises. This deviation stands basically for the additional binding energy due to a sizable tunneling effect, *i.e.*, a more extended radial wave function. When this energy is equal to the experimental energy,  $-0.43$  MeV, of the  $1/2^-$  state, the corresponding deviation is 130 keV (see the red arrow in Fig. 55 (b)). The  $2p_{3/2}$  orbit moves in parallel to the  $2p_{1/2}$  orbit for deeply bound cases, with almost no change of the  $2p_{3/2}$ - $2p_{1/2}$  splitting. Similarly to the  $2p_{1/2}$  orbit, a deviation appears, being  $\sim 70$  keV with the same depth as for the  $2p_{1/2}$  orbit at  $-0.43$  MeV. The difference is 60 keV, which appears to be a reasonable estimate of the loose-binding effect on the splitting, and we indicate the splitting including it (open circle) in Fig. 55 (a). Al-

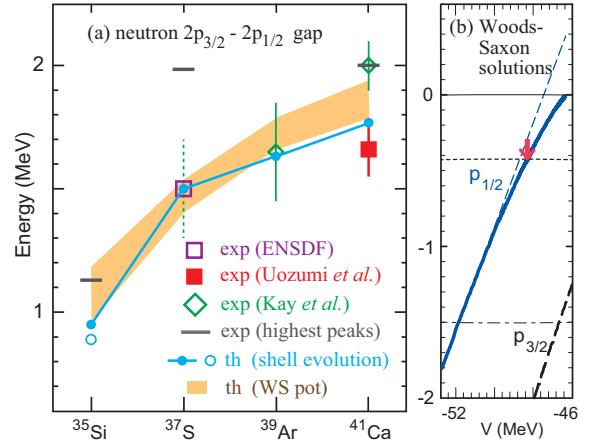


Figure 55 (a) Neutron  $2p_{3/2}$ - $2p_{1/2}$  spin-orbit splitting in the  $N = 21$  isotonic chain. The symbols denote the centroids for  $^{37}\text{S}$  (Evaluated Nuclear Structure Data File (ENSDF), 2017),  $^{39}\text{Ar}$  (Kay *et al.*, 2017) and  $^{41}\text{Ca}$  (Uozumi *et al.*, 1994a) and (Kay *et al.*, 2017). The horizontal bars imply the energy differences between relevant highest peaks (Burgunder *et al.*, 2014), (Kay *et al.*, 2017). Shell evolution predictions are shown by blue closed symbols and solid line connecting them. The loose binding effect is included in the open circle. The calculation with Woods-Saxon potential with parameters adjusted are shown by the yellowish shaded area (Kay *et al.*, 2017). (b) Neutron  $2p_{1/2}$  single-particle energy (blue solid line) obtained by a standard Woods-Saxon potential (Bohr and Mottelson, 1969) as a function of the depth parameter,  $V$ . The linear dependence of the deeply bound region is linearly extrapolated (blue dashed line). The dashed line is for the  $2p_{3/2}$  orbit. Horizontal lines denote their single-particle energies.

though this is a simple estimate, it most likely conveys the order of magnitude of the effect properly.

Thus, the major driving force of the sudden drop of the spin-orbit splitting from  $^{37}\text{S}$  to  $^{35}\text{Si}$  is indicated to be the 2b-*LS* force, with the effect an order of magnitude larger than the loose binding or, more generally the continuum. In other general cases, this competition depends on the degree of the binding, while an extreme weak binding may be required to compete against the shell evolution effect. The same splittings have been described by varying Wood-Saxon potential parameters in (Kay *et al.*, 2017), as shown in Fig. 55 (a) where the yellowish area represents the uncertainty of the parameters also. Although the two theoretical approaches yield somewhat similar trends, the underlying idea seems to be different. We emphasize that our present result is obtained with globally used nuclear forces with certain microscopic origins, explaining many data simultaneously. The same situation may be found in neutron-rich C-N-O nuclei, as discussed in sec. IV.A as well as in (Hoffman *et al.*, 2016).

Electron scattering off stable nuclei demonstrated that their central densities are saturated, as for a liquid drop,

for example. In rare isotopes at the extreme of isospin, the possibility of a depleted central density, or a “bubble” structure, has been discussed for more than 40 years. If observed, it will be of much interest. In general, central depletions will arise from the reduced occupation of low- $\ell$  single-particle orbits, as exemplified in Fig. 54 (b) for the  $N = 20$  isotones  $^{40}\text{Ca}$ ,  $^{36}\text{S}$ , and  $^{34}\text{Si}$  with calculated proton density distributions from a relativistic mean-field functional (DDME2). The central depletion in the proton density for  $^{34}\text{Si}$  is attributed to a vanishing occupancy of the proton  $2s_{1/2}$  orbital. A one-proton knockout measurement from a  $^{34}\text{Si}$  projectile beam at NSCL revealed indeed that the proton  $2s_{1/2}$  orbital in this nucleus is depleted, possibly leading to a depleted central proton density or “bubble” inside of neutron-rich  $^{34}\text{Si}$ , making this the best candidate for this phenomenon to date (Mutschler *et al.*, 2016a). For this, a beam of  $^{34}\text{Si}$  was produced by fragmentation of a  $^{48}\text{Ca}$  stable beam at NSCL’s A1900 fragment separator and guided onto a  $^9\text{Be}$  target placed in the center of GRETINA to induce the one-proton removal to  $^{33}\text{Al}$ . The projectile-like reaction residues were identified with the S800 spectrograph and the population of excited states in the knockout residue was identified and quantified with in-beam  $\gamma$ -ray spectroscopy using GRETINA. In knockout reactions, the shape of the parallel momentum distributions of the knockout residues is sensitive to the  $\ell$ -value of the removed nucleon and the partial cross sections for the population of individual final states can be used to extract spectroscopic factors in comparison to reaction theory (Hansen and Tostevin, 2003). With this approach, the cross section for the removal of an  $\ell = 0$  proton from  $^{34}\text{Si}$  was found to be only 10% of that for the proton removal from  $^{36}\text{S}$  (Mutschler *et al.*, 2016a,b). Since the cross section for the removal of protons from an orbit is proportional to the orbit’s proton occupancy, this difference in cross section was interpreted as evidence for a depleted  $2s_{1/2}$  proton orbital in  $^{34}\text{Si}$ , in striking contrast to the same orbital being fully occupied in the  $^{36}\text{S}$  isotope (Khan *et al.*, 1985; Mutschler *et al.*, 2016b). A possible central proton depletion in  $^{34}\text{Si}$  may open the door to many intriguing questions.

## 9. At the southern border: continuum and shell evolution

On the nuclear chart, two protons south of the island-of-inversion nucleus  $^{30}\text{Ne}$  lies  $^{28}\text{O}$ . The  $N = 20$  nucleus  $^{28}\text{O}$  has been suspected to be unbound with respect to neutron decay based on cross section or yield systematics established in its attempted production in the fragmentation of intermediate-energy  $^{36}\text{S}$  and  $^{40}\text{Ar}$  beams at GANIL and RIKEN, respectively (Sakurai *et al.*, 1999; Tarasov *et al.*, 1997). In fact, the neutron-rich oxygen isotopes at the southern border of the island of inversion have been a formidable testing ground for

nuclear theory since shell evolution, the effects of the neutron continuum, and many-body interactions are at play, leading to what is often referred to as the “oxygen anomaly” (Otsuka *et al.*, 2010a):  $^{24}\text{O}$  is the last bound oxygen isotope, while the fluorine isotopes with just one more proton exist out to at least mass number  $A = 31$ . Shell-model approaches (Otsuka *et al.*, 2010a; Tsukiyama *et al.*, 2015; Volya and Zelevinsky, 2005), mean-field theory (Co’ *et al.*, 2012; Erler *et al.*, 2012) and ab-initio type calculations (Bogner *et al.*, 2014; Cipollone *et al.*, 2013; Duguet and Hagen, 2012; Hagen *et al.*, 2010, 2009; Simonis *et al.*, 2016) have been made in the quest for new physics in nuclei near driplines. The incorporation of the continuum is an ongoing effort in the development of many-body approaches.

The nucleus  $^{26}\text{O}$  is a unique three-body system since it was found to be barely unbound, only able to decay by two-neutron emission with an energy of less than 20 keV (Kondo *et al.*, 2016). Two early measurements at NSCL and GSI provided the first evidence for the ground-state resonance of  $^{26}\text{O}$  at  $150^{+50}_{-150}$  keV (Lunderberg *et al.*, 2012) and 25±25 keV (Caesar *et al.*, 2013), respectively. In all measurements, the experimental scheme was very similar. The nucleus  $^{26}\text{O}$  was formed in the one-proton removal from a  $^{27}\text{F}$  projectile beam at energies around 440 MeV/u (Caesar *et al.*, 2013), ~200 MeV/u (Kondo *et al.*, 2016) or ~80 MeV/u (Lunderberg *et al.*, 2012). In kinematically complete measurements, the energy of decaying resonances was reconstructed in invariant mass spectroscopy from the momentum vectors of the two emitted neutrons and the residue in  $^{24}\text{O} + n + n$ . The highest-statistics measurement yet was performed at RIBF/RIKEN with the SAMURAI spectrometer (Kondo *et al.*, 2016; Nakamura *et al.*, 2017). For this measurement, a 1.8 g/cm<sup>2</sup> thick C target induced the one-proton knockout reaction at 201 MeV/u mid-target energy. The decay neutrons were characterized with the neutron detector array NEBULA in coincidence with the detection of  $^{24}\text{O}$  and its trajectory with the SAMURAI spectrometer (Kobayashi *et al.*, 2013). From reconstruction of the invariant mass, the ground state of  $^{26}\text{O}$  was found at only  $18 \pm 3(\text{stat}) \pm 4(\text{syst})$  keV above the two-neutron decay threshold (Kondo *et al.*, 2016). In addition, a candidate for the excited  $2_1^+$  state at  $1.28^{+0.11}_{-0.08}$  MeV was identified for the first time (see Fig. 57).

Regarding the shell evolution, one finds, in (Kondo *et al.*, 2016), “The structure of  $^{26}\text{O}$  may be influenced by shell evolution,  $nn$  correlations, and continuum effects.” It is, however, not trivial how and what “resonance” states can be created in multi-nucleon transfer heavy-ion reactions. Using Fig. 56, we shall explain schematically the relation between the shell evolution and the neutron emission after such reactions: panels (a)-(c) exhibit the doorway state in a  $(\gamma, n)$  process, while panels (d)-(f) depict a similar doorway state due to a sudden

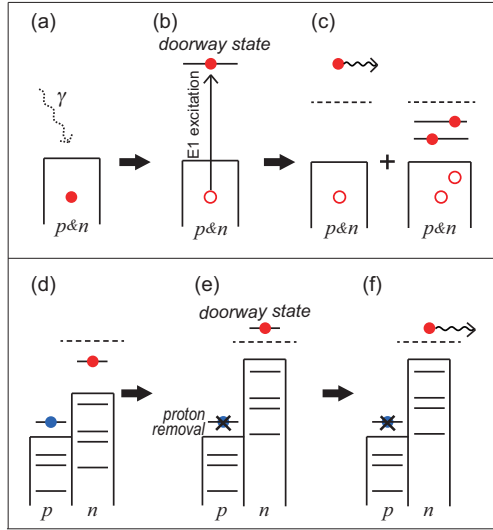


Figure 56 Schematic pictures of the doorway state for (a)-(c) E1 excitation and (d)-(f) a reaction induced by the removal of a proton. Dashed lines indicate the neutron threshold. Red filled circles indicate the neutron being discussed, while red open circles are neutron holes. Blue circles are protons, and crossed blue circles are absent after the initial impact of the reaction. From (Tsukiyama *et al.*, 2015).

removal of a proton by a transfer reaction. The removal of the proton lifts up neutron ESPEs by the amount of its monopole effect (see panel (d)). If this single-particle state is in the continuum, it becomes a doorway state as shown in panel (e). Its wave function is the same as the corresponding state before the reaction. The neutron in the doorway state goes away through one of the continuum state, with the probability given basically by the squared overlap between the doorway state and such continuum states. The shape of the energy spectrum is determined by this probability, with the peak shifted by continuum couplings. Thus, the neutron spectrum indicates the combined effect of the shell evolution and the continuum (see details in (Tsukiyama *et al.*, 2015)). Although actual situations may contain different details, the basic picture is expected to remain.

A possible long lifetime of the ground-state resonance that would allow for the term of “two-neutron radioactivity” is controversially discussed (Caesar *et al.*, 2013; Grigorenko *et al.*, 2013; Kohley *et al.*, 2013; Kondo *et al.*, 2016) and remains an interesting possibility for a new phenomenon beyond the neutron dripline.

We now turn to lighter nuclei. A new shell-model Hamiltonian for the  $p$ - $sd$  shell was developed by revising phenomenological CK (see Cohen and Kurath (1965)) and MK (see Millener and Kurath (1975)) interactions. The resulting interaction, denoted SFO hereafter (Suzuki *et al.*, 2003), contains a monopole interaction more consistent with that of the tensor force with proper reproduction of robust sign rules shown in Fig.17. This was not

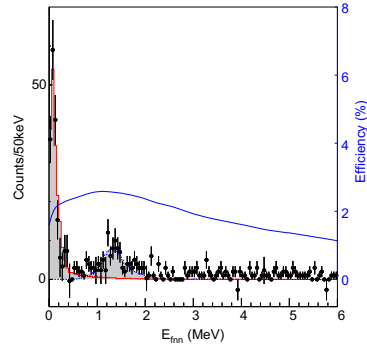


Figure 57  $^{24}\text{O}+n+n$  decay-energy spectrum of  $^{26}\text{O}$  as reconstructed from the momentum vectors of the fragment,  $^{24}\text{O}$ , and the two neutrons. The ground-state resonance at very low energy and the suggested  $2_1^+$  state at about 1.3 MeV are visible as peaks. The overall detection efficiency is superimposed (right axis). Reprinted with permission from Kondo *et al.* (2016).

necessarily the case for original CK or MK interactions. The SFO Hamiltonian then becomes capable of describing shell evolutions properly toward the dripline including the change of magic numbers; for example, from  $N=8$  to  $N=6$  near neutron dripline. The SFO Hamiltonian can also handle well, owing to the shell evolution appropriately incorporated, spin-degrees of freedom: magnetic moments of  $p$ -shell nuclei reproduced systematically, and Gamow-Teller (GT) strengths in  $^{12}\text{C}$  and  $^{14}\text{C}$  explained very well.

The SFO interaction is further expanded to be used for  $p$ - $sd$  shell nuclei. The tensor and 2b-LS components of the  $p$ - $sd$  cross-shell part are replaced by the tensor force in the  $V_{\text{MU}}$  interaction (see Sec.III.C) and the M3Y 2b-LS interaction (see texts below eq.(D4) in Appendix D), respectively. The  $sd$ -shell part of SFO is improved empirically by taking into account the effects of three-body forces (see Sec. IV.B). The resulting Hamiltonian, referred as SFO-tls (Suzuki and Otsuka, 2008), can be applied to study shell evolutions in  $N=9$  isotones,  $^{15}\text{C}$ - $^{16}\text{N}$ - $^{17}\text{O}$ , discussed in II.F.1 as well as in neutron-rich carbon isotopes.

The inversion of the relative position of the neutron  $1d_{5/2}$  and  $2s_{1/2}$  orbits from  $^{15}\text{C}$  to  $^{17}\text{O}$  is discussed in Sec. IV.A. As the SFO-tls interaction can describe it, we shall see other nuclei. Figure 58 (a) depicts neutron ESPEs of C isotopes thus obtained. While the  $2s_{1/2}$  orbit is below the  $1d_{5/2}$  orbit in  $^{12}\text{C}$ , its ESPE is raised through  $A=20$ , crossing the  $1d_{5/2}$  orbit on the way. This is because the neutron-neutron  $1p_{1/2}$ - $2s_{1/2}$  and  $1d_{5/2}$ - $2s_{1/2}$  monopole interactions are both repulsive, and push up the  $2s_{1/2}$  orbit as neutrons occupy the  $1p_{1/2}$  and  $1d_{5/2}$  orbits. This shell evolution produces the  $1/2^+$  ground state in  $^{15}\text{C}$ , and the  $3/2^+$  ground state in  $^{17}\text{C}$  which is natural with dominant neutron  $1d_{5/2}^3$  configuration. The present irregular variation of the ground-state spin can

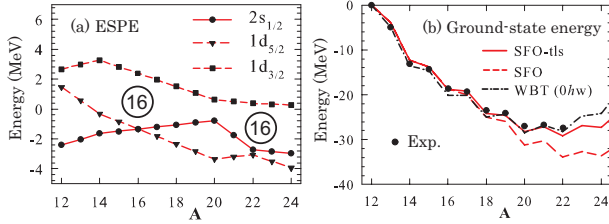


Figure 58 (a) ESPEs for neutron orbits in C isotopes obtained with SFO-tls interaction, (b) ground-state energies of C isotopes obtained with SFO-tls, SFO and WBT as well as experimental data. The twice appearance of  $N=16$  (sub-)magic gap is indicated by the circles with 16.

thus be understood. The anomalous suppression of the  $1/2^+ \rightarrow 3/2_g^+$  M1 transition in  $^{17}\text{C}$  is explained as a combined effect of the near degeneracy of the  $1d_{5/2}$  and  $2s_{1/2}$  orbits and the  $p - sd$  cross-shell interaction containing fully the tensor interaction (Suzuki and Otsuka, 2008).

We here present a rather unexpected interplay between the shell evolution and the neutron halo. Figure 58 (b) shows the ground-state energies of C isotopes relative to that of  $^{12}\text{C}$  for SFO-tls, SFO and WBT (Warburton and Brown, 1992) interactions in comparison to experiment. A repulsive neutron-neutron monopole interaction contained in the SFO-tls interaction pushes up the energy in the neutron-rich region, reproducing the experimental data, similarly to O isotopes discussed in Sec. IV.B. Figure 58 (a) shows that the  $2s_{1/2}$  orbit is rather well bound with an ESPE below -2 MeV at  $A=22$  in the filling scheme, indicative of a situation opposing a two-neutron halo. On the other hand, Fig. 58 (b) displays that  $^{22}\text{C}$  is barely bound with respect to  $^{20}\text{C}$  as far as the total binding energy is concerned. The many-body correlations in  $^{22}\text{C}$  bring about the formation of two-neutron halo, which is unlikely from the viewpoint of the mean potential. The neutron halo of  $^{22}\text{C}$  was reported experimentally in (Kobayashi *et al.*, 2012; Tanaka *et al.*, 2010; Togano *et al.*, 2016), while theoretical studies were performed with three-body models (Horiuchi *et al.*, 2006; Kucuk and Tostevin, 2014; Yamashita *et al.*, 2011). We report here a rather different approach: The extended shell-model calculation is performed not only by including usual shell-model correlations but also by taking into account the interaction between the halo neutrons taken from the low-energy limit of neutron-neutron scattering (Suzuki *et al.*, 2016a). Figure 59 depicts the radius of the two-neutron halo ( $\sim 6$ -7 fm) consistently with experiment (Togano *et al.*, 2016); the halo radius deduced from the matter radius (Togano *et al.*, 2016) appears to be  $6.74^{+0.71}_{-0.48}$  fm, which is well below the value obtained for such a small separation energy by the usual simple relation (halo radius  $> 10$  fm for  $S_{2n} < 0.3$  MeV) (Suzuki *et al.*, 2016a). Thus, the shell evolution and dynamical correlations can play crucial roles in the formation of the neutron halo.

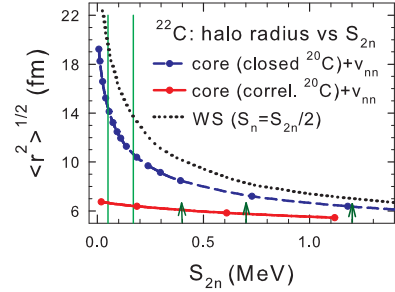


Figure 59 RMS radius of the halo neutron as a function of two-neutron separation energy,  $S_{2n}$ . Blue dashed line and filled circle indicate the result obtained with the core of the closed-shell  $^{20}\text{C}$ , while red solid line and filled circle the result with the core of the correlated  $^{20}\text{C}$ . The result obtained from WS potential ( $S_n=S_{2n}/2$ ) without  $v_{nn}$  is shown by the black dotted line. The range of  $S_{2n}$  obtained from (NNDC, 2016) is shown by green thin vertical lines. Green arrows denote values discussed in (Kobayashi *et al.*, 2012). From Suzuki *et al.* (2016a).

As  $Z$  becomes smaller, below  $Z=6$ , the neutron  $1p_{1/2}$  orbit is raised due to weakened attraction with the proton  $1p_{3/2}$  orbit, and approaches the  $2s_{1/2}$  orbit. This shell evolution leads to the vanishing of the shell closure at  $N=8$  and the SO magic number  $N=6$  becomes reinforced (see Fig. 2). The decrease of the gap between the  $1p_{1/2}$  and  $2s_{1/2}$  orbits enhances large admixture of  $sd$ -shell components in the ground states of nuclei such as  $^{12}\text{Be}$  as well as in the dripline nucleus  $^{11}\text{Li}$ .

## B. Neutron-rich $N = 28$ region

### 1. Overview

Ever since the disappearance of the  $N = 8$  and  $N = 20$  magic structure was established, the persistence or disappearance of the remaining  $j-j$  magic numbers has attracted much interest. The  $N = 28$  region below Ca has been extensively studied since the 1990s by using radioactive isotope beams [see also Sorlin and Porquet (2013)]. In Fig. 60, experimental  $2_1^+$  and  $4_1^+$  energy levels and  $B(E2)$  values measured so far in even- $A$   $^{20}\text{Ca}$ ,  $^{18}\text{Ar}$ ,  $^{16}\text{S}$ ,  $^{14}\text{Si}$  and  $^{12}\text{Mg}$  isotopes are presented. Here we provide a brief overview of those data, with a focus on recent experimental progresses.

a.  $\text{Ar}$  and  $\text{S}$  isotopes. Intermediate-energy Coulomb excitation, which was applied to  $^{32}\text{Mg}$  for the first time by Motobayashi *et al.* (1995) (see Sec. V.A.1), is a powerful tool to investigate quadrupole collectivity [see Glasmacher (1998) for an experimental review]. The  $B(E2; 0_1^+ \rightarrow 2_1^+)$  data in this region have been systematically taken at NSCL in the late 1990s, including  $^{38,40,42}\text{S}$

and  $^{44,46}\text{Ar}$  (Scheit *et al.*, 1996),  $^{44}\text{S}$  (Glasmacher *et al.*, 1997), and  $^{32,34,36,38}\text{Si}$  (Ibbotson *et al.*, 1998). One can discuss how the  $N = 28$  magic structure evolves in Ar and S isotopes by using these data. For Ca, Ti, and Cr isotope chains, the  $B(E2; 0_1^+ \rightarrow 2_1^+)$  values decrease almost by half in going from  $N = 26$  to  $N = 28$  (Raman *et al.*, 2001). This is a typical behavior when the magic number is robust. Although the Ar isotope chain well follows this trend, the  $B(E2)$  value in S isotopes does not sharply decrease as presented in Fig. 60 (c). This implies that the  $N = 28$  closure in  $^{44}\text{S}$  is weaker than in other larger- $Z$  isotopes. The weakening of the  $N = 28$  closure in S isotopes is also seen from the level structure of  $N = 27$  isotones. Dominated by the  $1f_{7/2}$  neutron hole state, the ground states of those isotopes are systematically  $7/2^-$  for the  $Z \geq 18$  even- $Z$  isotopes. On the other hand, having an isomeric  $7/2^-$  state at 0.32 MeV,  $^{43}\text{S}$  is considered to have a  $3/2^-$  ground state with strong prolate deformation (Gaudemar *et al.*, 2009). The detailed level schemes of S isotopes out to  $N=26$  were reported recently from in-beam  $\gamma$ -ray spectroscopy following fragmentation reactions (Lunderberg *et al.*, 2016).

The  $2_1^+$  energies have recently been extended to  $N = 32$  for Ar (Bhattacharyya *et al.*, 2008; Steppenbeck *et al.*, 2015) and to  $N = 30$  for S (Gade *et al.*, 2009). Note that for odd- $A$  isotopes  $\gamma$ -ray spectroscopy is performed up to  $^{47}\text{Ar}$  (Bhattacharyya *et al.*, 2008; Gade *et al.*, 2016; Winkler *et al.*, 2012) and  $^{45}\text{S}$  (Gade *et al.*, 2016). The effect of the  $N = 32$  sub-shell closure that is clearly seen in  $^{52}\text{Ca}$  is much less pronounced in  $^{50}\text{Ar}$  because of proton-neutron correlation.

b. *Si isotopes.* From the beginning of the 2000s, one- and two-nucleon knockout reactions have been utilized for studying exotic nuclei (Bazin *et al.*, 2003; Hansen and Tostevin, 2003; Yoneda *et al.*, 2001). Those reactions enable effectively populating more neutron-rich than the projectile nuclei, and have been applied to accessing exotic Si isotopes, which have two protons less than S. A signature of exotic structure in  $^{42}\text{Si}$  has been suggested by a reduced inclusive cross section of the  $^{44}\text{S} \rightarrow ^{42}\text{Si}$  reaction compared to that of  $^{46}\text{Ar} \rightarrow ^{44}\text{S}$  (Fridmann *et al.*, 2005, 2006). Later,  $\gamma$ -ray spectroscopy in  $^{42}\text{Si}$  using the same reaction has succeeded at GANIL (Bastin *et al.*, 2007). The obtained very low  $2_1^+$  energy in  $^{42}\text{Si}$  shown in Fig. 60 (a) constitutes decisive evidence for the strong breaking of the  $N = 28$  closed shell structure. Candidates for the  $4_1^+$  levels up to  $^{42}\text{Si}$  are also observed at RIKEN (Takeuchi *et al.*, 2012), and the reported  $E_x(4_1^+)$  to  $E_x(2_1^+)$  ratios are presented in Fig. 60 (b). The increasing  $E_x(4_1^+)$  to  $E_x(2_1^+)$  ratio toward the rotational limit of 3.33 indicates the development of deformation. It is noted that the onset of large deformation in  $^{42}\text{Si}$  has been suggested in terms of its  $\beta$ -decay half-life (Grévy *et al.*, 2004) and binding energy (Ju-

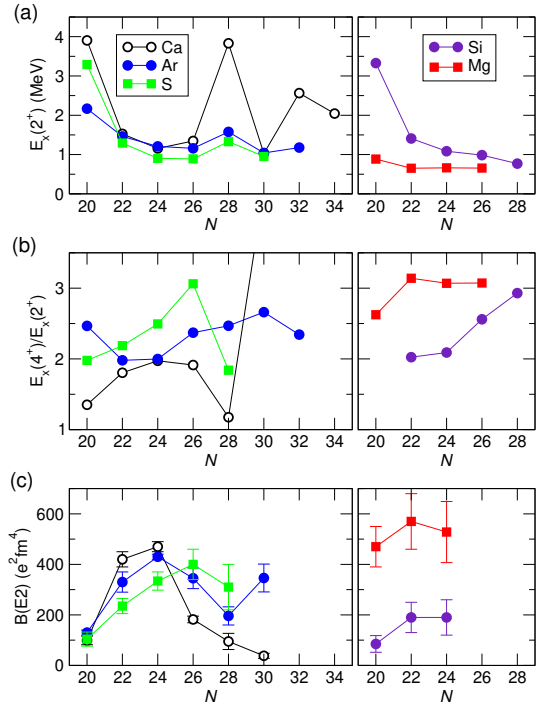


Figure 60 Experimental (a)  $2_1^+$  energy levels [ $E_x(2_1^+)$ ], (b)  $E_x(4_1^+)$  to  $E_x(2_1^+)$  ratios, and (c)  $B(E2; 0_1^+ \rightarrow 2_1^+)$  values for Ca, Ar, S, Si and Mg isotopes with  $N \geq 20$ . Data are taken from [Evaluated Nuclear Structure Data File \(ENSDF\) \(2017\)](#) unless otherwise mentioned in the text. In (b), the large value (4.40) for  $^{50}\text{Ca}$  is because the  $4_1^+$  state cannot be made in the  $(1p_{3/2}, 1p_{1/2})^2$  configuration space.

rado *et al.*, 2007), respectively. The single-proton and -neutron structure of Si isotopes approaching  $^{42}\text{Si}$  was systematically studied with one-nucleon knockout reactions reported in (Stroberg *et al.*, 2014, 2016).

c. *Mg isotopes.* One of the intriguing issues in Mg isotopes is how deformed structure in the island of inversion develops with increasing neutron number from  $N = 20$  to  $N = 28$ . The  $2_1^+$  levels in  $^{34,36,38}\text{Mg}$  are measured by Yoneda *et al.* (2001), Gade *et al.* (2007), and Doornenbal *et al.* (2013), respectively. For those nuclei, candidates for the  $4_1^+$  levels are also observed (Doornenbal *et al.*, 2013; Yoneda *et al.*, 2001). The measured  $2_1^+$  and  $4_1^+$  levels in  $^{34,36,38}\text{Mg}$  are very close to one another, indicating an extended area of deformation stretched out from the island of inversion. Although this seems to suggest that the  $N = 28$  closure is absent also in the Mg isotopes, no direct evidence is available yet.  $^{40}\text{Mg}$  is known as a bound nucleus (Baumann *et al.*, 2007), and the two-proton removal cross section for the  $^{42}\text{Si} \rightarrow ^{40}\text{Mg}$  suggests that only a few bound states exist there (Crawford *et al.*, 2014).

*d. Microscopic calculations.* Nuclear structure in this region has been studied with shell-model calculations and mean-field based calculations. Here we provide a brief overview of such theoretical activities which describe quadrupole deformed states.

For the shell-model calculation, the model space needed consists of the full *sd* shell for protons and the full *pf* shell for neutrons. The resulting dimension of the Hamiltonian matrix is typically the order of  $10^7$  in the *m*-scheme, and diagonalizing such a big matrix was not easy until the late 1990s when systematic calculations from Si to Ca were carried out by Retamosa *et al.* (1997). Concerning the effective interaction, good empirical interactions are known for the *sd* and *pf* shells, and they are usually adopted as the intra-shell interactions. Not well determined is, on the other hand, the cross-shell interaction, which connects the *sd* and the *pf* shells. As discussed in the next subsection, the cross-shell interaction plays a dominant role in shell evolution and relevant collective properties. In the work of Retamosa *et al.* (1997), the cross-shell interaction is taken from the Kahana-Lee-Scott interaction (Kahana *et al.*, 1969) with some modifications of the monopole matrix elements. Basically similar ways are chosen in their renewed interactions (Caurier *et al.*, 2004; Nowacki and Poves, 2009; Nummela *et al.*, 2001). Successfully reproducing the low  $2_1^+$  energy in  $^{42}\text{Si}$ , the latest version, named SDPF-U (Nowacki and Poves, 2009), is frequently used in this region. Another way of determining the cross-shell interaction is introduced by Utsuno *et al.* (2012a), where general knowledge of shell evolution discussed in Sec. III is utilized in the form of the  $V_{\text{MU}}$  interaction with the two-body spin-orbit force included. The resulting interaction, named SDPF-MU, is also well tested by recent experimental data. A more schematic approach called the EPQQM model is taken by Kaneko *et al.* (2011), where the two-body interaction consists of the pairing, quadrupole-quadrupole, and monopole interaction with some adjustable parameters. In spite of its simplicity, this model is able to satisfactorily reproduce experimental data over the region.

Mean-field calculations, or the nuclear energy density functionals, are also applied to this region from an early stage. The Skyrme Hartree-Fock and relativistic mean-field calculations are carried out in this region by Werner *et al.* (1996, 1994), obtaining the ground-state energies and deformation parameters from Si to Ca. Pairing correlations are more correctly treated by Terasaki *et al.* (1997) and Lalazissis *et al.* (1999) in the framework of the Skyrme Hartree-Fock-Bogoliubov (HFB) and the relativistic Hartree+Bogoliubov methods, respectively. In order to obtain energy levels and transition matrix elements, beyond-mean-field theory is needed. The generator coordinate method (GCM) is often adopted for this purpose, enabling angular-momentum projection and mixing with different quadrupole deformations. It requires much numerical computation to fully carry out

this configuration mixing, and the actual implementation is progressed gradually. Péru *et al.* (2000) use the Gaussian overlap approximation (Ring and Schuck, 1980) for calculating the overlap kernel. Rodríguez-Guzmán *et al.* (2002) perform the angular-momentum projection and the GCM calculation by using axially symmetric HFB basis states with different  $\beta$ , while particle-number projection is not included. This calculation well reproduces the  $2_1^+$  energy levels and the  $B(E2; 0_1^+ \rightarrow 2_1^+)$  values for S isotopes and  $N = 28$  isotones. More recently, Rodríguez and Egido (2011) carry out the full angular-momentum projection plus GCM calculation, using triaxially deformed HFB basis states with variation after particle-number projection. Furthermore, the most recent calculation of Egido *et al.* (2016) does not assume time-reversal symmetry in the basis states, enabling the description of the  $K = 4$  state in  $^{44}\text{S}$ . As another implementation of the GCM-based configuration mixing, the anti-symmetrized molecular dynamics (AMD) calculation is successfully applied to an odd-*A* nucleus  $^{43}\text{S}$  (Kimura *et al.*, 2013). In the work of Li *et al.* (2011), collective Hamiltonians having five coordinates, i.e., two deformation parameters  $(\beta, \gamma)$  and three Euler angles  $(\phi, \theta, \psi)$ , are constructed by using the Hartree-Bogoliubov model, and the energy levels are obtained by calculating the eigenstates of these collective Hamiltonians. As for the interaction, the usual Skyrme, Gogny or relativistic energy functionals without the tensor force are used for those calculations. There are some attempts that incorporate the tensor force, which are mentioned in the next subsection.

## 2. Shell evolution and its effect on nuclear structure

The disappearance of the  $N = 28$  closed shell structure presented in Sec. V.B.1 is strongly related to shell evolution. In this subsubsection, we discuss how proton and neutron shell structures evolve, on the basis of the analysis of experimental data using the SDPF-MU interaction (Utsuno *et al.*, 2012a). Since the cross-shell part of the SDPF-MU interaction is composed explicitly of the central, spin-orbit, and tensor forces, one can easily identify which part is the most relevant. In Figs. 61 (a) and (b), the evolution of proton shells with changing neutron number and that of neutron shells with changing proton number are presented, respectively.

Before considering individual cases, it is helpful to recall that with a proton orbital  $j^p$  filled completely, a neutron shell gap between two orbits  $j_1^n$  and  $j_2^n$  changes by the amount

$$\Delta_{j^p}(\epsilon_{j_1^n} - \epsilon_{j_2^n}) = (2j^p + 1)\{V_{pn}^m(j^p, j_1^n) - V_{pn}^m(j^p, j_2^n)\} \quad (72)$$

[see eq. (38), and eq. (41) for the example of  $^{15}\text{C}$ - $^{17}\text{O}$ ], where  $\epsilon_{j^n}$  is the ESPE of the neutron orbit  $j^n$ , and was

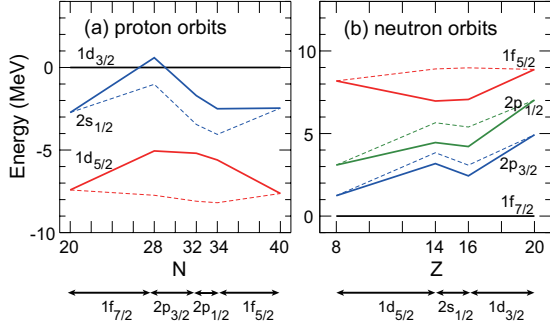


Figure 61 (a) Proton ESPEs (relative to  $1d_{3/2}$ ) for  $Z = 20$  isotopes and (b) neutron ESPEs (relative to  $1f_{7/2}$ ) for  $N = 28$  isotones calculated with the SDPF-MU interaction. The solid and dashed lines denote the ESPEs with and without the cross-shell tensor force, respectively.

expressed as  $\epsilon_j^n$  in eq. (36) with  $\hat{\cdot}$  omitted. We use this special notation in this subsubsection for the sake of convenience. Here,  $\Delta_{jp}$  stands for the difference before and after the filling of the proton orbit  $j^p$ . The value of  $\Delta_{jp}(\epsilon_{j_1^n} - \epsilon_{j_2^n})$  characterizes how the shell gap between the neutron orbits  $j_1^n$  and  $j_2^n$  evolves:  $\Delta_{jp}(\epsilon_{j_1^n} - \epsilon_{j_2^n}) = 0$  means that this shell gap is constant with  $j^p$  occupied, for instance. We should stress here that  $\Delta_{jp}(\epsilon_{j_1^n} - \epsilon_{j_2^n})$  does not depend on which inert core is assumed. Hence the  $\Delta_{jp}(\epsilon_{j_1^n} - \epsilon_{j_2^n})$  value for the  $N = 16$  core and that of the  $N = 20$  core are the same, for instance, if one uses an interaction whose strength does not depend on the mass number. This property is quite useful to examine shell evolution in a wide range of the nuclear chart, since experimentally accessible regions are rather limited.

a. *Proton spin-orbit splitting in  $^{48}\text{Ca}$ .* First we consider proton shell evolution shown in Fig. 61 (a). Starting with the  $^{40}\text{Ca}$  core, the neutron number is increased from  $N = 20$ . By filling the neutron  $1f_{7/2}$  orbit, the order of the proton  $1d_{3/2}$  and  $2s_{1/2}$  orbits is reversed due to a large negative value of  $\Delta_{1f_{7/2}}(\epsilon_{1d_{3/2}^p} - \epsilon_{2s_{1/2}^p})$ . The resulting lowest proton hole level shifts from  $1d_{3/2}$  to  $2s_{1/2}$ . This feature is observed: the  $1/2_1^+$  level lies at 2.53 MeV in  $^{39}\text{K}$ , and becomes the ground state in  $^{47}\text{K}$  with the  $3/2_1^+$  state located at 0.36 MeV. Since the lowest two levels in  $^{39}\text{K}$  and  $^{47}\text{K}$  have large spectroscopic strengths for one-proton removal, the -2.9 MeV ( $= -0.36 - 2.53$  MeV) change of the  $1/2_1^+$  level from  $N = 20$  to  $N = 28$  should be dominated by  $\Delta_{1f_{7/2}}(\epsilon_{1d_{3/2}^p} - \epsilon_{2s_{1/2}^p}) = 8\{V_{pn}^m(1f_{7/2}, 1d_{3/2}) - V_{pn}^m(1f_{7/2}, 2s_{1/2})\}$ . The SDPF-MU interaction well reproduces this sharp shift with  $\Delta_{1f_{7/2}}(\epsilon_{1d_{3/2}^p} - \epsilon_{2s_{1/2}^p}) = -3.3$  MeV. Having the  $\pi + \rho$  meson exchange potential, the tensor force in the SDPF-MU interaction accounts for -1.6 MeV, approximately half of this value. Namely, nuclear forces with-

out the tensor force produce only the half of the shift of the proton  $2s_{1/2}$  orbit, in consistent with the results of the Skyrme forces (Alex Brown, 1998; Grasso *et al.*, 2007; Wang *et al.*, 2011) and the Gogny forces [see for instance Sorlin and Porquet (2013)]. It should be noted that most of the mean-field potentials without the tensor force are designed to fit the single-particle and hole energies in  $^{48}\text{Ca}$  and that those of  $^{40}\text{Ca}$  do not agree well. The  $E_x(1/2_1^+) - E_x(3/2_1^+)$  values measured in Cl and P isotopes (Fridmann *et al.*, 2005, 2006; Gade *et al.*, 2006a), where quadrupole collectivity plays a certain role, shows a similar evolution to that of the K isotopes.

More direct information on the tensor-force driven shell evolution can be obtained from the evolution of spin-orbit splitting,  $\Delta_{1f_{7/2}}(\epsilon_{1d_{3/2}^p} - \epsilon_{1d_{5/2}^p}) = 8\{V_{pn}^m(1f_{7/2}, 1d_{3/2}) - V_{pn}^m(1f_{7/2}, 1d_{5/2})\}$ , where the effect of the central force is much smaller because of  $V_{pn}^m(1f_{7/2}, 1d_{3/2}) \approx V_{pn}^m(1f_{7/2}, 1d_{5/2})$  for the central force (see Sec. III.A). The proton spin-orbit splitting in  $^{48}\text{Ca}$  is accessible with the distribution of the proton-hole strengths measured with the  $^{48}\text{Ca}(e, e'p)^{47}\text{K}$  reaction (Kramer *et al.*, 2001). We stress here that the  $(e, e'p)$  reaction is capable of producing results more model-independent than other reactions. The measured distribution is compared to shell-model calculations using the SDPF-MU interaction with and without the tensor force in Fig. 62. The SDPF-MU interaction excellently reproduces the measurement with the proton  $1d_{5/2}$ - $1d_{3/2}$  splitting of 5.1 MeV, whereas the  $1d_{5/2}$  strengths are shifted to higher energy due to a larger spin-orbit splitting of 2.7 MeV when the tensor part of the interaction is switched off. The spin-orbit splitting in  $^{40}\text{Ca}$  is estimated to be  $\sim 6.7$  MeV on the basis of the centroid energy using the  $(d, ^3\text{He})$  reaction data (Doll *et al.*, 1976), where the  $1d_{5/2}$  strengths are highly fragmented in the  $E_x > 5$  MeV region. A precise measurement for  $^{40}\text{Ca}$  similarly to the one for  $^{48}\text{Ca}$  is of much interest. See Sorlin and Porquet (2008) for details of deducing proton-hole energies in the K isotopes from the  $(d, ^3\text{He})$  data.

b. *Reinversion of the proton  $1d_{3/2}$ - $2s_{1/2}$  ordering.* When the neutron  $2p_{3/2}$  orbit is filled beyond  $N = 28$ , the proton orbits evolve in a different way from those of  $N = 20 - 28$ . The most remarkable is that the proton  $2s_{1/2}$  orbit is pulled down again below proton  $1d_{3/2}$  due to  $\Delta_{2p_{3/2}}(\epsilon_{1d_{3/2}^n} - \epsilon_{2s_{1/2}^n}) = 4\{V_{pn}^m(2p_{3/2}, 1d_{3/2}) - V_{pn}^m(2p_{3/2}, 2s_{1/2})\} > 0$ . The tensor force leads to  $V_{pn}^m(2p_{3/2}, 1d_{3/2}) < 0$  and  $V_{pn}^m(2p_{3/2}, 2s_{1/2}) = 0$ , and the origins of this evolution are the central force and the two-body spin-orbit (2b-*LS*) force. The central force gives the strong attraction between  $2p_{3/2}$  and  $2s_{1/2}$  having  $\Delta n = 0$  and  $\Delta l = 1$ , and the 2b-*LS* force causes the attractive monopole matrix element between  $2p_{3/2}$  and  $2s_{1/2}$  but a repulsive one between  $2p_{3/2}$  and  $1d_{3/2}$  (see Appendix D

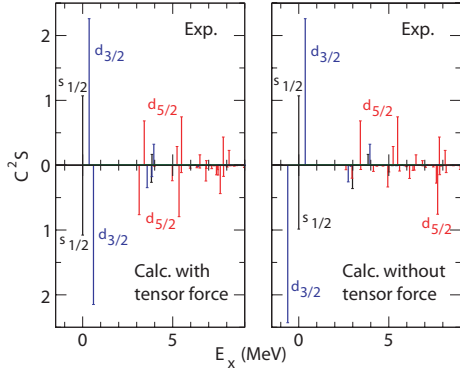


Figure 62 Distribution of proton hole strengths in  $^{48}\text{Ca}$  compared between the  $(e, e'p)$  data (Kramer *et al.*, 2001) and shell-model calculations with the SDPF-MU interaction. The left and right panels show the calculations with and without the cross-shell tensor force, respectively. The calculated overall spectroscopic factors are quenched by 0.7. From Utsuno *et al.* (2012a).

for the relevant sign rules). Since this phenomenon is caused by the usual central and  $2b$ - $LS$  forces, mean-field exhibit similar behaviors (Grasso *et al.*, 2007; Nakada *et al.*, 2013). The ground-state spin in  $^{51}\text{K}$ , which has recently been measured at ISOLDE (Papuga *et al.*, 2013), is  $3/2$ , and its  $g$  factor is very close to that of the proton  $1d_{3/2}^{-1}$  hole configuration. This measurement provides a direct evidence for the reinversion of the proton  $1d_{3/2}$ - $2s_{1/2}$  ordering realized beyond  $N = 28$ . Thus the proton  $1d_{3/2}$ - $2s_{1/2}$  gap changes in a non-monotonic way in going from  $N = 20$  to  $N = 32$ , and cannot be described by simple one-body potential models.

c. *Evolution of the  $N = 28$  shell gap.* Now we move on to neutron shell evolution shown in Fig. 61 (b), starting with the  $^{48}\text{Ca}$  core with  $Z = 20$ . First, removing the  $1d_{3/2}$  protons, we go to  $Z = 16$ . Here the  $N = 28$  shell gap, i.e., that between  $1f_{7/2}$  and  $2p_{3/2}$ , is reduced by  $\Delta_{1d_{3/2}^p}(\epsilon_{2p_{3/2}^n} - \epsilon_{1f_{7/2}^n}) = 2.5$  MeV. Although the tensor force works to some extent,  $\sim 70\%$  of this reduction comes from the central force due to the strong attraction between neutron  $1f_{7/2}$  and proton  $1d_{3/2}$  having  $\Delta n = 0$  and  $\Delta \ell = 1$ . Experimentally, the quenching of the  $N = 28$  shell gap toward smaller  $Z$  is seen in the  $^{46}\text{Ar}(d, p)^{47}\text{Ar}$  reaction in inverse kinematics performed at GANIL (Gaudefroy *et al.*, 2006), while a full strength distribution is needed to more accurately deduce the ESPE in  $^{47}\text{Ar}$  (Signoracci and Brown, 2007). The value of  $\Delta_{1d_{3/2}^p}(\epsilon_{2p_{3/2}^n} - \epsilon_{1f_{7/2}^n})$  can be probed also with the  $1f_{7/2}$  and  $2p_{3/2}$  single-neutron-like levels on top of the  $^{36}\text{S}$  and  $^{40}\text{Ca}$ , both of which can be regarded as doubly closed shell nuclei with rather high first excited levels. The observed  $3/2_1^-$  level goes down from 1.94 MeV for  $^{41}\text{Ca}$  to

0.65 MeV for  $^{37}\text{S}$ . The shell-model calculation with the SDPF-MU interaction gives  $E_x(3/2_1^-; {}^{37}\text{S}) = 0.56$  MeV, thus supporting the reduction of the  $N = 28$  gap presented in Fig. 61 (b).

Next, we consider the evolution of the  $N = 28$  gap in going from  $Z = 16$  to  $Z = 14$ , where protons in  $2s_{1/2}$  are removed. Owing to stronger attraction in the proton  $2s_{1/2}$ -neutron  $2p_{3/2}$  coupling than the one in the proton  $2s_{1/2}$ -neutron  $1f_{7/2}$  coupling, mainly due to the central force, the  $N = 28$  gap decreases with  $2s_{1/2}$  filled, or equivalently, it increases from  $Z = 16$  to  $Z = 14$ . This is consistent with the evolution of the  $3/2_1^-$  levels from  $^{37}\text{S}$  (0.65 MeV) to  $^{35}\text{Si}$  [0.91 MeV (Burgunder *et al.*, 2014; Nummela *et al.*, 2001; Stroberg *et al.*, 2014)] and the one from  $^{33}\text{S}$  (0.29 MeV) to  $^{31}\text{Si}$  (0.40 MeV). The  $N = 28$  shell gap again reduces below  $Z = 14$ . Its reduction from  $Z = 14$  to  $Z = 10$  is estimated to be  $\frac{4}{6}\Delta_{1d_{5/2}^p}(\epsilon_{2p_{3/2}^n} - \epsilon_{1f_{7/2}^n}) = 4\{V_{pn}^m(1d_{5/2}, 2p_{3/2}) - V_{pn}^m(1d_{5/2}, 1f_{7/2})\} = 1.3$  MeV. A strong proton  $1d_{5/2}$ -neutron  $1f_{7/2}$  attraction in the central force compensates the opposite contribution from the tensor force. Experimentally, with large spectroscopic strengths on top of the  $N = 16$  core,  $E_x(3/2_1^-) - E_x(7/2_1^-)$  decreases from 0.40 MeV in  $^{31}\text{Si}$  to  $-0.98$  MeV in  $^{27}\text{Ne}$ . This 1.38 MeV change is very close to the reduction of the  $N = 28$  gap thus estimated and to the one obtained with the actual shell-model calculation, 1.42 MeV.

The evolution of the  $N = 28$  shell gap presented in Fig. 61 (b) thus reasonably accounts for experimental data from  $Z = 10$  to  $Z = 20$ . Since both  $1f_{7/2}$  and  $2p_{3/2}$  are  $j>$  orbitals, the effect of the tensor force on the evolution of the  $N = 28$  shell gap is modest, and the central force plays the dominant role in its reduction with decreasing proton number.

d. *Evolution of the  $N = 32$  and  $N = 34$  shell gaps.* The evolution of the  $N = 32$  shell gap from  $Z = 16$  to  $Z = 14$  provides a unique opportunity to probe shell evolution due to the two-body spin-orbit force, because the central and tensor contributions to  $\Delta_{2s_{1/2}^p}(\epsilon_{2p_{1/2}^n} - \epsilon_{2p_{3/2}^n}) = 2\{V_{pn}^m(2s_{1/2}, 2p_{1/2}) - V_{pn}^m(2s_{1/2}, 2p_{3/2})\}$  vanish. In a recent  $(d, p)$  reaction measurement (Burgunder *et al.*, 2014) strong  $l = 1$  strengths are observed at 0.91 MeV and 2.04 MeV in  $^{35}\text{Si}$ , as presented in Fig. 54. They are considered as  $3/2^-$  and  $1/2^-$  levels, respectively. Since the corresponding states in  $^{37}\text{S}$  are located at 0.65 MeV and 2.64 MeV, respectively, the value of  $E_x(1/2^-) - E_x(3/2^-)$  decreases by 0.86 MeV. This value is close to that of the shell-model calculation with the SDPF-MU interaction, 0.76 MeV, and is somewhat larger than the change in the ESPEs, 0.50 MeV. Interestingly, a similar change of  $E_x(1/2^-) - E_x(3/2^-)$  is observed for the  $N = 17$  isotones of  $^{31}\text{Si}$  and  $^{33}\text{S}$ . The measured (Evaluated Nuclear Structure Data File (ENSDF), 2017; Piskoř *et al.*, 2000)

changes of  $E_x(1/2^-) - E_x(3/2^-)$  from  $^{33}\text{S}$  to  $^{31}\text{Si}$  is 0.74 MeV, in good agreement with the calculated value of 0.74 MeV using the SDPF-MU interaction. This leads to a consistent understanding of the evolution of the  $1p_{3/2}$ - $1p_{1/2}$  splitting between the  $N = 16$  and  $N = 20$  cores. Although the  $N = 32$  shell gap is thus reduced in Si isotopes from S isotopes, it is predicted that the  $2_1^+$  level in the  $N = 32$  nucleus  $^{46}\text{Si}$  is higher than that of  $^{48}\text{S}$  (Utsuno *et al.*, 2015a) because of a relatively large  $Z = 14$  sub-shell gap.

It is an interesting question whether the  $N = 34$  magic number observed for  $^{54}\text{Ca}$  (see Sec. III.D.4) persists or disappears below  $Z = 20$ . The SDPF-MU interaction suggests that this gap enlarges in going from  $Z = 20$  to  $Z = 16$  (Steppenbeck *et al.*, 2015; Utsuno *et al.*, 2015a) with  $\Delta_{1d_{3/2}^p}(\epsilon_{1f_{5/2}^n} - \epsilon_{2p_{1/2}^n}) = 4\{V_{pn}^m(1d_{3/2}, 1f_{5/2}) - V_{pn}^m(1d_{3/2}, 2p_{1/2})\} = -1.0$  MeV which is dominated by the central force. Since the central force of the SDPF-MU interaction gives a good  $V_{pn}^m(1d, 1f) - V_{pn}^m(1d, 2p)$  value as confirmed by the evolution of the  $N = 28$  shell gap, the negative  $\Delta_{1d_{3/2}^p}(\epsilon_{1f_{5/2}^n} - \epsilon_{2p_{1/2}^n})$  seems reasonable. Although no quantitative evaluation of this value is available, experimental neutron  $1f_{5/2}$  strength distributions shown in Fig. 54 appear consistent with the prediction. At least a sharp decrease of the  $N = 34$  shell gap toward smaller  $Z$  is not suggested. The actual shell-model calculation shows that the effect of the enlarged  $N = 34$  shell gap is seen in the  $2_1^+$  levels of  $N = 34$  isotones (Steppenbeck *et al.*, 2015; Utsuno *et al.*, 2015a); in particular,  $^{48}\text{Si}$  is a doubly-magic nucleus.

e. *Impact on collectivity.* As discussed already, the  $N = 28$  shell gap is reduced from  $Z = 20$  to  $Z = 16$ , and the experimental evidence is found in the evolution of the value of  $E_x(7/2^-) - E_x(3/2^-)$  in  $N = 21$  isotones. This works to weaken the  $N = 28$  closed-shell structure in the  $N = 28$  isotones below  $^{48}\text{Ca}$ . The  $1f_{7/2}$  and  $2p_{3/2}$  orbits are connected by  $\Delta j = 2$ , and the increase of their coupling through near degeneracy enhances quadrupole collectivity as observed in  $^{44}\text{S}$  and  $^{42}\text{Si}$ . This situation is sometimes expressed in terms of the quasi-SU(3) symmetry (Caurier *et al.*, 2005).

Besides the quenching of the  $N = 28$  shell gap, proton shell structure plays an essential role in the enhanced quadrupole collectivity via the interplay between protons and neutrons. Concerning the S isotopes, the  $Z = 16$  shell gap that is rather stable in the vicinity of  $^{36}\text{S}$  is completely washed out around  $N = 28$ , as already discussed for the K isotopes. Note that the systematic degeneracy of the  $3/2_1^+$  and  $1/2_1^+$  levels is observed in K, Cl and P isotopes (Gade *et al.*, 2006a). As pointed out by Cottle and Kemper (1998), this causes more quadrupole collectivity through the mixing between proton  $1d_{3/2}$  and  $2s_{1/2}$  orbits.

In the Ar isotope chain, it appears that the  $N = 28$  closure is well conserved in terms of the relatively high  $2_1^+$  level and the low  $B(E2; 0_1^+ \rightarrow 2_1^+)$  value in  $^{46}\text{Ar}$ . However, when comparing to Ti isotopes, one can find a fingerprint of the weakening of the  $N = 28$  closure. While Ti and Ar isotopes have the same number of valence protons (two particles vs. two holes), the Ti isotopes have larger quadrupole collectivity because of larger proton-neutron overlap through occupation of the same valence shell. Nevertheless, the breaking of the  $N = 28$  shell closure is more significant in  $^{46}\text{Ar}$  than in  $^{50}\text{Ti}$ : the one-neutron removal spectroscopic factors from the ground states of  $^{46}\text{Ar}$  and  $^{50}\text{Ti}$  to the  $3/2_1^-$  level in  $^{45}\text{Ar}$  and  $^{49}\text{Ti}$  are 0.51(6) (Lu *et al.*, 2013) and 0.13 (or 0.14) (Evaluated Nuclear Structure Data File (ENSDF), 2017), respectively, suggesting that the neutron  $2p_{3/2}$  occupation probability is about four times larger in  $^{46}\text{Ar}$  than in  $^{50}\text{Ti}$ . Note that this is consistent with the neutron adding  $(2J + 1)C^2S$  value obtained from  $^{46}\text{Ar}(d, p)^{47}\text{Ar}$  that amounts to 2.44(20) (Gauderoy *et al.*, 2006), indicating that about one neutron already occupies the  $2p_{3/2}$  in  $^{46}\text{Ar}$ . From this point of view, the observed small  $B(E2; 0_1^+ \rightarrow 2_1^+)$  may be a puzzle. All the shell-model calculations in the proton  $sd$  + neutron  $pf$  model space available (Caurier *et al.*, 2004; Kaneko *et al.*, 2011; Nowacki and Poves, 2009; Retamosa *et al.*, 1997; Utsuno *et al.*, 2012a) overestimate the  $B(E2; 0_1^+ \rightarrow 2_1^+)$  by a factor of two. Experimentally, intermediate-energy Coulomb excitation has been performed several times (Calinescu *et al.*, 2016; Gade *et al.*, 2003; Scheit *et al.*, 1996), consistently obtaining small  $B(E2)$  values. A recent lifetime measurement (Mengoni *et al.*, 2010) reports a larger  $B(E2; 0_1^+ \rightarrow 2_1^+) = 570_{-160}^{+335} e^2\text{fm}^4$ , but its uncertainty is still large. The proton and neutron deformation lengths in  $^{46}\text{Ar}$  extracted from the  $(p, p')$  reaction are close (Riley *et al.*, 2005), suggesting a deviation from the typical  $N = 28$  isotopes having a good neutron closed shell. The discrepancy of the  $B(E2)$  values between the shell model and the intermediate-energy Coulomb excitation is reported also for  $^{47}\text{Ar}$  (Winkler *et al.*, 2012). In this way, the structure of Ar isotopes around  $N = 28$  is not fully understood.

The neutron-rich S isotopes around  $N = 28$  exhibit quite a unique nuclear structure, which draws much experimental and theoretical attention. The  $0_2^+$  level in  $^{44}\text{S}$  is located at as low as 1365 keV (Force *et al.*, 2010; Grévy *et al.*, 2005), and the  $E2$  decay rate from  $7/2_1^-$  to  $3/2_1^-$  in  $^{43}\text{S}$  is strongly hindered (Gauderoy *et al.*, 2009). Although those states were initially interpreted as spherical-deformed shape coexistence, this idea seems to contradict a relatively large amplitude of the quadrupole moment in the  $7/2_1^-$  level of  $^{43}\text{S}$  measured later (Chevrier *et al.*, 2012). Moreover, the properties of the  $4^+$  level in  $^{44}\text{S}$  measured by Santiago-Gonzalez *et al.* (2011) are very strange. First, the  $E_x(4^+) - E_x(2_1^+)$  ratio sharply drops from  $N = 26$  to  $N = 28$  in spite of similar quadrupole

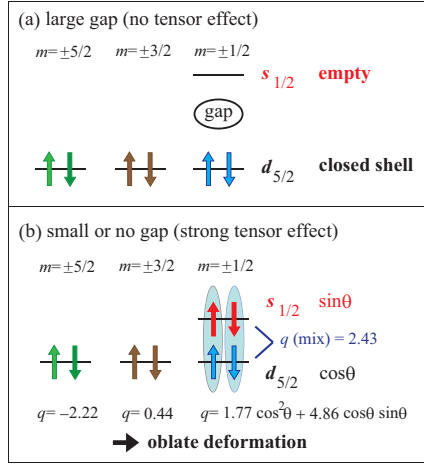


Figure 63 Schematic illustration of the mechanism of oblate deformation in  $^{42}\text{Si}$  with a reduced  $Z = 14$  shell gap due to the tensor force. From [Utsuno \*et al.\* \(2012a\)](#).

collectivity as shown in Fig. 60 (b). Second, its  $E2$  decay probability to the  $2_1^+$  level is much smaller than that of typical yrast levels, as confirmed by a recent lifetime measurement ([Parker \*et al.\*, 2017](#)). These exotic characteristics in S isotopes are analyzed by introducing the variation after angular-momentum projection into the shell model ([Utsuno \*et al.\*, 2015b](#)). The calculation shows that the  $4_1^+$  level in  $^{44}\text{S}$  is dominated by the  $K = 4$  two-quasiparticle configuration  $7/2[303] \otimes 1/2[321]$  and that the  $3/2^-$  and the  $7/2^-$  levels in  $^{43}\text{S}$  are dominated by the one-quasiparticle configurations  $1/2[321]$  and  $7/2[303]$ , respectively [see also [Kimura \*et al.\* \(2013\)](#) for  $^{43}\text{S}$ ]. The  $4^+$  level of the  $K = 0$  ground-state band is predicted to be higher than the  $K = 4$  state. The  $K = 4$  interpretation of the  $4_1^+$  level is consistent with a recent beyond mean-field calculation of [Egido \*et al.\* \(2016\)](#), who have introduced basis states with broken time-reversal symmetry. The low  $0_2^+$  level in  $^{44}\text{S}$  is brought by the mixing of two  $K = 0$  quasiparticle configurations  $(7/2[303])^2$  and  $(1/2[321])^2$ . Thus the structure of S isotopes around  $N = 28$  is basically understood in terms of deformed shell structure, which is developed by proton ( $Z = 16$ ) and neutron ( $N = 28$ ) shell evolutions due to the central and tensor forces.

In Si isotopes, the experimental  $2_1^+$  energies and the  $E_x(4_1^+)/E_x(2_1^+)$  values presented in Fig. 60 indicate that quadrupole collectivity keeps enhancing until  $N = 28$ . Shell-model calculations show that the structure of  $^{42}\text{Si}$  is quite sensitive to the effective interaction used ([Bastin \*et al.\*, 2007](#); [Caurier \*et al.\*, 2004](#); [Kaneko \*et al.\*, 2011](#); [Nowacki and Poves, 2009](#); [Retamosa \*et al.\*, 1997](#); [Utsuno \*et al.\*, 2012a](#)), ranging from doubly magic structure to strong deformation. It is pointed out that the proton  $1d_{5/2}$ - $1d_{3/2}$  splitting plays an important role in obtaining large deformation in  $^{42}\text{Si}$  ([Bastin \*et al.\*, 2007](#)). It is also

shown that the inclusion of the tensor force in the cross-shell interaction drives  $^{42}\text{Si}$  oblate by reducing the proton  $1d_{5/2}$ - $1d_{3/2}$  gap ([Otsuka \*et al.\*, 2008](#); [Utsuno \*et al.\*, 2006](#)). Note that the same result is obtained with the mean-field calculation of ([Suzuki \*et al.\*, 2016b](#)). Now we provide a comprehensive picture as to how proton shell structure is sensitive to deformation in Si isotopes, following the argument of [Utsuno \*et al.\* \(2012a\)](#). In Fig. 63 (a) and (b), two extreme cases of large and very small  $Z = 14$  shell gaps are considered, respectively. Here we assume a schematic Hamiltonian  $H = \epsilon_{2s_{1/2}} \hat{n}_{2s_{1/2}} - \kappa Q \cdot Q$ , where  $\epsilon_{2s_{1/2}}$  stands for the  $Z = 14$  shell gap, and consider a Slater determinant as a many-body state. If the  $Z = 14$  gap is large enough to overwhelm the  $Q \cdot Q$  term, all the valence protons occupy the  $1d_{5/2}$  orbital and form a spherical shape. On the other hand, when the  $Z = 14$  shell gap is smaller and the  $Q \cdot Q$  term becomes dominant, the proton wave function is made so that the absolute value of  $Q = \sum_{i:\text{occupied}} q_i = \sum_{k:\text{unoccupied}} (-q_k)$  is the largest, where  $q_i$  denotes the quadrupole moment of the nucleon  $i$ . Taking axially symmetric shapes into account, we consider the degrees of mixing between two  $|m| = 1/2$  orbitals originating from  $1d_{5/2}$  and  $2s_{1/2}$ , where the  $1d_{5/2}$  amplitude is represented by  $\cos \theta$ . Under this situation, the  $m = 1/2$  orbital with  $\cos \theta = 0.82$  takes the largest  $|q|$  value with  $q = 3.47$ . It is clear that a positive value is favored because of the  $1.77 \cos^2 \theta > 0$  term. Having two proton holes in this orbital, the resulting optimum  $Q$  value becomes  $Q = 2 \times (-3.47) = -6.94$ , thus leading to an oblate shape. A similar argument can be applied to the neutron side by assuming near degenerate  $1f_{7/2}$  and  $2p_{3/2}$  orbitals, where the  $|m| = 1/2$  and  $|m| = 3/2$  orbitals can be mixed. The  $N = 28$  case corresponds to eight neutron particles, i.e., four neutron holes because the total number of nucleons that can occupy  $1f_{7/2}$  and  $2p_{3/2}$  is 12. When the hole levels occupy the  $m = \pm 1/2$  and  $m = \pm 3/2$  orbitals with  $q > 0$ , the total  $|Q|$  value becomes the largest, where eight neutrons form an oblate shape. Hence the  $^{42}\text{Si}$  nucleus becomes oblate due to the strong proton-neutron  $Q_\pi \cdot Q_\nu$  force which favors coherent proton-neutron deformation. Since this deformation is triggered by the reduction of the  $Z = 14$  and  $N = 28$  shell gaps due to the tensor force, it is called tensor-force-driven Jahn-Teller effect in [Utsuno \*et al.\* \(2012a\)](#). The present picture accounts for the reason why the largest deformation is realized at  $N = 28$  in Si isotopes. Among the six orbitals that are composed of  $1f_{7/2}$  and  $2p_{3/2}$  (one  $|m| = 7/2$ , one  $|m| = 5/2$ , two  $|m| = 3/2$ , and two  $|m| = 1/2$ ), two orbitals with  $|m| = 3/2$  and  $|m| = 1/2$  have prolate shapes and the others have oblate shapes. Thus the largest prolate deformation is achieved for the four-neutron configuration which occupies the prolate  $|m| = 3/2$  and  $|m| = 1/2$  levels. This means that the largest oblate deformation is realized for the eight-neutron configuration. Note that this property is also obtained from the quasi-SU(3) scheme

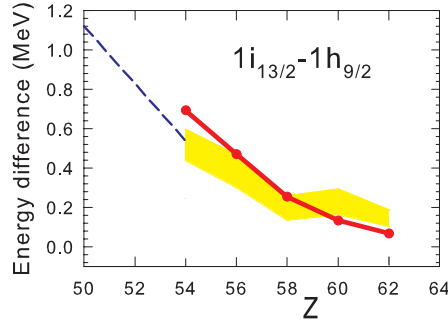


Figure 64 Experimental energy difference (filled circles) in the centroids of neutron  $i_{13/2}$  and  $h_{9/2}$  orbits compared to the tensor-force prediction (yellow band), where the band reflects the uncertainties in the proton  $1g_{7/2}$  and  $2d_{5/2}$  occupancies. Dashed line is the tensor-force prediction for the lowest  $13/2^+$  and  $9/2^-$  states obtained with the 85% (15%) proton  $1g_{7/2}$  ( $2d_{5/2}$ ) occupancy extracted in (Wildenthal *et al.*, 1971). Based on Kay *et al.* (2011).

with a set of completely degenerate  $\Delta j = 2$  orbitals (Caurier *et al.*, 2005).

For the Mg isotopes, most of the microscopic calculations predict that the  $N = 28$  closure is completely broken with large prolate deformation. This is a natural consequence of the quenched  $N = 28$  shell gap in Mg isotopes (see Fig. 61) and the proton number 12 which favors deformation. Now we consider deformation in  $^{40}\text{Mg}$  in terms of the single-particle energies and the  $Q \cdot Q$  force in a similar way to  $^{42}\text{Si}$ . As discussed above, the neutron number 28 favors oblate deformation, but can also produce relatively large prolate deformation. On the proton side, since prolate and oblate deformations take the same  $|Q|$  values, these shapes have the same energy if the proton  $1d_{5/2}$  and  $2s_{1/2}$  orbits are completely degenerate. In the actual situation, however, the proton  $1d_{5/2}$  orbit is lower and hence the prolate deformation is more favored because the prolate configuration contains more  $1d_{5/2}$  protons than the oblate one. The realistic calculations thus predict a prolate ground state in  $^{40}\text{Mg}$ , whereas prolate-oblate shape coexistence may occur. The shell-model calculation with the SDPF-MU interaction indicates the occurrence of prolate-oblate shape coexistence in  $^{40}\text{Mg}$  from its  $0^+$  and  $2^+$  energy levels and  $E2$  matrix elements, as well as from the so-called T-plot analysis in the Monte Carlo shell model calculation (Otsuka and Tsunoda, 2016; Tsunoda *et al.*, 2014b).

### C. Other cases in heavy nuclei

The shell evolution can be found in many cases with heavy nuclei.

An example is the separation between the neutron  $1i_{13/2}$  and  $1h_{9/2}$  orbits in  $N = 83$  isotones with even  $Z = 54\text{--}62$  (Kay *et al.*, 2008, 2011). The centroids of the

strengths of  $1i_{13/2}$  and  $1h_{9/2}$  single-neutron states were obtained by using spectroscopic factors measured by  $(\alpha, ^3\text{He})$  and  $(d, p)$  reactions. As proton  $1g_{7/2}$  ( $2d_{5/2}$ ) orbit is occupied for larger  $Z$ , attraction and repulsion (repulsion and attraction) increase for neutron  $i_{13/2}$  and  $h_{9/2}$  orbits, respectively, due to the tensor interaction (see Fig. 17 for instance)). Thus, the separation between the  $1i_{13/2}$  and  $1h_{9/2}$  states decreases (increases) as the  $1g_{7/2}$  ( $2d_{5/2}$ ) orbit is occupied by more protons. Figure 64 indicates that the observed energy difference of the centroids of  $13/2^+$  and  $9/2^-$  states can be compared well to the calculation with the tensor interaction, by using proton occupation numbers of  $1g_{7/2}$  and  $2d_{5/2}$  orbits deduced from one-nucleon transfer reactions (Wildenthal *et al.*, 1971).

Another example is the  $Z = 64$  gap, which is seen at  $N = 82$  (Ogawa *et al.*, 1978) but disappears as  $N$  increases (see, *e.g.*, (Casten *et al.*, 1981)). This gap is washed away for  $N > 82$ , largely because neutrons in  $2f_{7/2}$  orbits decreases the proton  $2d_{5/2}$ - $2d_{3/2}$  splitting (see Fig. 17 for instance)). Many similar cases have been and will be found in other isotopic and isotonic chains, for instance, the  $N = 40$  gap is influenced by proton  $1f_{7/2}$  occupancy (as a recent example, see (Santamaría *et al.*, 2015)).

## VI. SHELL EVOLUTION AND NUCLEAR SHAPE

The shell evolution occurs due to the monopole interaction, and characteristic effects can be connected to some basic nature of the  $NN$  interaction. Those effects are induced by the changes of the occupation numbers of certain single-particle orbits, which originate in changes of  $Z$  and/or  $N$ . Such changes mean that the nucleus moves on the nuclear (Segrè) chart. This case corresponds to the upper part of Fig. 21. The same monopole interactions can produce another type of significant effects by changing occupation numbers with particle-hole excitations, as shown in the lower part of Fig. 21. This is called *Type II Shell Evolution*, and the shell evolution discussed so far may be called *Type I Shell Evolution*, if one has to distinguish these two (Otsuka and Tsunoda, 2016).

Such particle-hole excitations can drive strong deformation, and deformation may enhance relevant particle-hole excitations. This self-consistent and often non-linear process is the most important outcome of Type II Shell Evolution (Otsuka and Tsunoda, 2016). Type II Shell Evolution was first discussed for the shape coexistence in Ni isotopes involving massive particle-hole excitations to the neutron  $1g_{9/2}$  orbit (Otsuka and Tsunoda, 2016; Tsunoda *et al.*, 2014b) followed by (Leoni *et al.*, 2017; Morales *et al.*, 2017; Prokop *et al.*, 2015). A recent prominent example is the quantum phase transition driven by massive particle-hole excitations to the proton  $1g_{9/2}$  orbit in Zr isotopes (Togashi *et al.*, 2016), predicting the abrupt change at the right place (Kremer *et al.*, 2016;

Paul *et al.*, 2017; Régis *et al.*, 2017). There are many other cases that could be discussed but we will not do that here, as this subject deserves its own review article.

## VII. SUMMARY AND REMARKS

This article presents a review of the structure of exotic nuclei mainly from the viewpoint of the shell evolution due to nuclear forces. This shell evolution is driven by the monopole interaction, which is a characteristic part of the nuclear forces in nuclei.

Although the monopole interaction has been discussed in many ways since 1964, we presented its possible definition in Sec. II for general open-shell nuclei without referring to any closed-shell properties. The relations to other approaches and simple applications are worked out. It may be worth commenting that the essence of the present definition is an assembly of two-body diagonal operators, and this idea can be extended to other many-body systems. In the case of atomic nuclei, the rotational invariance is imposed as a symmetry constraint, restricting this object of diagonal two-body terms being a “monopole” operator in the angular momentum algebra. The resulting monopole interaction contains somewhat complicated additional terms of charge exchange nature besides the simple terms composed only of the particle-number operators for individual orbits. This additional term is shown, in Sec. II, to be approximated by renormalizing the simple terms, where the approximation becomes exact at closed shells. Thus, the monopole interaction can be formulated entirely in open-shell systems, while all closed-shell properties fulfill the known features. Note that the original form before this approximation may be of interest for  $N=Z$  nuclei.

The monopole interactions of the central, tensor, 2-body spin-orbit and three-nucleon forces produce different characteristic features in the variations of the ESPEs (*i.e.*, shell evolution) as illustrated in Sec. III and Sec. IV. The tensor and 2-body spin-orbit forces provide unique and notable effects because of their spin dependences. Many of the underlying properties of these many-body effects were clarified rather recently or even only in this article, while these forces have been known for several decades. The central force basically senses similarities of radial single-particle wave functions. Some aspects of these effects, especially from the central force, have been the subjects of nuclear physics since its early days as mentioned above for the monopole interaction, and those effects are indeed discussed throughout the text (see also the reviews (Sorlin and Porquet, 2008, 2013)). The origin and derivation of nuclear forces, particularly the central force, is being studied in modern approaches, although their primary features relevant to the shell evolution are known and consistent with experiment. It is an open question how the shell evolution appears in the

presence of other sizable correlations such as surface vibration. The three-nucleon force has been studied for decades, but its general relevance to the structure and existence of exotic nuclei is a rather new topic. This review article mainly discussed the Fujita-Miyazawa three-nucleon force and its direct link to the shell evolution and dripline. This field is being developed, and more outcomes and scope can be expected.

The shell evolution due to nuclear forces is evaluated throughout this article mainly in terms of the  $V_{MU}$  interaction and the 2-body spin-orbit force in the M3Y interaction. These are given in simple analytic forms, and provide us with a consistent assessment in a unified way. Although these interactions can be improved individually, we put more emphasis on the global trends. The tensor force shows the property of the renormalization persistency (see Sec. III.E).

The effects of the shell evolution have been seen in actual nuclei experimentally as shown throughout this review, particularly in Sec. V, providing underlying mechanisms for differentiating exotic nuclei from stable ones all over the Segrè (or nuclear) chart. A wide variety of properties and phenomena have been discussed: they start from arising new magic numbers, 16, 32, 34, ..., and vanishing traditional ones, 8, 20, 28, ..., while including various consequences of the shell evolution, *e.g.* deformed intruder states such as in the island of inversion, crossings or repelling of single-particle states against the conventional picture, shape transitions associated with a changing magic gap (*e.g.*  $N=28$ ), interplay of the shell evolution with the continuum or weakly bound states, *etc.*

The driving forces for the shell evolution are shown to play a crucial role also for nuclear shapes by a mechanism analogous to the shell evolution, which occurs inside a nucleus associated with massive particle-hole excitations. This Type II shell evolution is briefly discussed in Sec. VI, while a review will remain a project for the future.

As the shell evolution, including Type II, will keep unveiling static and dynamic features of exotic nuclei not expected within the conventional view, there will be intriguing, diverse and glorious frontiers emerging in many ways in nuclear structure physics.

## VIII. ACKNOWLEDGMENTS

Useful discussions with Drs. J.P. Schiffer, B. Kay, A. Poves, F. Nowacki, H. Grawe, M. Gorska and P. Ring are acknowledged. T.O. thanks particularly Drs. Y. Tsunoda and J. Menendez for valuable discussions on the monopole interaction. He is grateful also to Drs. M. Honma, R. Fujimoto, T. Matsuo, D. Abe and K. Tsukiyama, and Profs. Y. Akaishi and A. Schwenk for

many relevant productive collaborations. He acknowledges Dr. N. Tsunoda for private communications and a related figure besides fruitful collaborations. This work was supported in part by the HPCI Strategic Program (The origin of matter and the universe) and “Priority Issue on Post-K computer” (Elucidation of the Fundamental Laws and Evolution of the Universe) from MEXT and JICFuS (hp140210, hp150224, hp160211, hp170230), and is a part of the RIKEN-CNS joint research project on large-scale nuclear-structure calculations. T.O. acknowledges support in part by the Grant-in-Aids for Scientific Research (A) 20244022 of the JSPS. A.G. acknowledges support from the US National Science Foundation under Grant No. PHY-1102511 and PHY-1565546 (NSCL). T.S. acknowledges support in part by the Grant-in-Aids for Scientific Research under Grant No. JP15K05090 of the JSPS. Y.U. acknowledges support in part by the Grant-in-Aids for Scientific Research under Grant No. JP15K05094 of the JSPS.

## Appendix A: Proton-neutron monopole interaction

The basic idea of the proton-neutron monopole interaction remains the same as in the case for two neutrons. A proton in the state  $j, m$  and a neutron in  $j', m'$  are considered. We first treat the proton and the neutron as different kinds of fermions with no mutual relation such as the isospin. A two-body state is expressed as

$$|\pi(j, m) \otimes \nu(j', m')\rangle, \quad (\text{A1})$$

similarly to eq. (2). We use, when appropriate, indices  $\pi$  and  $\nu$  for quantities related to protons and neutrons, respectively. Note that the proton state comes first and the neutron state second. The state  $(j, m)$  is abbreviated as  $m$  hereafter for brevity, except for the cases that explicit expressions are needed or would help. The proton-neutron interaction can be written as

$$\hat{v}_{pn} = \Sigma_{\pi m_1, \nu m_2, \pi m'_1, \nu m'_2} (\pi m_1 \otimes \nu m_2 | \hat{v}_{pn} | \pi m'_1 \otimes \nu m'_2) a_{\pi m_1}^\dagger a_{\nu m_2}^\dagger a_{\nu m'_2} a_{\pi m'_1}. \quad (\text{A2})$$

Here,  $(\pi m_1 \otimes \nu m_2 | \hat{v}_{pn} | \pi m'_1 \otimes \nu m'_2)$  denotes two-body matrix element.

We shall show that the monopole matrix element for the proton-neutron system has a different feature from that for the neutron-neutron system, because the states comprised of a proton and a neutron can be decomposed into two groups according to the symmetry with respect to the exchange between proton and neutron. The symmetric state is defined by

$$|\pi m; \nu m' : \mathcal{S}\rangle = \{|\pi m \otimes \nu m'\rangle + |\pi m' \otimes \nu m'\rangle\}/\sqrt{2},$$

for  $\pi j \neq \nu j'$ , or for  $\pi j = \nu j'$  but  $\pi m \neq \nu m'$ , (A3)

and for  $\pi j = \nu j'$  and  $\pi m = \nu m'$  by,

$$|\pi m; \nu m' : \mathcal{S}\rangle = |\pi m \otimes \nu m'\rangle. \quad (\text{A4})$$

The monopole matrix element is defined, in this case, as an average over all symmetric states with all possible orientations. It is therefore given by

$$V_{pn,s}^m(j, j') = \frac{\sum_{(m, m')} (m; m' : \mathcal{S} | \hat{v}_{pn} | m; m' : \mathcal{S})}{\sum_{m, m'} 1} \quad (\text{A5})$$

We shall denote the creation operators for a proton and a neutron in the state  $j, m$  as  $c_{j,m}^\dagger$  and  $a_{j,m}^\dagger$ , respectively. Likewise, the annihilation operators are denoted as  $c_{j,m}$  and  $a_{j,m}$ . Here, the proton operators, creation and annihilation, commute with the neutron operators, creation and annihilation. The state in eq. (A3) is then created by the operator

$$\frac{1}{\sqrt{2}} \left\{ c_{j,m}^\dagger a_{j',m'}^\dagger + c_{j',m'}^\dagger a_{j,m}^\dagger \right\}, \quad (\text{A6})$$

while the state in eq. (A4) is created by the operator

$$c_{j,m}^\dagger a_{j',m'}^\dagger. \quad (\text{A7})$$

Pair annihilation operators can be introduced similarly as hermitian conjugates of eqs. (A6) and (A7).

By combining eqs. (A5), (A6), and (A7), the monopole-interaction operator is written as

$$\hat{v}_{pn,mono,s} = \sum_{j \leq j'} \hat{v}_{pn,s}^m(j, j'). \quad (\text{A8})$$

Here,  $\hat{v}_{pn,s}^m(j, j')$  is given for  $j \neq j'$  as

$$\hat{v}_{pn,s}^m(j, j') = V_{pn,s}^m(j, j') \frac{1}{2} \Sigma_{m, m'} (c_{j,m}^\dagger a_{j',m'}^\dagger + c_{j',m'}^\dagger a_{j,m}^\dagger) (a_{j',m'} c_{j,m} + a_{j,m} c_{j',m'}). \quad (\text{A9})$$

Based on eqs. (A6, A7), it is written for  $j = j'$  as

$$\hat{v}_{pn,s}^m(j, j) = V_{pn,s}^m(j, j) \left\{ \frac{1}{2} \Sigma_{m < m'} (c_{j,m}^\dagger a_{j,m'}^\dagger + c_{j,m'}^\dagger a_{j,m}^\dagger) (a_{j,m'} c_{j,m} + a_{j,m} c_{j,m'}) + \Sigma_m c_{j,m}^\dagger a_{j,m}^\dagger a_{j,m} c_{j,m} \right\}. \quad (\text{A10})$$

We introduce the proton and neutron number operators in the orbit  $j$  as,

$$\hat{n}_j^p = \sum_m c_{j,m}^\dagger c_{j,m} \text{ and } \hat{n}_j^n = \sum_m a_{j,m}^\dagger a_{j,m}. \quad (\text{A11})$$

In addition, we introduce the following operators,

$$\hat{\tau}_j^+ = \sum_m c_{j,m}^\dagger a_{j,m}, \text{ and } \hat{\tau}_j^- = \sum_m a_{j,m}^\dagger c_{j,m}. \quad (\text{A12})$$

We note here that the operators in eq. (A12) are nothing but the isospin raising and lowering operators restricted to the orbit  $j$ . Here, we take the convention that protons are in the state of isospin  $z$ -component  $\tau_z = +1/2$ , whereas neutrons are in  $\tau_z = -1/2$ .

With these operators, the monopole interaction can be rewritten as

$$\begin{aligned} \hat{v}_{pn,mono,s} &= \sum_{j < j'} V_{pn,s}^m(j, j') \frac{1}{2} \\ &\quad \left\{ \hat{n}_j^p \hat{n}_{j'}^n + \hat{n}_{j'}^p \hat{n}_j^n - \hat{\tau}_j^+ \hat{\tau}_{j'}^- - \hat{\tau}_{j'}^+ \hat{\tau}_j^- \right\} \\ &\quad + \sum_j V_{pn,s}^m(j, j) \frac{1}{2} \left\{ \hat{n}_j^p \hat{n}_j^n - : \hat{\tau}_j^+ \hat{\tau}_j^- : \right\}, \end{aligned} \quad (\text{A13})$$

where the symbol  $: \dots :$  denotes a normal product. This equation can be rewritten as

$$\begin{aligned} \hat{v}_{pn,mono,s} &= \sum_{j j'} V_{pn,s}^m(j, j') \frac{1}{2} \hat{n}_j^p \hat{n}_{j'}^n \\ &\quad - \sum_{j < j'} V_{pn,s}^m(j, j') \frac{1}{2} \left\{ \hat{\tau}_j^+ \hat{\tau}_{j'}^- + \hat{\tau}_{j'}^- \hat{\tau}_j^+ \right\} \\ &\quad - \sum_j V_{pn,s}^m(j, j) \frac{1}{2} : \hat{\tau}_j^+ \hat{\tau}_j^- : . \end{aligned} \quad (\text{A14})$$

Some visual explanation of the last two terms on the right-hand side are displayed in Fig. 5.

We shall now move to the isospin scheme. The total wave function must be antisymmetric with respect to the exchange of any pair of nucleons in the isospin scheme, and the total wave function is a product of the coordinate-spin wave function and the isospin wave function. The present case, where the coordinate-spin wave function is symmetric, corresponds to the isospin wave function being anti-symmetric, which means that the proton and neutron couple to isospin  $T = 0$ . Thus, the states belonging to eqs. (A3,A4) are  $T = 0$  states. Equation (A14) represents the  $T = 0$  part of the proton-neutron monopole interaction with the  $T = 0$  monopole matrix elements given by,

$$V_{T=0}^m(j, j') = V_{pn,s}^m(j, j'), \quad (\text{A15})$$

where  $V_{pn,s}^m(j, j')$  is defined in eq. (A5).

Equation (A14) can then be expressed as,

$$\begin{aligned} \hat{v}_{pn,mono,T=0} &= \sum_{j, j'} V_{T=0}^m(j, j') \frac{1}{2} \hat{n}_j^p \hat{n}_{j'}^n \\ &\quad - \sum_{j < j'} V_{T=0}^m(j, j') \frac{1}{2} \left\{ \hat{\tau}_j^+ \hat{\tau}_{j'}^- + \hat{\tau}_{j'}^- \hat{\tau}_j^+ \right\} \\ &\quad - \sum_j V_{T=0}^m(j, j) \frac{1}{2} : \hat{\tau}_j^+ \hat{\tau}_j^- : . \end{aligned} \quad (\text{A16})$$

This is the  $T = 0$  monopole interaction within the present scheme.

We next discuss antisymmetric proton-neutron states as

$$|m; m' : \mathcal{A}) = \{|m \otimes m') - |m' \otimes m)\}/\sqrt{2} . \quad (\text{A17})$$

The state in eq. (A17) is then created by the operator

$$\frac{1}{\sqrt{2}} \left\{ c_{j,m}^\dagger a_{j',m'}^\dagger - c_{j',m'}^\dagger a_{j,m}^\dagger \right\}, \quad (\text{A18})$$

acting on the appropriate vacuum (*i.e.*, a closed shell).

The state in this category is antisymmetric with respect to the exchange between proton and neutron, which means that the isospin part should be symmetric. If the proton and neutron form a state with total isospin  $T = 1$ , its wave function does not change the sign upon exchange of proton and neutron. Thus, the states in eq. (A17) are  $T = 1$  states.

The state in eq. (3) can be generated by changing a proton in the state of eq. (A18) into a neutron. Indeed, by using the isospin-lowering operator mentioned above, we obtain

$$\begin{aligned} |j, m; j', m' > \\ &= a_{j,m}^\dagger a_{j',m'}^\dagger |0 > \\ &\propto \{\tau_j^- + \tau_{j'}^-\} \left\{ c_{j,m}^\dagger a_{j',m'}^\dagger - c_{j',m'}^\dagger a_{j,m}^\dagger \right\} |0 >, \end{aligned} \quad (\text{A19})$$

where  $|0 >$  indicates the relevant vacuum as usual. We can include states of two protons,

$$c_{j,m}^\dagger c_{j',m'}^\dagger |0 >, \quad (\text{A20})$$

in the same way. We note that the three states in eqs. (3,A18,A20) form the isospin multiplet with  $T = 1$ . If the interaction  $\hat{v}$  is isospin invariant as usual, the isospin operators  $\tau^+$  and  $\tau^-$  commute with  $\hat{v}$ , and the monopole matrix element in eq. (5) is the  $T = 1$  monopole matrix element to be used commonly for these isospin multiplet states:

$$V_{T=1}^m(j, j') = V_{nn}^m(j, j') . \quad (\text{A21})$$

Coming back to the proton-neutron state, we apply procedures similar to those for the  $T = 0$  states, and obtain

$$\begin{aligned} \hat{v}_{pn,mono,T=1} &= \sum_{j, j'} V_{T=1}^m(j, j') \frac{1}{2} \hat{n}_j^p \hat{n}_{j'}^n \\ &\quad + \sum_{j < j'} V_{T=1}^m(j, j') \frac{1}{2} \left\{ \hat{\tau}_j^+ \hat{\tau}_{j'}^- + \hat{\tau}_{j'}^- \hat{\tau}_j^+ \right\} \\ &\quad + \sum_j V_{T=1}^m(j, j) \frac{1}{2} : \hat{\tau}_j^+ \hat{\tau}_j^- : . \end{aligned} \quad (\text{A22})$$

## Appendix B: Alternative definition of the monopole interaction

An alternative but equivalent expression of the monopole matrix element is indicated here. In the case of  $j < j'$ , eq. (3) can be rewritten as

$$\begin{aligned} & |j, m; j', m' > \\ &= \sum_{J_1} (jmj'm' | J_1 M = m + m' ) \\ & \quad \sum_{m_1 m'_1} (jm_1 j'm'_1 | J_1 M = m + m' ) | m_1 m'_1 >, \end{aligned} \quad (B1)$$

where  $J_1$  in the summation runs through all possible values (i.e., from  $J_1 = |j - j'|$  up to  $j + j'$ ), and the symbols like  $(jmj'm' | J_1 M_1)$  are Clebsch-Gordan coefficients. We apply this expansion to the ket state of the numerator of eq. (5) as well as a similar expansion to its bra state, and come up with the following equation by using the orthonormal relation of the Clebsch-Gordan coefficient:

$$\begin{aligned} & \sum_{m, m'} \langle j, m; j', m' | \hat{v}_{nn} | j, m; j', m' \rangle \\ &= \sum_{J_1} \sum_{J_2} \sum_{m, m'} (jmj'm' | J_2 M = m + m' ) \\ & \quad (jmj'm' | J_1 M = m + m' ) \langle j, j'; J_2 | \hat{v}_{nn} | j, j'; J_1 \rangle \\ &= \sum_{J_1} (2J_1 + 1) \langle j, j'; J_1 | \hat{v}_{nn} | j, j'; J_1 \rangle. \end{aligned} \quad (B2)$$

Likewise, the denominator of eq. (5) is rewritten as

$$\sum_{m, m'} 1 = \sum_{J_1} (2J_1 + 1), \quad (B3)$$

where the factor  $(2J + 1)$  is the degeneracy of the two-particle states having the same value of  $J$ . We finally obtain

$$V_{nn}^m(j, j') = \frac{\sum_J (2J + 1) \langle j, j'; J | \hat{v}_{nn} | j, j'; J \rangle}{\sum_J (2J + 1)}. \quad (B4)$$

In the case of  $j = j'$ ,  $J_1$  in the summation takes only even integers due to the antisymmetrization. The neutron-neutron interaction corresponds to the  $T = 1$  interaction. The  $T = 0$  interaction can be treated similarly as symmetric combinations between proton and neutron. Combining all these relations, we can obtain

$$\begin{aligned} V_T^m(j, j') &= \frac{\sum_J (2J + 1) \langle j, j'; J, T | \hat{v} | j, j'; J, T \rangle}{\sum_J (2J + 1)} \\ & \quad \text{for } T = 0 \text{ and } 1, \end{aligned} \quad (B5)$$

where  $J$  takes only even (odd) integers for  $j = j'$  with  $T = 1$  ( $T = 0$ ). This is nothing but eq. (19) in II.C.

## Appendix C: Closed-shell properties

We discuss properties of closed-shell states in this appendix. We assume that the orbits  $j_1, j_2, \dots, j_k$  form the shell for both protons and neutrons.

We start with the neutron closed shell where all these orbits are completely filled by neutrons. The expectation value of  $\hat{v}_{nn}$  is then given by the straightforward calculation as

$$\begin{aligned} E_{nn} &= \sum_j \sum_{m_1 < m_2} \langle j, m_1; j, m_2 | \hat{v}_{nn} | j, m_1; j, m_2 \rangle \\ &+ \sum_{j < j'} \sum_{m_1, m_2} \langle j, m_1; j', m_2 | \hat{v}_{nn} | j, m_1; j', m_2 \rangle. \end{aligned} \quad (C1)$$

Considering  $\sum_{m < m'} 1 = (2j + 1)j$  as well as  $\sum_{m, m'} 1 = (2j + 1)(2j' + 1)$  for  $j \neq j'$ , we can rewrite  $E_{nn}$  in eq. (C1) as

$$\begin{aligned} E_{nn} &= \sum_j (2j + 1) j V_{T=1}^m(j, j) \\ &+ \sum_{j < j'} (2j + 1)(2j' + 1) V_{T=1}^m(j, j'), \end{aligned} \quad (C2)$$

where  $V_{T=1}^m(j, j')$  is defined in eq. (A21). We compare this result with the expectation value of  $\hat{v}_{nn,mono}$  in eq. (15) with respect to the present closed-shell state:

$$\begin{aligned} & \langle \hat{v}_{nn,mono} \rangle \\ &= \sum_j V_{T=1}^m(j, j) (2j + 1) j \\ &+ \sum_{j < j'} V_{T=1}^m(j, j') (2j + 1) (2j' + 1), \end{aligned} \quad (C3)$$

where the following substitution is made:

$$\langle \hat{n}_j^n \rangle = (2j + 1) \quad (C4)$$

The quantity in eq. (C3) is exactly the same as the one in eq. (C2). We point out that the closed-shell properties are not used in the derivation of the present monopole interaction.

We next consider the case with both protons and neutrons. To start, we assume that protons and neutrons occupy the same orbit  $j$ . More general cases will be discussed later. The contributions from the proton-proton and neutron-neutron interactions have been indicated just above. The remaining point is the contribution from the proton-neutron interaction. The proton-neutron interaction depends on the symmetry with respect to the exchange of proton and neutron, as discussed in the previous subsection. For a closed shell with  $2j + 1$  protons and  $2j + 1$  neutrons, each state with a pair of a proton and neutron is specified by  $m, m'$ , where  $m$  ( $m'$ ) refers to a proton (neutron) state. As  $m$  runs from  $m = -j$  to  $m = +j$ , the total number of those states is  $(2j + 1)^2$ .

The direct product  $|m \otimes m'\rangle$  spans those states. In order to incorporate the symmetry dependence of the nuclear forces, such direct-product states are transformed by an appropriate unitary transformation into symmetric and antisymmetric combinations. The symmetric states are given by eq. (A3) for  $m \neq m'$  (with  $j = j'$ ) and by eq. (A4) for  $m = m'$ . The total contribution from those symmetric states is nothing but

$$E_{pn,s} = \sum_{(m,m')} (m; m' : \mathcal{S} | \hat{v}_{pn} | m; m' : \mathcal{S}). \quad (\text{C5})$$

As the quantity on the right hand side is used in eq. (A5) and the number of symmetric pairs turns out to be

$$\sum_{m,m'} 1 = \frac{1}{2} (2j+1+1)(2j+1) = (j+1)(2j+1), \quad (\text{C6})$$

eq. (A5) leads us to

$$E_{pn,s} = V_{pn,s}^m(j, j) (j+1)(2j+1). \quad (\text{C7})$$

The antisymmetric combinations are treated similarly. The antisymmetric state is shown in eq. (A17). Due to the isospin invariance of the interaction and the isospin multiplet property, their total contribution can be taken from eq. (C2), and is explicitly given as

$$E_{pn,a} = (2j+1) j V_{T=1}^m(j, j). \quad (\text{C8})$$

Combining eqs. (C7, C8), we obtain

$$E_{pn} = V_{T=0}^m(j, j) (j+1)(2j+1) + V_{T=1}^m(j, j) (2j+1) j. \quad (\text{C9})$$

We compare this result with the expectation value of  $\hat{v}_{pn,mono}$  in eq. (15) with respect to the present closed-shell state :

$$\begin{aligned} \langle \hat{v}_{pn,mono} \rangle &= \frac{1}{2} \left\{ V_{T=0}^m(j, j) + V_{T=1}^m(j, j) \right\} (2j+1)^2 \\ &\quad - \frac{1}{2} \left\{ V_{T=0}^m(j, j) - V_{T=1}^m(j, j) \right\} \langle : \hat{\tau}_j^+ \hat{\tau}_j^- : \rangle. \end{aligned} \quad (\text{C10})$$

where eq. (C4) is used for protons as well as for neutrons. The expectation value of the second term on the right hand side,  $- : \hat{\tau}_j^+ \hat{\tau}_j^- :$ , counts the number of the pairs of a proton and a neutron both in the state  $m$ , and its value is obviously  $(2j+1)$  for the closed shell. By substituting this, we finally obtain

$$\begin{aligned} \langle \hat{v}_{pn,mono} \rangle &= V_{T=0}^m(j, j) (2j^2 + 3j + 1) \\ &\quad + V_{T=1}^m(j, j) (2j^2 + j). \end{aligned} \quad (\text{C11})$$

This is exactly the same as the result of eq. (C9).

More general cases can be formulated in a straightforward way based on the arguments here. The second term  $(\hat{\tau}_j^+ \hat{\tau}_{j'}^- + \hat{\tau}_j^- \hat{\tau}_{j'}^+)$  on the right hand side of eq. (A22) does not contribute to the energy of the closed shell, because it

transforms a proton into a neutron or vice versa. Thus, a generalization of eq. (C9) (or equivalently eq. (C11)) becomes

$$\begin{aligned} E_{pn} &= \sum_{j, j'} \frac{1}{2} \{ V_{T=0}^m(j, j') + V_{T=1}^m(j, j') \} (2j+1)(2j'+1) \\ &\quad + \sum_j \frac{1}{2} \{ V_{T=0}^m(j, j) - V_{T=1}^m(j, j) \} (2j+1). \end{aligned} \quad (\text{C12})$$

The total contribution is obtained by summation as

$$E_{tot} = E_{pp} + E_{nn} + E_{pn}. \quad (\text{C13})$$

This becomes for the case of the orbit  $j$  only

$$\begin{aligned} E_{tot} &= V_{T=0}^m(j, j) (j+1)(2j+1) \\ &\quad + V_{T=1}^m(j, j) 3j(2j+1). \end{aligned} \quad (\text{C14})$$

This expression is in agreement with the result shown in Ref. (Poves and Zuker, 1981).

## Appendix D: 2-body LS force

We describe here the monopole component of the 2-body LS (2b-LS) force and its effect in some details but with simple terms, partly because the following discussions may not be found elsewhere.

The 2b-LS force between the particles indexed as 1 and 2 contains a scalar product of the orbital angular momentum of the relative motion, denoted as  $\vec{L}_{rel;12}$ , and the total spin,  $\vec{S}_{12}$ . Here, these operators can be written as

$$\vec{L}_{rel;12} = (\vec{r}_1 - \vec{r}_2) \times (\vec{p}_1 - \vec{p}_2), \quad (\text{D1})$$

with  $\vec{r}_{1,2}$  ( $\vec{p}_{1,2}$ ) being the coordinate (momentum) of the particles 1 and 2, respectively. The total spin is defined as

$$\vec{S}_{12} = \vec{s}_1 + \vec{s}_2, \quad (\text{D2})$$

where  $\vec{s}_{1,2}$  implies the spin operator of the particles 1 and 2, respectively.

They are coupled to the 2b-LS operator

$$W_{LS} = (\vec{L}_{rel;12} \cdot \vec{S}_{12}), \quad (\text{D3})$$

where the symbol  $(\cdot)$  indicates a scalar product as usual.

The 2-body LS force is then given by

$$V_{LS} = w_0(r) W_{LS} + w_1(r) (\vec{r}_1 \cdot \vec{r}_2) W_{LS}, \quad (\text{D4})$$

where  $w_0(r)$  and  $w_1(r)$  are appropriate functions of the relative distance  $r$ . The functions depend on the choice of the 2b-LS interaction. We choose the 2b-LS interaction of the M3Y interaction (Bertsch *et al.*, 1977). We emphasize that the 2b-LS interaction is characterized

as a short-range interaction, and is indeed described, in this paper, by a short-range Yukawa-type  $r$ -dependence (range parameter being 0.25 and 0.4 fm), with  $w_0(r)$  and  $w_1(r)$  being negative. This short range is considered to be induced by  $\sigma + \rho + \omega$  meson exchanges (Bertsch *et al.*, 1977), and can be compared to that of the corresponding parameter of the Millner-Kurath interaction,  $\sim 0.7$  fm (Millener and Kurath, 1975). Because of the negative  $w_0(r)$  and  $w_1(r)$ , if  $\vec{L}_{rel;12}$  and  $\vec{S}_{12}$  are oriented to the same (opposite) direction, an attractive (repulsive) effect is produced. It is noted that between the total spin  $S=0$  and 1 states of particles 1 and 2, only the  $S=1$  state is affected by the 2b-*LS* interaction, implying that the spins of the particles 1 and 2 must be parallel.

We here show the relations

$$V_{odd}(T=1) = (w_0(r) + \frac{1}{4}w_1(r)) W_{LS} \quad (D5)$$

and

$$V_{even}(T=0) = (w_0(r) - \frac{3}{4}w_1(r)) W_{LS}. \quad (D6)$$

If  $w_0(r)$  and  $w_1(r)$  are both negative as in the M3Y interaction (Bertsch *et al.*, 1977), the  $T=1$  interaction becomes stronger in magnitude than the  $T=0$  interaction.

Based on these basic features, we can draw an intuitive schematic picture, Fig. 65, as to how the 2b-*LS* force works. This figure shows that the 2b-*LS* force acts on the nucleon A (red star) circulating on an orbit (black big circle), and this force was due to the nucleon B (green hexagon) being either (a) inside the orbit or (b) outside the orbit. The spin is assumed to be upward, without generality. The spins are shown by small red and green arrows next to the corresponding nucleons in the figure.

We assume that the nucleon A is moving in the direction shown by the dashed arrows in the figure. The nucleon B is assumed to be at rest for the time being, while we will come back to this point.

In Fig. 65 (a), the orbital angular momentum of the relative motion between the two nucleons is invoked by the motion of the nucleon A as depicted by the blue small circle, which is represented by the  $\vec{L}_{rel;12}$  (blue middle-sized arrow in the figure). In this case,  $\vec{L}_{rel;12}$  and  $\vec{S}_{12}$  are in the same direction, which makes the 2b-*LS* force attractive, as described above. In Fig 65 (b), the nucleon B is located outside the orbit of the nucleon A, and the  $\vec{L}_{rel;12}$  points to the opposite direction, but the spins are the same as in Fig 65 (a). Thus, the effect is opposite, *i.e.*, repulsive. The net effect is obtained by combining the cases (a) and (b) over all possible locations of nucleon B. We emphasize here that the cases (a) and (b) cancel each other in general. If the density of nucleon B inside the orbit of nucleon A is higher than that outside, the case (a) survives the cancellation, and the monopole matrix element becomes negative, yielding the normal spin-orbit splitting for  $j_>$  ( $= \ell + 1/2$ ). If one reverses the orbital

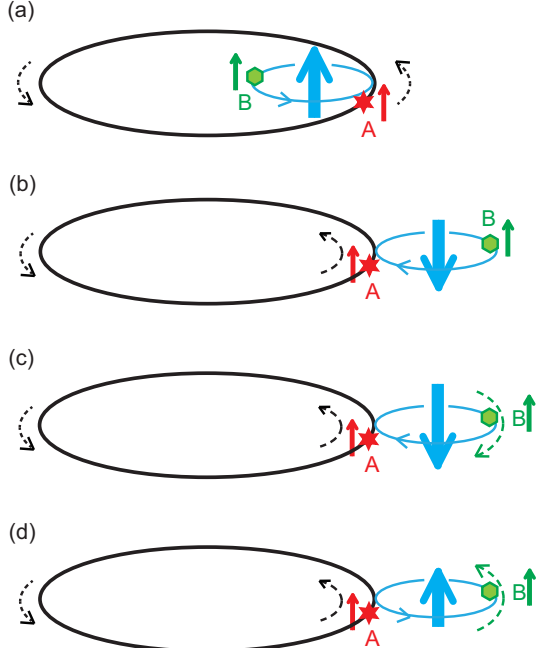


Figure 65 Schematic illustration of the monopole matrix elements of the 2-body LS (2b-LS) force. Black large circle stands for the orbit of nucleon A (red star) with spin (red short arrow). The 2-body LS force works between this nucleon and another nucleon B (green hexagon) (a) inside or (b) outside the orbit of A. The spin of the other nucleon is depicted by a green short arrow. Nucleon B is assumed to be at rest in (a,b), whereas the motion of B is activated in (c) and (d) as indicated by outmost green dashed arrows. In (d), nucleon B is assumed to have an angular momentum larger than that of nucleon A. Blue large arrows indicate the orbital angular momentum of the relative motion between A and B.

motion of nucleon A, one ends up again with the normal spin-orbit splitting for  $j_<$  ( $= \ell - 1/2$ ).

Because the 2b-*LS* force is of short range, the present cancellation effect may be well simulated by the radial derivative of the density of nucleon B at the location of nucleon A. This approximation becomes generally better with a large number of nucleons due to growing collectivity, and appears to be in accordance with the usual argument with the radial derivative of the density (Bohr and Mottelson, 1969). The approximation is expected to be particularly adequate if nucleon B runs through all nucleons in a closed shell, yielding the final spin-orbit splitting. However, there are different aspects also, as discussed below.

We shall look into actual monopole matrix elements of the 2b-*LS* force. We here introduce, for the sake of a global comparison, a normalization factor for the monopole matrix element based on the usual spin-orbit splitting (Bohr and Mottelson, 1969) with an additional division by the mass number,  $A$ . The factor is given as

$$- 20 (\vec{\ell} \cdot \vec{s}) A^{-5/3} \text{ MeV.} \quad (D7)$$

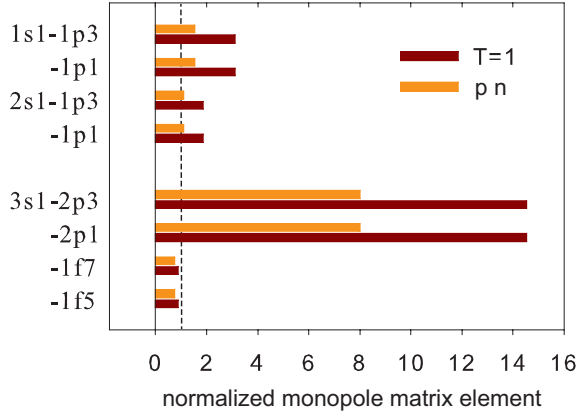


Figure 66 Monopole matrix elements obtained from the 2-body spin-orbit (2b-*LS*) force. The orbit on the far left indicates the orbit for nucleon B and that on the second left for nucleon A in Fig. 65, while the same entry for B is omitted. The matrix elements are normalized by referring a standard spin-orbit splitting (see the text for eq. (D7)). The mass number  $A=16$  is taken for the upper part, while  $A=80$  was chosen for the lower part. The vertical dashed line means the unity.

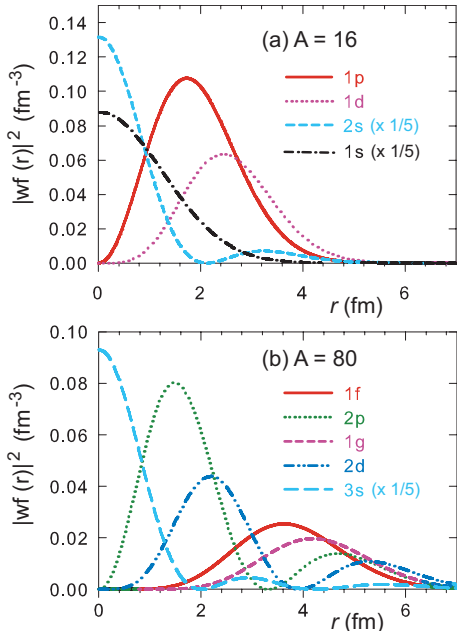


Figure 67 Radial wave functions squared for (a) 1p, 1d and 2s orbits with  $A=16$  and (b) 1f, 2p, 1g, 2d and 3s orbits with  $A=80$ . Harmonic Oscillator wave functions are taken.

The division by  $A$  gives a better scaling for the comparison to the monopole matrix element, as the spin-orbit splitting is due to all other nucleons in the nucleus. Throughout this article, unless otherwise specified, each monopole matrix element of the 2b-*LS* force is divided by this factor, where the  $\ell$  and  $j$  stand for those of nucleon

A. Actual values are calculated with Harmonic Oscillator radial wave functions for a given mass number  $A$ .

Figure 66 shows several cases with nucleon B in the 1, 2 or  $3s_{1/2}$ -orbit. In Fig 66, the orbital entries like “1s1-1p3” are given to the left. This means that nucleon A is in the  $1p_{3/2}$  orbit and nucleon B is in the  $1s_{1/2}$  orbit; nucleon B is the source of the monopole matrix element appearing first, and nucleon A is its recipient appearing next. Each case (*i.e.*, orbital combination) is composed of two horizontal histograms; the upper one stands for the proton-neutron matrix element and the lower for the  $T=1$  one. Both are normalized by the factor in eq. (D7). The second case implies that nucleon B is the same as above but nucleon A is in the orbit  $1p_{1/2}$ . The first four cases (from the top) are calculated with  $A=16$ , and indicate that (i) those monopole matrix elements show values  $\approx 1-3$  in the present scaling, and (ii)  $T=1$  contributions are larger than the proton-neutron ones, with the latter being about one half of the former. Point (i) suggests that the 2b-*LS* force is, in these cases, one of the primary origins of the spin-orbit splitting. Point (ii) implies that the dominant contribution from the present 2b-*LS* force is in the  $T=1$  channel. We show the radial wave functions in Fig 67 (a) as functions of the distance from the center of the nucleus,  $r$ , in order to understand these monopole matrix elements. The squared radial wave function of the  $1s$  orbits decreases for  $r=0-3$  fm, while the  $1p$  orbit is well outside of it. The squared radial wave function of the  $2s$  orbit decreases for  $r=0-2$  fm. Although it increases for  $r \approx 2-3$  fm, the magnitude is much smaller, and does not reverse the final result. Thus, the argument presented with Fig 65 (a,b) can be applied.

The lower part of Fig. 66 is calculated with  $A=80$ , and shows the monopole matrix elements for the *pf*-shell orbit due to nucleon B on the  $3s_{1/2}$  orbit. The contributions to the  $1f_{7/2,5/2}$  orbits appear to be close to unity.

Notable are large values of the contributions to the  $2p_{3/2,1/2}$  orbits which are much larger than those involving  $1f$ . They are different by a factor of 15. We shall discuss this intriguing problem now. In the coupling between the  $3s$  and  $2p$  orbits, the major components of the wave function of the relative motion correspond to small values of  $L_{rel;AB}$ . On the other hand, in the coupling between the  $3s$  and  $1f$  orbits,  $L_{rel;AB}$  is shifted naturally to larger values. Because of the short-range character of the 2b-*LS* force, if relevant  $L_{rel;AB}$  values are larger, the effect of the 2b-*LS* force becomes weaker. In fact, the combination of  $3s$  and  $2p$  produces the relative motion in the  $s$  or  $p$  state with high probabilities, and then the larger monopole matrix elements are a natural consequence. Thus, large monopole matrix elements between  $s$  and  $p$  orbits are a general feature, and monopole matrix elements can take larger values in the combinations of other  $s$  and  $p$  orbits. Without the normalization in eq. (D7), the monopole matrix element between the  $3s_{1/2}$  and  $2p_{3/2}$  is smaller only by a factor of about two

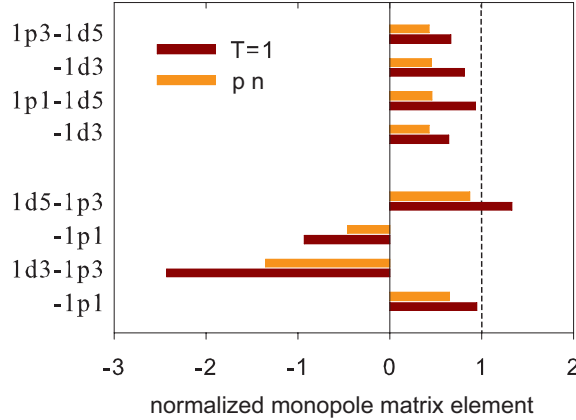


Figure 68 Monopole matrix elements obtained from the 2-body spin-orbit (2b-LS) force between the  $p$  and  $sd$  shells. See the caption of Fig. 66.

from that between the  $2s_{1/2}$  and  $1p_{3/2}$ . This can be understood from a similarity between the relevant parts of the panels (a) and (b) of Fig 67. On the other hand, the factor  $A^{5/3}$  in eq. (D7) yields about 1/15 from  $A=16$  to 80, and the case with the  $1f$  orbit fits well to this change. It is thus of much interest and significance that the  $s$ - $p$  coupling deviates from the trend given by eq. (D7).

Figure 68 presents the monopole matrix element between  $1p$  and  $1d$  orbits for  $A = 16$ . The upper four cases are in accordance with the usual spin-orbit splitting shown in eq. (D7). Figure 67 (a) indicates that the  $1p$  orbit is inside the  $1d$  orbit for the dominant part of  $1d$  orbit, and then the picture explained by Fig. 65 works again with nucleon A (B) in the  $1d$  ( $1p$ ) orbit.

We now exchange the orbits for nucleons A and B; A in  $1p$  and B in  $1d$ . As the radial inner-outer relation is reversed, the sign of the monopole matrix elements are altered. There is, however, another factor to be considered now. We assumed so far that nucleon B is at rest. We now include the motion of nucleon B, and B is either in the orbit  $j'_>$  or  $j'_<$ . Let us start with the case that nucleon A is in the  $j'_>$  orbit, whereas B is in the  $j'_<$ , as shown in Fig. 65 (c). The axial vector  $\vec{L}_{rel;AB}$  in Fig. 65 (c) increases its magnitude keeping the direction as in Fig. 65 (b). Because  $\vec{L}_{rel;AB}$  and  $\vec{S}_{12}$  are anti-parallel now, the monopole matrix element is positive (repulsive), and the value normalized by the spin-orbit splitting turns out to be negative, because of the  $j'_>$  orbit for nucleon A. Such a case is found in the entry “ $1d3-1p3$ ” in Fig. 68. A similar case is seen in the entry “ $1d5-1p1$ ” of the same figure.

We next consider, in Fig. 65 (d), nucleon B in  $j'_>$  with the orbital angular momentum for B greater than the orbital angular momentum for A. The axial vector  $\vec{L}_{rel;AB}$  becomes reversed as compared to Fig. 65 (b). This occurs, for instance, if  $j = p_{3/2}$  and  $j' = d_{5/2}$ . In such a case, the radial inner-outer inversion and the reversed

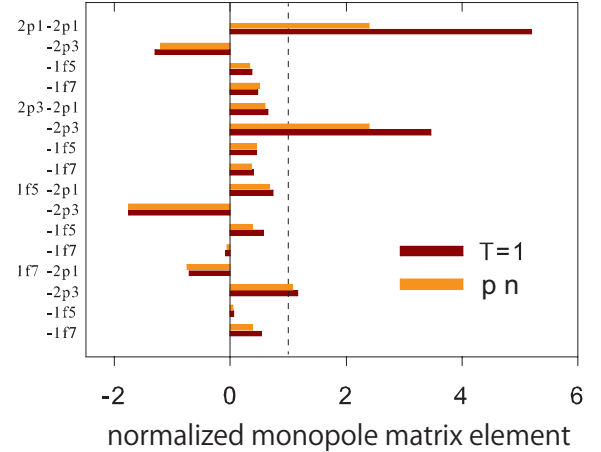


Figure 69 Monopole matrix elements obtained from the 2-body spin-orbit (2b-LS) force in the  $pf$  shell. See the caption of Fig. 66.

relative rotation make sign changes twice with no net change. This is the case with “ $1d5-1p3$ ” and “ $1d3-1p1$ ” in Fig. 68. The unusual cases (“ $1d3-1p3$ ” and “ $1d5-1p1$ ” in Fig. 68) may not be so important practically but may be of certain interest; for instance, the occupation of the  $1d_{3/2}$  orbits reduces the  $1p_{3/2}-1p_{1/2}$  splitting by  $\sim 0.05$  MeV with the  $T = 1$  interaction by raising the  $1p_{3/2}$  orbit more.

Figure 69 displays the monopole matrix elements between two nucleons in the same ( $pf$ ) shell with normalization by eq. (D7). Many cases show values less than unity in magnitude. This is expected from the argument of the inside/outside cancellations discussed for Fig. 65, because nucleons A and B are on orbits in the same shell. There are anomalously large values in the cases the  $2p_{1/2}-2p_{1/2}$  and  $2p_{3/2}-2p_{3/2}$  combinations. For instance, the  $T=1$  monopole matrix element before the normalization is as large as 0.223 MeV for  $A=40$ . The interpretation of this matrix element in terms of Fig. 65 seems to be inappropriate, because such interpretation is somewhat classical but the two-nucleon state in the  $2p_{1/2}$  orbit can be treated only quantum mechanically. Instead, we can present a clear quantum mechanical picture. The  $T=1$  state in the  $2p_{1/2}$  orbit is nothing but a  $J=0$  state. This  $J=0$  is coupled by the spin  $\vec{S}_{12}$  in eq. (D2) and the orbital angular momentum. The former must fulfill  $S_{12} = 1$  for the 2b-LS force, and the latter is composed of  $\vec{L}_{rel;AB}$  in eq. (D1) as well as the corresponding center-of-mass angular momentum  $\vec{L}_{cm;AB}$ . The component with  $L_{rel;AB} = 0$  and  $L_{cm;AB} = 1$  does not contribute to the present case, whereas that with  $L_{rel;AB} = 1$  and  $L_{cm;AB} = 0$  gives a large contribution because of the short-range character of the 2b-LS force. The  $J=0$  coupling implies  $(\vec{L}_{rel;AB} \cdot \vec{S}_{12}) < 0$ , leading to the repulsive contribution. Thus, we can expect a rather

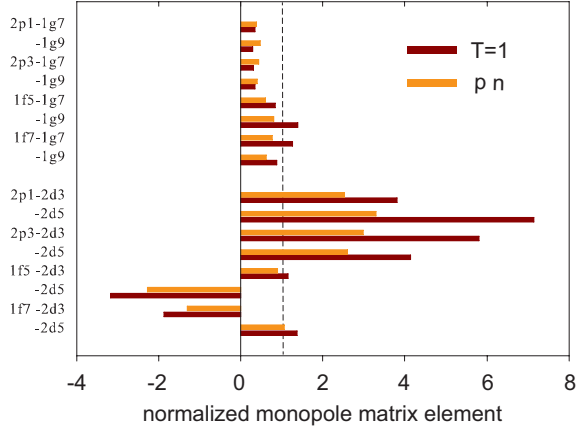


Figure 70 Monopole matrix elements obtained from the 2-body spin-orbit (2b- $LS$ ) force between the  $pf$  and  $sdg$  shells. See the caption of Fig. 66.

strong repulsive effect on the  $2p_{1/2}$ - $2p_{1/2}$  case.

This mechanism can be applied to the  $2p_{3/2}$ - $2p_{3/2}$  case for its  $J=0$  component, but its  $J=2$  component may contain  $L_{rel;AB} = 1$  and  $S_{12} = 1$  coupled in parallel, leading to an opposite effect. Thus, the net contribution becomes smaller than for the  $2p_{1/2}$ - $2p_{1/2}$  case. The cases containing both the  $p$  and  $f$  orbits can be interpreted already with Fig. 65.

Thus, the two nucleons in the same shell can be explained, and the exceptionally strong monopole matrix element between the two  $p_{1/2}$  orbits is emphasized once more, as its origin is general and robust. This feature produces visible effects on the appearance of the  $N=34$  new magic number (see Sec. III.D.4).

Figure 70 depicts monopole matrix elements for the  $pf$ - $sdg$  shell, as examples for the generality of the various effects discussed so far. Figure 67 (b) shows that the  $1g$  orbits are located in the outermost region. The large values for the  $p$ - $d$  combinations in Fig. 70 are due to small values of  $L_{rel;AB}$  in major components of the relative-motion wave functions. They increase the spin-orbit splitting also because the  $2p$  orbits are inside the  $1d$  orbit as can be seen from Fig. 70. The negative values appears in the  $f$ - $d$  combination, where  $j = 7/2 > j' = 3/2$  occurs and the  $1f$  orbits is outside the  $2d$  (see Fig. 70).

## REFERENCES

Alder, K., A. Bohr, T. Huus, B. Mottelson, and A. Winther (1956), *Rev. Mod. Phys.* **28**, 432.

Alex Brown, B. (1998), *Phys. Rev. C* **58**, 220.

Angeli, I., and K. Marinova (2013), *At. Data and Nucl. Data Tables* **99** (1), 69.

Audi, G., M. Wang, A. Wapstra, F. Kondev, M. MacCormick, X. Xu, and B. Pfeiffer (2012), *Chinese Physics C* **36** (12), 1287.

Bansal, R. K., and J. B. French (1964), *Phys. Lett.* **11**, 145.

Bastin, B., S. Grévy, D. Sohler, O. Sorlin, Z. Dombrádi, N. L. Achouri, J. C. Angélique, F. Azaiez, D. Baiborodin, R. Borcea, C. Bourgeois, A. Buta, A. Bürger, R. Chapman, J. C. Dalouzy, Z. Dlouhy, A. Drouard, Z. Elekes, S. Franchoo, S. Iacob, B. Laurent, M. Lazar, X. Liang, E. Liénard, J. Mrazek, L. Nalpas, F. Negoita, N. A. Orr, Y. Penionzhkevich, Z. Podolyák, F. Pougeon, P. Roussel-Chomaz, M. G. Saint-Laurent, M. Stanoiu, I. Stefan, F. Nowacki, and A. Poves (2007), *Phys. Rev. Lett.* **99**, 022503.

Baumann, T., A. M. Amthor, D. Bazin, B. A. Brown, C. M. F. III, A. Gade, T. N. Ginter, M. Hausmann, M. Matos, D. J. Morrissey, M. Portillo, A. Schiller, B. M. Sherrill, A. Stolz, O. B. Tarasov, and M. Thoennessen (2007), *Nature* **449** (7165), 1022.

Baumann, T., A. Spyrou, and M. Thoennessen (2012), *Reports on Progress in Physics* **75** (3), 036301.

Bazin, D., B. A. Brown, C. M. Campbell, J. A. Church, D. C. Dinca, J. Enders, A. Gade, T. Glasmacher, P. G. Hansen, W. F. Mueller, H. Olliver, B. C. Perry, B. M. Sherrill, J. R. Terry, and J. A. Tostevin (2003), *Phys. Rev. Lett.* **91**, 012501.

Bender, M., K. Bennaceur, T. Duguet, P. H. Heenen, T. Lesinski, and J. Meyer (2009a), *Phys. Rev. C* **80**, 064302.

Bender, M., K. Bennaceur, T. Duguet, P. H. Heenen, T. Lesinski, and J. Meyer (2009b), *Phys. Rev. C* **80**, 064302.

Bender, M., P.-H. Heenen, and P.-G. Reinhard (2003), *Rev. Mod. Phys.* **75**, 121.

Bertsch, G., J. Borysowicz, H. McManus, and W. Love (1977), *Nucl. Phys. A* **284** (3), 399.

Bethe, H. A. (1940a), *Phys. Rev.* **57**, 260.

Bethe, H. A. (1940b), *Phys. Rev.* **57**, 260.

Bethe, H. A., and R. F. Bacher (1936), *Rev. Mod. Phys.* **8**, 82.

Bhattacharyya, S., M. Rejmund, A. Navin, E. Caurier, F. Nowacki, A. Poves, R. Chapman, D. O'Donnell, M. Gelin, A. Hodsdon, X. Liang, W. Mittig, G. Mukherjee, F. Rejmund, M. Rousseau, P. Roussel-Chomaz, K.-M. Spohr, and C. Theisen (2008), *Phys. Rev. Lett.* **101**, 032501.

Blaum, K. (2006), *Physics Reports* **425** (1), 1.

Blaum, K., J. Dilling, and W. Nörtershäuser (2013), *Physica Scripta* **2013** (T152), 014017.

Block, M., C. Bachelet, G. Bollen, M. Facina, C. M. Folden, C. Guénaut, A. A. Kwiatkowski, D. J. Morrissey, G. K. Pang, A. Prinke, R. Ringle, J. Savory, P. Schury, and S. Schwarz (2008), *Phys. Rev. Lett.* **100**, 132501.

Blumenfeld, Y., T. Nilsson, and P. V. Duppen (2013), *Physica Scripta* **2013** (T152), 014023.

Bogner, S., et al. (2009), arXiv:0903.3366 [nucl-th].

Bogner, S. K., H. Hergert, J. D. Holt, A. Schwenk, S. Binder, A. Calci, J. Langhammer, and R. Roth (2014), *Phys. Rev. Lett.* **113**, 142501.

Bogner, S. K., T. T. S. Kuo, and A. Schwenk (2003), *Phys. Rep.* **386**, 1.

Bogner, S. K., et al. (2007), *Nucl. Phys. A* **784**, 79.

Bohr, A., and B. R. Mottelson (1969), *Nuclear Structure*, Vol. 1 (W. A. Benjamin, Inc., New York).

Bollen, G., R. B. Moore, G. Savard, and H. Stolzenberg (1990), *Journal of Applied Physics* **68** (9), 4355.

Bouyssy, A., J.-F. Mathiot, N. Van Giai, and S. Marcos (1987), *Phys. Rev. C* **36**, 380.

Brink, D. M., and F. Stancu (2007), *Phys. Rev. C* **75**, 064311.

Broda, R. (2006), *Journal of Physics G: Nuclear and Particle Physics* **32** (6), R151.

Brown, B. (1993), *Revista Mexicana de Física* **39**, 21.

Brown, B., and A. F. Lisetskiy (2009), private communication.

Brown, B., and B. Wildenthal (1988), *Annu. Rev. Nucl. Part. Sci.* **38**, 29.

Brown, B. A. (2013), *Phys. Rev. Lett.* **111**, 162502.

Brown, B. A., T. Duguet, T. Otsuka, D. Abe, and T. Suzuki (2006), *Phys. Rev. C* **74**, 061303(R).

Brown, B. A., and W. A. Richter (2006), *Phys. Rev. C* **74**, 034315.

Brown, B. A., W. A. Richter, R. E. Julies, and B. H. Wildenthal (1988), *Ann. Phys.* **182**, 191.

Brown, G. E., and A. M. Green (1969), *Nucl. Phys. A* **137**, 1.

Brown, S. M., W. N. Catford, J. S. Thomas, B. Fernández-Domínguez, N. A. Orr, M. Labiche, M. Rejmund, N. L. Achouri, H. Al Falou, N. I. Ashwood, D. Beaumel, Y. Blumenfeld, B. A. Brown, R. Chapman, M. Chartier, N. Curtis, G. de France, N. de Sereville, F. Delaunay, A. Drouart, C. Force, S. Franchoo, J. Guillot, P. Haigh, F. Hammache, V. Lapoux, R. C. Lemmon, A. Leprince, F. Maréchal, X. Mougeot, B. Mouginot, L. Nalpas, A. Navin, N. P. Patterson, B. Pietras, E. C. Pollacco, A. Ramus, J. A. Scarpaci, I. Stefan, and G. L. Wilson (2012), *Phys. Rev. C* **85**, 011302.

Bürger, A., et al. (2005), *Phys. Lett. B* **622**, 29.

Burgunder, G., O. Sorlin, F. Nowacki, S. Giron, F. Hammache, M. Moukaddam, N. de Sereville, D. Beaumel, L. Cáceres, E. Clément, G. Duchêne, J. P. Ebran, B. Fernandez-Dominguez, F. Flavigny, S. Franchoo, J. Gibelin, A. Gillibert, S. Grévy, J. Guillot, A. Lepailleur, I. Matea, A. Matta, L. Nalpas, A. Obertelli, T. Otsuka, J. Pancin, A. Poves, R. Raabe, J. A. Scarpaci, I. Stefan, C. Stodel, T. Suzuki, and J. C. Thomas (2014), *Phys. Rev. Lett.* **112**, 042502.

Caesar, C., et al. (R3B collaboration) (2013), *Phys. Rev. C* **88**, 034313.

Calinescu, S., L. Cáceres, S. Grévy, O. Sorlin, Z. Dombrádi, M. Stanoiu, R. Astabatyan, C. Borcea, R. Borcea, M. Bowry, W. Catford, E. Clément, S. Franchoo, R. García, R. Gillibert, I. H. Guerin, I. Kuti, S. Lukyanov, A. Lepailleur, V. Maslov, P. Morfouace, J. Mrazek, F. Negoita, M. Niikura, L. Perrot, Z. Podolyák, C. Petrone, Y. Penionzhkevich, T. Roger, F. Rotaru, D. Sohler, I. Stefan, J. C. Thomas, Z. Vajta, and E. Wilson (2016), *Phys. Rev. C* **93**, 044333.

Campi, X., H. Focard, A. Kerman, and S. Koonin (1975), *Nucl. Phys. A* **251**, 193.

Casten, R. F., D. D. Warner, D. S. Brenner, and R. L. Gill (1981), *Phys. Rev. Lett.* **47**, 1433.

Casten, R. F., and N. V. Zamfir (1993), *Phys. Rev. Lett.* **70**, 402.

Catford, W. N., C. N. Timis, R. C. Lemmon, M. Labiche, N. A. Orr, B. Fernández-Domínguez, R. Chapman, M. Freer, M. Chartier, H. Savajols, M. Rejmund, N. L. Achouri, N. Amzal, N. I. Ashwood, T. D. Baldwin, M. Burns, L. Caballero, J. M. Casadjian, N. Curtis, G. de France, W. Gelletly, X. Liang, S. D. Pain, V. P. E. Pucknell, B. Rubio, O. Sorlin, K. Spohr, C. Theisen, and D. D. Warner (2010), *Phys. Rev. Lett.* **104**, 192501.

Caurier, E., G. Martínez-Pinedo, F. Nowacki, A. Poves, and A. P. Zuker (2005), *Rev. Mod. Phys.* **77**, 427.

Caurier, E., F. Nowacki, and A. Poves (2004), *Nuclear Physics A* **742** (1), 14.

Caurier, E., F. Nowacki, and A. Poves (2014a), *Phys. Rev. C* **90**, 014302.

Caurier, E., F. Nowacki, and A. Poves (2014b), *Phys. Rev. C* **90** (1), 014302.

Caurier, E., F. Nowacki, A. Poves, and J. Retamosa (1998), *Phys. Rev. C* **58** (1), 2033.

Cheal, B., and K. T. Flanagan (2010), *J. Phys. G* **37** (11), 113101.

Chevrier, R., J. M. Daugas, L. Gaudemar, Y. Ichikawa, H. Ueno, M. Hass, H. Haas, S. Cottenier, N. Aoi, K. Asahi, D. L. Balabanski, N. Fukuda, T. Furukawa, G. Georgiev, H. Hayashi, H. Iijima, N. Inabe, T. Inoue, M. Ishihara, Y. Ishii, D. Kameda, T. Kubo, T. Nanao, G. Neyens, T. Ohnishi, M. M. Rajabali, K. Suzuki, H. Takeda, M. Tsuchiya, N. Vermeulen, H. Watanabe, and A. Yoshimi (2012), *Phys. Rev. Lett.* **108**, 162501.

Cippolone, A., C. Barbieri, and P. Navrátil (2013), *Phys. Rev. Lett.* **111**, 062501.

Cline, D. (1986), *Ann. Rev. Nucl. Part. Sci.* **36**, 683.

Co', G., V. De Donno, P. Finelli, M. Grasso, M. Anguiano, A. M. Lallena, C. Giusti, A. Meucci, and F. D. Pacati (2012), *Phys. Rev. C* **85**, 024322.

Cohen, S., and D. Kurath (1965), *Nucl. Phys.* **73** (1), 1.

Colò, G., H. Sagawa, S. Fracasso, and P. Bortignon (2007), *Phys. Lett. B* **646** (5-6), 227.

Coraggio, L., A. Covello, A. Gargano, and N. Itaco (2009), *Phys. Rev. C* **80**, 044311.

Cottle, P. D., and K. W. Kemper (1998), *Phys. Rev. C* **58**, 3761.

Crawford, H. L., P. Fallon, A. O. Macchiavelli, R. M. Clark, B. A. Brown, J. A. Tostevin, D. Bazin, N. Aoi, P. Doornenbal, M. Matsushita, H. Scheit, D. Steppenbeck, S. Takeuchi, H. Baba, C. M. Campbell, M. Cromaz, E. Ideguchi, N. Kobayashi, Y. Kondo, G. Lee, I. Y. Lee, J. Lee, K. Li, S. Michimasa, T. Motobayashi, T. Nakamura, S. Ota, S. Paschalidis, M. Petri, T. Sako, H. Sakurai, S. Shimoura, M. Takechi, Y. Togano, H. Wang, and K. Yoneda (2014), *Phys. Rev. C* **89**, 041303.

Crawford, H. L., P. Fallon, A. O. Macchiavelli, A. Poves, V. M. Bader, D. Bazin, M. Bowry, C. M. Campbell, M. P. Carpenter, R. M. Clark, M. Cromaz, A. Gade, E. Ideguchi, H. Iwasaki, C. Langer, I. Y. Lee, C. Loelius, E. Lunderberg, C. Morse, A. L. Richard, J. Rissanen, D. Smalley, S. R. Stroberg, D. Weisshaar, K. Whitmore, A. Wiens, S. J. Williams, K. Wimmer, and T. Yamamoto (2016), *Phys. Rev. C* **93**, 031303.

Crawford, H. L., et al. (2010), *Phys. Rev. C* **82**, 014311.

Darby, I. G., R. K. Grzywacz, J. C. Batchelder, C. R. Birmingham, L. Cartegni, C. J. Gross, M. Hjorth-Jensen, D. T. Joss, S. N. Liddick, W. Nazarewicz, S. Padgett, R. D. Page, T. Papenbrock, M. M. Rajabali, J. Rotureau, and K. P. Rykaczewski (2010), *Phys. Rev. Lett.* **105**, 162502.

Daugas, J., et al. (2010), *Phys. Rev. C* **81**, 034304.

DeRydt, M., R. Lozeva, N. Vermeulen, F. de Oliveira Santos, S. Grévy, P. Himpe, C. Stodel, J. Thomas, P. Vingerhoets, and G. Neyens (2009), *Nucl. Instrum. Methods Phys. Res. A* **612** (2), 112.

Détraz, C., D. Guillemaud, G. Huber, R. Klapisch, M. Langevin, F. Naulin, C. Thibault, L. C. Carraz, and F. Touchard (1979), *Phys. Rev. C* **19**, 164.

Dewald, A., O. Möller, and P. Petkov (2012), *Progress in Particle and Nuclear Physics* **67** (3), 786.

Dilling, J., R. Baartman, P. Bricault, M. Brodeur, L. Blomeley, F. Buchinger, J. Crawford, J. C. Lopez-Urrutia, P. Delheij, M. Froese, G. Gwinner, Z. Ke, J. Lee, R. Moore, V. Ryjkov, G. Sikler, M. Smith, J. Ullrich, and J. Vaz (2006), *International Journal of Mass Spectrometry* **251** (2-3), 198.

Dinca, D. C., *et al.* (2005), *Phys. Rev. C* **71**, 041302(R).

Diriken, J., N. Patronis, A. Andreyev, S. Antalic, V. Bildstein, A. Blazhev, I. Darby, H. D. Witte, J. Eberth, J. Elseviers, V. Fedosseev, F. Flavigny, C. Fransen, G. Georgiev, R. Gernhauser, H. Hess, M. Huyse, J. Jolie, T. Kröll, R. Krücken, R. Lutter, B. Marsh, T. Mertzimekis, D. Muecher, F. Nowacki, R. Orlandi, A. Pakou, R. Raabe, G. Randisi, P. Reiter, T. Roger, M. Seidlitz, M. Seliverstov, K. Sieja, C. Sotty, H. Tornqvist, J. V. D. Walle, P. V. Duppen, D. Voulot, N. Warr, F. Wenander, and K. Wimmer (2014), *Physics Letters B* **736**, 533.

Diriken, J., N. Patronis, A. Andreyev, S. Antalic, V. Bildstein, A. Blazhev, I. G. Darby, H. De Witte, J. Eberth, J. Elseviers, V. N. Fedosseev, F. Flavigny, C. Fransen, G. Georgiev, R. Gernhauser, H. Hess, M. Huyse, J. Jolie, T. Kröll, R. Krücken, R. Lutter, B. A. Marsh, T. Mertzimekis, D. Muecher, R. Orlandi, A. Pakou, R. Raabe, G. Randisi, P. Reiter, T. Roger, M. Seidlitz, M. Seliverstov, C. Sotty, H. Tornqvist, J. Van De Walle, P. Van Duppen, D. Voulot, N. Warr, F. Wenander, and K. Wimmer (2015), *Phys. Rev. C* **91**, 054321.

Dobaczewski, J., I. Hamamoto, W. Nazarewicz, and J. Sheikh (1994), *Phys. Rev. Lett.* **72**, 981.

Doll, P., G. Wagner, K. Knöpfle, and G. Mairle (1976), *Nuclear Physics A* **263** (2), 210.

Doornenbal, P., H. Scheit, S. Takeuchi, N. Aoi, K. Li, M. Matsushita, D. Stepenbeck, H. Wang, H. Baba, H. Crawford, C. R. Hoffman, R. Hughes, E. Ideguchi, N. Kobayashi, Y. Kondo, J. Lee, S. Michimasa, T. Motobayashi, H. Sakurai, M. Takechi, Y. Togano, R. Winkler, and K. Yoneda (2013), *Phys. Rev. Lett.* **111**, 212502.

Doornenbal, P., H. Scheit, S. Takeuchi, N. Aoi, K. Li, M. Matsushita, D. Stepenbeck, H. Wang, H. Baba, E. Ideguchi, N. Kobayashi, Y. Kondo, J. Lee, S. Michimasa, T. Motobayashi, A. Poves, H. Sakurai, M. Takechi, Y. Togano, and K. Yoneda (2016), *Phys. Rev. C* **93**, 044306.

Duguet, T., and G. Hagen (2012), *Phys. Rev. C* **85**, 034330.

Egidio, J. L., M. Borrajo, and T. R. Rodríguez (2016), *Phys. Rev. Lett.* **116**, 052502.

Elliott, J. P., A. D. Jackson, H. A. Mavromatis, E. A. Sander-son, and B. Singh (1968), *Nucl. Phys. A* **121**, 241.

Entem, D. R., and R. Machleidt (2003), *Phys. Rev. C* **68**, 041001.

Epelbaum, E. (2006), *Prog. Part. Nucl. Phys.* **57**, 654.

Epelbaum, E., H.-W. Hammer, and U.-G. Meißner (2009), *Rev. Mod. Phys.* **81**, 1773.

Epelbaum, E., *et al.* (2002), *Phys. Rev. C* **66**, 064001.

Erler, J., N. Birge, M. Kortelainen, W. Nazarewicz, E. Olsen, A. M. Perhac, and M. Stoitsov (2012), *Nature* **486** (7404), 509.

Evaluated Nuclear Structure Data File (ENSDF), (2017), <http://www.nndc.bnl.gov/ensdf/>.

Federman, P., and S. Pittel (1977), *Phys. Lett. B* **69** (4), 385.

Federman, P., S. Pittel, and R. Campos (1979), *Phys. Lett. B* **82** (1), 9.

Federman, P., S. Pittel, and A. Etchegoyen (1984), *Phys. Lett. B* **140**, 269.

Fernández-Domínguez, B., J. S. Thomas, W. N. Catford, F. Delaunay, S. M. Brown, N. A. Orr, M. Rejmund, M. Labiche, M. Chartier, N. L. Achouri, H. Al Falou, N. I. Ashwood, D. Beaumel, Y. Blumenfeld, B. A. Brown, R. Chapman, N. Curtis, C. Force, G. de France, S. Franchoo, J. Guillot, P. Haigh, F. Hammache, V. Lapoux, R. C. Lemmon, F. Maréchal, A. M. Moro, X. Mougeot, B. Mouginot, L. Nalpas, A. Navin, N. Patterson, B. Pietras, E. C. Pollacco, A. Leprince, A. Ramus, J. A. Scarpaci, N. de Séréville, I. Stephan, O. Sorlin, and G. L. Wilson (2011), *Phys. Rev. C* **84**, 011301.

Flanagan, K. T., P. Vingerhoets, M. Avgoulea, J. Billowes, M. L. Bissell, K. Blaum, B. Cheal, M. De Rydt, V. N. Fedosseev, D. H. Forest, C. Geppert, U. Köster, M. Kowalska, J. Krämer, K. L. Kratz, A. Krieger, E. Mané, B. A. Marsh, T. Materna, L. Mathieu, P. L. Molkanov, R. Neugart, G. Neyens, W. Nörtershäuser, M. D. Seliverstov, O. Serot, M. Schug, M. A. Sjoedin, J. R. Stone, N. J. Stone, H. H. Stroke, G. Tungate, D. T. Yordanov, and Y. M. Volkov (2009), *Phys. Rev. Lett.* **103**, 142501.

Force, C., S. Grévy, L. Gaudefroy, O. Sorlin, L. Cáceres, F. Rotaru, J. Mrazek, N. L. Achouri, J. C. Angélique, F. Azaiez, B. Bastin, R. Borcea, A. Buta, J. M. Daugas, Z. Dlouhy, Z. Dombrádi, F. De Oliveira, F. Negoita, Y. Penionzhkevich, M. G. Saint-Laurent, D. Sohler, M. Stanoiu, I. Stefan, C. Stodel, and F. Nowacki (2010), *Phys. Rev. Lett.* **105**, 102501.

Fornal, B., S. Zhu, R. Janssens, M. Honma, *et al.* (2004), *Phys. Rev. C* **70**, 072502.

Fornal, B., S. Zhu, R. Janssens, M. Honma, *et al.* (2005), *Phys. Rev. C* **72**, 044315.

Franchoo, S., *et al.* (1998), *Phys. Rev. Lett.* **81**, 3100.

Franchoo, S., *et al.* (2001), *Phys. Rev. C* **64**, 054308.

Franzke, B., H. Geissel, and G. Münzenberg (2008), *Mass Spectrometry Reviews* **27** (5), 428.

Fridmann, J., I. Wiedenhofer, A. Gade, L. T. Baby, D. Bazin, B. A. Brown, C. M. Campbell, J. M. Cook, P. D. Cottle, E. Diffenderfer, D.-C. Dinca, T. Glasmacher, P. G. Hansen, K. W. Kemper, J. L. Lecouey, W. F. Mueller, H. Olliver, E. Rodriguez-Vieitez, J. R. Terry, J. A. Tostevin, and K. Yoneda (2005), *Nature* **435** (7044), 922.

Fridmann, J., *et al.* (2006), *Phys. Rev. C* **74**, 034313.

Fritsch, S., N. Kaiser, and W. Weise (2005), *Nucl. Phys. A* **750**, 259.

Fujita, J., and H. Miyazawa (1957), *Prog. Theor. Phys.* **17**, 360.

Fukunishi, N., T. Otsuka, and T. Sebe (1992), *Phys. Lett. B* **296**, 279.

Gade, A. (2015), *Eur. Phys. J. A* **51** (9), 1.

Gade, A., P. Adrich, D. Bazin, M. D. Bowen, B. A. Brown, C. M. Campbell, J. M. Cook, S. Ettenauer, T. Glasmacher, K. W. Kemper, S. McDaniel, A. Obertelli, T. Otsuka, A. Ratkiewicz, K. Siwek, J. R. Terry, J. A. Tostevin, Y. Utsuno, and D. Weisshaar (2007), *Phys. Rev. Lett.* **99**, 072502.

Gade, A., P. Adrich, D. Bazin, M. D. Bowen, B. A. Brown, C. M. Campbell, J. M. Cook, T. Glasmacher, P. G. Hansen, K. Hosier, S. McDaniel, D. McGlinchery, A. Obertelli, K. Siwek, L. A. Riley, J. A. Tostevin, and D. Weisshaar (2008), *Phys. Rev. C* **77**, 044306.

Gade, A., P. Adrich, D. Bazin, B. A. Brown, J. M. Cook, C. A. Diget, T. Glasmacher, S. McDaniel, A. Ratkiewicz,

K. Siwek, and D. Weisshaar (2009), *Phys. Rev. Lett.* **102**, 182502.

Gade, A., D. Bazin, C. M. Campbell, J. A. Church, D. C. Dinca, J. Enders, T. Glasmacher, Z. Hu, K. W. Kemper, W. F. Mueller, H. Olliver, B. C. Perry, L. A. Riley, B. T. Roeder, B. M. Sherrill, and J. R. Terry (2003), *Phys. Rev. C* **68**, 014302.

Gade, A., B. A. Brown, D. Bazin, C. M. Campbell, J. A. Church, D. C. Dinca, J. Enders, T. Glasmacher, M. Horoi, Z. Hu, K. W. Kemper, W. F. Mueller, T. Otsuka, L. A. Riley, B. T. Roeder, T. Suzuki, J. R. Terry, K. L. Yurkewicz, and H. Zwahlen (2006a), *Phys. Rev. C* **74**, 034322.

Gade, A., and T. Glasmacher (2008), *Progress in Particle and Nuclear Physics* **60** (1), 161 .

Gade, A., and S. N. Liddick (2016), *J. Phys. G* **43** (2), 024001.

Gade, A., and B. M. Sherrill (2016), *Physica Scripta* **91** (5), 053003.

Gade, A., J. A. Tostevin, V. Bader, T. Baugher, D. Bazin, J. S. Berryman, B. A. Brown, C. A. Diget, T. Glasmacher, D. J. Hartley, E. Lunderberg, S. R. Stroberg, F. Recchia, A. Ratkiewicz, D. Weisshaar, and K. Wimmer (2016), *Phys. Rev. C* **93**, 054315.

Gade, A., *et al.* (2006b), *Phys. Rev. C* **74**, 021302(R).

Gaudefroy, L., J. M. Daugas, M. Hass, S. Grévy, C. Stödel, J. C. Thomas, L. Perrot, M. Girod, B. Rossé, J. C. Angélique, D. L. Balabanski, E. Fiori, C. Force, G. Georgiev, D. Kameda, V. Kumar, R. L. Lozeva, I. Matea, V. Méot, P. Morel, B. S. N. Singh, F. Nowacki, and G. Simpson (2009), *Phys. Rev. Lett.* **102**, 092501.

Gaudefroy, L., O. Sorlin, D. Beaumel, Y. Blumenfeld, Z. Dombrádi, S. Fortier, S. Franchoo, M. Gélin, J. Gélin, S. Grévy, F. Hammache, F. Ibrahim, K. W. Kemper, K.-L. Kratz, S. M. Lukyanov, C. Monrozeau, L. Nalpas, F. Nowacki, A. N. Ostrowski, T. Otsuka, Y.-E. Penionzhkevich, J. Piekariewicz, E. C. Pollacco, P. Roussel-Chomaz, E. Rich, J. A. Scarpaci, M. G. St. Laurent, D. Sohler, M. Stanoiu, T. Suzuki, E. Tryggestad, and D. Verney (2006), *Phys. Rev. Lett.* **97**, 092501.

Glasmacher, T. (1998), *Annu. Rev. of Nucl. and Part. Sci.* **48** (1), 1.

Glasmacher, T., B. Brown, M. Chromik, P. Cottle, M. Fauerbach, R. Ibbotson, K. Kemper, D. Morrissey, H. Scheit, D. Sklenicka, and M. Steiner (1997), *Physics Letters B* **395** (3), 163 .

Goodman, A. L. (1977), *Nucl. Phys. A* **287**, 1.

Grasso, M., Z. Y. Ma, E. Khan, J. Margueron, and N. V. Giai (2007), *Phys. Rev. C* **76**, 044319.

Grawe, H. (2004), “Shell model from a practitioner’s point of view,” in *The Euroschool Lectures on Physics with Exotic Beams, Vol. I*, edited by J. Al-Khalili and E. Roeckl (Springer Berlin Heidelberg, Berlin, Heidelberg) pp. 33–75.

Grawe, H., *et al.* (2005), *Eur. Phys. J. A* **25**, 357.

Grévy, S., J. Angélique, P. Baumann, C. Borcea, A. Buta, G. Canel, W. Catford, S. Courtin, J. Daugas, F. de Oliveira, P. Dessagne, Z. Dlouhy, A. Knipper, K. Kratz, F. Lecolley, J. Lecouey, G. Lehrsenneau, M. Lewitowicz, E. Liénard, S. Lukyanov, F. Maréchal, C. Miehé, J. Mrazek, F. Negoita, N. Orr, D. Pantelica, Y. Penionzhkevich, J. Péter, B. Pfeiffer, S. Pietri, E. Poirier, O. Sorlin, M. Stanoiu, I. Stefan, C. Stödel, and C. Timis (2004), *Physics Letters B* **594**, 252 .

Grévy, S., F. Negoita, I. Stefan, N. L. Achouri, J. C. Angélique, B. Bastin, R. Borcea, A. Buta, J. M. Daugas, F. De Oliveira, O. Giarmana, C. Jollet, B. Laurent, M. Lazar, E. Liénard, F. Maréchal, J. Mrázek, D. Pantelica, Y. Penionzhkevich, S. Piétri, O. Sorlin, M. Stanoiu, C. Stödel, and M. G. St-Laurent (2005), *Eur. Phys. J. A* **25**, 111.

Grigorenko, L. V., I. G. Mukha, and M. V. Zhukov (2013), *Phys. Rev. Lett.* **111**, 042501.

Guillemaud-Mueller, D., C. Detraz, M. Langevin, F. Naulin, M. de Saint-Simon, C. Thibault, F. Touchard, and M. Epherre (1984), *Nucl. Phys. A* **426** (1), 37 .

Hagen, G., M. Hjorth-Jensen, G. R. Jansen, R. Machleidt, and T. Papenbrock (2012), *Phys. Rev. Lett.* **109**, 032502.

Hagen, G., T. Papenbrock, D. J. Dean, and M. Hjorth-Jensen (2010), *Phys. Rev. C* **82**, 034330.

Hagen, G., T. Papenbrock, D. J. Dean, M. Hjorth-Jensen, and B. V. Asokan (2009), *Phys. Rev. C* **80**, 021306.

Hammer, H.-W., A. Nogga, and A. Schwenk (2013), *Rev. Mod. Phys.* **85**, 197.

Hansen, P. G., and B. Jonson (1987), *Europhys. Lett.* **4**, 409.

Hansen, P. G., and J. A. Tostevin (2003), *Annu. Rev. of Nucl. and Part. Sci.* **53**, 219.

Haxel, O., J. H. D. Jensen, and H. E. Suess (1949), *Phys. Rev.* **75**, 1766.

Hebeler, K., and A. Schwenk (2009), arXiv:0911.0483 [nucl-th].

Heyde, K., and J. Wood (1991), *J. Phys. G* **17**, 135.

Heylen, H., M. De Rydt, G. Neyens, M. L. Bissell, L. Caceres, R. Chevrier, J. M. Daugas, Y. Ichikawa, Y. Ishibashi, O. Kamalou, T. J. Mertzimekis, P. Morel, J. Papuga, A. Poves, M. M. Rajabali, C. Stödel, J. C. Thomas, H. Ueno, Y. Utsuno, N. Yoshida, and A. Yoshimi (2016), *Phys. Rev. C* **94**, 034312.

Hjorth-Jensen, M., T. T. S. Kuo, and E. Osnes (1995), *Phys. Rep.* **261**, 125.

Hoffman, C. R., T. Baumann, D. Bazin, J. Brown, G. Christian, P. A. DeYoung, J. E. Finck, N. Frank, J. Hinnefeld, R. Howes, P. Mears, E. Mosby, S. Mosby, J. Reith, B. Rizzo, W. F. Rogers, G. Peaslee, W. A. Peters, A. Schiller, M. J. Scott, S. L. Tabor, M. Thoennessen, P. J. Voss, , and T. Williams (2008), *Phys. Rev. Lett.* **100**, 152502.

Hoffman, C. R., B. P. Kay, and J. P. Schiffer (2016), *Phys. Rev. C* **94**, 024330.

Holt, J., T. Otsuka, A. Schwenk, and T. Suzuki (2012a), *J. Phys. G* **39**, 085111.

Holt, J. D., T. Otsuka, A. Schwenk, and T. Suzuki (2012b), *J. Phys. G: Nucl. Part. Phys.* **39**, 085111.

Honma, M., T. Otsuka, and T. Mizusaki (2008), *RIKEN Accel. Prog. Rep.* **41**, 32.

Honma, M., T. Otsuka, *et al.* (2005), *Eur. Phys. J. A* **25**, 499.

Horiuchi, W., *et al.* (2006), *Phys. Rev. C* **74**, 034311.

Huber, G., F. Touchard, S. Büttgenbach, C. Thibault, R. Klapisch, H. T. Duong, S. Liberman, J. Pinard, J. L. Vialle, P. Juncar, and P. Jacquinot (1978), *Phys. Rev. C* **18**, 2342.

Huck, A., *et al.* (1985), *Phys. Rev. C* **31**, 2226.

Ibbotson, R. W., T. Glasmacher, B. A. Brown, L. Chen, M. J. Chromik, P. D. Cottle, M. Fauerbach, K. W. Kemper, D. J. Morrissey, H. Scheit, and M. Thoennessen (1998), *Phys. Rev. Lett.* **80**, 2081.

Janssens, R., B. Fornal, P. Mantica, *et al.* (2002a), *Phys. Lett. B* **546**, 55.

Janssens, R. V. F. (2005), *Nature* **435**, 897.

Janssens, R. V. F., *et al.* (2002b), *Phys. Lett. B* **546**, 55.

Ji, X., and B. Wildenthal (1989), *Phys. Rev. C* **40**, 389.

Jurado, B., H. Savajols, W. Mittig, N. Orr, P. Roussel-Chomaz, D. Baiborodin, W. Catford, M. Chartier, C. Demchchy, Z. Dlouhý, A. Gillibert, L. Giot, A. Khouaja, A. Lépine-Szily, S. Lukyanov, J. Mrazek, Y. Penionzhkevich, S. Pita, M. Rousseau, and A. Villari (2007), *Physics Letters B* **649** (1), 43 .

Kahana, S., H. C. Lee, and C. K. Scott (1969), *Phys. Rev.* **180**, 956.

Kaneko, K., Y. Sun, T. Mizusaki, and M. Hasegawa (2011), *Phys. Rev. C* **83**, 014320.

Kanungo, R., A. Gallant, M. Uchida, C. Andreoiu, R. Austin, D. Bandyopadhyay, G. Ball, J. Becker, A. Boston, H. Boston, B. Brown, L. Buchmann, S. Colosimo, R. Clark, D. Cline, D. Cross, H. Dare, B. Davids, T. Drake, M. Djongolov, P. Finlay, N. Galinski, P. Garrett, A. Garnsworthy, K. Green, S. Grist, G. Hackman, L. Harkness, A. Hayes, D. Howell, A. Hurst, H. Jeppesen, K. Leach, A. Macchiavelli, D. Oxley, C. Pearson, B. Pietras, A. Phillips, S. Rigby, C. Ruiz, G. Ruprecht, F. Sarazin, M. Schumaker, A. Shotter, C. Sumitharachchi, C. Svensson, I. Tanihata, S. Triambak, C. Unsworth, S. Williams, P. Walden, J. Wong, and C. Wu (2010), *Phys. Lett. B* **682**, 391 .

Kanungo, R., *et al.* (2009), *Phys. Rev. Lett.* **102**, 152501.

Kay, B., S. Freeman, J. Schiffer, J. Clark, C. Deibel, A. Heinz, A. Parikh, and C. Wrede (2008), *Physics Letters B* **658** (5), 216 .

Kay, B. P., C. R. Hoffman, and A. O. Macchiavelli (2017), *Phys. Rev. Lett.* **119**, 182502.

Kay, B. P., J. P. Schiffer, S. J. Freeman, C. R. Hoffman, B. B. Back, S. I. Baker, S. Bedoor, T. Bloxham, J. A. Clark, C. M. Deibel, A. M. Howard, J. C. Lighthall, S. T. Marley, K. E. Rehm, D. K. Sharp, D. V. Shetty, J. S. Thomas, and A. H. Wuosmaa (2011), *Phys. Rev. C* **84**, 024325.

Khan, S., T. Kihm, K. Knopfle, G. Mairle, V. Bechtold, and L. Freidrich (1985), *Phys. Lett. B* **156** (3), 155 .

Kimura, M. (2007), *Phys. Rev. C* **75** (4), 041302.

Kimura, M., Y. Taniguchi, Y. Kanada-En'yo, H. Horiuchi, and K. Ikeda (2013), *Phys. Rev. C* **87**, 011301.

Kirson, M. W. (1973), *Phys. Lett. B* **47**, 110.

Klingenbeck, K., W. Knüpfer, M. G. Huber, and P. W. M. Glaudemans (1977), *Phys. Rev. C* **15**, 1483.

Kobayashi, N., T. Nakamura, Y. Kondo, J. A. Tostevin, Y. Utsuno, N. Aoi, H. Baba, R. Barthelemy, M. A. Famiano, N. Fukuda, N. Inabe, M. Ishihara, R. Kanungo, S. Kim, T. Kubo, G. S. Lee, H. S. Lee, M. Matsushita, T. Motobayashi, T. Ohnishi, N. A. Orr, H. Otsu, T. Otsuka, T. Sako, H. Sakurai, Y. Satou, T. Sumikama, H. Takeda, S. Takeuchi, R. Tanaka, Y. Togano, and K. Yoneda (2014), *Phys. Rev. Lett.* **112**, 242501.

Kobayashi, N., *et al.* (2012), *Phys. Rev. C* **86**, 054604.

Kobayashi, T., N. Chiga, T. Isobe, Y. Kondo, T. Kubo, K. Kusaka, T. Motobayashi, T. Nakamura, J. Ohnishi, H. Okuno, H. Otsu, T. Sako, H. Sato, Y. Shimizu, K. Sekiguchi, K. Takahashi, R. Tanaka, and K. Yoneda (2013), *Nucl. Instrum. Methods Phys. Res. B* **317**, 294 .

Kohley, Z., T. Baumann, D. Bazin, G. Christian, P. A. DeYoung, J. E. Finck, N. Frank, M. Jones, E. Lunderberg, B. Luther, S. Mosby, T. Nagi, J. K. Smith, J. Snyder, A. Spyrou, and M. Thoennessen (2013), *Phys. Rev. Lett.* **110**, 152501.

van Kolck, U. (1994), *Phys. Rev. C* **49**, 2932.

Kondo, Y., T. Nakamura, R. Tanaka, R. Minakata, S. Ogoshi, N. A. Orr, N. L. Achouri, T. Aumann, H. Baba, F. Delaunay, P. Doornenbal, N. Fukuda, J. Gibelin, J. W. Hwang, N. Inabe, T. Isobe, D. Kameda, D. Kanno, S. Kim, N. Kobayashi, T. Kobayashi, T. Kubo, S. Leblond, J. Lee, F. M. Marqué, T. Motobayashi, D. Murai, T. Murakami, K. Muto, T. Nakashima, N. Nakatsuka, A. Navin, S. Nishi, H. Otsu, H. Sato, Y. Satou, Y. Shimizu, H. Suzuki, K. Takahashi, H. Takeda, S. Takeuchi, Y. Togano, A. G. Tuff, M. Vandebrouck, and K. Yoneda (2016), *Phys. Rev. Lett.* **116**, 102503.

Köster, U., *et al.* (2011), *Phys. Rev. C* **84**, 034320.

Koura, H. (2005), *Prog. Theor. Phys.* **113**, 305.

Kramer, G., H. Blok, J. V. Hienen, S. Brandenburg, M. Harakeh, S. V. D. Werf, P. Glaudemans, and A. Wolters (1988), *Nucl. Phys. A* **477** (1), 55 .

Kramer, G., H. Blok, and L. Lapikás (2001), *Nuclear Physics A* **679** (3), 267 .

Kremer, C., *et al.* (2016), *Phys. Rev. Lett.* **117**, 172503.

Kucuk, Y., and J. Tostevin (2014), *Phys. Rev. C* **89**, 034607.

Kuo, T. T. S. (1967), *Nucl. Phys. A* **103**, 71.

Kuo, T. T. S., and G. E. Brown (1966), *Nucl. Phys.* **85**, 40.

Kwiatkowski, A. A., C. Andreoiu, J. C. Bale, A. Chaudhuri, U. Chowdhury, S. Malbrunot-Ettenauer, A. T. Gallant, A. Grossheim, G. Gwinner, A. Lennarz, T. D. Macdonald, T. J. M. Rauch, B. E. Schultz, S. Seeraji, M. C. Simon, V. V. Simon, D. Lunney, A. Poves, and J. Dilling (2015), *Phys. Rev. C* **92**, 061301.

Lalazissis, G. A., S. Karatzikos, M. Serra, T. Otsuka, and P. Ring (2009), *Phys. Rev. C* **80**, 041301(R).

Lalazissis, G. A., D. Vretenar, P. Ring, M. Stoitsov, and L. M. Robledo (1999), *Phys. Rev. C* **60**, 014310.

Leoni, S., B. Fornal, N. Mărginean, M. Sferrazza, Y. Tsunoda, T. Otsuka, *et al.* (2017), *Phys. Rev. Lett.* **118**, 162502.

Lesinski, T., M. Bender, K. Bennaceur, T. Duguet, and J. Meyer (2007), *Phys. Rev. C* **76**, 014312.

Li, Z. P., J. M. Yao, D. Vretenar, T. Nikšić, H. Chen, and J. Meng (2011), *Phys. Rev. C* **84**, 054304.

Liang, H., N. Van Giai, and J. Meng (2008), *Phys. Rev. Lett.* **101**, 122502.

Liddick, S., P. Mantica, R. Janssens, R. Broda, *et al.* (2013), *Phys. Rev. Lett.* **92**, 152501.

Liddick, S. N., *et al.* (2004), *Phys. Rev. Lett.* **92**, 072502.

Lisetskiy, A., B. Barrett, M. Kruse, P. Navratil, I. Stetcu, and J. Vary (2008), *Phys. Rev. C* **78**, 044302.

Lisetskiy, A., *et al.* (2004), *Phys. Rev. C* **70**, 044314.

Lisetskiy, A., *et al.* (2005), *Eur. Phys. J. A* **25**, 95.

Litvinova, E. (2016), *Physics Letters B* **755**, 138 .

Litvinova, E., and P. Ring (2006), *Phys. Rev. C* **73**, 044328.

Long, W., H. Sagawa, N. V. Giai, and J. Meng (2007a), *Phys. Rev. C* **76**, 034314.

Long, W., H. Sagawa, N. V. Giai, and J. Meng (2007b), *Phys. Rev. C* **76**, 034314.

Long, W.-H., N. V. Giai, and J. Meng (2006), *Physics Letters B* **640** (4), 150 .

Lu, F., J. Lee, M. B. Tsang, D. Bazin, D. Coupland, V. Henzl, D. Henzlova, M. Kilburn, W. G. Lynch, A. M. Rogers, A. Sanetullaev, Z. Y. Sun, M. Youngs, R. J. Charity, L. G. Sobotka, M. Famiano, S. Hudan, M. Horoi, and Y. L. Ye (2013), *Phys. Rev. C* **88**, 017604.

Lunderberg, E., P. A. DeYoung, Z. Kohley, H. Attanayake, T. Baumann, D. Bazin, G. Christian, D. Divaratne, S. M. Grimes, A. Haagsma, J. E. Finck, N. Frank, B. Luther, S. Mosby, T. Nagi, G. F. Peaslee, A. Schiller, J. Snyder, A. Spyrou, M. J. Strongman, and M. Thoennessen (2012), *Phys. Rev. Lett.* **108**, 142503.

Lunderberg, E., *et al.* (2016), *Phys. Rev. C* **94**, 064327.

Macfarlane, M. H., and J. B. French (1960), *Rev. Mod. Phys.* **32**, 567.

Mairle, G. (1993), *Phys. Lett. B* **304**, 39.

Marinova, K., W. Geithner, M. Kowalska, K. Blaum, S. Kappertz, M. Keim, S. Kloos, G. Kotrotsios, P. Lievens, R. Neugart, H. Simon, and S. Wilbert (2011), *Phys. Rev. C* **84**, 034313.

Mayer, M. G. (1949), *Phys. Rev.* **75**, 1969.

McGrory, J. B., B. H. Wildenthal, and E. C. Halbert (1970), *Phys. Rev. C* **2**, 186.

Mengoni, D., J. J. Valiente-Dobón, A. Gadea, S. Lunardi, S. M. Lenzi, R. Broda, A. Dewald, T. Pissulla, L. J. Angus, S. Aydin, D. Bazzacco, G. Benzoni, P. G. Bizzeti, A. M. Bizzeti-Sona, P. Boutachkov, L. Corradi, F. Crespi, G. de Angelis, E. Farnea, E. Fioretto, A. Goergen, M. Gorska, A. Gottardo, E. Grodner, A. M. Howard, W. Królas, S. Leoni, P. Mason, D. Montanari, G. Montagnoli, D. R. Napoli, A. Obertelli, R. Orlandi, T. Pawłat, G. Pollarolo, F. Recchia, A. Algora, B. Rubio, E. Sahin, F. Scarlassara, R. Silvestri, J. F. Smith, A. M. Stefanini, D. Steppenbeck, S. Szilner, C. A. Ur, P. T. Wady, and J. Wrzesiński (2010), *Phys. Rev. C* **82**, 024308.

Millener, D., and D. Kurath (1975), *Nucl. Phys. A* **255** (2), 315.

Montanari, D., S. Leoni, D. Mengoni, G. Benzoni, N. Blasi, G. Bocchi, P. Bortignon, A. Bracco, F. Camera, G. Col??, A. Corsi, F. Crespi, B. Million, R. Nicolini, O. Wieland, J. Valiente-Dobon, L. Corradi, G. de Angelis, F. D. Vedova, E. Fioretto, A. Gadea, D. Napoli, R. Orlandi, F. Recchia, E. Sahin, R. Silvestri, A. Stefanini, R. Singh, S. Szilner, D. Bazzacco, E. Farnea, R. Menegazzo, A. Gottardo, S. Lenzi, S. Lunardi, G. Montagnoli, F. Scarlassara, C. Ur, G. L. Bianco, A. Zucchiatti, M. Kmiecik, A. Maj, W. Meczynski, A. Dewald, T. Pissulla, and G. Pollarolo (2011), *Physics Letters B* **697** (4), 288.

Morales, A., G. Benzoni, H. Watanabe, Y. Tsunoda, T. Otsuka, *et al.* (2017), *Phys. Lett. B* **765**, 328.

Morfouace, P., *et al.* (2015), *Physics Letters B* **751**, 306.

Motobayashi, T., Y. Ikeda, K. Ieki, M. Inoue, N. Iwasa, T. Kikuchi, M. Kurokawa, S. Moriya, S. Ogawa, H. Murakami, S. Shimoura, Y. Yanagisawa, T. Nakamura, Y. Watanabe, M. Ishihara, T. Teranishi, H. Okuno, and R. Casten (1995), *Physics Letters B* **346** (1), 9.

Mutschler, A., A. Lemasson, O. Sorlin, D. Bazin, C. Borcea, R. Borcea, Z. Dombradi, J.-P. Ebran, A. Gade, H. Iwasaki, E. Khan, A. Lepailleur, F. Recchia, T. Roger, F. Rotaru, D. Sohler, M. Stanoiu, S. R. Stroberg, J. A. Tostevin, M. Vandebrouck, D. Weisshaar, and K. Wimmer (2016a), *Nature Physics* **in press**.

Mutschler, A., O. Sorlin, A. Lemasson, D. Bazin, C. Borcea, R. Borcea, A. Gade, H. Iwasaki, E. Khan, A. Lepailleur, F. Recchia, T. Roger, F. Rotaru, M. Stanoiu, S. R. Stroberg, J. A. Tostevin, M. Vandebrouck, D. Weisshaar, and K. Wimmer (2016b), *Phys. Rev. C* **93**, 034333.

Myers, E. G. (2013), *International Journal of Mass Spectrometry* **349-350**, 107, 100 years of Mass Spectrometry.

Nakada, H. (2008), *Phys. Rev. C* **78**, 054301.

Nakada, H., K. Sugiura, and J. Margueron (2013), *Phys. Rev. C* **87**, 067305.

Nakamura, T., N. Kobayashi, Y. Kondo, Y. Satou, N. Aoi, H. Baba, S. Deguchi, N. Fukuda, J. Gibelin, N. Inabe, M. Ishihara, D. Kameda, Y. Kawada, T. Kubo, K. Kusaka, A. Mengoni, T. Motobayashi, T. Ohnishi, M. Ohtake, N. A. Orr, H. Otsu, T. Otsuka, A. Saito, H. Sakurai, S. Shimoura, T. Sumikama, H. Takeda, E. Takeshita, M. Takechi, S. Takeuchi, Y. Togano, K. Yoneda, A. Yoshida, and K. Yoshida (2009), *Phys. Rev. Lett.* **103**, 262501.

Nakamura, T., N. Kobayashi, Y. Kondo, Y. Satou, J. A. Tostevin, Y. Utsuno, N. Aoi, H. Baba, N. Fukuda, J. Gibelin, N. Inabe, M. Ishihara, D. Kameda, T. Kubo, T. Motobayashi, T. Ohnishi, N. A. Orr, H. Otsu, T. Otsuka, H. Sakurai, T. Sumikama, H. Takeda, E. Takeshita, M. Takechi, S. Takeuchi, Y. Togano, and K. Yoneda (2014), *Phys. Rev. Lett.* **112**, 142501.

Nakamura, T., H. Sakurai, and H. Watanabe (2017), *Progress in Particle and Nuclear Physics* **97**, 53.

Navratil, P., *et al.* (2007), *Phys. Rev. Lett.* **99**, 042501.

NNDC, (2016), “Nudat 2,” <http://www.nndc.bnl.gov/nudat2/>.

Nowacki, F., and A. Poves (2009), *Phys. Rev. C* **79**, 014310.

Nummela, S., P. Baumann, E. Caurier, P. Dessagne, A. Jokinen, A. Knipper, G. Le Scornet, C. Miehé, F. Nowacki, M. Oinonen, Z. Radivojevic, M. Ramdhane, G. Walter, and J. Äystö (2001), *Phys. Rev. C* **63**, 044316.

Ogawa, M., *et al.* (1978), *Phys. Rev. Lett.* **41**, 289.

Orlandi, R., D. Mücher, R. Raabe, A. Jungclaus, S. Pain, V. Bildstein, R. Chapman, G. de Angelis, J. Johansen, P. V. Duppén, A. Andreyev, S. Bottoni, T. Cocolios, H. D. Witte, J. Diriken, J. Elseviers, F. Flavigny, L. Gaffney, R. Gernhäuser, A. Gottardo, M. Huyse, A. Illana, J. Konki, T. Kröll, R. Krücken, J. Lane, V. Liberati, B. Marsh, K. Nowak, F. Nowacki, J. Pakarinen, E. Rapisarda, F. Recchia, P. Reiter, T. Roger, E. Sahin, M. Seidlitz, K. Sieja, J. Smith, J. V. Dobón, M. von Schmid, D. Voulot, N. Warr, F. Wenander, and K. Wimmer (2015), *Physics Letters B* **740**, 298.

Osnes, E., and D. Strottman (1992), *Phys. Rev. C* **45**, 662.

Osterfeld, F. (1992), *Rev. Mod. Phys.* **64**, 491.

Otsuka, T. (2002), *Progress of Theoretical Physics Supplement* **146**, 6.

Otsuka, T. (2013), *Phys. Scr. T152*, 014007.

Otsuka, T. (2014), *GENSHIKAKU KENKYU* **59**, 86.

Otsuka, T., R. Fujimoto, Y. Utsuno, B. A. Brown, M. Honma, and T. Mizusaki (2001), *Phys. Rev. Lett.* **87**, 082502.

Otsuka, T., T. Matsuo, and D. Abe (2006), *Phys. Rev. Lett.* **97**, 162501.

Otsuka, T., and A. Schwenk (2012), *Nucl. Phys. News* **22**, 12.

Otsuka, T., and T. Suzuki (2013), *Few-Body Syst.* **54**, 891.

Otsuka, T., T. Suzuki, R. Fujimoto, H. Grawe, and Y. Akaishi (2005), *Phys. Rev. Lett.* **95**, 232502.

Otsuka, T., T. Suzuki, J. D. Holt, A. Schwenk, and Y. Akaishi (2010a), *Phys. Rev. Lett.* **105**, 032501.

Otsuka, T., T. Suzuki, M. Honma, Y. Utsuno, N. Tsunoda, K. Tsukiyama, and M. Hjorth-Jensen (2010b), *Phys. Rev. Lett.* **104**, 012501.

Otsuka, T., T. Suzuki, and Y. Utsuno (2008), *Nuclear Physics A* **805** (1), 127c.

Otsuka, T., and Y. Tsunoda (2016), *J. Phys. G: Nucl. Part. Phys.* **43**, 024009.

Ozawa, A., T. Suzuki, and I. Tanihata (2001), *Nucl. Phys. A* **693** (1), 32.

Ozawa, A., *et al.* (2000), *Phys. Rev. Lett.* **84**, 5493.

Papuga, J., M. L. Bissell, K. Kreim, K. Blaum, B. A. Brown, M. De Rydt, R. F. Garcia Ruiz, H. Heylen, M. Kowalska, R. Neugart, G. Neyens, W. Nörtershäuser, T. Otsuka, M. M. Rajabali, R. Sánchez, Y. Utsuno, and D. T. Yor-

danov (2013), *Phys. Rev. Lett.* **110**, 172503.

Parker, J. J., I. Wiedenhöver, P. D. Cottle, J. Baker, D. McPherson, M. A. Riley, D. Santiago-Gonzalez, A. Volya, V. M. Bader, T. Baugher, D. Bazin, A. Gade, T. Ginter, H. Iwasaki, C. Loelius, C. Morse, F. Recchia, D. Smalley, S. R. Stroberg, K. Whitmore, D. Weisshaar, A. Lemasson, H. L. Crawford, A. O. Macchiavelli, and K. Wimmer (2017), *Phys. Rev. Lett.* **118**, 052501.

Paschalis, S., I. Lee, A. Macchiavelli, C. Campbell, M. Cromaz, S. Gros, J. Pavan, J. Qian, R. Clark, H. Crawford, D. Doering, P. Fallon, C. Lionberger, T. Loew, M. Petri, T. Stezelberger, S. Zimmermann, D. Radford, K. Lagergren, D. Weisshaar, R. Winkler, T. Glasmacher, J. Anderson, and C. Beausang (2013), *Nucl. Instrum. Methods Phys. Res. A* **709**, 44.

Paul, N., et al. (2017), *Phys. Rev. Lett.* **118**, 032501.

Péru, S., M. Girod, and J. F. Berger (2000), *Eur. Phys. J. A* **9** (1), 35.

Pieper, S. C. (2005), *Nucl. Phys. A* **751**, 516.

Pieper, S. C., and R. B. Wiringa (2001), *Annu. Rev. Nucl. Part. Sci.* **51**, 53.

Piskoř, Š., J. Novák, E. Šimečková, J. Cejpek, V. Kroha, J. Dobeš, and P. Navrátil (2000), *Nuclear Physics A* **662**, 112.

Pittel, S., P. Federman, G. E. Arenas Peris, R. F. Casten, and W. T. Chou (1993), *Phys. Rev. C* **48**, 1050.

Pollacco, E., D. Beaumel, P. Roussel-Chomaz, E. Atkin, P. Baron, J. P. Baronick, E. Becheva, Y. Blumenfeld, A. Boujrad, A. Drouart, F. Druilhole, P. Edelbruck, M. Gelin, A. Gillibert, C. Houarner, V. Lapoux, L. Lavergne, G. Leberthe, L. Leterrier, V. Le Ven, F. Lugiez, L. Nalpas, L. Olivier, B. Paul, B. Raine, A. Richard, M. Rouger, F. Saillant, F. Skaza, M. Triponez, M. Vilmay, E. Wanlin, and M. Wittwer (2005), *Eur. Phys. J. A* **25** (1), 287.

Poves, A., and J. Retamosa (1987), *Phys. Lett. B* **184**, 311.

Poves, A., and A. Zuker (1981), *Phys. Rep.* **70** (4), 235.

Prisciandaro, J. I., et al. (2001), *Phys. Lett. B* **510**, 17.

Prokop, C. J., et al. (2015), *Phys. Rev. C* **92**, 061302.

Pudliner, B. S., et al. (1997), *Phys. Rev. C* **56**, 1720.

Raman, S., C. N. Jr., and P. Tikkkanen (2001), *Atomic Data and Nuclear Data Tables* **78** (1), 1.

Reed, M. W., I. J. Cullen, P. M. Walker, Y. A. Litvinov, K. Blaum, F. Bosch, C. Brandau, J. J. Carroll, D. M. Cullen, A. Y. Deo, B. Detwiler, C. Dimopoulou, G. D. Dracoulis, F. Farinon, H. Geissel, E. Haettner, M. Heil, R. S. Kempley, R. Knöbel, C. Kozhuharov, J. Kurcewicz, N. Kuzminchuk, S. Litvinov, Z. Liu, R. Mao, C. Nociforo, F. Nolden, W. R. Plass, A. Prochazka, C. Scheidenberger, M. Steck, T. Stöhlker, B. Sun, T. P. D. Swan, G. Trees, H. Weick, N. Winckler, M. Winkler, P. J. Woods, and T. Yamaguchi (2010), *Phys. Rev. Lett.* **105**, 172501.

Régis, J.-M., et al. (2017), *Phys. Rev. C* **95**, 054319.

Rejmund, M., et al. (2007), *Phys. Rev. C* **76**, 021304(R).

Retamosa, J., E. Caurier, F. Nowacki, and A. Poves (1997), *Phys. Rev. C* **55**, 1266.

Riley, L. A., M. A. Abdelqader, D. Bazin, M. J. Bojazi, B. A. Brown, C. M. Campbell, J. A. Church, P. D. Cottle, D. C. Dinca, J. Enders, A. Gade, T. Glasmacher, M. Honma, S. Horibe, Z. Hu, K. W. Kemper, W. F. Mueller, H. Olliver, T. Otsuka, B. C. Perry, B. T. Roeder, B. M. Sherrill, T. P. Spencer, and J. R. Terry (2005), *Phys. Rev. C* **72**, 024311.

Ring, P., and P. Schuck (1980), *The Nuclear Many-Body Problem* (Springer-Verlag, Berlin).

Rodríguez, T. R., and J. L. Egido (2007), *Phys. Rev. Lett.* **99**, 062501.

Rodríguez, T. R., and J. L. Egido (2011), *Phys. Rev. C* **84**, 051307.

Rodríguez-Guzmán, R., J. L. Egido, and L. M. Robledo (2002), *Phys. Rev. C* **65**, 024304.

Rotaru, F., F. Negoita, S. Grévy, J. Mrazek, S. Lukyanov, F. Nowacki, A. Poves, O. Sorlin, C. Borcea, R. Borcea, A. Buta, L. Cáceres, S. Calinescu, R. Chevrier, Z. Dombrádi, J. M. Daugas, D. Lebhertz, Y. Penionzhkevich, C. Petrone, D. Sohler, M. Stanoi, and J. C. Thomas (2012), *Phys. Rev. Lett.* **109**, 092503.

Rubio, B., and W. Gelletly (2009), in *The Euroschool Lectures on Physics with Exotic Beams, Vol. III*, Lecture Notes in Physics, Vol. 764, edited by J. Al-Khalili and E. Roeckl (Springer Berlin Heidelberg) pp. 99–151.

Rutherford, H. (1911), *Philosophical Magazine* **21**, 669?

Sagawa, H., and G. Colò (2014), *Progress in Particle and Nuclear Physics* **76**, 76.

Sahin, E., et al. (2017), *Phys. Rev. Lett.* **118**, 242502.

Sakurai, H., S. Lukyanov, M. Notani, N. Aoi, D. Beaumel, N. Fukuda, M. Hirai, E. Ideguchi, N. Imai, M. Ishihara, H. Iwasaki, T. Kubo, K. Kusaka, H. Kumagai, T. Nakamura, H. Ogawa, Y. Penionzhkevich, T. Teranishi, Y. Watanabe, K. Yoneda, and A. Yoshida (1999), *Phys. Lett. B* **448**, 180.

Santamaría, C., C. Louchart, A. Obertelli, V. Werner, P. Doornenbal, F. Nowacki, G. Authelet, H. Baba, D. Calvet, F. Château, A. Corsi, A. Delbart, J.-M. Gheller, A. Gillibert, T. Isobe, V. Lapoux, M. Matsushita, S. Momiyama, T. Motobayashi, M. Niikura, H. Otsu, C. Péron, A. Peyaud, E. C. Pollacco, J.-Y. Roussé, H. Sakurai, M. Sasano, Y. Shiga, S. Takeuchi, R. Taniuchi, T. Uesaka, H. Wang, K. Yoneda, F. Browne, L. X. Chung, Z. Dombrádi, S. Franchoo, F. Giacoppo, A. Gottardo, K. Hadynska-Klek, Z. Korkulu, S. Koyama, Y. Kubota, J. Lee, M. Lettmann, R. Lozeva, K. Matsui, T. Miyazaki, S. Nishimura, L. Olivier, S. Ota, Z. Patel, N. Pietralla, E. Sahin, C. Shand, P.-A. Söderström, I. Stefan, D. Steppenbeck, T. Sumikama, D. Suzuki, Z. Vajta, J. Wu, and Z. Xu (2015), *Phys. Rev. Lett.* **115**, 192501.

Santiago-Gonzalez, D., I. Wiedenhöver, V. Abramkina, M. L. Avila, T. Baugher, D. Bazin, B. A. Brown, P. D. Cottle, A. Gade, T. Glasmacher, K. W. Kemper, S. McDaniel, A. Rojas, A. Ratkiewicz, R. Meharchand, E. C. Simpson, J. A. Tostevin, A. Volya, and D. Weisshaar (2011), *Phys. Rev. C* **83**, 061305.

Scheit, H., T. Glasmacher, B. A. Brown, J. A. Brown, P. D. Cottle, P. G. Hansen, R. Harkewicz, M. Hellström, R. W. Ibbotson, J. K. Jewell, K. W. Kemper, D. J. Morrissey, M. Steiner, P. Thiroff, and M. Thoennessen (1996), *Phys. Rev. Lett.* **77**, 3967.

Schiffer, J. P., and W. W. True (1976), *Rev. Mod. Phys.* **48**, 191.

Schiffer, J. P., et al. (2004), *Phys. Rev. Lett.* **92**, 162501.

Schwerdtfeger, W., P. G. Thiroff, K. Wimmer, D. Habs, H. Mach, T. R. Rodriguez, V. Bildstein, J. L. Egido, L. M. Fraile, R. Gernhäuser, R. Hertenberger, K. Heyde, P. Hoff, H. Hübel, U. Köster, T. Kröll, R. Krücken, R. Lutter, T. Morgan, and P. Ring (2009), *Phys. Rev. Lett.* **103**, 012501.

Seweryniak, D., et al. (2007), *Phys. Rev. Lett.* **99**, 022504.

de Shalit, A., and M. Goldhaber (1953), *Phys. Rev.* **92**, 1211.

Shimizu, K., M. Ichimura, and A. Arima (1974), Nucl. Phys. A **226**, 282.

Signoracci, A., and B. A. Brown (2007), Phys. Rev. Lett. **99**, 099201.

Simonis, J., K. Hebeler, J. D. Holt, J. Menéndez, and A. Schwenk (2016), Phys. Rev. C **93**, 011302.

Simpson, E. C., and J. A. Tostevin (2010), Phys. Rev. C **82**, 044616.

Simpson, E. C., J. A. Tostevin, D. Bazin, B. A. Brown, and A. Gade (2009), Phys. Rev. Lett. **102**, 132502.

Sinatkas, J., L. Skouras, D. Strottman, and J. Vergados (1992), J. Phys. G **18**, 1377.

Skyrme, T. (1958), Nuclear Physics **9** (4), 615 .

Smirnova, N. A., B. Bally, K. Heyde, F. Nowacki, and K. Sieja (2010), Phys. Lett. B **686**, 109.

Smirnova, N. A., K. Heyde, B. Bally, F. Nowacki, and K. Sieja (2012), Phys. Rev. C **86**, 034314.

Sorlin, O., and M.-G. Porquet (2008), Progress in Particle and Nuclear Physics **61** (2), 602 .

Sorlin, O., and M.-G. Porquet (2013), Phys. Scr. **T152**, 014003.

Stancu, F., D. M. Brink, and H. Flocard (1977), Phys. Lett. B **68**, 108.

Stanoiu, M., et al. (2004), Phys. Rev. C **69**, 034312.

Steppenbeck, D., S. Takeuchi, N. Aoi, P. Doornenbal, M. Matsushita, H. Wang, H. Baba, N. Fukuda, S. Go, M. Honma, J. Lee, K. Matsui, S. Michimasa, T. Motobayashi, D. Nishimura, T. Otsuka, H. Sakurai, Y. Shiga, P.-A. Söderström, T. Sumikama, H. Suzuki, R. Taniuchi, Y. Utsuno, J. J. Valiente-Dobón, and K. Yoneda (2013), Nature **502**, 207.

Steppenbeck, D., et al. (2015), Phys. Rev. Lett. **114**, 252501.

Storm, M., A. Watt, and R. Whitehead (1983), J. Phys. G **9**, L165.

Stroberg, S. R., A. Gade, J. A. Tostevin, V. M. Bader, T. Baugher, D. Bazin, J. S. Berryman, B. A. Brown, C. M. Campbell, K. W. Kemper, C. Langer, E. Lunderberg, A. Lemasson, S. Noji, F. Recchia, C. Walz, D. Weisshaar, and S. J. Williams (2014), Phys. Rev. C **90**, 034301.

Stroberg, S. R., et al. (2016), Phys. Rev. C **91**, 041302 (R).

Sugano, S. (1991), “Microcluster physics,” in *Springer Series in Materials Science, Vol. 20*, edited by J. Toennies (Springer-Verlag, Berlin Heidelberg).

Suzuki, T., R. Fujimoto, and T. Otsuka (2003), Phys. Rev. C **67**, 044302.

Suzuki, T., and T. Otsuka (2008), Phys. Rev. C **78**, 061301.

Suzuki, T., T. Otsuka, C. Yuan, and N. Alahari (2016a), Phys. Lett. B **753**, 199.

Suzuki, Y., H. Nakada, and S. Miyahara (2016b), Phys. Rev. C **94**, 024343.

Takeuchi, S., M. Matsushita, N. Aoi, P. Doornenbal, K. Li, T. Motobayashi, H. Scheit, D. Steppenbeck, H. Wang, H. Baba, D. Bazin, L. Cáceres, H. Crawford, P. Fallon, R. Gernhäuser, J. Gibelin, S. Go, S. Grévy, C. Hinke, C. R. Hoffman, R. Hughes, E. Ideguchi, D. Jenkins, N. Kobayashi, Y. Kondo, R. Krücken, T. Le Bleis, J. Lee, G. Lee, A. Matta, S. Michimasa, T. Nakamura, S. Ota, M. Petri, T. Sako, H. Sakurai, S. Shimoura, K. Steiger, K. Takahashi, M. Takechi, Y. Togano, R. Winkler, and K. Yoneda (2012), Phys. Rev. Lett. **109**, 182501.

Takeuchi, S., T. Motobayashi, Y. Togano, M. Matsushita, N. Aoi, K. Demichi, H. Hasegawa, and H. Murakami (2014), Nucl. Instrum. Methods Phys. Res. A **763**, 596 .

Talmi, I., and I. Unna (1960), Phys. Rev. Lett. **4**, 469.

Tanaka, K., et al. (2010), Phys. Rev. Lett. **104**, 062701.

Tanihata, I., H. Hamagaki, O. Hashimoto, Y. Shida, N. Yoshikawa, K. Sugimoto, O. Yamakawa, T. Kobayashi, and N. Takahashi (1985), Phys. Rev. Lett. **55**, 2676.

Tarasov, O., R. Allatt, J. Angélique, R. Anne, C. Borcea, Z. Dlouhy, C. Donzaud, S. Grévy, D. Guillemaud-Mueller, M. Lewitowicz, S. Lukyanov, A. Mueller, F. Nowacki, Y. Oganessian, N. Orr, A. Ostrowski, R. Page, Y. Peñionzhkevich, F. Pougheon, A. Reed, M. Saint-Laurent, W. Schwab, E. Sokol, O. Sorlin, W. Trinder, and J. Winfield (1997), Phys. Lett. B **409** (1), 64 .

Terasaki, J., H. Flocard, P.-H. Heenen, and P. Bonche (1997), Nuclear Physics A **621** (3), 706 .

Terry, J., D. Bazin, B. Brown, C. Campbell, J. Church, J. Cook, A. Davies, D.-C. Dinca, J. Enders, A. Gade, T. Glasmacher, P. Hansen, J. Lecouey, T. Otsuka, B. Pritychenko, B. Sherrill, J. Tostevin, Y. Utsuno, K. Yoneda, and H. Zwahlen (2006), Phys. Lett. B **640** (3), 86 .

Terry, J. R., B. A. Brown, C. M. Campbell, J. M. Cook, A. D. Davies, D.-C. Dinca, A. Gade, T. Glasmacher, P. G. Hansen, B. M. Sherrill, H. Zwahlen, D. Bazin, K. Yoneda, J. A. Tostevin, T. Otsuka, Y. Utsuno, and B. Pritychenko (2008), Phys. Rev. C **77**, 014316.

Thibault, C., R. Klapisch, C. Rigaud, A. M. Poskanzer, R. Prieels, L. Lessard, and W. Reisdorf (1975), Phys. Rev. C **12**, 644.

Thirolf, P., B. Pritychenko, B. Brown, P. Cottle, M. Chromik, T. Glasmacher, G. Hackman, R. Ibbotson, K. Kemper, T. Otsuka, L. Riley, and H. Scheit (2000), Physics Letters B **485**, 16 .

Togano, Y., et al. (2016), Phys. Lett. B **761**, 412 .

Togashi, T., Y. Tsunoda, T. Otsuka, and N. Shimizu (2016), Phys. Rev. Lett. **117**, 172502.

Tolos, L., B. Friman, and A. Schwenk (2008), Nucl. Phys. A **806**, 105.

Tostevin, J., and A. Gade (2014), Phys. Rev. C **90**, 057602.

Tostevin, J. A. (1999), J. Phys. G **25** (4), 735.

Tostevin, J. A., G. Podolyák, B. A. Brown, and P. G. Hansen (2004), Phys. Rev. C **70**, 064602.

Towner, I. S. (1987), Phys. Rep. **155**, 263.

Tsukiyama, K., T. Otsuka, and R. Fujimoto (2015), Prog. Theor. Exp. Phys. **2015**, 093D01.

Tsunoda, N. (2018), private communication.

Tsunoda, N., T. Otsuka, N. Shimizu, M. Hjorth-Jensen, K. Takayanagi, and T. Suzuki (2017), Phys. Rev. C **95**, 021304.

Tsunoda, N., T. Otsuka, K. Tsukiyama, and M. Hjorth-Jensen (2011), Phys. Rev. C **84**, 044322.

Tsunoda, N., K. Takayanagi, M. Hjorth-Jensen, and T. Otsuka (2014a), Phys. Rev. C **89**, 024309.

Tsunoda, Y., T. Otsuka, N. Shimizu, M. Honma, and Y. Utsuno (2014b), Phys. Rev. C **89**, 031301 (R).

Umeya, A., and K. Muto (2004), Phys. Rev. C **69**, 024306.

Umeya, A., and K. Muto (2006), Phys. Rev. C **74**, 034330.

Uozumi, Y., et al. (1994a), Phys. Rev. C **50**, 263.

Uozumi, Y., et al. (1994b), Nucl. Phys. A **576**, 123.

Utsuno, Y., T. Otsuka, B. A. Brown, M. Honma, T. Mizusaki, and N. Shimizu (2012a), Phys. Rev. C **86**, 051301.

Utsuno, Y., T. Otsuka, B. A. Brown, M. Honma, T. Mizusaki, and N. Shimizu (2012b), Prog. Theor. Phys. Suppl. **196**, 304.

Utsuno, Y., T. Otsuka, T. Mizusaki, and M. Honma (1999), Phys. Rev. C **60**, 054315.

Utsuno, Y., T. Otsuka, T. Mizusaki, and M. Honma (2004), *Phys. Rev. C* **70**, 044307.

Utsuno, Y., T. Otsuka, T. Mizusaki, and M. Honma (2006), *Journal of Physics: Conference Series* **49** (1), 126.

Utsuno, Y., T. Otsuka, Y. Tsunoda, N. Shimizu, M. Honma, T. Togashi, and T. Mizusaki (2015a), *JPS Conference Proceedings* **6**, 010007.

Utsuno, Y., N. Shimizu, T. Otsuka, T. Yoshida, and Y. Tsunoda (2015b), *Phys. Rev. Lett.* **114**, 032501.

Vautherin, D., and D. Brink (1970), *Physics Letters B* **32** (3), 149 .

Volya, A., and V. Zelevinsky (2005), *Phys. Rev. Lett.* **94**, 052501.

Wang, Y. Z., J. Z. Gu, X. Z. Zhang, and J. M. Dong (2011), *Phys. Rev. C* **84**, 044333.

Warburton, E. K., J. A. Becker, and B. A. Brown (1990), *Phys. Rev. C* **41**, 1147.

Warburton, E. K., and B. A. Brown (1992), *Phys. Rev. C* **46**, 923.

Watanabe, H., G. Lorusso, S. Nishimura, Z. Xu, *et al.* (2013), *Phys. Rev. Lett.* **111**, 152501.

von Weizsäcker, C. F. (1935), *Z. Phys.* **96**, 431.

Werner, T., J. Sheikh, M. Misu, W. Nazarewicz, J. Rikovska, K. Heeger, A. Umar, and M. Strayer (1996), *Nuclear Physics A* **597** (3), 327 .

Werner, T., J. Sheikh, W. Nazarewicz, M. Strayer, A. Umar, and M. Misu (1994), *Physics Letters B* **335** (3), 259 .

Wienholtz, F., *et al.* (2013), *Nature* **498**, 346.

Wildenthal, B. H., E. Newman, and R. L. Auble (1971), *Phys. Rev. C* **3**, 1199.

Wilkinson, D., and D. Alburger (1959), *Phys. Rev.* **113**.

Wimmer, K., T. Kröll, R. Krücke, V. Bildstein, R. Gernhäuser, B. Bastin, N. Bree, J. Diriken, P. Van Duppen, M. Huyse, N. Patronis, P. Vermaelen, D. Voulot, J. Van de Walle, F. Wenander, L. M. Fraile, R. Chapman, B. Hadinia, R. Orlandi, J. F. Smith, R. Lutter, P. G. Thirolf, M. Labiche, A. Blazhev, M. Kalkühler, P. Reiter, M. Seidlitz, N. Warr, A. O. Macchiavelli, H. B. Jeppe- sen, E. Fiori, G. Georgiev, G. Schrieder, S. Das Gupta, G. Lo Bianco, S. Nardelli, J. Butterworth, J. Johansen, and K. Riisager (2010), *Phys. Rev. Lett.* **105**, 252501.

Winkler, R., A. Gade, T. Baugher, D. Bazin, B. A. Brown, T. Glasmacher, G. F. Grinyer, R. Meharchand, S. McDaniel, A. Ratkiewicz, and D. Weisshaar (2012), *Phys. Rev. Lett.* **108**, 182501.

Wood, J., E. Zganjar, C. D. Coster, and K. Heyde (1999), *Nucl. Phys. A* **651** (4), 323 .

Yamashita, M., *et al.* (2011), *Phys. Lett. B* **697**, 90.

Yazaki, K. (1977), *Nucl. Phys. A* **277**, 189.

Yoneda, K., A. Obertelli, A. Gade, D. Bazin, B. A. Brown, C. M. Campbell, J. M. Cook, P. D. Cottle, A. D. Davies, D.-C. Dinca, T. Glasmacher, P. G. Hansen, T. Hoagland, K. W. Kemper, J.-L. Lecouey, W. F. Mueller, R. R. Reynolds, B. T. Roeder, J. R. Terry, J. A. Tostevin, and H. Zwahlen (2006), *Phys. Rev. C* **74**, 021303.

Yoneda, K., H. Sakurai, T. Gomi, T. Motobayashi, N. Aoi, N. Fukuda, U. Futakami, Z. Gacs, Y. Higurashi, N. Imai, N. Iwasa, H. Iwasaki, T. Kubo, M. Kunib, M. Kurokawa, Z. Liu, T. Minemura, A. Saito, M. Serata, S. Shimoura, S. Takeuchi, Y. Watanabe, K. Yamada, Y. Yanagisawa, K. Yogo, A. Yoshida, and M. Ishihara (2001), *Physics Letters B* **499** (3-4), 233 .

Yordanov, D. T., M. L. Bissell, K. Blaum, M. De Rydt, C. Geppert, M. Kowalska, J. Krämer, K. Kreim, A. Krieger, P. Lievens, T. Neff, R. Neugart, G. Neyens, W. Nörterhäuser, R. Sánchez, and P. Vingerhoets (2012), *Phys. Rev. Lett.* **108**, 042504.

Yoro, K. (1980), *Nucl. Phys. A* **333**, 67.

Yoshida, S. (2017), Master Thesis, University of Tokyo.

Yuan, C., T. Suzuki, T. Otsuka, F. Xu, and N. Tsunoda (2012), *Phys. Rev. C* **85**, 064324.

Yukawa, H. (1935), *Proc. Phys. Math. Soc. Japan* **17**, 48.

Zeldes, N., T. S. Dumitrescu, and H. S. Köhler (1983), *Nucl. Phys. A* **399**, 11.

Zuker, A. (2003), *Phys. Rev. Lett.* **90**, 042502.